Observing High Redshift Galaxy Clusters At Sub-millimetre Wavelengths

Connor Michael Anthony Smith

A Thesis submitted to
Cardiff University
for the degree of
Doctor of Philosophy

March 2020

"You don't want to be good...you want to be memorable"
Professor Patrick Sutton

Acknowledgements

"Can I be in your thesis?"

Alasdair 'Ali' James

Blimey I made it. When I got my PhD offer I was convinced that it was some prank, and even when I turned up and they did not tell me to go away, I was still convinced they sent the e-mail to the wrong person. But here I am just about surviving the last 3.5 years, and I suppose this is the bit I thank those who helped with my survival.

Obviously I would like to thank my family, especially my parents. You guys have always been there for me. Even though you still have no idea what I actually do, you have always been supportive, helpful and encouraging, for which I will always be eternally grateful.

Of course I would not be able to do this PhD without the help of my supervisors Walter Gear and Stephen Eales. You guys never stopped being supportive and continued to push me, even when things were not going well. You guys have always been there for me* and been incredibly helpful, patient and knowledgeable. Even when I came to you with stupid questions, or helped me see my stupid mistakes, you guys were always there for me and always took the time out to help me. I will always be thankful to you guys, and apologise for all the questionable English I inflicted on you. You also let me go to Hawaii which was pretty cool.

I would like to thank my examiners Jim Geach and Tim Davis for giving me a good grilling in my viva. Even though the viva was done in the middle of a global pandemic you guys made it fun and enjoyable, and your comments have definitely improved the quality of this thesis.

Next is all the people in the Galaxy office. Andy, Aris, Brad, Chris, Dan, Eleonora, Eve, Gayathri, Hannah, James, Jeni, Lil Dan, Lottie, Nikki, Olivia, Phil, Rosie, Ruth, Tom, Tom, Zoe, some of you have gone on to better things/places, but you guys have made the my time here some of the best. I will always remember the random chats we have had in the office, the random lunch outings, the Christmas meals, summer BBQs, and of course special tea. I never had a dull day working with you guys and you helped me keep my sanity when things were getting a bit crap, so for that I thank you.

Of course I want to thank everyone else in the department. I would list you all by name but I think that would take up too much space. But I want to thank you

*Even when Walter ran to Ireland

all for all the bowling trips, go-karting, rugby trips, the pub trips, and coffee/cake. Everyone in this department has made me feel welcome and made working here an absolute pleasure, and I will never forget my time here.

Now for some special mentions. Firstly I want to thank stack overflow for solving the majority of my coding woes. Next I thank Andy for keeping the Flute and Tankard stocked with a good variety of ciders, and a place I can go in and simply say "the usual please". Finally thank you to Maddie and the Bandaoke band for providing some of the best drunken entertainment I have had, and not telling me to go away when I want to sing Mamma Mia for the 6th time.

Of course there is one person who has given me the most help and had the biggest impact on my PhD, and that is of course Dr Matthew Smith[†]. Without you Matt I would still be trying to log into my computer on my first day. Even though you have questionable tastes in which federation star ship is the best, your knowledge has been invaluable, and you always had the time to help me (even with my stupidest questions and questionable coding). I would not have been able to finish this PhD without your assistance and for that you will always have my thanks.

So I suppose that is everyone. Hope you enjoy the thesis (apologies for any boring bits).

[†]Doctor of Philiosphy

Abstract

This thesis aims to investigate high redshift galaxy clusters, focusing on Far Infrared (FIR) and Sub-millimeter (sub-mm) observations. The main focus is to observe the potential environmental effects on cluster galaxies, and see if and how these these processes effect the evolutionary path a galaxy is on.

Using SCUBA-2 and *Herschel* data I investigate the star forming properties of two mature, high redshift galaxy clusters, CLJ1449 (at redshift two) and JKCS041 (at redshift 1.8). Using high-resolution Atacama Large Millimetre Array (ALMA) and Jansky Very Large Array data I identify potentially confused galaxies, and use the Bayesian inference tool XID+ to estimate fluxes for them. Using archival optical and near-infrared data with the energy-balance code CIGALE I calculate star formation rates and stellar masses for all our cluster members. For both clusters I estimate star formation rates (SFRs) between 12-1600 $\mathrm{M_\odot\,yr^{-1}}$ over the entire 3 Mpc radial range. In the central 0.5 Mpc region I find SFRs of 800 ± 200 $\mathrm{M_\odot\,yr^{-1}}$ for CLJ1449, and 770 ± 100 $\mathrm{M_\odot\,yr^{-1}}$ for JKCS041. When converted to a SFR-density this gives $(1.2 \pm 0.3) \times 10^4$ and $(1.3 \pm 0.1) \times 10^4\,\mathrm{M_\odot\,yr^{-1}Mpc^{-3}}$ for CLJ144 and JKCS041 respectively, which are five orders of magnitude greater then expected field values. This indicates that there is indeed a reversal in the SFR-density relation in both of these clusters,and the majority of the star formation is occurring in the densest regions of the cluster (opposed to what happens in local clusters).

When I look at the SFR-stellar mass relation I find a deviation between the two clusters. For CLJ1449, I find that all the cluster galaxies either exist on the galaxy main sequence, or just above it in a region dominated by star burst galaxies. There does appear to be a radial trend, with those galaxies closest to the cluster core showing the lowest stellar masses, which could indicate environmental influences quenching these galaxies. For JKCS041, the majority of galaxies lie below the main sequence, with very few galaxies exhibiting star-burst behaviour. This could show that the galaxies within are being quenched and the environment is having a profound effect. When comparing these clusters to other high redshift clusters, I see that CLJ1449 seems to follow expected scaling relations for clusters. JKCS041 on the other hand deviates significantly. Since the mass of JKCS041 is significantly larger then other clusters at this redshift, it could show some of the first direct evidence that a clusters mass has an effect on the galaxies that reside within it.

Using band 3 ALMA spectral scans, I searched for a potential proto-cluster in an over-density of red *Herschel* sources. I used a match filter technique to try and identify any potential spectral lines in the ALMA data, and identified 57 detections

greater than 4σ (six of these are associated with continuum sources). Assigning redshifts to all the sources, I identified an over-density at redshift 3.64, which I take as the redshift of the cluster. Using velocity dispersions I assign proto-cluster membership, with 10 sources being a part of the structure.

From the cluster members I estimate a velocity dispersion for the cluster of $\sim$570 kms^{-1}, which corresponds to a mass of $\sim 2.5 \times 10^{13}\,\mathrm{M}_{\odot}$. This means this proto-cluster is the progenitor to a Coma like cluster. Calculating gas masses (directly from the CO spectra) and stellar masses (from *Spitzer* IRAC data) I find gas fractions of $\sim$35%. These gas fractions fall below expected scaling relations, and could show that these galaxies are undergoing a period of extreme star formation. These galaxies also have gas fractions that fall below what is seen in field galaxies. This could indicate that environmental processes are already at work.

With those sources with continuum measurements, high SFRs were found (greater then $1500\,\mathrm{M}_{\odot}\mathrm{yr}^{-1}$), and they exhibit behaviour similar to sub-mm galaxies. This extreme star formation cannot be supported for long, and will start to passively evolve after $\sim$50 Myr, and could be the beginning of a red sequence of galaxies.

Publications

First Author Publications

Smith, C. M. A., Gear, W. K., Smith, M. W. L., et al. 2019; *Revealing dust-obscured star formation in CLJ1449+0856, a cluster at z=2*, MNRAS, 486, 4304

Smith, C. M. A., Smith, M. W. L., Gear, W. K., et al. 2019; *Star formation in JKCS041: A high redshift cluster caught in the middle of transitioning?*, Submitted to MNRAS

Co-Author Publications

Saintonge, A. Wilson, C. D., Xiao, T., et al. 2018; *JINGLE, a JCMT legacy survey of dust and gas for galaxy evolution studies - I. Survey overview and first results*, MNRAS, 481, 3497

Smith, M. W. L., Clark, C. J. R., De Looze, I., et al. 2019; *JINGLE, a JCMT legacy survey of dust and gas for galaxy evolution studies: II. SCUBA-2 850 μm data reduction and dust flux density catalogues* , MNRAS, 486, 4166

Smirnova-Pinchukova, I., Husemann, B., CARS Team, 2020; *CARS: Star formation rate properties of nearby luminous unobscured AGN hosts* , In Prep

Contents

List of Tables

List of Figures

Chapter 1
Introduction

xcolor

"I canna' change the laws of physics."

Commander Montgomery Scott - *Star Trek: The Original Series*

1.1 A Brief History Of Extragalactic Astronomy

The first recorded observation of a galaxy was conducted in the 10th century by the Persian astronomer Abd al-Rahman al-Sufi. He observed the Andromeda galaxy and described it as a "nebulous smear" (al-Sufi 964). It was unknown what this nebulae was actually comprised of, and whether or not it was part of our own galaxy. It wouldn't be until the 17th century that Thomas Wright suggested that nebulae like Andromeda and the Magellanic clouds actually existed outside of our own galaxy (Wright 1750). Building on this Immanuael Kant termed these nebulae as "island universes", and postulated the idea that many of them existed. Observations of hundreds of these nebulae were conducted by both Charles Messier and William Herschel, yet the exact nature of them was still unknown.

Due to a lack of key observations, such as spectroscopy, high resolution images or accurate photometry, it was impossible to determine whether or not these objects were external to our own Galaxy. Many people still believed they were part of the Milky Way, with this argument coming to a head in 1920 in the now famous "great debate". Harlow Shapley argued that the distances these nebulae would need to be at for them to be outside our own galaxy were impossibly large, and could not be

external to the Milky Way. Heber Curtis agreed with Kant saying that these nebulae were "island universes", showing that Andromeda had obvious dust lanes and nova rates comparable to the Milky Way.

Both of these men could not provide definitive evidence for there arguments, with both theories being treated with equal validity. This would change in 1925 with Edwin Hubble and the publication of his pioneering work. Henrietta Swan Leavitt found a relation between a Cepheid's luminosity and its period (Leavitt & Pickering 1912), which Hubble was able to use to calculate the luminosity of Cephids in Androemda and use them as "standard candles". From this he was able to calculate the distance, and found it to be 1.5 million light years (460 kpc) away, well beyond the boundary of the Milky Way. This proved that these "island universes" were galaxies just like our own, and thus began the fields of both extragalactic astronomy, and modern cosmology.

With the ability to conduct deep surveys of large portions of the sky, we can push back the frontier of our observations. Deep observations of space such as the Hubble Ultra Deep Field (HUDF, Figure 1.1) allow us to study large populations of galaxies at all ages, including the epoch of the first galaxies.

1.2 Galaxy Formation And Evolution

1.2.1 Galaxy Formation

The current paradigm for the formation and evolution of galaxies is based on a ΛCDM cosmology. This assumes that the universe is dominated by both cold dark matter (CDM) and dark energy (Λ) which drives the expansion of the universe. After the big bang there were tiny perturbations in the matter density of the universe (most likely due to quantum fluctuations). As dark matter falls into these regions they begin to grow, and form the first dark matter halos in the early universe. Eventually gas begins to accrete onto these halos, cools, and forms stars, giving birth to the first galaxies.

These early galaxies were very small but as they accrete more gas they grow larger and also merge with other galaxies, increasing their mass even more. This is known as the hierarchical model of galaxy formation, and is currently accepted by many as the mechanism of galaxy formation. However, this model is not perfect, and there are several issues with it. Observations have showed populations of massive galaxies with old populations of stars and high metallicities, indicating that they must have formed their stars much earlier then expected and simply been passively

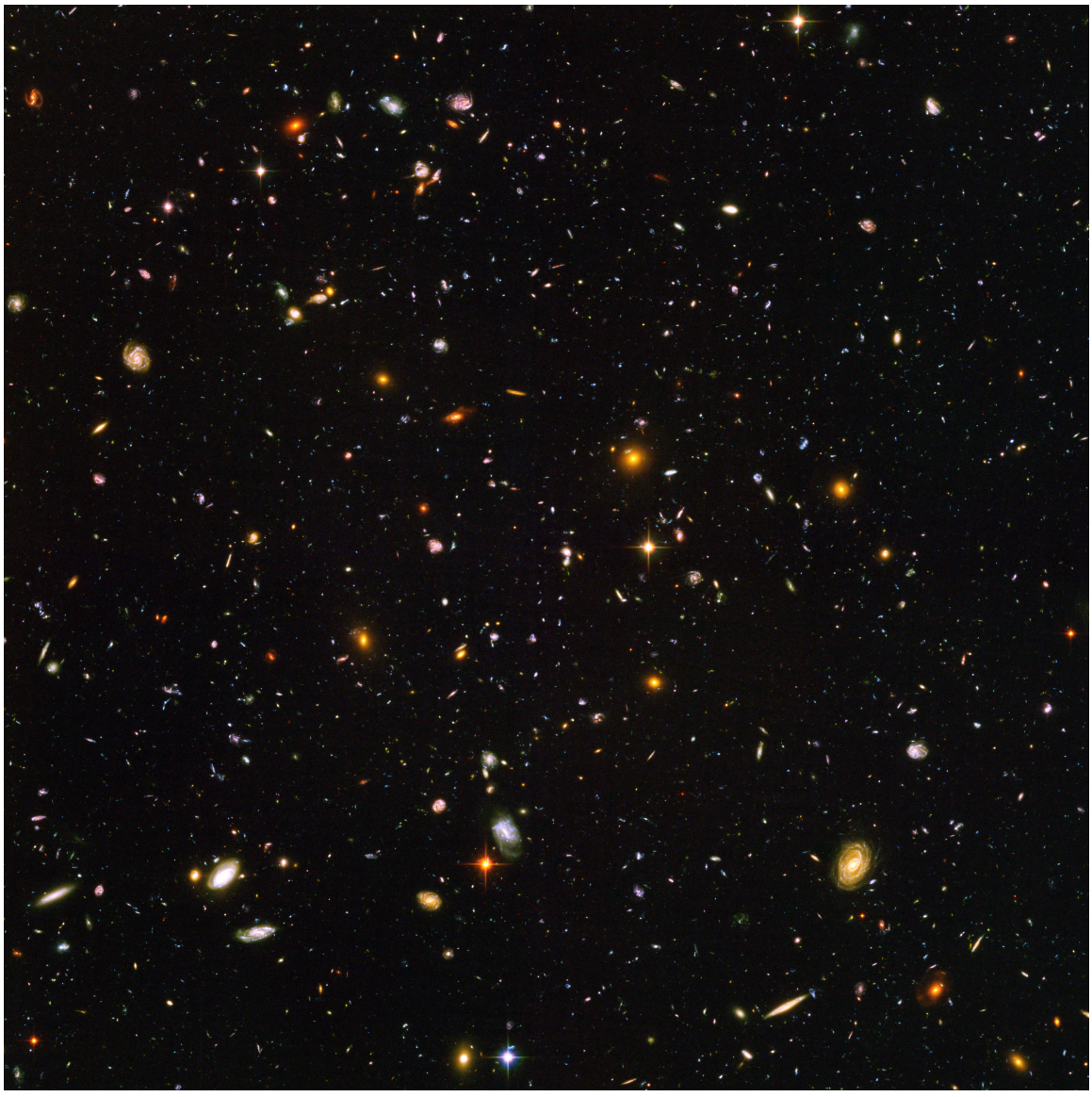

Figure 1.1. The Hubble Ultra Deep Field. This image shows close to 10,000 galaxies, extending all the way back to the age of the first galaxies. Image credit: ESA

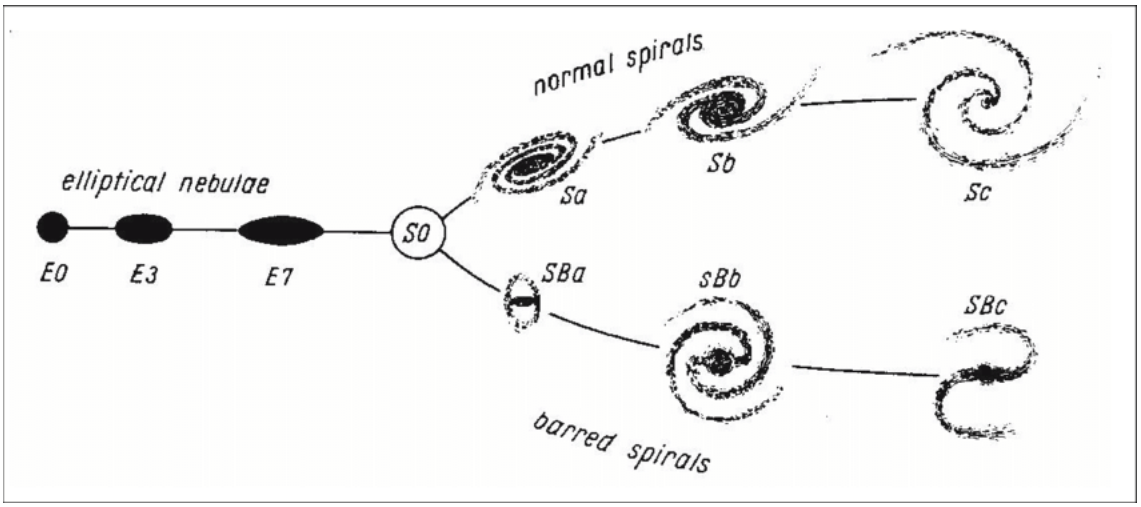

Figure 1.2. The original diagram of the Hubble sequence of galaxies, also known as Hubble's tuning fork. Image credit: Hubble (1936).

evolving ever since.

1.2.2 Galaxy Morphology

Galaxies come in all different shapes sizes and colours, which can be seen in Figure 1.1. Hubble was one of the first people to observe the different types of galaxies, and he tried to classify galaxies via the Hubble sequence of galaxies (later known as the Hubble tuning fork, Figure 1.2).

The classical approach to identify and assign a galaxies morphology was to use the Hubble tuning fork, and decide on the shape alone. This was done by classifying the galaxy "by eye" and determining if it looked like a spiral, elliptical or something in between.

Spiral galaxies (or late type galaxies) are rotating disk-shaped galaxies, with a bright bulge dominating the central region. The stellar populations of these galaxies tend to be young resulting in a much bluer colour, with the exception of the bulge which tends to have populations of much older stars. The disk is arranged into a spiral shape, with the tightness of the spiral arms allowing us to classify different types of galaxies (Figure 1.2). Further classification can also come from whether or not a bar is present within the central bulge, which again can be seen in Figure 1.2.

Classically elliptical galaxies (or early type galaxies) were seen as the exact opposite of a spiral galaxy. They tend to have no definite structure and tend to be quiet elliptical in shape. There is very little star formation happening within them, and hence they have much older populations of stars causing them to have a much

redder colour. They also tend to have very little gas and dust left with most of it having been used to make stars.

Irregular galaxies are very varied in their morphology. These show no regular shape and are thought to be galaxies that were once elliptical or spirals but that have been disturbed by some interaction.

The specifics of galaxy formation and evolution are still largely unknown. Observational evidence has shown that galaxies at high redshift do tend to be disk like (e.g. Eales et al. 2015), and this population has to evolve to account for the large number of spheroid galaxies seen in the local universe, but the exact processes are still unknown. It is thought that external events such as mergers, or environmental processes (see Section 1.4) cause this change, but there is still a lot of debate over this.

Another traditional way to classify galaxies is to use the colour of the galaxy. It was shown by Baum (1959) that galaxies fit into three distinct areas on a colour-magnitude diagram (CMD, Figure 1.3). These are the red sequence, green valley and blue cloud, with these 3 categories matching up with the different galaxy morphologies. In the CMD there is a very distinct bi-modality, with galaxies being separated into a blue cloud and red sequence. There is also a small region called the green valley, which is believed to be some transitional region (e.g. Eales et al. 2018). As mentioned it is widely believed that galaxies start off as a star forming disk, with a young stellar population, and appear blue in colour. These galaxies reside in the blue cloud, and it is believed they migrate to the red sequence. It is in this red sequence where the most massive galaxies live with older stellar populations, causing them to appear red in colour. The exact mechanisms that causes a galaxy to migrate from the blue cloud to the red sequence is still debated, with one of the most likely candidates being external factors interfering with the gas within the galaxy (see Section 1.4.1).

In recent years the idea of classifying a galaxy based entirely on what it looks like (or its colour) has fallen out of favour. Using images alone introduces large sources of errors and the process is difficult to automate, since a computer struggles to differentiate the different galaxy types. Also classifying by shape does not account for phenomena such as pseudo bulges (Kormendy & Kennicutt 2004). This is a morphological feature, where a galaxy appears as a elliptical galaxy but actually has the kinematics of a spiral galaxy. Also recent observations of galaxies that were believed to be elliptical galaxies have actually shown large supplies of cold gas and ongoing star formation (e.g. Crocker et al. 2011; Davis et al. 2011; Smith et al. 2012a).

Instead of appearance, a more robust classification system suggested uses the

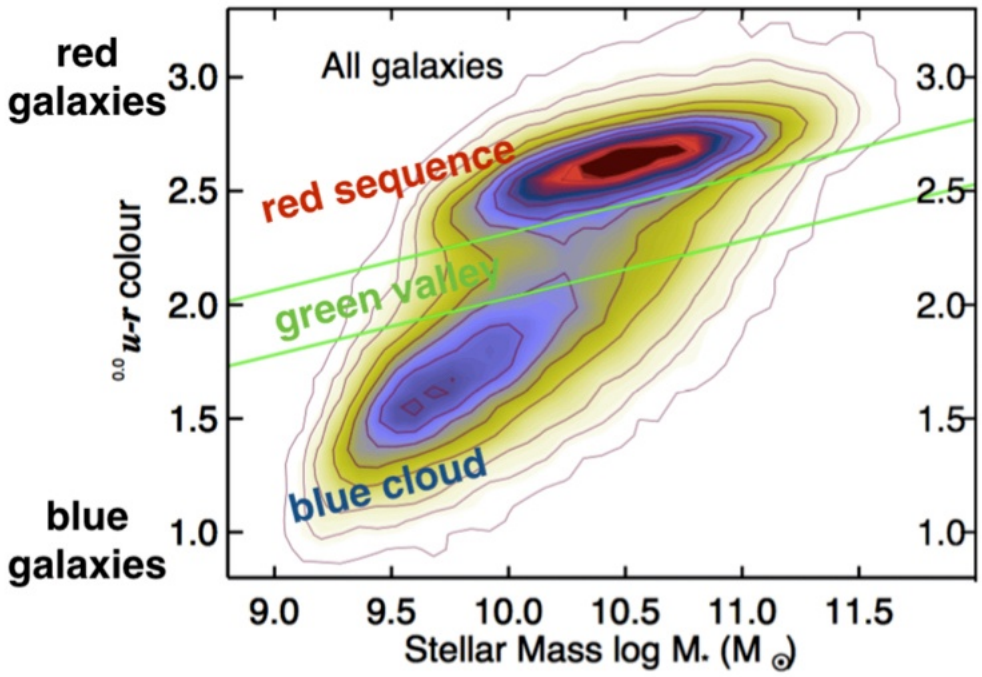

Figure 1.3. The galaxy colour magnitude diagram. Image credit: Galaxy zoo.

kinematics of a galaxy. This system instead splits the two types of galaxies based on their rotation speed. The slow rotators are morphologically similar to the elliptical galaxies, and the fast rotators are akin to the spiral galaxies (e.g. Cappellari et al. 2011). The advantage of this classification system is that it is entirely quantitative, whereas the traditional approach is too subjective.

1.2.3 Evolution of star formation

The evolution of star formation (SF) allows us to understand how the heavy elements in the universe were formed, and how they got distributed into the inter-stellar medium (ISM). There are two ways to understand star formation and how it evolves with redshift, with the first being the "archaeological" approach. By studying local galaxies you can try and re-construct the star formation history and understand how the galaxy behaved at earlier times. The other is to simply observe high redshift galaxies and directly measure the star formation.

Using current facilities we are able to track the cosmic star formation out to redshifts of 7-8. Figure 1.4 shows the cosmic star formation rate density (SFRD) for the universe from Madau & Dickinson (2014), showing that the star formation rate (SFR) of the universe peaks around redshift two, being almost two orders of magnitude greater than today. From this peak there is a steady decline in the SFR,

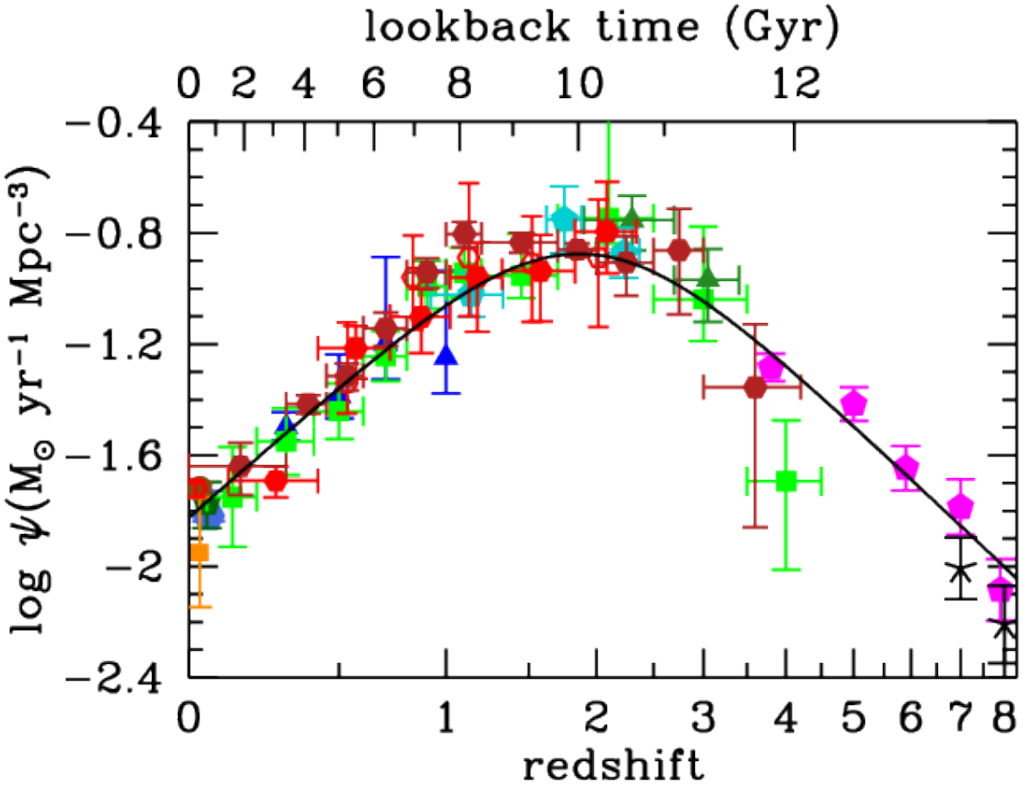

Figure 1.4. The star formation rate density of the universe, and its evolution with redshift. Image credit: Madau & Dickinson (2014)

the exact cause of the decline being unknown, with potential causes being, dwindling gas supplies, stellar feedback or mergers.

There are several key quantities that are related to the star formation properties such as, stellar mass, gas mass and dust mass (and other properties related to dust). These all need to be considered when trying to understand the evolution of star formation in a galaxy. All of these quantities have been studied in great detail, both in terms of evolution with redshift, and how they relate to one another.

One key relation is the link between the SFR of a galaxy and its stellar mass (i.e. the mass of all the stars within a galaxy). This relation allows us to understand the conversion of gas into stars and the subsequent stellar mass build up. The SFR-stellar mass plane is broken up into 3 distinct areas, the main sequence (where the majority of galaxies reside), the starburst region, and the passive galaxy region (Figure 1.5).

A "normal" star forming galaxy will follow the galaxy main sequence, analogous to the main sequence found on a Hertzsprung-Russell diagram. Whilst there is a redshift dependence on the positioning of this main sequence (e.g. Noeske et al.

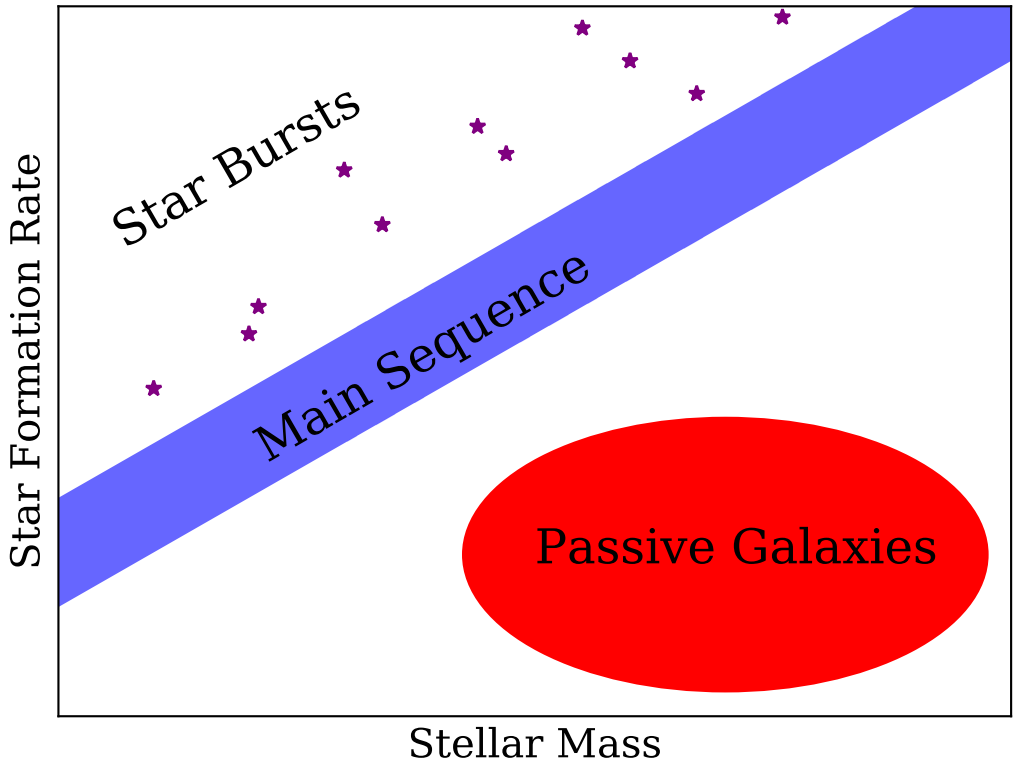

Figure 1.5. Cartoon of the SFR against stellar mass plane. Indicated are the positions of the main sequence, passive galaxies, and starburst galaxies.

2007; Elbaz et al. 2011; Sargent et al. 2014), the scatter of the main sequence has been used to suggest homogeneity among star forming galaxies as the relatively small scatter at all redshifts suggests most galaxies follow the same evolutionary paths.

Above the main sequence we have small subset of galaxies that are forming more stars then expected for their stellar mass. The galaxies in this area are classified as starbursts, and are going through extreme (but short lived) bursts of star formation. The exact nature of the star burst behaviour is unknown, however the most likely cause is down to merging activity (e.g.Hung et al. 2013; Luo et al. 2014; Cibinel et al. 2019).

The final region is below the main sequence, and is dominated by the passive galaxies. This region consists of galaxies with very low SFRs, yet are very massive. Whilst these galaxies locally do not have much star formation occurring and are populated by old stars, it is believed that they evolved from highly star forming galaxies, forming most of their stars at high redshift (e.g. De Lucia et al. 2006).

1.3 Far Infrared And Sub-millimeter Astronomy

Infrared radiation was first theorised by Émile du Châtelet in the 1700s based on her work into the science of fire (du Châtelet 1737). In 1800 William Hershcel first detected infrared radiation by splitting sunlight through a prism, and finding an increase in the temperature of the light beyond the red part of the optical spectrum (Herschel 1800). The first observations of astronomical objects were made in the mid 18th century, yet it would not be until the mid 20th century that the technology was available to fully exploit these vital wavelengths.

Infrared radiation can broadly be broken up into 4 categories. Near infrared (NIR) is considered anything from the end of the visible spectrum ($\sim 0.7\,\mu$m) to $\sim 8\,\mu$m. Mid infrared (MIR) covers $\sim$8-30 μm and far infrared (FIR) covers $\sim$30-500 μm. The final band, sub-millimeter (sub-mm) covers from $\sim$500-1000 μm. This means that with infrared radiation we can probe the ISM within galaxies to temperatures of 10-1000 K.

1.3.1 Dust And Sub-millimeter Galaxies

Dust makes up only $\sim 1\%$ of the total mass of a galaxy, but its effects are some of the most profound. Dust absorbs light at UV and optical wavelengths and re-emits them at IR wavelengths. This effect can be seen in Figure 1.6, where the dark dust lanes in Andromeda in the optical are observable with dust emission at FIR wavelengths. Measurements of the Cosmic Infrared Background (CIB) have shown that half of the energy emitted by stars has been absorbed and re-emitted by dust. This is seen by comparing the CIB to that of the Cosmic Optical Background (COB, e.g. Gorjian et al. 1999, Wright & Reese 2000, Dole et al. 2006, Andrews et al. 2018). We see in Figure 1.7 that the area under the emission from infrared is almost the same as that from optical. This means that if we only observe a galaxy at optical wavelengths we miss out on half of the information, and cannot get an accurate picture of the processes occurring within the galaxy.

With the first sub-mm surveys new populations of very luminous galaxies were being discovered. These galaxies were found to have luminosities in excess of $10^{12}\,L_\odot$, and SFRs greater then a $1000\,M_\odot yr^{-1}$. These sub-mm galaxies (SMGs) are very rare in the local universe, yet are abundant in the high redshift universe. Studies have also shown that between redshifts 2-4 these SMGs make up $\sim$10% of the total SFR of the universe (e.g. Hughes et al. 1998; Blain et al. 1999; Eales et al. 1999; Smail et al.; Wardlow et al. 2011; Casey et al. 2012; Noble et al. 2012; Michałowski et al.

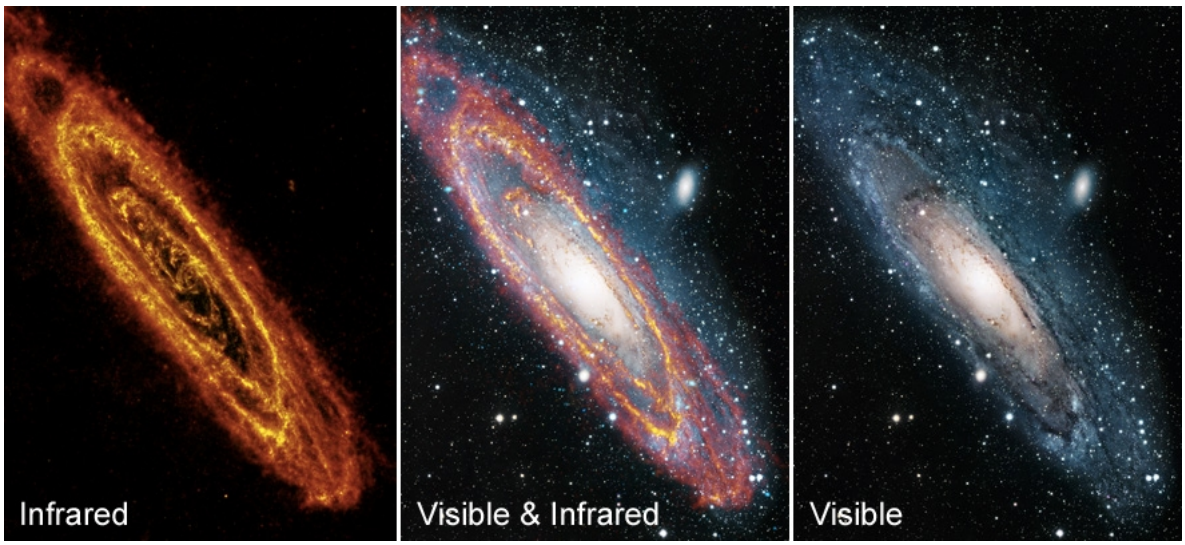

Figure 1.6. Andromeda observed at both optical, and FIR wavelengths. Notice that the dark dust lanes observed in the optical are observable in the FIR. Image credit: ESA

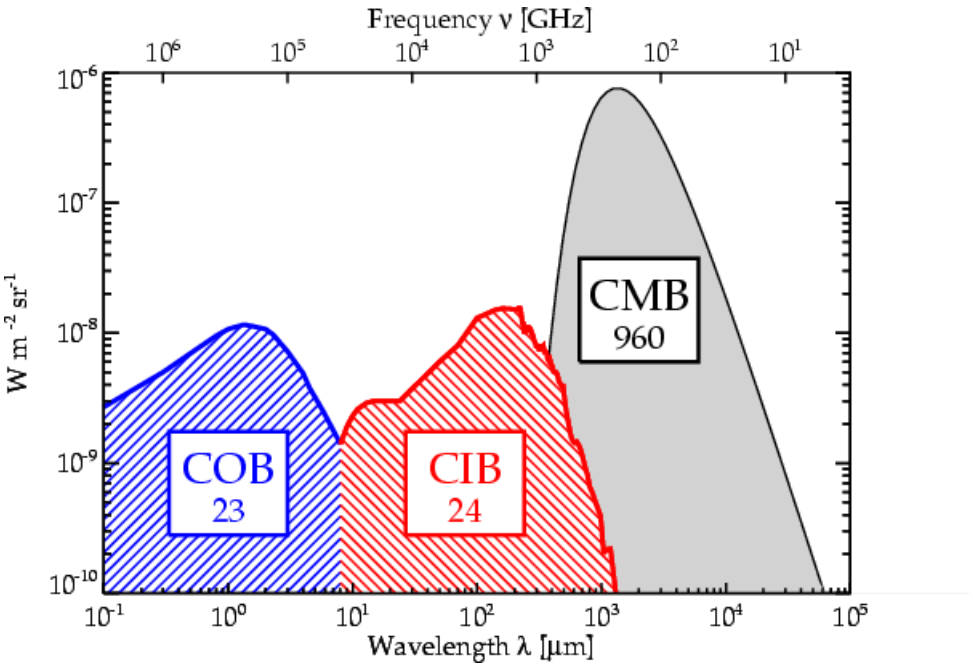

Figure 1.7. The CIB compared to both the COB and Cosmic Microwave Background (CMB). Since the COB and CIB have roughly the same area, this means that half of the optical light absorbed is re-emitted at longer wavelengths. Image credit: Dole et al. (2006).

2017), meaning SMGs are a major contributor to the peak of cosmic star formation (Chapman et al. 2005; Casey et al. 2018).

The mechanisms that cause this extreme star formation is still unknown, with the most likely cause being down to mergers (e.g. Lilly et al. 1999; Conselice et al. 2003; Swinbank et al. 2006; Engel et al. 2010; McAlpine et al. 2019). However when comparing the SFRs of SMGs to local galaxies (which on average have a SFR of $\sim 1\,\mathrm{M_{\odot}yr^{-1}}$), these galaxies would be able to form the stellar masses seen in local ellipticals in less then 1% of the age of the universe. It has therefore been theorised that the SMGs in the high redshift universe are the progenitors to the ellipticals seen in the local universe (e.g. Dunne et al. 2003; Swinbank et al. 2006; Michałowski et al. 2010; Wang et al. 2013; Williams et al. 2014; Cooke et al. 2019).

At optical wavelengths observing high redshift galaxies is extremely challenging. The vast distances the light has to travel causes it to dim and be shifted out of the optical bands. So to observe these galaxies you need long exposures, with sensitive long wavelength instruments (with there being only a handful of telescopes being able to achieve this). At FIR and sub-mm wavelengths this is mitigated due to the negative K-correction. The peak of FIR emission for a galaxy is $\sim$100-150 μm, but at higher redshifts this peak will shift to longer wavelengths. For galaxies between a redshift of 1-8 the observed flux density at sub-mm wavelengths is roughly constant, or in some cases increases. This increase includes the effect due to dimming, and thus high redshift galaxies remain very bright at FIR and sub-mm wavelengths. The negative-K correction can be seen in Figure 1.8

A limiting factor with FIR and sub-mm observations is the resolution the can be achieved. The resolution of a telescope is

$$\theta = 1.22\,\frac{\lambda}{D}, \tag{1.1}$$

where λ is the wavelength being observed, and D is the aperture of your telescope. This means that to observe at FIR and sub-mm wavelengths a large telescope is needed. However due to engineering challenges producing large telescopes is not trivial, and the resolution that can be achieved by single dish telescope tend to be on the order of 10 arcseconds. This issue is particularly bad at high redshift, since the physical scale of the beam is many kpc. This means that if several galaxies were close together, they would exist in one beam and be blended together. This is known as source confusion, and makes cross-matching with optical and NIR measurements very difficult. This issue, and how to deal with it is discussed further in Chapters 3 and 4.

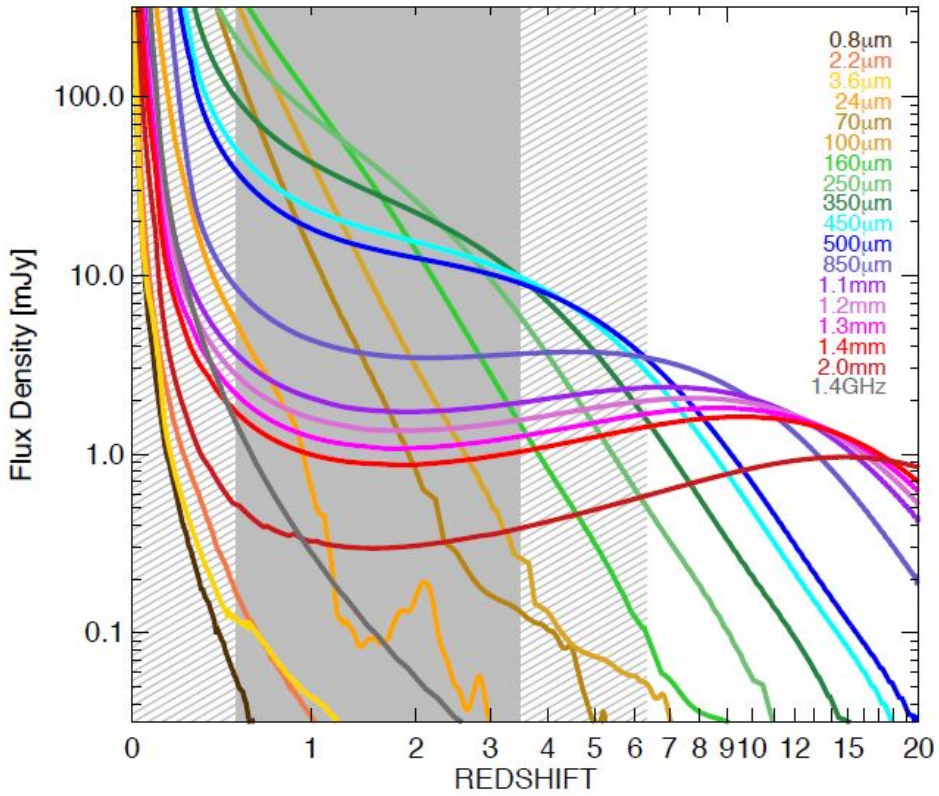

Figure 1.8. The observed flux densities for a typical $10^{12.5}L_{\odot}$ SMG as a function of redshift. This illustrates the nearly-unchanged flux densities which SMGs have in the ∼1 mm bands across a wide range of epochs. Image credit: Casey et al. (2014)

1.3.2 Far Infrared and Sub-millimetre Observatories

FIR and sub-mm astronomy is still a young field in astrophysics. FIR/sub-mm telescopes can either be built on the ground, or sent into space. Ground based observatories are "easier" to build and maintain, and are less limited on how large the telescope can be. However, due to the water vapour in the atmosphere most FIR and sub-mm wavelengths get absorbed. This means observatories can only be built in certain locations (normally very dry and arid locations that are difficult to reach), and even then the atmosphere is only transparent in small windows, limiting the wavelength coverage that can be achieved (Figure 1.9).

Space based telescopes do not have the issue of an atmosphere, so can observe a much wider range of wavelengths. However due to weight and size limitations, the dish tends to be much smaller than ground based observatories, which limits resolution. The telescope has to be cooled to near absolute zero, so the amount of coolant that can be carried limits the lifetime of the telescope (something that does not limit ground based observatories).

The first FIR observatory was launched in 1983. The *Infrared Astronomical*

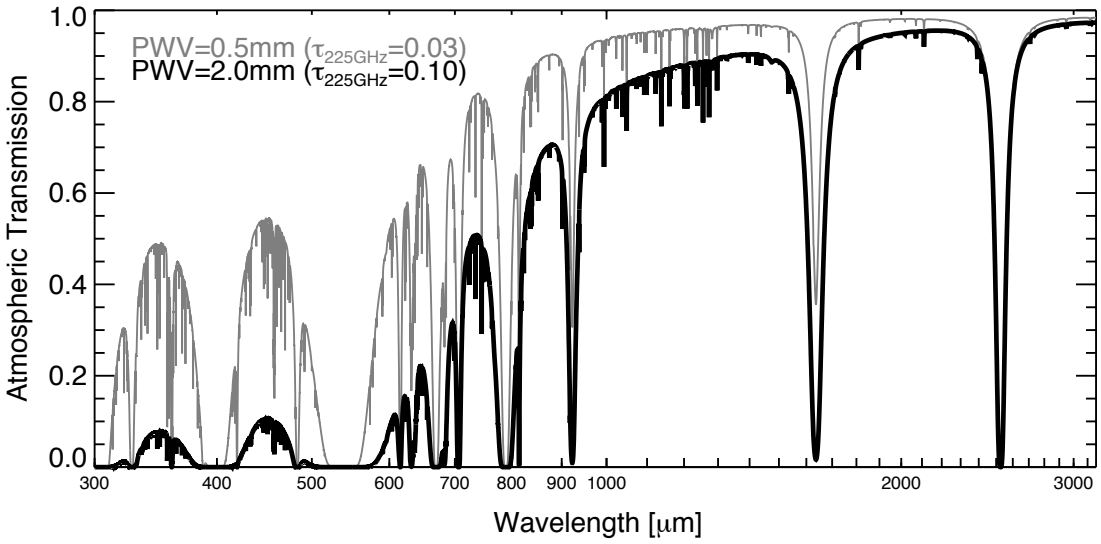

Figure 1.9. The atmospheric transmission of sub-mm wavelengths at the summit of Mauna Kea, at an altitude of 4200 m. Most of the available windows can only be found at the longest wavelengths. As mentioned there is also a strong dependence on the level of Precipitable Water Vapour (PWV) in the atmosphere, represented by the two different lines. Image credit: Casey et al. (2014).

Satellite (*IRAS*, Neugebauer et al. 1984) was the first space based observatory to observe the whole sky between 10-100 μm. *IRAS* revolutionised our view of the universe in its 10 month mission. It observed close to 350,000 IR sources, and even managed to observe the centre of our galaxy for the first time. It was also able to make the first observations of starburst galaxies, cataloging 75,000 of these highly star forming galaxies (Sekiguchi 1987; Carico et al. 1988)

Following from the success of *IRAS*, in 1995 the European Space Agency launched the *Infrared Space Observatory* (*ISO*, Kessler et al. 1996). Not only was *ISO* far more sensitive then *IRAS*, it had much better resolution, and a much larger observing window being able to observe between 2.5-240 μm. It was also able to do both imaging and spectroscopy. Just like *IRAS*, *ISO* made several key discoveries including the first detailed observations of a supernova remnant at FIR wavelengths, showing evidence of dust production within it (Lagage et al. 1996). *ISO* was also able to show that the energy source for ultra luminous IR galaxies (ULIRGs) is powered by star formation, rather then by the central black hole (Sturm et al. 1996).

In 2004 the *Spitzer* space telescope (Werner et al. 2004) was launched. *Spitzer* revolutionised our understanding of dust in the universe, both at low and high redshift. Observing between 3-160 μm, *Spitzer* has provided some of the greatest scientific discoveries of the last decade, including: identifying molecules in the atmosphere of

an exoplanet for the first time (Vidal-Madjar et al. 2003) and aiding in the detection of one of the most distant galaxy proto-clusters (Capak et al. 2011). Studies of high redshift galaxies with *Spitzer* have shown that the majority of SF can only be traced at IR wavelengths (e.g. Metcalfe et al. 2005; Geach et al. 2006; Marcillac et al. 2008), with Le Floc'h et al. (2005) showing that luminous IR galaxies (LIRGs) contribute 70% of the energy density at redshift one.

Following on from *Spitzer* other missions were launched such as *AKARI* (Murakami et al. 2007 and *WISE* (Wright et al. 2010), observing at similar wavelengths to *Spitzer*, and again helping the understanding of dust obscured star formation, exoplanet detections, and understanding the birthplace of stars.

On the ground there have been several single dish observatories such as the 15 m James Clark Maxwell Telescope (JCMT), the IRAM 30 m, and the Atacama Pathfinder Experiment (APEX) telescope. Whilst all these telescopes have advanced the field they still suffer several issues, with resolution being the most limiting. A way of achieving higher resolution is to use an interferometer, which uses many dishes spaced apart to simulate one large dish.

There are already several interferometers in use such as the Sub-mm array (SMA), the Jansky Very Large Array (JVLA), the Australia Telescope Compact Array (ATCA), and the Northern Extended Millimeter Array (NOEMA). However the biggest, and most advanced is the Atacama Large Millimeter/Sub-mm Array (ALMA).

ALMA situated in the Atacama desert in Chile, is one of the largest interferometers in use, probing wavelengths from 0.3-4 mm. Consisting of over 50 12 m dishes ALMA can achieve milli-arcsecond resolution allowing it to probe scales not seen before. At high redshift, whilst the resolution is worse, it has the sensitivity to observe both dust and gas out to a redshift of seven (e.g. Ouchi et al. 2013; Maiolino et al. 2015; Knudsen et al. 2017), and do follow up of known SMGs to get a better understanding of their properties (e.g. Hodge et al. 2013; Weiß et al. 2013).

1.3.3 The James Clark Maxwell Telescope

The James Clark Maxwell Telescope (JCMT) was the first and (still to this day) largest sub-mm telescope constructed (Figure 1.10). Built in 1987 the telescope and its 15m dish sits atop Mauna Kea in Hawaii at an altitude of 4200 m. At this altitude the telescope is in the key position to observe at sub-mm wavelengths (Figure 1.9), and is equipped to observe both continuum and spectra between the wavelengths of 0.4-2.5 mm .

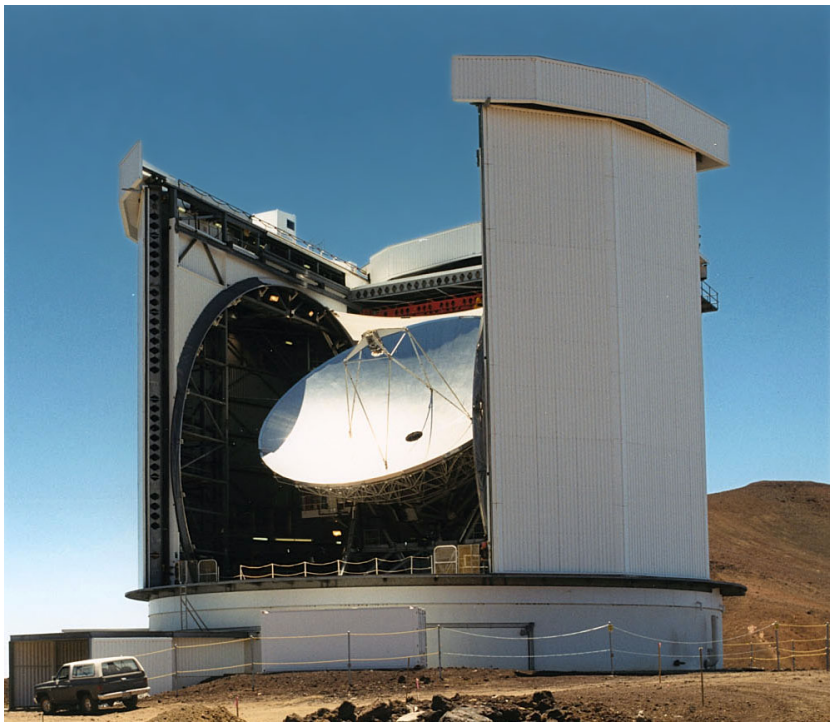

Figure 1.10. The James Clark Maxwell telescope with the dome open, showing the 15m dish. Image credit: East Asian Observatory

The Sub-mm Common User Bolometer Array (SCUBA, Holland et al. 1999) was one of the first sub-mm cameras installed on the JCMT. Installed in 1997 the camera was capable of observing at both 450 and 850 μm simultaneously, observing with both 91 and 37 pixels respectively. Since the diameter of the dish was 15 m, SCUBA was able to achieve some the highest resolution sub-mm images. In our own galaxy SCUBA was able to observe the first debris disks around stars (e.g. Holland et al. 1998; Greaves et al. 1998), and carry out large scale studies of star forming regions (e.g. Johnstone & Bally 1999).

On extragalactic scales, SCUBA was able to utilise the negative-K correction, and was able to detect hundreds of SMGs at high redshift (e.g. Smail et al. 1997; Barger et al. 1998), including detections in the Hubble Deep Field (HDF, Hughes et al. 1998, Figure 1.11).

In 2011 the follow up to SCUBA, SCUBA-2 (Holland et al. 2013) was installed onto the JCMT. Just like its predecessor, SCUBA-2 could observe at both 450 and 850 μm simultaneously, but this time 10,000 pixels were available, allowing for a 100 times greater mapping speed. SCUBA-2 also has a larger field of view, being able to observe 50 arcmin^2, 13 times that of SCUBA. This makes SCUBA-2 the perfect instrument to produce very large and very deep maps of the night sky.

Since its commissioning SCUBA-2 has already produced some of the deepest

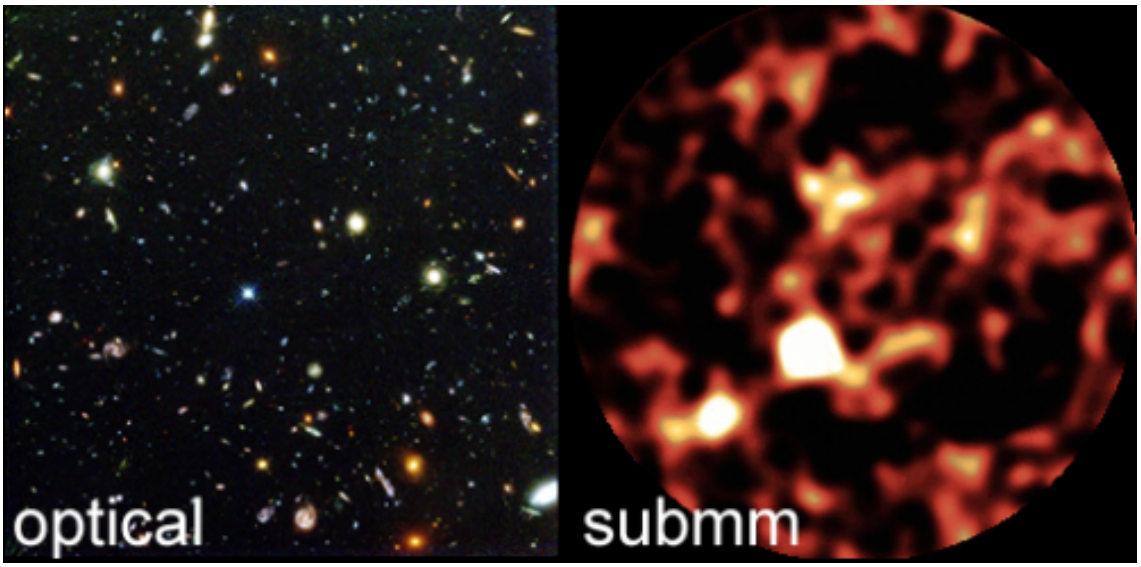

Figure 1.11. A comparison of the HDF at both optical wavelengths and sub-mm. Image credit: ESA and NASA.

sub-mm maps, in projects such as the SCUBA-2 Cosmology Legacy Survey (S2CLS, Geach et al. 2013, 2017) and the SCUBA-2 Ultra Deep Imaging EAO Survey (STUDIES, Wang et al. 2017). These studies have already detected thousands of SMGs, out to a redshift of 4.

JCMT also has two hetrodyne detectors, Heterodyne Array Receiver Program (HARP), and RxA3*. Both of these instruments can probe the millimeter wavelengths, observing lines such as CO, HCN and HCO^+. These hetrodyne instruments were recently used in the Event Horizon Telescope and aided in taking the first image of a black hole (Event Horizon Telescope Collaboration et al. 2019).

1.3.4 The Herschel Space Observatory

The *Herschel* space observatory (Pilbratt et al. 2010) was launched in 2009, and has been the biggest advance in FIR astronomy since the launch of *IRAS*. *Herschel* had a mirror with a diameter of 3.5 m, making it one of the largest mirrors in space, and allowing for the highest resolution images at these wavelengths. The wavelengths covered ranged from 60-680 μm, placing the FIR emission for galaxies right in the middle of the detection range for *Herschel*. This detection range, the resolution possible and the sensitivity offered made *Herschel* vital for studies across many different fields in astrophysics.

*At time of writing RxA3 has been retired. Its replacement Nāmakanui has not been fully commissioned but it will be able to observe at 86, 230, 340 GHz.

Herschel was equipped with 3 different instruments. The Photodetector Array Camera and Spectrometer (PACS, Poglitsch et al. 2010) was the shortest wavelength detector, offering both imaging and spectra. The spectrometer had a range from 60-210 μm, and the photometer had 3 arrays centered on 70, 100 and 160 μm. This means PACS is ideal for observing the peak of FIR emission in the Milky Way and local galaxies.

The Spectral and Photometric Imaging REceiver (SPIRE, Griffin et al. 2010) is the longest wavelength instrument on *Herschel*, offering both imaging and spectroscopy. The photometer again had 3 arrays, centered on 250, 350 and 500 μm. The spectrometer works in the wavelength range of 190-670 μm. This allows SPIRE to detect very cold dust in local galaxies, and thanks to the negative K-correction allows for the detection of high redshift galaxies (Figure 1.8).

The final instrument is the Heterodyne Instrument for the Far-Infrared (HIFI, de Graauw et al. 2010). HIFI was a dedicated high resolution spectrograph allowing for coverage between 157-212 μm and 240-625μm. The main goal of the instrument was investigate the ISM and its interaction with stars in galaxies by searching for molecular rotational lines.

Herschel was key in several fields of astrophysics. Our understanding of dust has been completely changed thanks to the work of *Herschel*. Thanks to observations of nearby supernova it is now believed that the majority of dust is produced in these dying stars (e.g. Barlow et al. 2010; Gomez et al. 2012). Observations of local galaxies have shown that dust properties can vary over an entire galaxy, helping us understand the processes that are occurring within galaxies (e.g. Smith et al. 2012b). At high redshift *Herschel* has been able to detect populations of extreme star-bursting galaxies, some of the brightest ever seen (Riechers et al. 2013; Huang et al. 2014). This work is key in helping us understand how galaxies evolve, and give us an insight into the formation of the elliptical galaxies we see in abundance today. *Herschel* (and SCUBA-2) are also key in understanding the star forming properties of high redshift galaxies. At high redshift the MIR becomes a less reliable estimate for the total star formation in the most obscured systems (e.g. Calzetti et al. 2007; Hainline et al. 2009) and FIR and sub-mm tracers are needed.

1.4 Galaxy Clusters

Galaxy clusters are some of the largest structures in the universe, home to thousands of galaxies. The tendency for galaxies to cluster was first observed by both Charles Messier (Messier 1784), and William Hershel (Herschel 1811) who constructed

some of the first catalogues of Galaxy clusters. However the true scale of these clusters would not be realised until the work by Hubble, showing these nebulae were actually galaxies outside the Milky Way. The fact that so many galaxies exist in such a small area meant these structures must be some of the most massive, and dense in the universe.

Clusters are very common place within the local universe. George O. Abell discovered and catalogued over 2000 clusters out to a redshift of 0.2, with a further 2000 being catalogued after his death. This is now known as the Abell catalogue and is one of the largest catalogues of clusters to date (Abell 1958; Abell et al. 1989). Clusters can be categorised in very different ways, such as mass, richness (i.e. how many galaxies are associated with the cluster), and compactness (i.e. how many galaxies lie within a certain radius). For example the Fornax cluster is a very low richness cluster, with there being only $\sim$100 galaxies within it. However, it is a very compact cluster with all of the galaxies residing in a very small radius. Coma on the other hand is a very rich cluster, with over 1000 galaxies within it. However it's far less compact as all its galaxies are spread out to much larger radii.

Hubble & Humason (1931) were the first people to use spectra of galaxies to calculate the velocities of a galaxy, which both Zwicky (1937) and Smith (1936) used to calculate the masses of the Coma and Virgo clusters respectively. When Zwicky compared the cluster mass from measuring the velocity of galaxies to that of the stellar mass of all galaxies within Coma, he found there to be a ~ 300 times difference between the 2 mass estimates. This prompted Zwicky to postulate that there must be an extra component to galaxies, a type of matter that could not be detected, which we know today as dark matter. Whilst the claim Zwicky made was hotly disputed for many years, it was ultimately confirmed when an extended hot Intra Cluster Medium (ICM) was discovered emitting X-rays by thermal bremsstrahlung that was found to be smoothly filling intergalactic space within the Coma cluster (Cavaliere et al. 1971,Gursky et al. 1971, Meekins et al. 1971).

The detection of X-rays shows that there must be a very deep potential well, deep enough to heat in-falling gas to the thousands of Kelvin needed to emit X-rays. Only dark matter can produce a halo with a potential deep enough to do this. It is now known that a galaxy cluster is a large virialised dark matter halo, believed to be the end point of merging halos in the hierarchical model of structure formation (Section 1.2.1). This X-ray emitting intra-cluster medium (Figure 1.12) helped answer the discrepancy between the mass estimates Zwicky discovered. The detection of X-rays also helps give us a unambiguous detection method for galaxy clusters, at both low and high redshift (Rosati et al. 2002). The mass of clusters can reach masses between

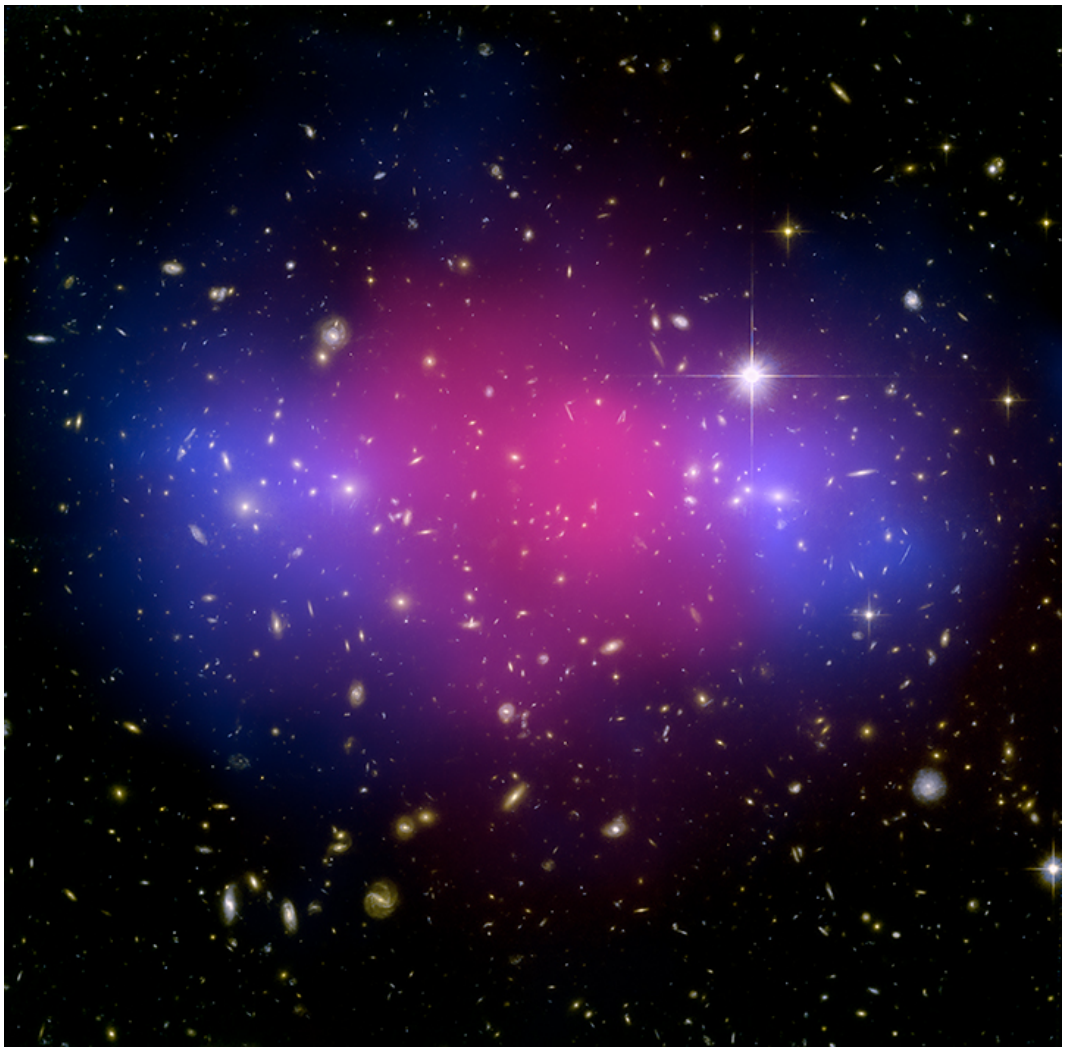

Figure 1.12. The galaxy cluster MACS J0025. The blue traces the dark matter via gravitational lensing, whilst the pink traces the hot ICM via X-rays. Image credit: NASA

10^{13} - 10^{15} $M_{\odot}$, with about 90% being dark matter, 9% the warm ICM and the final 1% being galaxies and other Barayonic matter.

An interesting discovery that came from clusters is the Sunyaev-Zel'dovich (SZ) effect (Sunyaev & Zeldovich 1972). As a CMB photon travels through the hot ICM it will interact with the electrons within it and be inversely Compton scattered. This means the CMB photons will gain energy, and in CMB maps will appear as "hot" patches (Figure 1.13). Since the SZ effect is so small (due to it being a scattering effect), it is independent of redshift, so a redshift 0 cluster will have the same SZ signal as a redshift two cluster. This proves very useful as X-ray measurements can be very difficult to acquire, whereas large scale SZ surveys are very easy to conduct, with several large surveys already being completed (e.g. Schwan et al. 2003; Staniszewski

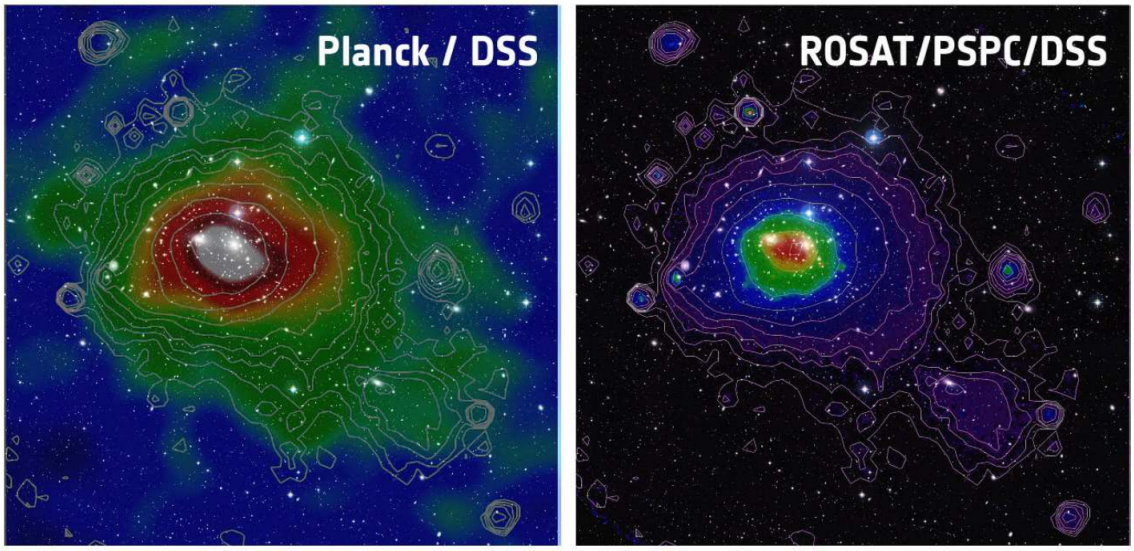

Figure 1.13. Left: An image of the Coma cluster from Planck, via the SZ effect. Right: An image in X-ray from the ROSAT satellite. Image credit: Giodini et al. (2013).

et al. 2009; Marriage et al. 2011). These surveys have already detected thousands of clusters, especially in the high redshift universe where "standard" methods of cluster detection are very difficult.

1.4.1 Galaxy Evolution And Star Formation In Clusters

Clusters are very useful tools in both astrophysics and cosmology. In cosmology they allow us to place constraints on cosmological parameters, such as the amount of matter in the universe. Due to their extreme masses, clusters act as gravitational lenses bending the light from distant galaxies and magnifying it. This again has uses in cosmology, and allow us to observe populations of very high redshift galaxies, which normally would not be observable.

Since the cluster environment is so dense, we can directly observe the effects environment is having on how a galaxy evolves, giving a better understanding of the processes that shape a galaxy. This allows us to test the nature vs nurture argument of how a galaxy evolves. Is the evolution of the galaxy driven by the environment and where it exists in the universe, the nurture, or is the evolution driven by its initial conditions when it formed i.e. when was it formed and how massive was it, the nature.

Some of the first observations of potential cluster environment effects was observed in 1978 by Harvey Butcher and Augustus Oemler Jr. When looking at the colours of galaxies in clusters they found that high redshift clusters are dominated

by blue (and hence star forming) galaxies (now known as the Butcher-Oemler effect, Butcher & Oemler 1978).

Follow up studies have studies have shown that the Butcher-Oemler effect is significant, with ∼70% of a high redshift (z∼1) clusters galaxy population being blue in colour (compared to low redshift where ∼3% is blue, Couch et al. 1983; Couch & Newell 1984). When comparing observations with simulations, it has been found that the only way to reproduce the Butcher-Oemler effect is via mergers or environmental effects (e.g. Evrard 1991; Kauffmann 1995; Bekki 1999; Bekki et al. 2001).

Further evidence that there could be an environmental effect on galaxy evolution was investigated by Alan Dressler in the 1980's. He looked at the different populations of galaxies, and how these fractions changed with different environments. He found that in the densest environments (i.e. the very centre of the clusters) the dominant galaxy type was ellipticals, and spiral galaxies were virtually absent. This was the complete opposite to what was found in field galaxies, where the star forming spirals dominate (Figure 1.14, Dressler 1980).

This relation was also observed by both Goto et al. (2003) and Smith et al. (2005), who observed local clusters being dominated by massive elliptical galaxies. This could indicate that the cluster environment is having some effect on the galaxies, and driving its evolution. However it can also be argued that these are the oldest galaxies within the system and have just evolved earlier.

Other tracers of galaxy evolution such as colour (Figure 1.15, e.g. Baldry et al. 2006; Haines et al. 2006), SFR (Figure 1.15, e.g. Lewis et al. 2002; Gómez et al. 2003), mass (e.g. Bower et al. 1992; Kauffmann et al. 2004), and age of stellar population (e.g. Weinmann et al. 2006; Peng et al. 2010), have all shown that in local clusters the centre is dominated by the most massive elliptical galaxies. Again this could show that the environment is having an effect on the cluster galaxies and driving their evolution, or again they could just be galaxies that evolved quicker.

The ICM in a cluster can reach temperatures on order of 10^8 K, which can have a dramatic effect on the cold gas of galaxies within it. Also due to the dense environment of clusters, interactions between galaxies can again disturb the cold gas within a galaxy. The processes that can occur are ram pressure stripping (Gunn & Gott 1972), harassment (Richstone 1976; Moore et al. 1996), strangulation (Larson et al. 1980; Peng et al. 2015), mergers and cannibalism. All of them affect the cold gas some way, either by removing the gas completely, heating it up so it can no longer form stars, or simply shutting off supplies of fresh gas. Observing these effects within cluster galaxies can help us understand if the environment is the main driving force for the evolution of galaxies.

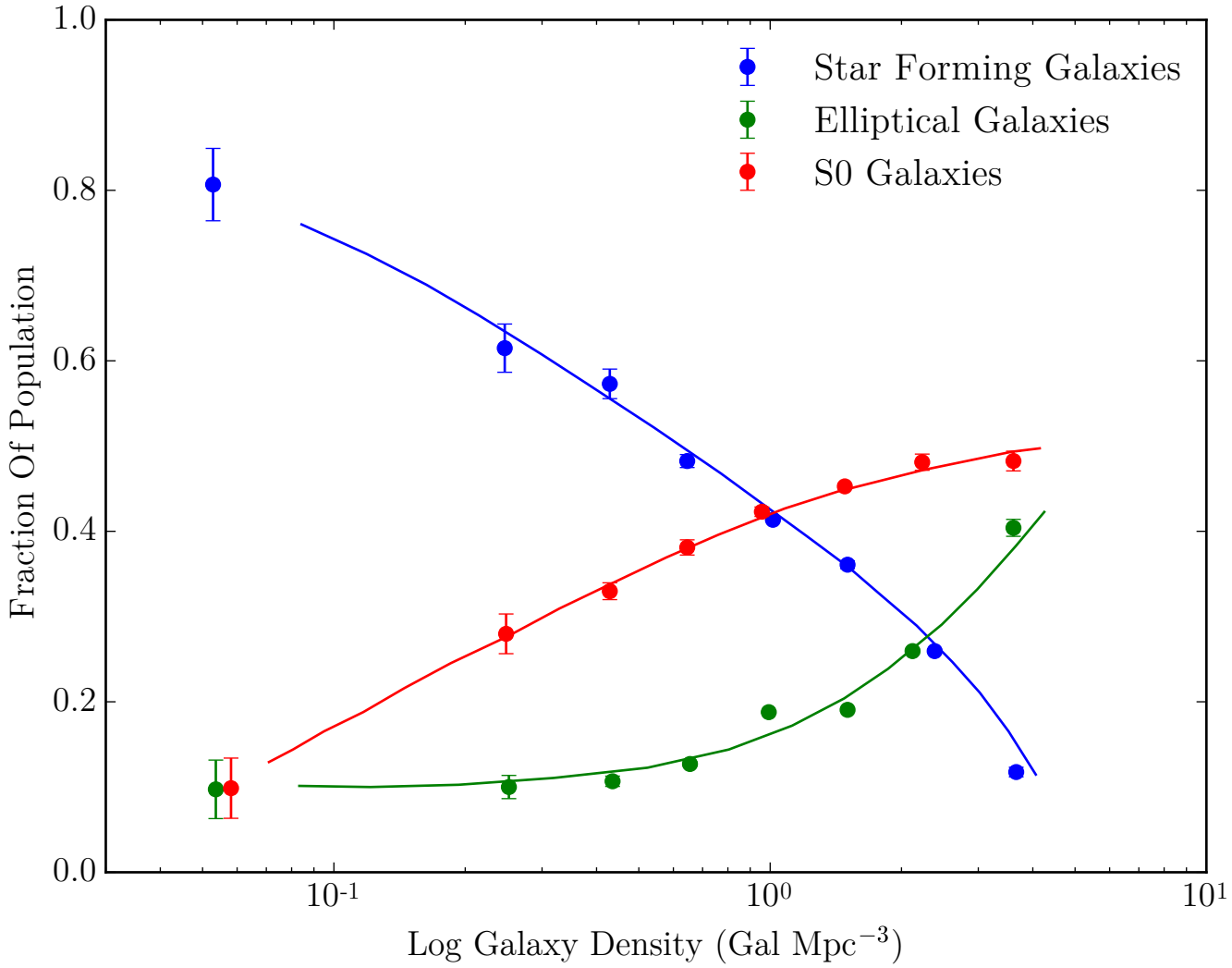

Figure 1.14. Recreation of the morphology-density plot from Dressler (1980). This shows that as galaxy density increases (or cluster radius decreases) the number of spiral galaxies (blue line) decreases, and the number of ellipticals (green line) and S0 galaxies (red line) increases.

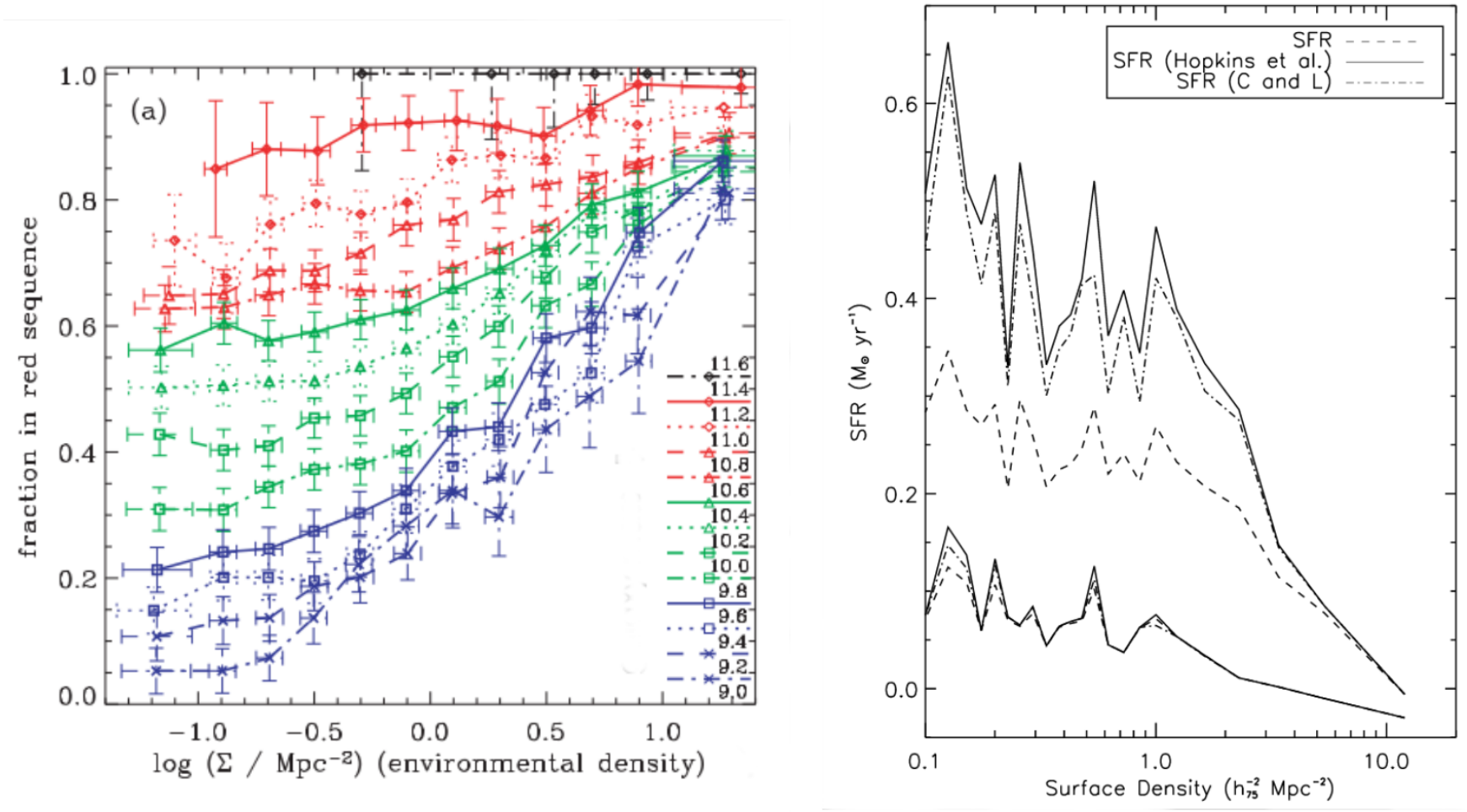

Figure 1.15. Left: The colours of galaxies, for different stellar masses as a function of galaxy density. Image credit: Baldry et al. (2006). Right: The SFR as a function of galaxy density, with each different line showing a different dust extinction model. Image credit: Gómez et al. (2003).

1.4.2 HIGH REDSHIFT CLUSTERS

Beyond the local universe, studies of galaxy clusters at higher redshifts is proving a key insight into how the environment is transforming the SF galaxies into the ellipticals we see today, especially at the epoch of star formation, at z∼2, (Madau & Dickinson 2014). Observations of clusters have shown the fraction of LIRGs and ULIRGs start to increase with increasing redshift, when they are absent in local clusters (e.g. Coia et al. 2005; Koyama et al. 2008; Haines et al. 2013; Webb et al. 2013). Based on recent theoretical work, it has been suggested that the majority of star formation in the early universe took place in over-dense proto-clusters, the progenitors to clusters we see today (e.g. Governato et al. 1998; Chiang et al. 2013, 2017).

The evolution of star formation has been well documented in clusters up to z∼1, and the mass normalised SFR (SFR/cluster mass) is shown to follow an empirical power law of the form $(1+z)^n$, with n being around 5-7 for clusters (e.g. Cowie et al. 2004; Kodama et al. 2004; Geach et al. 2006; Saintonge et al. 2008; Koyama et al. 2010, 2011). In the high redshift universe ($z > 1$) statistics are difficult, due to the small number of studied systems. These systems all seem to suggest (out to a redshift of 2 at least) that this power law is still valid (e.g. Smail et al. 2014; Santos et al. 2014, 2015; Ma et al. 2015; Webb et al. 2015; Casey 2016; Cooke et al. 2019).

The first evidence for a reversal of the SFR-density relation was reported by Elbaz et al. (2007) who showed that for field galaxies in the range $0.8< z <1.2$, the SFR increased with galaxy density, which is in stark contrast to what is seen at low redshift. The first work on clusters at high redshift was by Hayashi et al. (2010) and Tran et al. (2010), who looked at $z \sim 1.4$ and $z \sim 1.6$ respectively. Again they found evidence for an increase in the star formation with increasing galaxy density. On the other hand Santos et al. (2013) found no evidence for a reversal of the SFR-density relation in a cluster at $z = 1.4$.

Most of these early studies focused on NIR and MIR instruments such as those found on *Spitzer*. However, to get a accurate picture of the SF properties of high redshift galaxies, you need a probe of star formation that is not effected by dust. This is found by looking at the FIR and sub-mm emission of these galaxies.

Such FIR/sub-mm studies has indeed shown that in high redshift clusters there are large populations of SMGs (e.g. Fassbender et al. 2011; Brodwin et al. 2013; Zeimann et al. 2013; Alberts et al. 2014, 2016; Clements et al. 2014; Santos et al. 2014, 2015; Smail et al. 2014; Ma et al. 2015; Kato et al. 2016; Cooke et al. 2019). This indicates that there is a reversal in the SFR-density relation that is

observed in local clusters.

The limiting factor for studies of high redshift clusters is the number of discovered systems. Statistics are still small, but with the advent of new facilities (e.g. ALMA) larger populations of high redhsift (proto-)clusters are being discovered, and detailed follow ups are being conducted on those already known (e.g. Umehata et al. 2015; Franck & McGaugh 2016; Wang et al. 2016; Mantz et al. 2017; Arrigoni Battaia et al. 2018; Jiang et al. 2018; Lewis et al. 2018; Martinache et al. 2018; Oteo et al. 2018; Gómez-Guijarro et al. 2019). This allows us to understand the properties of the galaxies within them, and help us understand the environmental effects at higher redshifts.

However, there is evidence to suggest that redshift 1.4 is a very key moment in the evolution of a cluster. Many studies have shown that it is at this redshift that many galaxies go from star forming to being quenched, and there is some sort of transitioning phase occurring (e.g. Brodwin et al. 2013; Santos et al. 2013; Alberts et al. 2014, 2016, Stach et al. 2017; Hayashi et al. 2018). No reason is known as to why this occurs, but it is believed that some of the processes mentioned above have long time-scales, and it is by this redshift they have become dominant and begun to suppress star formation.

1.5 Thesis Outline

The main aim of this thesis is to use brand new SCUBA-2 and ALMA data to observe and understand high redshift clusters. I use this data to investigate the star formation properties of these galaxies, and see if there is any evidence of the cluster environment having an impact on the evolution of the residing cluster galaxies. The thesis is outlined as:

- Chapter 2 discusses the SCUBA-2 data reduction pipeline. I discuss the steps needed to reduce SCUBA-2 data, and how to modify it to reduce data for high redshift clusters.

- Chapter 3 discusses the analysis I did on the star forming properties of CLJ1449+0856, a cluster at redshift 2. Using brand new SCUBA-2 data, and archival *Herschel* data, I am able to probe star formation out to a radius of 3 Mpc.

- Chapter 4 goes over the star formation properties of JKCS041. I use both SCUBA-2 and *Herschel* images to explore star formation to a radius of 3 Mpc. I also investigate the possible link between mass of a cluster and the galaxies within it.

- Chapter 5 presents brand new ALMA data of a proto-cluster at redshift 3.6. I discuss the method used to identify any spectral lines within the data, and use them to confirm the redshift of the cluster. I then look at the properties of the proto-cluster galaxies.

- Chapter 6 summarises the main results from the entire thesis and describes some possible future investigations.

Throughout this thesis I assume a ΛCDM cosmology with H_0=70 $kms^{-1}Mpc^{-1}$, Ω_Λ=0.7 and Ω_m=0.3. The scale at both redshift 1.8 and 2 is $\sim$8.6 kpc $arcsec^{-1}$. At redshift 3.6 the scale is $\sim$7.4 kpc $arcsec^{-1}$. All magnitudes are given in the AB system, and all uncertainties are given at the 1 σ level.

Chapter 2
SCUBA-2 Data Reduction

"Without data, you're just another person with an opinion."

William Edwards Deming

In this chapter I will be discussing the reduction process used to reduce SCUBA-2 data of the galaxy clusters CLJ1449 and JKCS041. I discuss the basic pipeline used, and the modifications I made to suit my data.

2.1 SCUBA-2

As mentioned, SCUBA-2 is the second generation sub-mm camera installed on the JCMT (Figure 2.1). It consists of 10,000 bolometers and is able to observe at both 450 and 850 μm simultaneously. At the heart of SCUBA-2 are the bolometers, which are Transition-edge sensors (TES). These TES bolometers are kept at a very cold temperature ($\sim$0.1K) allowing super-conduction to occur (and thus very sensitive to any temperature input). The bolometers have a constant voltage running through them, so when a photon hits the bolometer, it heats up and causes an increase in resistance. This increase in resistance causes a decrease in current which is detected by another system and converted into a digital signal.

Thanks to the 15 m dish of the JCMT, SCUBA-2 is able to reach a resolution of 7 and 15 arcsec for 450 and 850 μm respectively. This makes SCUBA-2 one of the highest resolution instruments (on a single dish telescope) available for sub-mm astronomy.

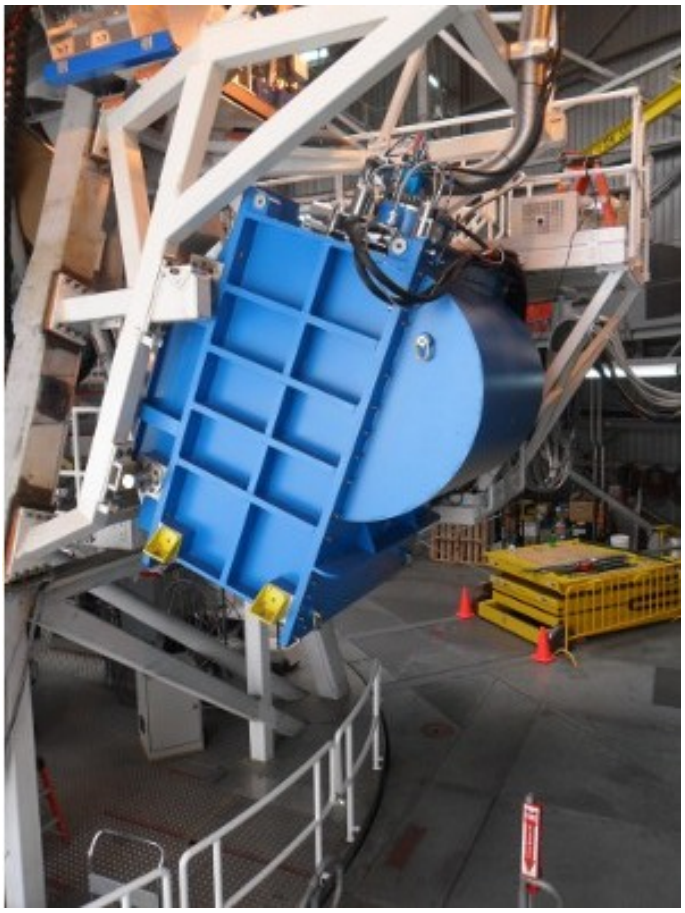

Figure 2.1. The SCUBA-2 instrument attached to the JCMT. Image credit: East Asian Observatory.

2.1.1 SCUBA-2 OBSERVING MODES

The 10,000 bolometers are split into 8 arrays (4 for each wavelength) meaning various scanning modes need to be employed to ensure full coverage of an observational target, and take advantage of the large mapping speeds available to SCUBA-2.

PONG maps are designed to cover a large area of the sky. PONG paths are determined by constructing a box (with dimensions of either 900, 1800, 3600 or 7200 arcsec) around the target area and the telescope moves across it. When it hits an edge it "bounces" off and moves in a different direction. It continues to do this until the entire box has been well covered. To assure an equal coverage over the whole region, multiple PONG maps are conducted, with a rotation introduced so a circular pattern is built up (Figure 2.2).

DAISY maps are used when dealing with individual point like sources. This strategy keeps the desired source in the center and the telescope scans at a constant speed in a "Spirograph" pattern. The advantage of this is that the source will always

Table 2.1. The $3\,\sigma$ sensitivities for SCUBA-2 after an integration time of one hour.

Observing Mode	$450\,\mu$m (mJy)	$850\,\mu$m (mJy)
DAISY	39.0	5.6
PONG900	85.0	11.9
PONG1800	166.0	23.0
PONG3600	361.0	49.0
PONG7200	732.0	98.0

be on the array throughout the observation, minimizing noise (Figure 2.2). Unlike the PONG maps, DAISY maps have a fixed size of 3 arcmin.

These patterns were designed to help reduce the instrumentation noise. The noise power spectrum for SCUBA-2 has a $1/f$ noise curve at low frequencies, so to make sure that the astronomical signal is far away from this $1/f$ noise, fast scanning speeds are required. The other reason these patterns are used is to help remove slowly varying signals, such as extinction or sky noise. To identify these sources the scan pattern must pass across the same region many times from varying directions. These patterns have been designed to meet this criteria.

Before each observation a flat field is taken. This is where heaters are used to heat up the bolometers and measure how they behave. This way bolometers that do not fall within threshold limits, display odd responses or have poor S/N are flagged and rejected. Another flat field is performed after the observation to flag those who have had their behaviour change over the course of the observation.

Table 2.1 show the $3\,\sigma$ sensitivities that can be achieved for different observing modes, after one hour of observations (Holland et al. 2013). Whilst these do not improve significantly from SCUBA, SCUBA-2 can achieve these sensitivities over larger areas, and at greater mapping speeds.

2.2 The SCUBA-2 data reduction pipeline

The raw data consists of a time varying signal from each bolometer that consists of: the atmospheric extinction, the astronomical signal, both correlated and uncorrelated noise and low frequency noise. The map maker iteratively tries and models each of these components and removes them. This results in a signal that is simply the astronomical signal with some residual noise.

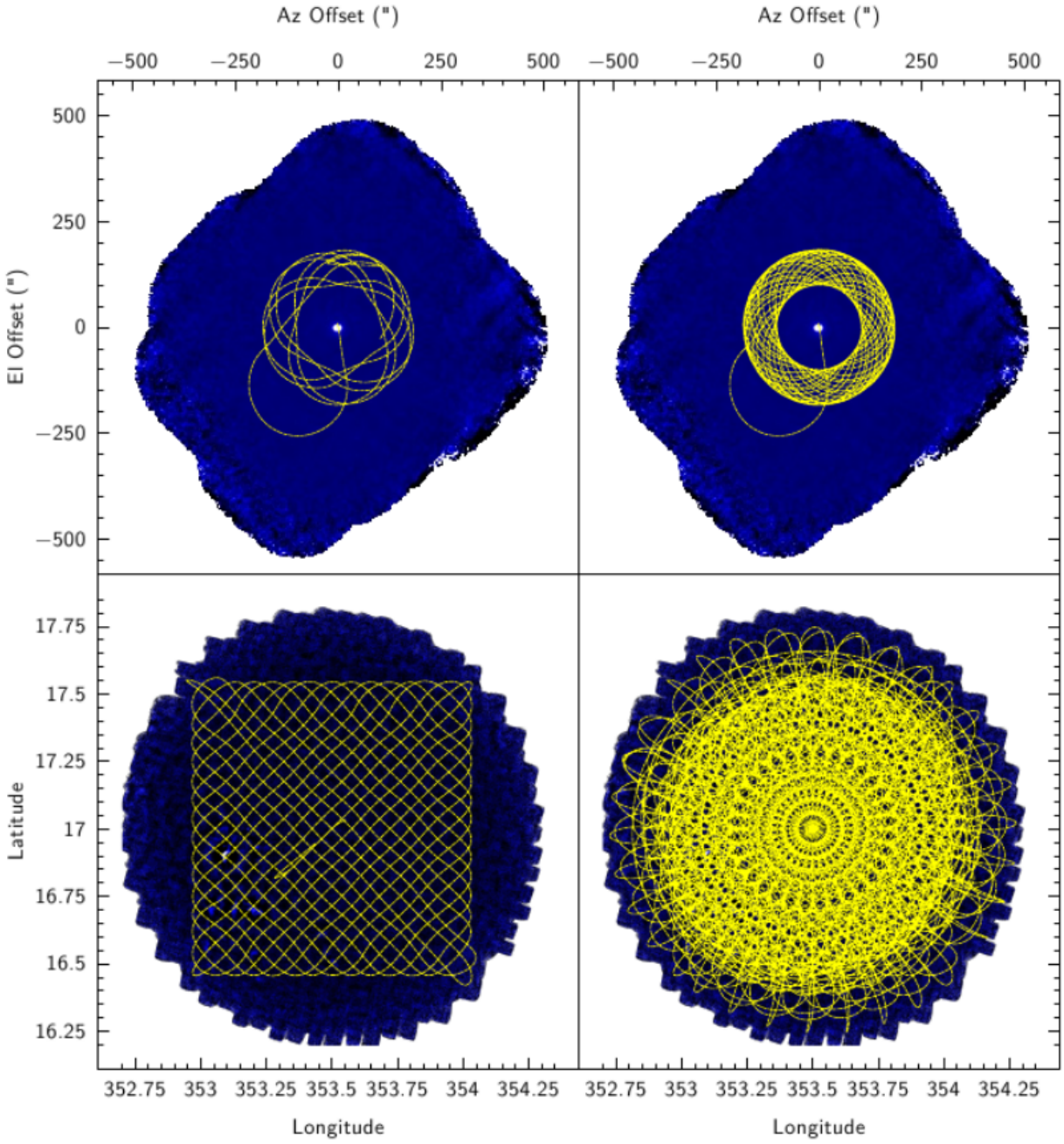

Figure 2.2. The 2 SCUBA-2 observing modes. Top: The DAISY scan pattern. Bottom: the PONG scan pattern. The left hand column shows the pattern after one scan, and the right shows multiple observations. Image credit: SCUBA-2 data reduction cookbook

2.2.1 The Dynamic Iterative Map Maker

The whole reduction procedure is done within the The Dynamic Iterative Map Maker (DIMM, Chapin et al. 2013) which uses the Kernel Application Package (KAPPA) and the Sub-Millimetre User Reduction Facility (SMURF) packages from STARLINK. The whole data reduction process can be found in Figure 2.3. The process is divided up into two sections: pre-processing and the iterative stages. The pre-processing steps includes concatenating the raw data files for each sub-array such that they make one single time series. Any short duration spikes in the time series are also removed, since they can cause issues later on in the reduction procedure. The time series have the flat fields applied with the resulting time series being in pW. The data is then down-sampled and any bolometers with unusually high noise levels are flagged and do not contribute to the rest of the reduction. The map maker then moves onto the iterative steps. An example of a time series from one bolometer can be seen in Figure 2.4.

In each iteration the map maker tries and models the components of the time signal for each bolometer. These are then removed from the time series and the remaining signal, which should be the astronomical signal, is formed into a map. However, in practice the presence of the astronomical signal in the original time series could cause issues modeling the noise and cause inaccuracies in the final map. Therefore this initial astronomical signal is subtracted from the original time series, and the models are re-estimated. This results in a more accurate map, and this process is repeated until the map has converged (this is discussed further on).

The first component to be modelled is the Common Mode (COM) signal. This signal is common to all the bolometers, with the dominate cause of it being the sky and thermal emission. This emission is determined by simply averaging over all bolometers for each time slice. This also allows for bolometers to be flagged and removed if their COM model deviates from the majority of other bolometers. The COM signal can be derived from all the bolometers, or each array individually. This has advantages depending on the sources being observed, and is discussed more in Section 2.3.

Working with the COM, you have the Gain (GAI) model. This consists of a time varying scale and offset that scales the COM model for each bolometer, such that it resembles the original data as closely as possible. It is this scaled COM model that is removed from the time series. Extinction corrections (the EXT model) are then applied based on measurements from the JCMT water-vapour radiometer, and models from Dempsey et al. (2013).

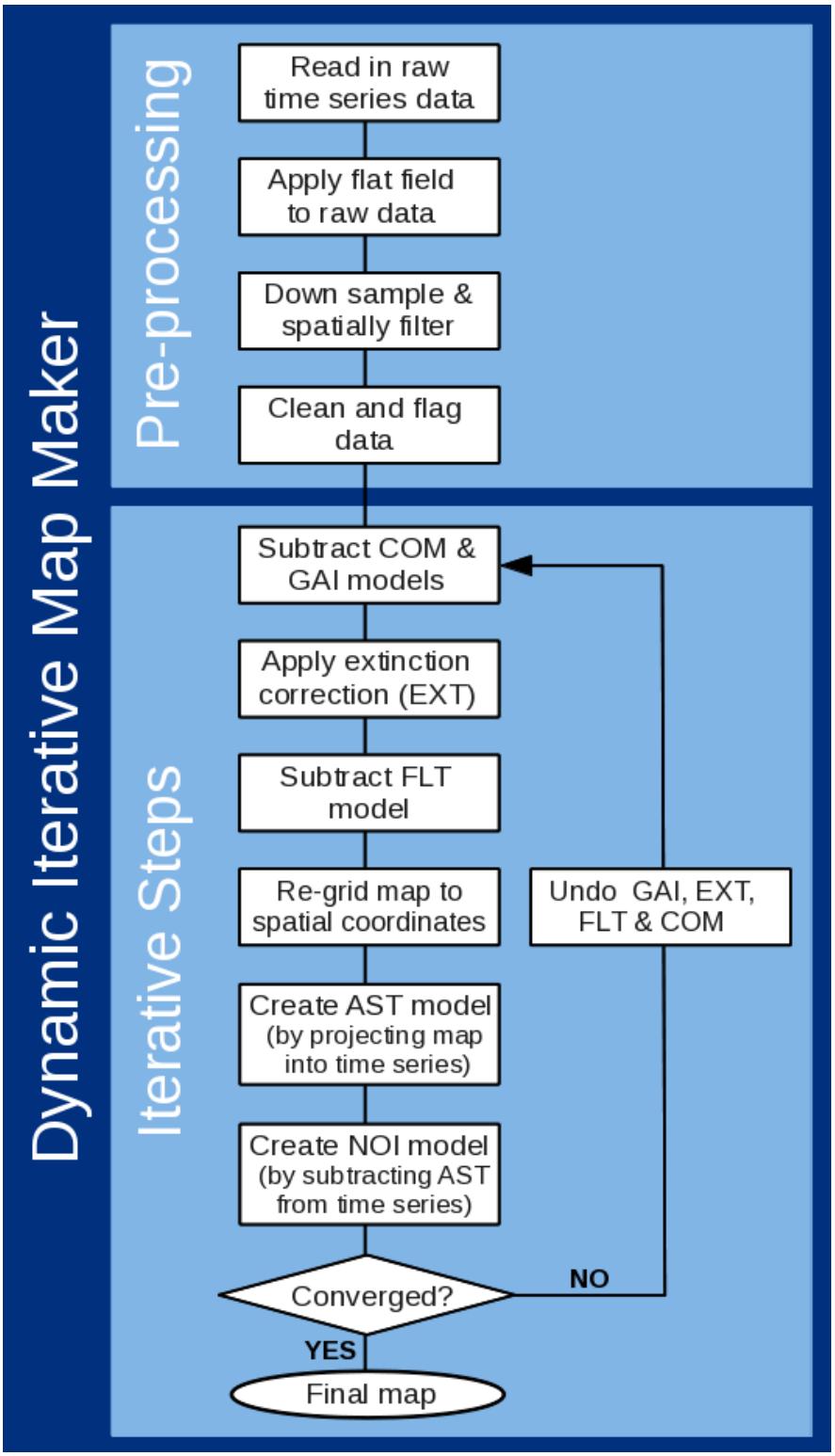

Figure 2.3. The flow chart showing the steps in the reduction process. Image credit: SCUBA-2 data reduction cookbook

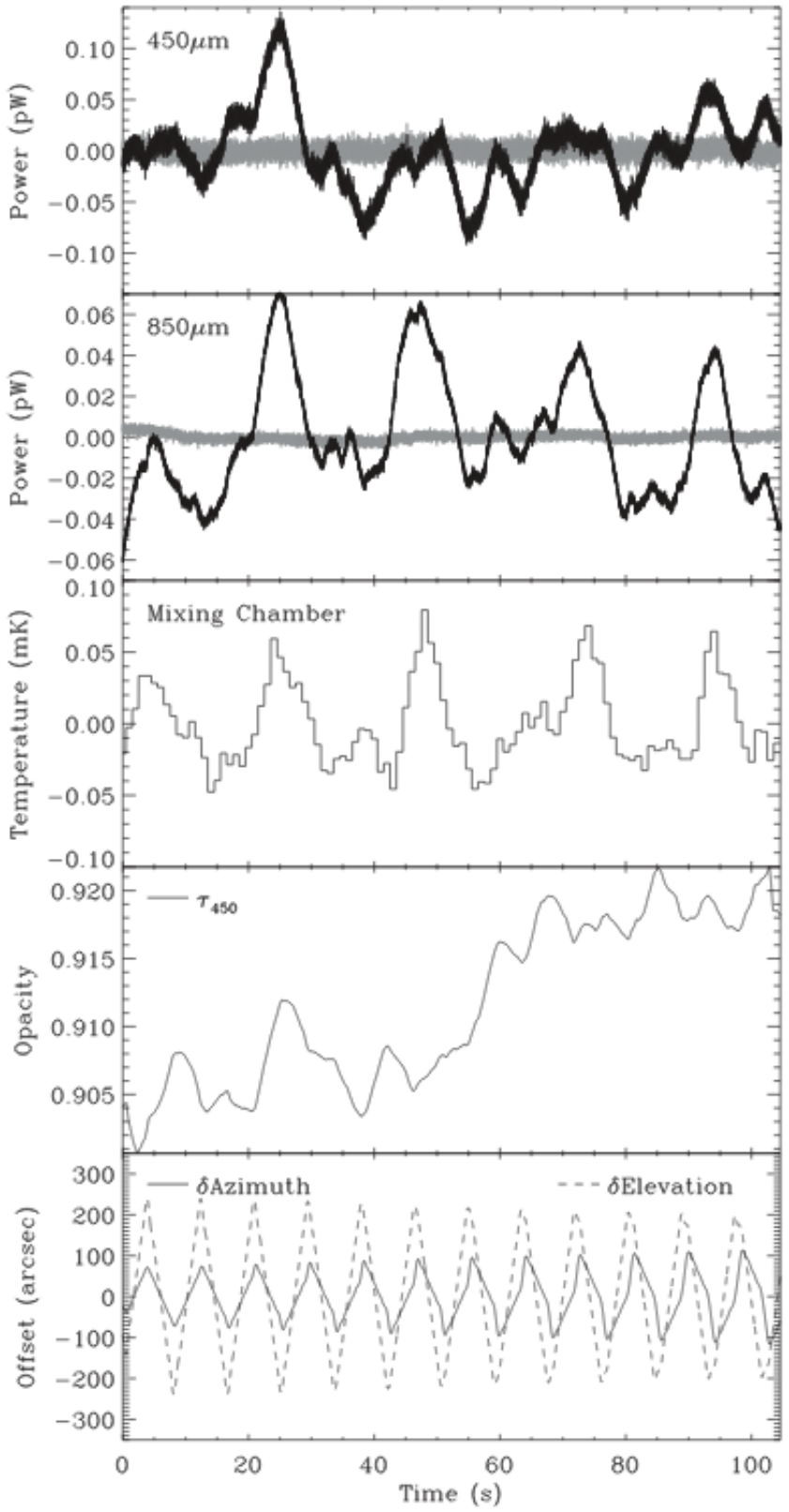

Figure 2.4. A typical time series for both 450 and 850 μm. The top 2 panels show the raw time series (with the grey bar showing the COM signal), and the third panel showing the change of temperature within the instrument. The fourth panel shows the change in the 450μm opacity, and the final panel shows the azimuth and elevation offsets. Image credit: Chapin et al. (2013).

The DIMM then calculates the Filtering (FLT) model, which uses both low and high pass filters to remove certain frequencies (which represent angular scales). The key role this model has is applying a high pass filter to remove the low frequency $1/f$ noise.

Once all these models have been removed the astronomical signal (AST) model is calculated. This is done by first subtracting the AST model from the previous iteration (with exception for the first iteration) and the remaining data is binned into a final science map. Following this the map is then converted back into the time domain and becomes the next AST model.

The final model is the noise (NOI) model. This is the last model and is only calculated on the first iteration, and calculates the RMS noise in each bolometer. This noise is then used in all other iterations to weight the bolometer values when binning into the final map. The different models for a single bolometer can be seen in Figure 2.5

Once an iteration has been completed convergence is checked, with convergence being defined one of two ways. The first is by specifying a certain number of iterations to pass. The second is by measuring the mean change in the pixels of the map between iterations. If the mean change falls below a certain threshold the map is considered converged and the process stops. If the map has not converged yet, all the models *except* the AST model are added back onto the time series and the process repeats until convergence has been reached.

2.3 TAILORING THE PIPELINE

The pipeline above can be altered when processing data from different astronomical sources, or different weather conditions. For example when dealing with an extended source (e.g. a nearby galaxy) care has to be done when dealing with the filtering so large scale structure is not lost. Point sources on the other-hand (e.g. high redshift galaxies), require little filtering as there is no structure to worry about. However, care does has to be taken due to the low brightness of these sources.

There are several pre-made configuration files available, all tailored to deal with different astronomical sources. Since I will be dealing with high redshift galaxies the blank field configuration is best suited, as it has been specially created to detect low signal to noise point sources in blank fields.

The biggest difference between the blank field reduction, and a "standard" reduction is the omission of the FLT model. Applying a high pass filter multiple times to a map with little signal in could cause convergence issues, so instead a

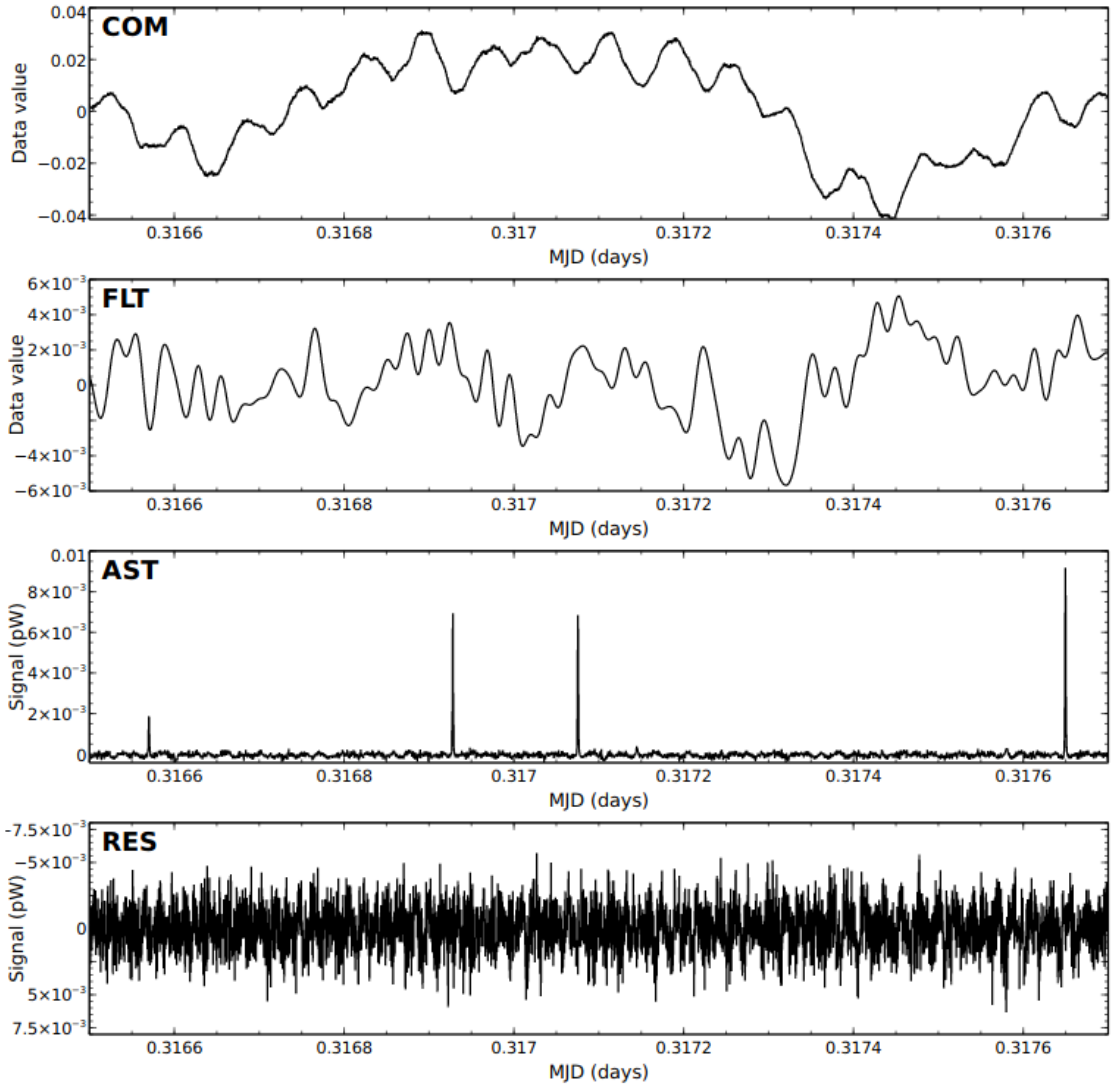

Figure 2.5. The different models for a single bolometer. The COM model is showing the average signal for all bolometers, and the FLT model is showing residual low frequency noise. The AST model shows spikes whenever the telescope passes over the source, and the RES model just shows white noise. Image credit: SCUBA-2 data reduction cookbook.

much harsher high-pass filter is applied once in the pre-process stage to remove any large scale structure. Other changes include more conservative cuts when removing problematic bolometers, and measuring the COM model on each sub-array rather then all 4 sub-arrays. These all help to remove large scale structure and detect the faint sources.

Figure 2.6 shows the 850 μm data for CLJ1449 after being reduced with the standard blank field pipeline. Whilst there are sources visible there is still a large amount of noise present, and some areas it seems there could still be some slight large scale emission. This is because the default filtering only filters out any scale larger then 200 arcsec. Given the scale at the redshift of my clusters (1 arcsec $\sim$ 8.6 kpc), I can decrease the filtering setting, and filter out structures on smaller scales than 200 arcsec. Due to the faintness of the sources, I can apply a matched filter to aid in the detection of sources similar in size to the beam. The matched filter and its application is discussed more in Section 2.3.2.

Following settings similar to the SCUBA-2 Cosmology Legacy Survey (S2CLS, Geach et al. 2013, 2017) I apply a filter that preserves any structure with $\theta < 120$ arcsec for 850 μm and $\theta < 100$ for 450 μm. I set a lower limit for the 450 μm map since the atmosphere has a more profound effects on those wavelengths to a greater degree then the 850 μm. A comparison of the 850 μ image made with the default filtering and a 850 μm image made with a harsher filter chosen to preserve the structure < 120 arcsec is shown in Figure 2.6.

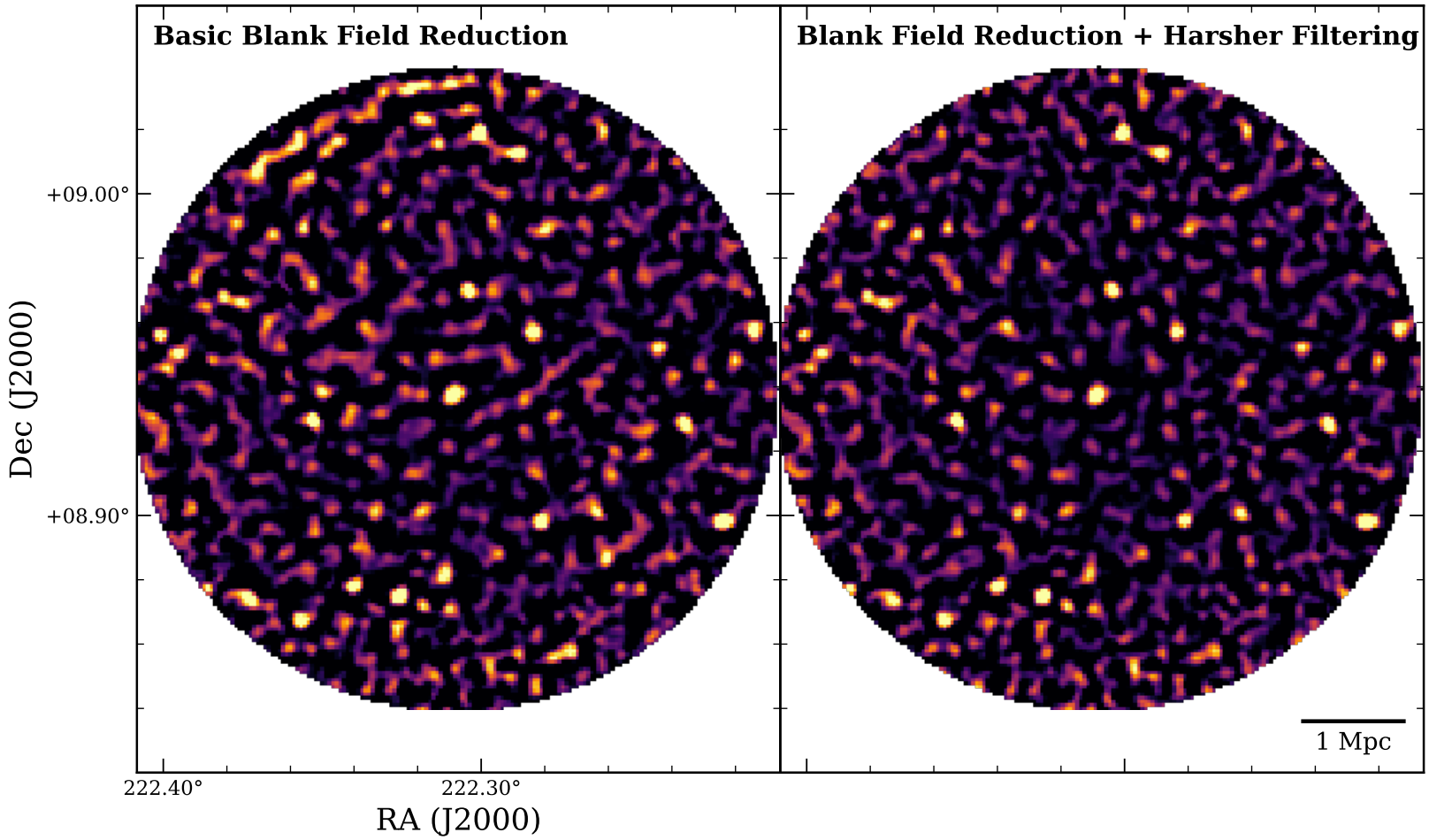

Figure 2.6. Left: The SCUBA-2 850 μm map of CLJ1449 after being passed through the basic blank field reduction configuration. Right: The SCUBA-2 850 μm map of CLJ1449 after being processed with a modified blank field reduction script, that includes much harsher filtering. Note that both of these maps have been matched filtered, and cropped to a radius of 360 arcsec.

2.3.1 MASKING

Another technique I used to improve the quality of my maps is masking. Masking can either include or exclude certain bolometers when calculating certain models (AST, COM, FLT). The choice to include or exclude a bolometer is based on its position within the map. A mask therefore is simply a collection of pixels within the output map, which could contain a potential source.

Two types of masks can be used, dynamic and static. Dynamic masks change from iteration to iteration and are used when there is no prior knowledge of where the emission will be, and need to constantly be adapted depending on the results in the iteration. Static masks remain constant throughout the whole reduction procedure, and are designed to be used for locations of known emission. Masking can either be applied to one model, or multiple models at the same time. The aim of masking is to try and break the degeneracies between the models and get more accurate answers for each model.

The aim of the AST mask is to break the degeneracy between the AST and COM models (which can cause large scale structure to appear in the map). The AST mask simply works by forcing all the values in the AST model to zero apart from areas which fall within the mask. On the next iteration this allows the COM model to be better constrained.

Since the COM model is the average of all the bolometers in any given time slice, bright sources can easily bias this. The COM mask, masks out these bright sources and allows a far more accurate model to be predicted. This mask also helps get a better estimate for the number of bad bolometers, and reduce the amount of rejected data.

I decide to apply a mask to my data to optimise the detection of sources. Whilst I do not know the positions of the sources, a dynamic mask would seem logical to use. However I decide to use a static mask instead. The first step is to do a "rough" reduction using the setting described above. I make a mask from this "rough" map and repeat the map making procedure with the mask. The first step is to apply a threshold to a signal to noise (S/N) map, that sets any value below 3σ to 0 and anything above is set to one. This means any potential source will be given a value, and the background is set to 0. The map is smoothed with a Gaussian, and re-scaled to have values between 0 and 1. A second threshold is then applied setting anything within the mask to 1 and outside the mask to 0. This second threshold is applied since a harsh cut at the edge of a map is very unrealistic. An example of a mask can be found in Figure 2.7.

With the introduction of a mask, the noise decreased by 10-15% both the 450 and 850 μm maps.

A big advantage of to using masking in the 450 μm is in aiding the detection of faint, sources that are blended in the 850 μm image. Due to the shorter wavelength the 450 μm map has about twice the resolution of the 850 μm map. This means sources that are blended at longer wavelengths can start to be resolved. This can be seen in Figure 2.8, where three sources are just about visible in the un-masked map. Applying a mask helps bring out these galaxies, and makes them more detectable.

2.3.2 Matched Filtering

Since I am expecting these sources to be at high redshift, they will have a size similar to that of the telescope beam (7 arcsec at 450 μm and 15 arcsec at 850 μm), so the maps have to be optimised to detect these sources. To do this I apply a matched filter to the maps (Serjeant et al. 2003). The matched filter takes the telescope point spread function (PSF), and convolves it with every pixel, allowing for better detection of faint sub-mm sources. The PSF used in this convolution is a Gaussian, normalised to one and has the same FWHM of the telescope beam. The result of matched filtering can be found in Figure 2.9.

As can be seen in Figure 2.9 , there is still a rather large amount of large scale structure that has been missed off during the reduction. To account for this an additional step is applied, before the matched filter is used. The map is smoothed with a very broad Gaussian (30 arcsec in this case) and then subtracts it from the map. This results in a map with no large scale structure and just the faint point sources. It should be noted that it is this large scale removal that contributes to the negative bowling around the very bright sources. Once the background has been subtracted, the matched filter is applied.

The effectiveness of using a matched filter can be seen in Figure 2.10. Before matched filtering was applied the maps are dominated by noise, and it is impossible to detect any signal. After matched filtering there is a lot more pixels that have high S/N, and these are my astronomical sources.

Once a matched filter has been applied, the maps are cropped to a radius of 360 arcsec, which corresponds to a physical scale of 3 Mpc. This is because SCUBA-2 maps actually observe a slightly larger radius then requested (this is to assure that the central source has equal coverage and depth), and the noise is greater in the very edges of the map.

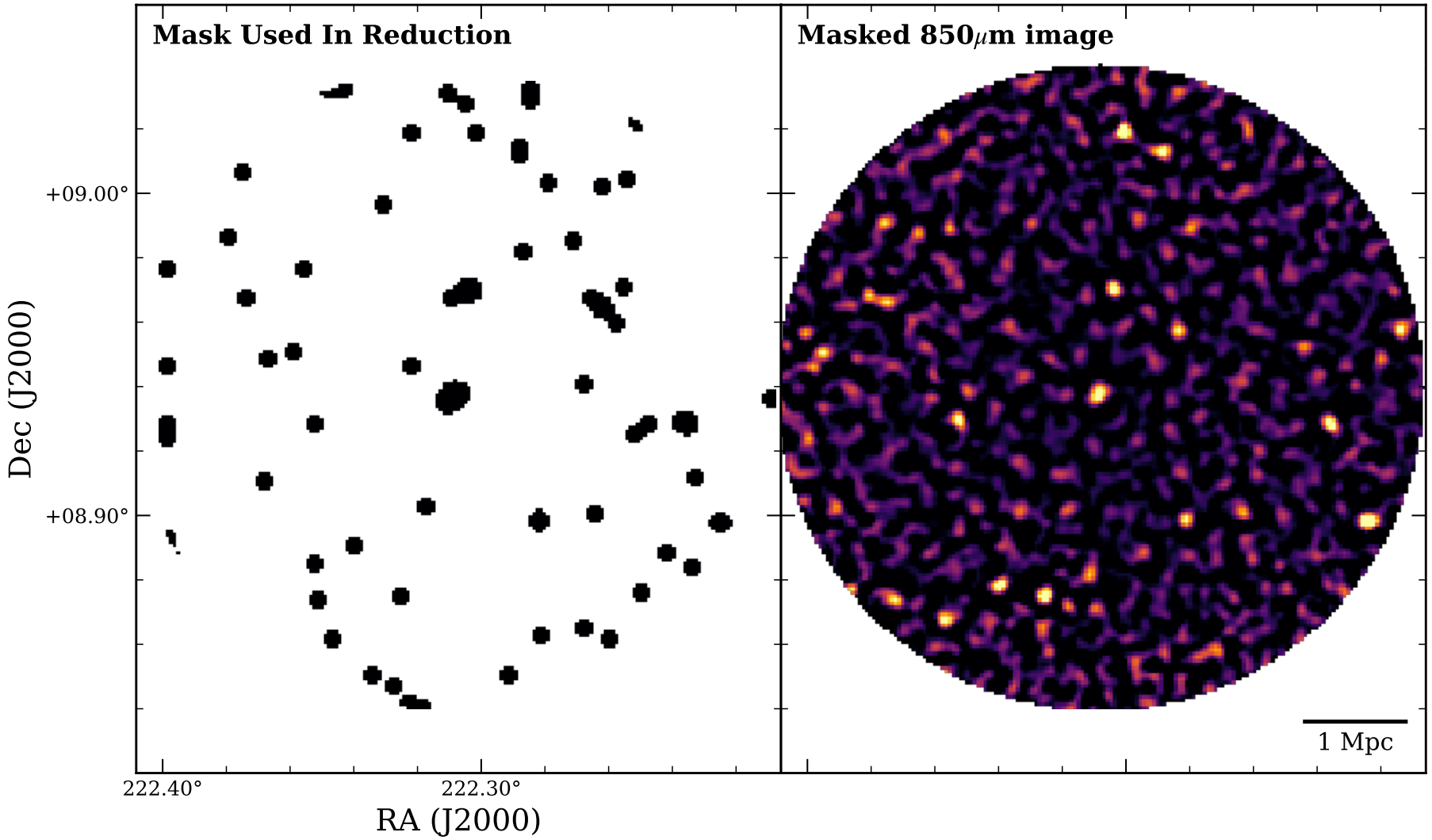

Figure 2.7. Left: An example of the mask used for the 850 μm map. Right: The final 850 μm after it has been reduced using a mask. Note that this image have been matched filtered.

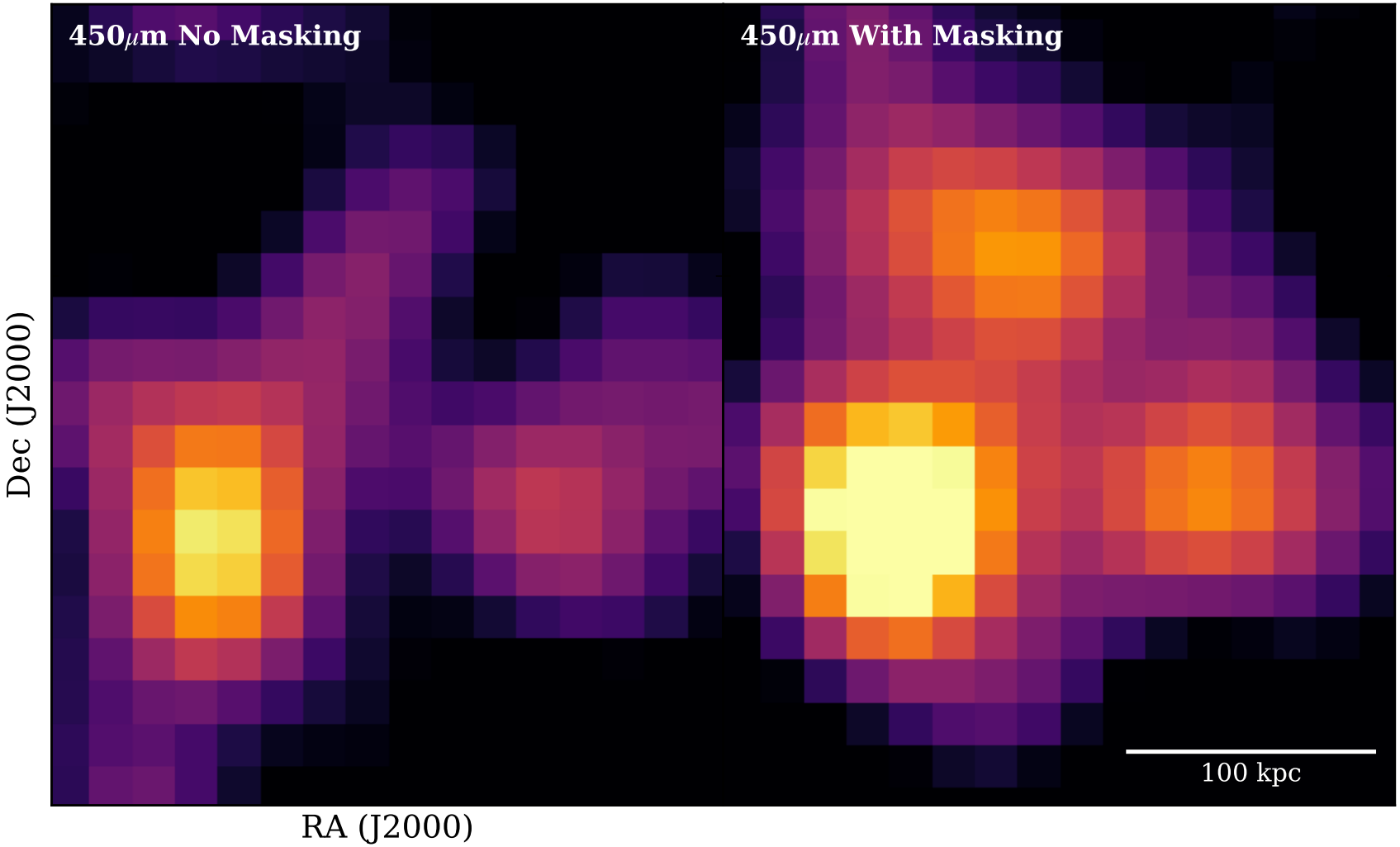

Figure 2.8. The center of the 450 μm map before (left) and after (right) being masked. After masking the three sources are clearly distinguishable. Note that both of these images has been matched filtered.

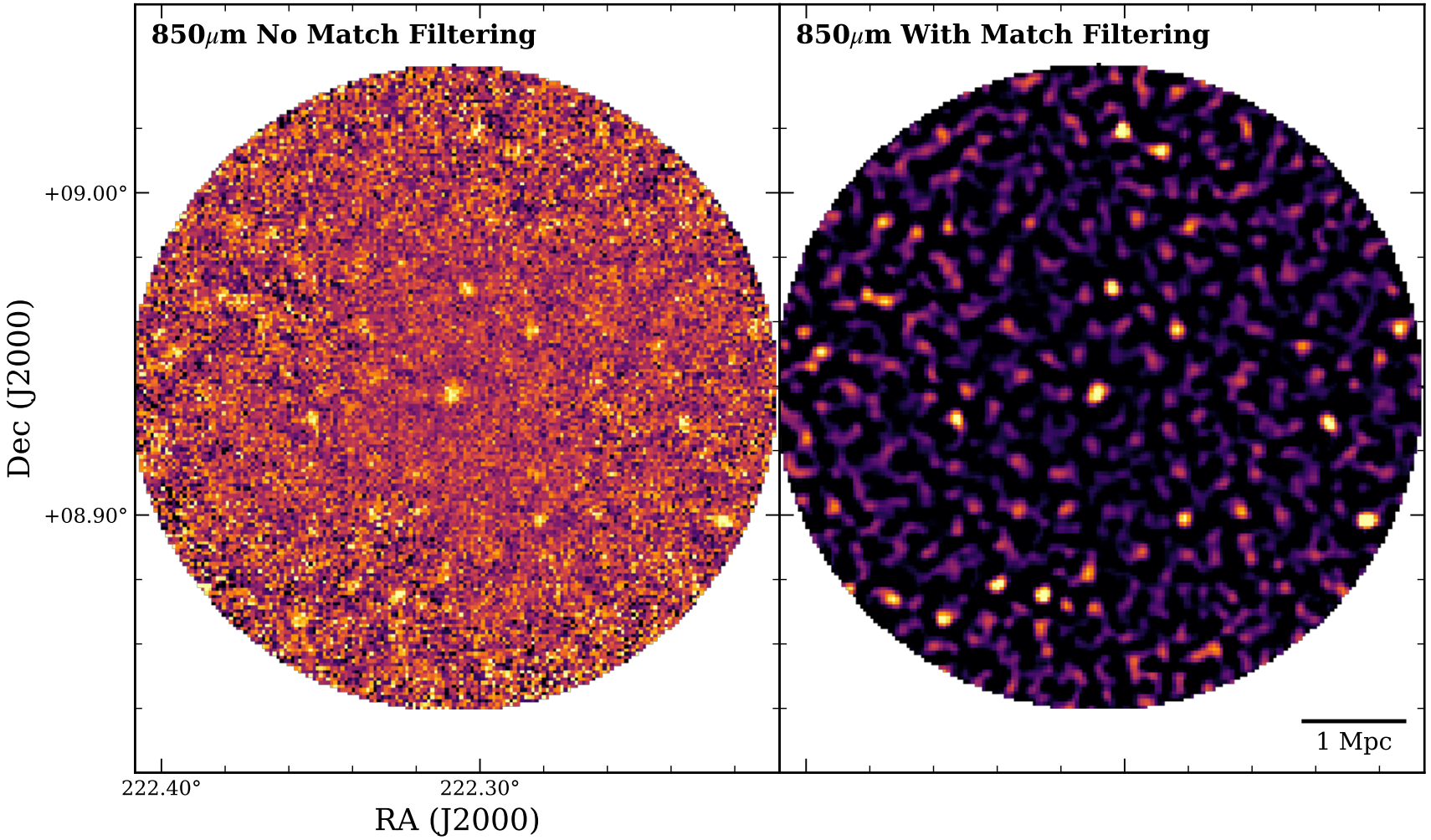

Figure 2.9. Left: The 850 μm map without any matched filtering. The sources are just about visible but still difficult to detect. There is also still some large scale emission that has not been filtered out yet. Right: The 850 μm map after a matched filter has been applied. All the large scale structure has been removed, and the sources are clearly visible.

2.4 Calibration

Once the reduction is complete the maps need to be calibrated, and converted from the raw units of the map (pW) to a flux density (Jy beam^{-1}). This is done by observing sources of known brightness, and using them to scale the flux (whilst accounting for any changes caused by the atmosphere).

For SCUBA-2, extinction models from Dempsey et al. (2013) are applied to sources with well known fluxes. This in turn generates a flux conversion factor (FCF) which converts from pW to Jy beam^{-1}. Whilst there are standard FCFs* (derived from hundreds of observations), there are two issues when applying them to my data. The first stems from the way I reduced the data. Due to the filtering used, there is a noticeable loss in the flux, which needs to be accounted for when applying the FCF. Also several studies (e.g. Chen et al. 2013; Hsu et al. 2016) have found that they obtain better results by calibrating each observation individually, based on the calibrators before and after observation. However, the difference at 850 μm is less noticeable then 450 μm (Smith et al. 2019a).

I derive my own FCFs to account for both of these issues. The first step is to account for the loss in flux from the reduction procedure. To do this I create fake sources of known brightness and inject them into the map. These sources were Gaussian with the same shape of the beam, and the peak flux was the mean of all sources greater then 3σ (1.2×10^{-5} pW for 850 μm and 1.5×10^{-5} pW for 450 μm). I injected 11 sources into each map, with the positions being chosen at random. These can be seen in Figure 2.11.

Once these sources were injected I re-ran the same reduction procedure (including masking) to these maps. With this final map I subtracted off the original, non-injected map and compare the flux before and after reduction (Figure 2.12). Figure 2.13 shows the radial profile before and after reduction. When taking the average loss over all 11 sources, I found for both 450 and 850 μm, there was an $\sim$10% loss in flux. This means when applying the FCF to my maps, I include an additional 10% to account for the loss in flux from the reduction procedure.

*The standard FCFs are 491 ± 88 and 537 ± 47 Jy pw^{-1} beam^{-1} for 450 and 850 μm respectively

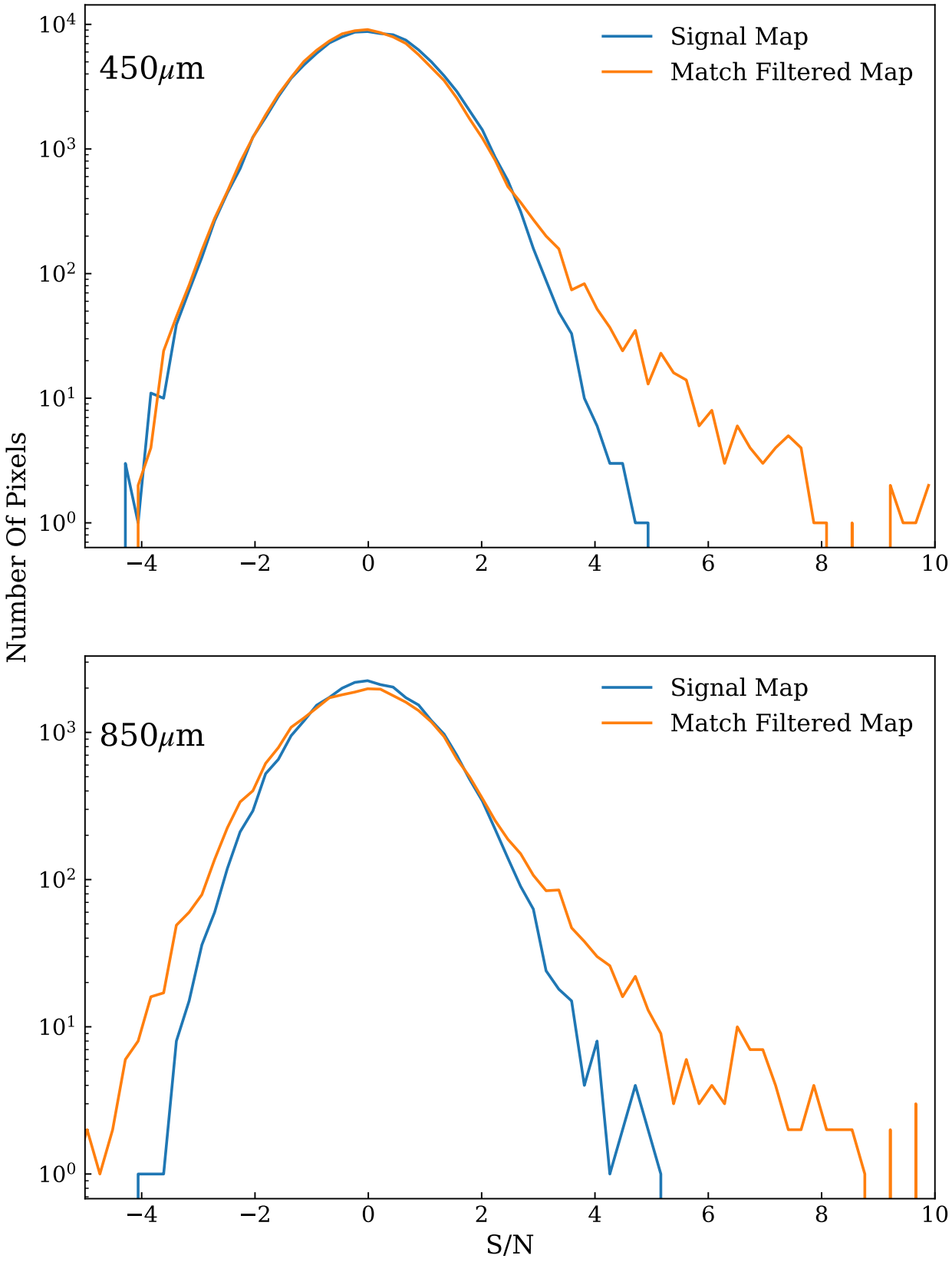

Figure 2.10. Comparing the S/N of pixels in both the 450 and 850 μm maps, before and after matched filtering.

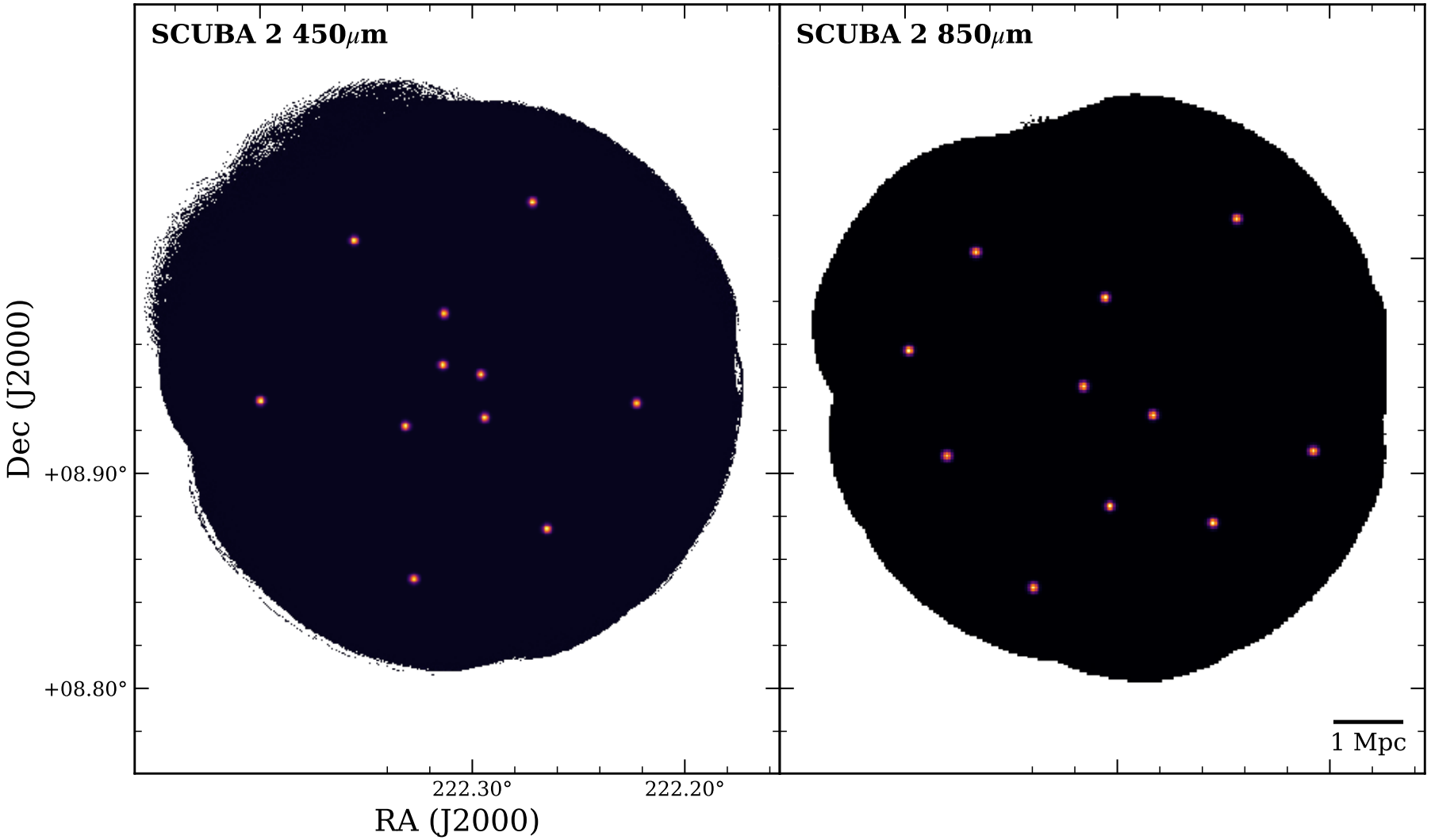

Figure 2.11. The 2 injected maps used to test the loss in flux due to the reduction procedure.

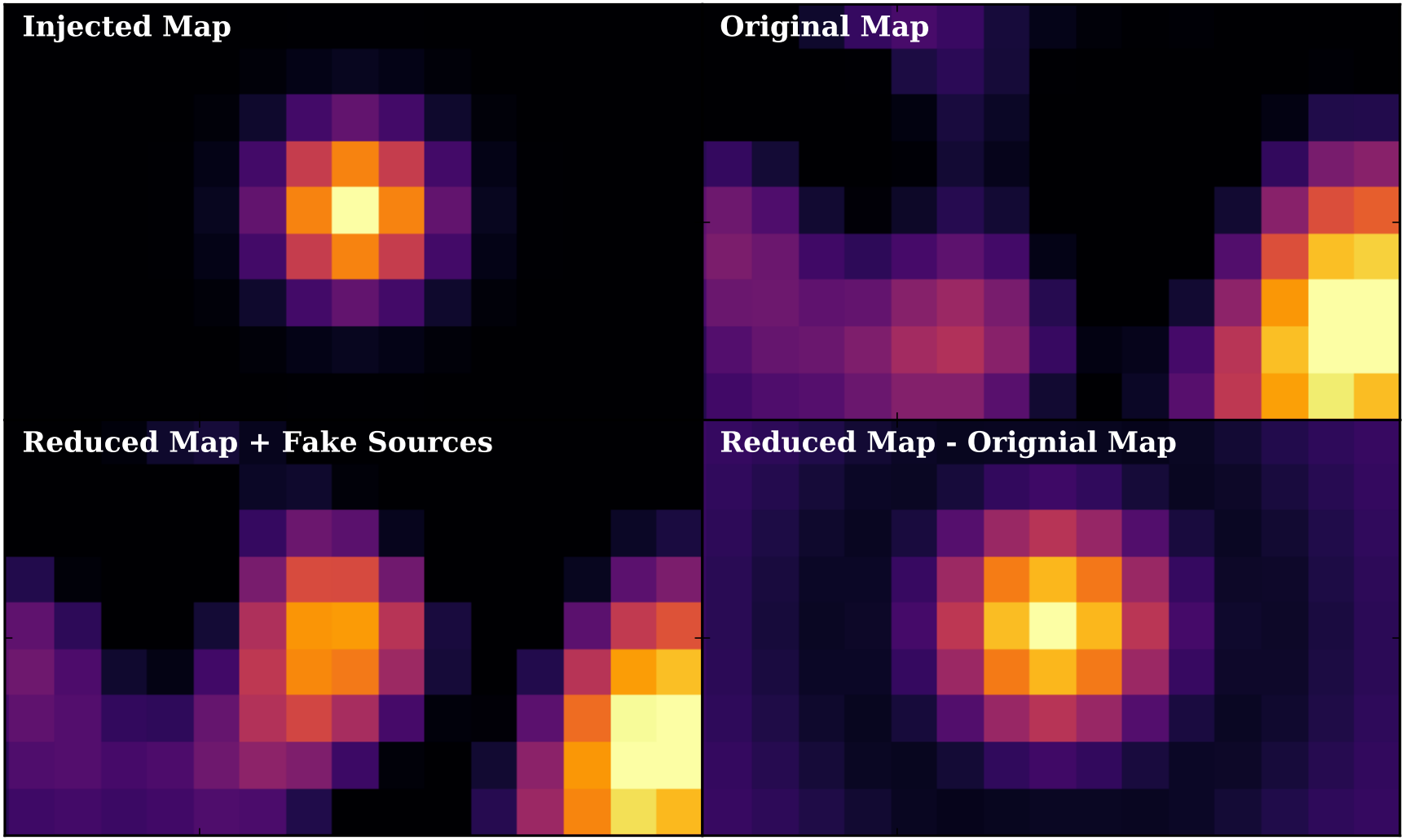

Figure 2.12. Comparison of an injected source before and after reduction.

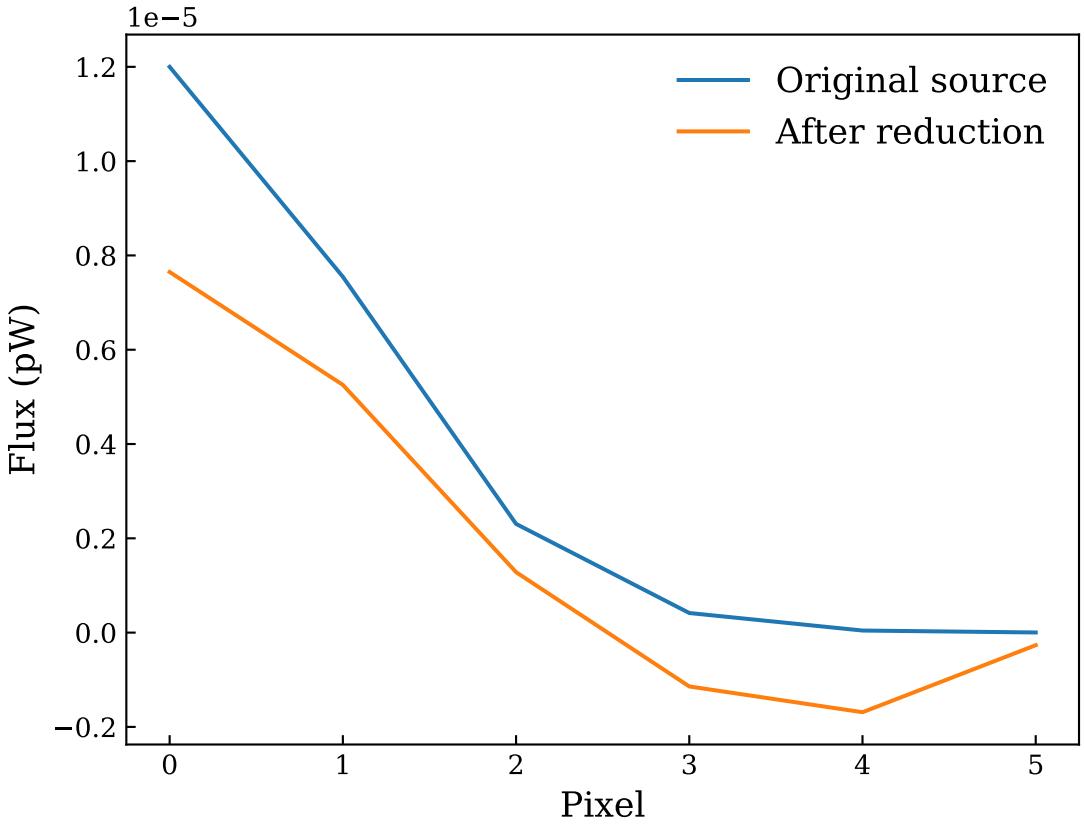

Figure 2.13. Radial profile comparing the change in flux before and after reduction for a fake source.

I then checked to see if calibrating each observation individually improved the data. As multiple calibrators are taken throughout the night, it is possible to create a calibration graph for each night. I can then take each individual observation and find what the FCF should be at the time it was observed. For both clusters there were 8 hours integration time, which equals 16 observations. CLJ1449 was observed over 6 nights between April 2015 and March 2016, and JKCS041 was observed over 3 nights between September 2015 to November 2015.

For each night the calibrators were downloaded, reduced and had their FCF calculated using packages within the SCUBA-2 data reduction pipeline. This FCF was recorded and plotted against the time of observation. I then fitted a second order polynomial to the data, so I can estimate the FCF for any time throughout the night. An example of one such plot from the 19th February 2016 can be seen in Figure 2.14. It can be seen that the 450 μm FCF varies by at least 30% over the night, and deviates from the standard FCF. This change is due to the change in temperature throughout the night. At the beginning of the night, the dish is often warm but as the night goes on it cools down. This can cause changes in the shape of the telescope

and hence the FCF.

For each observation I calculated the FCF at the start of the observation, and then at the end (each observation is 30 minutes) and took an average of the two. Whilst there was only a minimal reduction in the noise (less than 10%), the fact that the FCFs vary so much throughout the night highlights the importance of calibrating them this way. If I used the standard FCF for each observation, there is a chance I would over-estimate the flux and get inaccurate results in my analysis.

Each observation then had their FCF applied to it, and then mosaicked together to form one final calibrated map. Table 2.2 shows the average FCF for both clusters, and the number of calibrators used over all observations.

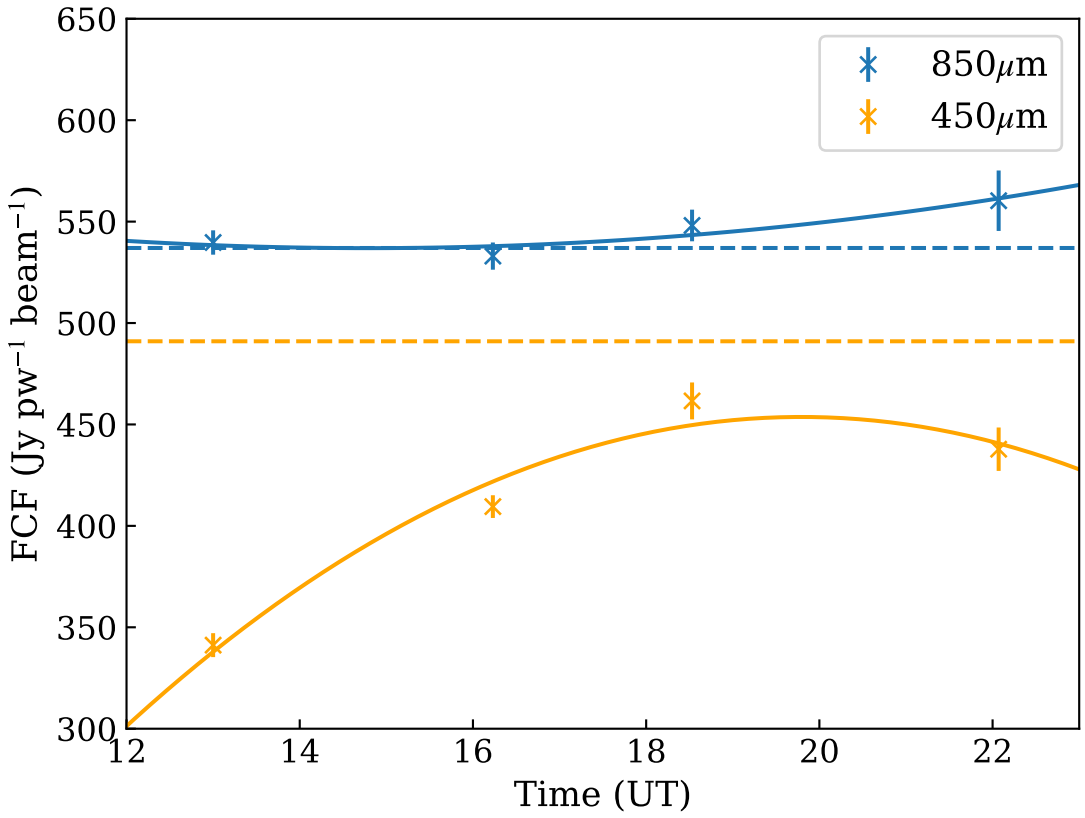

Figure 2.14. A calibration graph for 19th February 2016. Note that the whilst the 850 μm FCF stays constant, the 450 μm FCF varies by 30%. The dashed horizontal lines show the standard FCFs, which means in this situation for 450 μm the standard FCF would not be appropriate. Note this FCFs have also had an additional 10% added on to account for flux lost in the reduction procedure.

Table 2.2. Details of the FCFs for my clusters (taken by averaging the FCFs for all observations). The units of the FCFs are Jy pw^{-1} beam^{-1}

Cluster	No. calibrators	450 μm FCF	850 μm FCF
CLJ1449	20	460	552
JKCS041	14	456	540

2.5 SUMMARY

In this chapter I have described the reduction and calibration procedure used in reducing SCUBA-2 data, and how it has been tailored to deal with my cluster data. The procedure uses a modified blank field reduction configuration, which is ideal for dealing with faint point source objects. Other processes such as masking and matched filtering are used to help identify my sources. Deviations from the standard calibration procedure is also used, to account for both loss in flux due to the reduction procedure, and the atmospheric sensitivity of the 450 μm data. I use this procedure to reduce data for both CLJ1449 (Chapter 3) and JKCS041 (Chapter 4).

Chapter 3
Star Formation In CLJ1449+0856

"The universe is big. Its vast and complicated and ridiculous. And sometimes, very rarely, impossible things just happen and we call them miracles."

The 11th Doctor - *Doctor Who*

This chapter presents a study into the SFR-density relation in the redshift 2 cluster CLJ1449+0856. The work in this chapter was published in Smith et al. (2019b) and entitled "*Revealing dust-obscured star formation in CLJ1449+0856, a cluster at z=2*". The JVLA map used in this study was reduced by Andreas Papageorgiou, and the optical and NIR maps were provided by Raphaël Gobat.

3.1 CLJ1449+0856

CLJ1449+0856 (hereafter CLJ1449, RA=222.3083, Dec.=8.9392) is one of the highest redshift, fully virialized, mature X-ray-emitting clusters known. The cluster was first identified as an over-density of red galaxies during *Spitzer* observations of the so-called "Daddi Fields" (Daddi et al. 2000). Optical, NIR and X-ray follow-ups confirmed that this is a fully virialised cluster (Kong et al. 2006; Gobat et al.). Follow-up spectroscopy eventually identified the cluster redshift to be 1.99, making it one of the most distant clusters discovered (Gobat et al. 2013). Using the X-ray luminosity-mass correlation, the mass of the cluster was found to be $\sim 5 \times 10^{13}\,\mathrm{M}_{\odot}$, making it a relatively low mass cluster, and a typical progenitor to clusters seen today (Gobat et al. 2011).

Several studies have already been conducted on CLJ1449. Optical studies have shown that there is both a population of dust obscured star forming galaxies, and a

population of passive galaxies no longer forming stars, which is the beginning of a red sequence (Strazzullo et al. 2013, 2016). Using data from ALMA and the JVLA both Coogan et al. (2018) (hereafter C18) and Strazzullo et al. (2018) (hereafter S18) have found that the very centre of this cluster is still actively forming stars. S18 showed that within the central 200 kpc region, stars are forming at a rate of 700 $M_{\odot}yr^{-1}$. However C18 argued that based on the gas depletion times this SF cannot be maintained and the gas will soon be used up on short time-scales. It has also been suggested in C18 that the main cause of the high SF is down to mergers between cluster galaxies.

3.2 Observations and Reductions

Due to the facilities used, previous studies were only limited to the very central region of the cluster. In this section I present new SCUBA-2 observations, which when combined with archival Herschel, optical, and NIR data, allows me to observe both the entire cluster and the outlying field regions. This allows me to fully investigate the SF-density relation in and around CLJ1449.

3.2.1 SCUBA-2

The SCUBA-2 observations were carried out over 6 nights between April 2015 and March 2016 as part of projects M15AI51 and M16AP047 (PI: W. Gear). A total integration time of 8 hours was performed using 3 arcmin daisy scans, with all the observations being carried out in good grade one weather ($\tau_{225} \leq 0.05$). The data was reduced in the same way discussed in Chapter 2.

After the reduction the final rms values were 0.96 mJy beam^{-1} for 850 μm and 4.27 mJy beam^{-1} for 450 μm. The images can be seen in Figure 3.1.

3.2.2 *Herschel*

For *Hershcel* publicly available data from both PACS and SPIRE were available. The PACS observations were acquired in July 2011 (ObsId 1342224474, PI: R. Gobat). Both 100 μm and 160 μm were observed over 10 hours in large scan map mode. The noise for these maps are 1.9 and 3.2 mJy and achieve a resolution of 7.7 arcsec and 12 arcsec for 100 and 160 μm respectively. All 3 SPIRE bands were observed with an integration time of 4 hours in January 2013 (ObsId 1342259448, PI: H. Dannerbauer). The noise in the maps were 4.7, 5.5 and 6.2 mJy with a resolution

of 18, 26 and 36 arcsec for at 250, 350 and 500 μm respectively. Both the PACS and SPIRE level 2.5 data products were downloaded from the *Herschel* ESA archive*.

3.2.3 ALMA

As part of cycle 1 the central area of the cluster was observed at 870 μm using ALMA (Project code 2012.1.00885.S, P.I: V. Strazzullo). The cluster was observed for 2.5 hours and only covers a small area of the core of the cluster (0.3 arcmin^2). The map reaches a noise of 70 μJy beam^{-1} and has a resolution of $\sim$1 arcsec. For more information see C18. The data were acquired from the ALMA ESO science archive†.

Even though the data only cover the central region of the cluster (see Figure 3.2), the higher resolution means that I will be able to detect confused source members that cannot be resolved in the SCUBA-2 images. This will be discussed further in Section 3.3.

3.2.4 JVLA - S band

The S band radio data consist of observations from 2012 of JVLA S band (2-4GHz, project code: 12A-188, PI: V. Strazzullo.) using 16 spectral widows (128MHz bandwidth, 64 channels). The raw data were downloaded from the NRAO's VLA archive‡, and each observation separately reduced using NRAO's Astronomical Image Processing System (AIPS), following the standard VLA data calibration procedure described in the AIPS cookbook. For each observation, the calibrated UV data of the target field have been thoroughly flagged for radio-frequency interference and separated without averaging the frequency channels to avoid bandwidth smearing (chromatic aberrations). All of the resulting UV data sets have been combined for the final imaging, which consisted of a single phase-only and a final amplitude-and-phase calibration.

3.2.5 Spitzer

Complimentary IR data of CLJ1449 were obtained with *Spitzer's* Infrared Array Camera (IRAC, Fazio et al. 2004). All 4 bands (3.6, 4.5, 5.8, and 8 μm, PI: F. Giovanni, ObsId 4393984) were observed and used. Each of the IRAC bands covers the same area (27 arcmin $\times$ 22 arcmin) but due to offset between arrays, only the

*http://archives.esac.esa.int/hsa/
†http://almascience.eso.org/aq/
‡https://science.nrao.edu/facilities/vla/archive/

Table 3.1. Summary of the data sets used in my analysis.

Telescope	Instrument	Observed band	FOV
VLT	FORS 2	U, V	7 arcmin × 7 arcmin
Subaru	Suprime	B,I,z	27 arcmin × 35 arcmin
Subaru	MOIRCS	Y,H	7 arcmin × 4 arcmin
VLT	ISAAC	J, Ks	7 arcmin × 4 arcmin
Spitzer	IRAC	3.6/4.5/5.8/8 μm	27 arcmin × 22 arcmin
Herschel	PACS	100/160 μm	15 arcmin × 15 arcmin
Herschel	SPIRE	250/350/500 μm	35 arcmin × 35 arcmin
JCMT	SCUBA-2	450/850 μm	113 arcmin^2
ALMA	-	870 μm	0.3 arcmin^2
JVLA	-	10 cm	20 arcmin × 20 arcmin

3.6 μm and 5.8 μm data cover the same area as that in the SCUBA-2 maps. As part of the *Spitzer* warm mission the cluster was re-observed at 3.6 and 4.5 μm (PI: R. Gobat, ObsId 42576640) and when combined with the pre-existing data complete coverage of the cluster is achieved for 3 of the 4 bands.

3.2.6 ADDITIONAL DATA

I also utilise archival optical and NIR maps for CLJ1449. Deep B, I and z were taken with Suprime-cam (Miyazaki et al. 2002) on the Subaru telescope achieving 5 σ magnitudes depths of 26.95, 26.03, and 25.91, respectively. I also have NIR data (Y, H, J and Ks) taken with both the Multi-Object Infrared Camera and Spectrograph (MOIRCS, Ichikawa et al. 2006, Suzuki et al. 2008) on Subaru and the Infrared Spectrometer And Array Camera (ISAAC, Moorwood et al. 1998) on the Very Large Telescope (VLT). These images reach depths at 5 σ of 25.64, 25.47, 23.66, and 24.74 for Y, H, J, and Ks, respectively. Finally I have U and V band data taken with the FOcal Reducer and low dispersion Spectrograph (FORS, Appenzeller et al. 1998) also on the VLT, reaching 5 σ depths of 28.1 and 26.52 for U and V. For more information on these data sets I refer to Kong et al. (2006), Gobat et al. (2011) and Strazzullo et al. (2013). A summary of all data used in this analysis can be found in Table 3.1, and the fields of view (FOV) for all the maps used can be found in Figure 3.2.

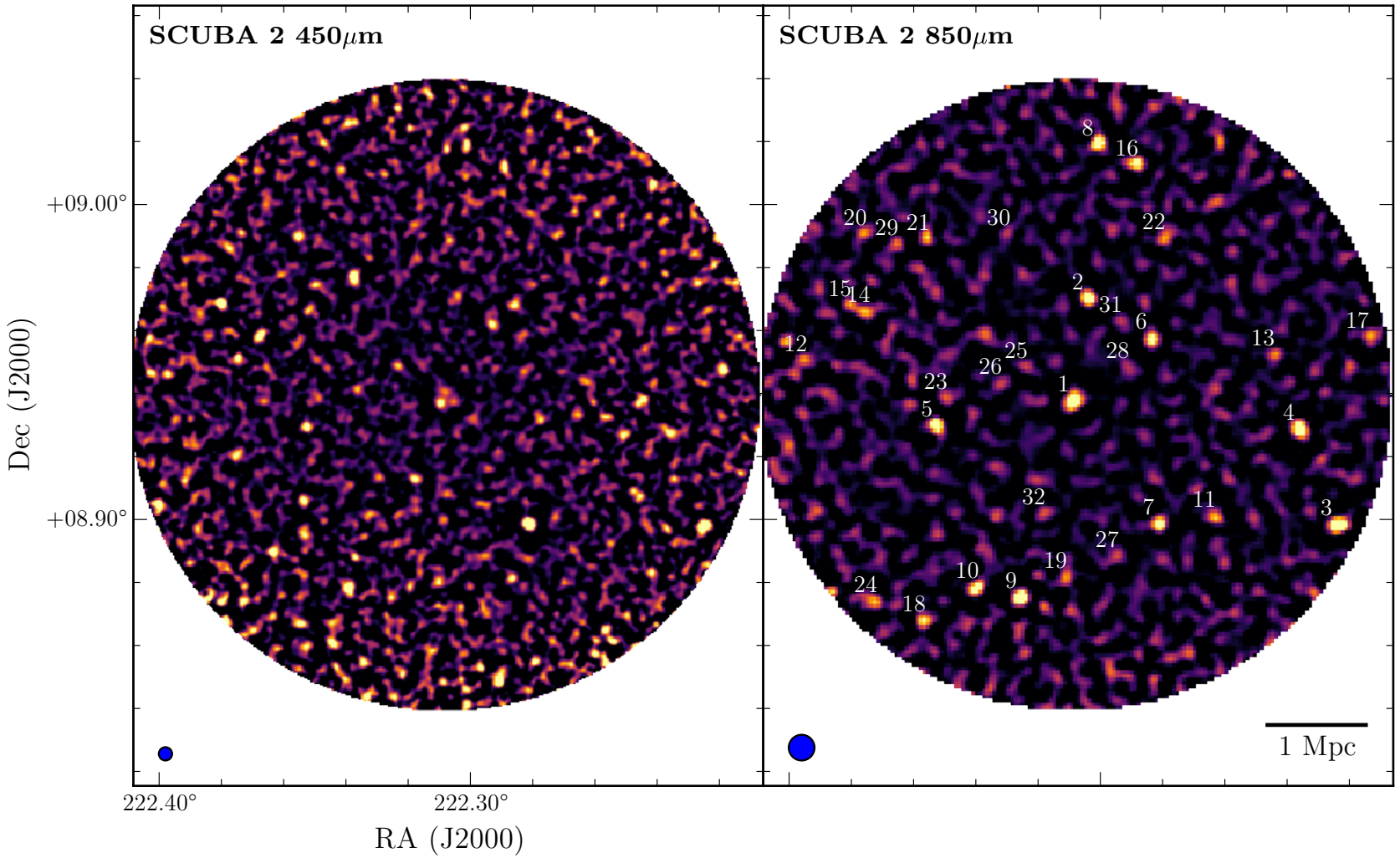

Figure 3.1. The SCUBA-2 maps of CLJ1449 with a radius of 3 Mpc. The FWHM size of the PSF can be found in the lower left corner. The positions of all 32 SCUBA-2 sources with an S/N greater than 4 are labelled on the 850 μm image, with the numbering being the same as that in Table 3.2

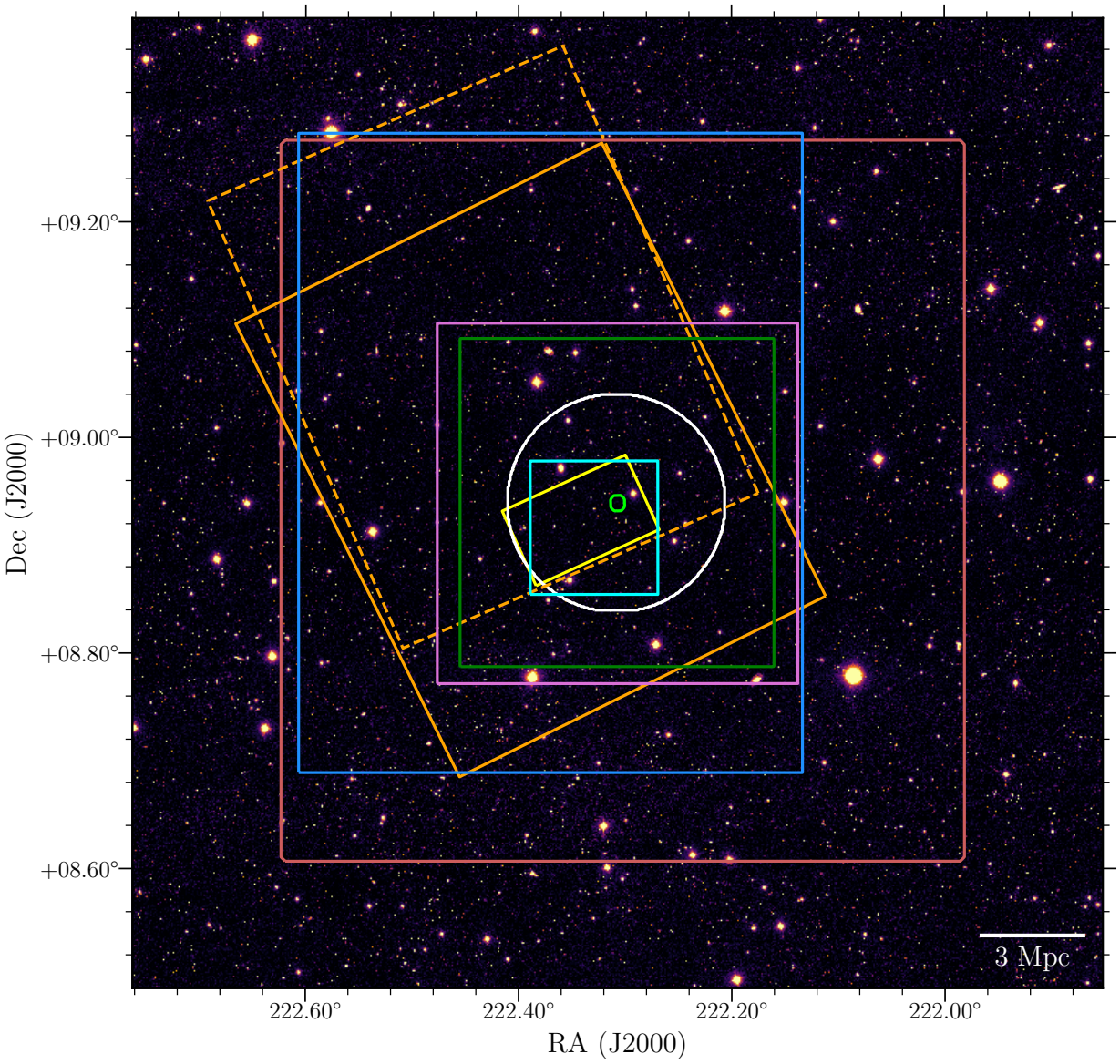

Figure 3.2. FOVs of all the data used in this analysis. The white circle represents the SCUBA-2 coverage (450/850 μm), while the small lime green circle represents the ALMA coverage. The yellow rectangle is the MOIRCS and ISAAC coverage (Y, H, J, and Ks bands), while the cyan square is the FORS 2 coverage (U and V band). The green square shows the PACS coverage (100/160 μm) and the purple square shows the radio data (10 cm). The solid orange rectangle shows the IRAC coverage at 3.6,4.6 and 5.8 μm, with the dashed orange rectangle showing the 8 μm coverage. The blue square shows the Suprime cam coverage (B, I and z bands) and the red square shows the SPIRE coverage (250/350/500 μm). The background is a g band image from SDSS.

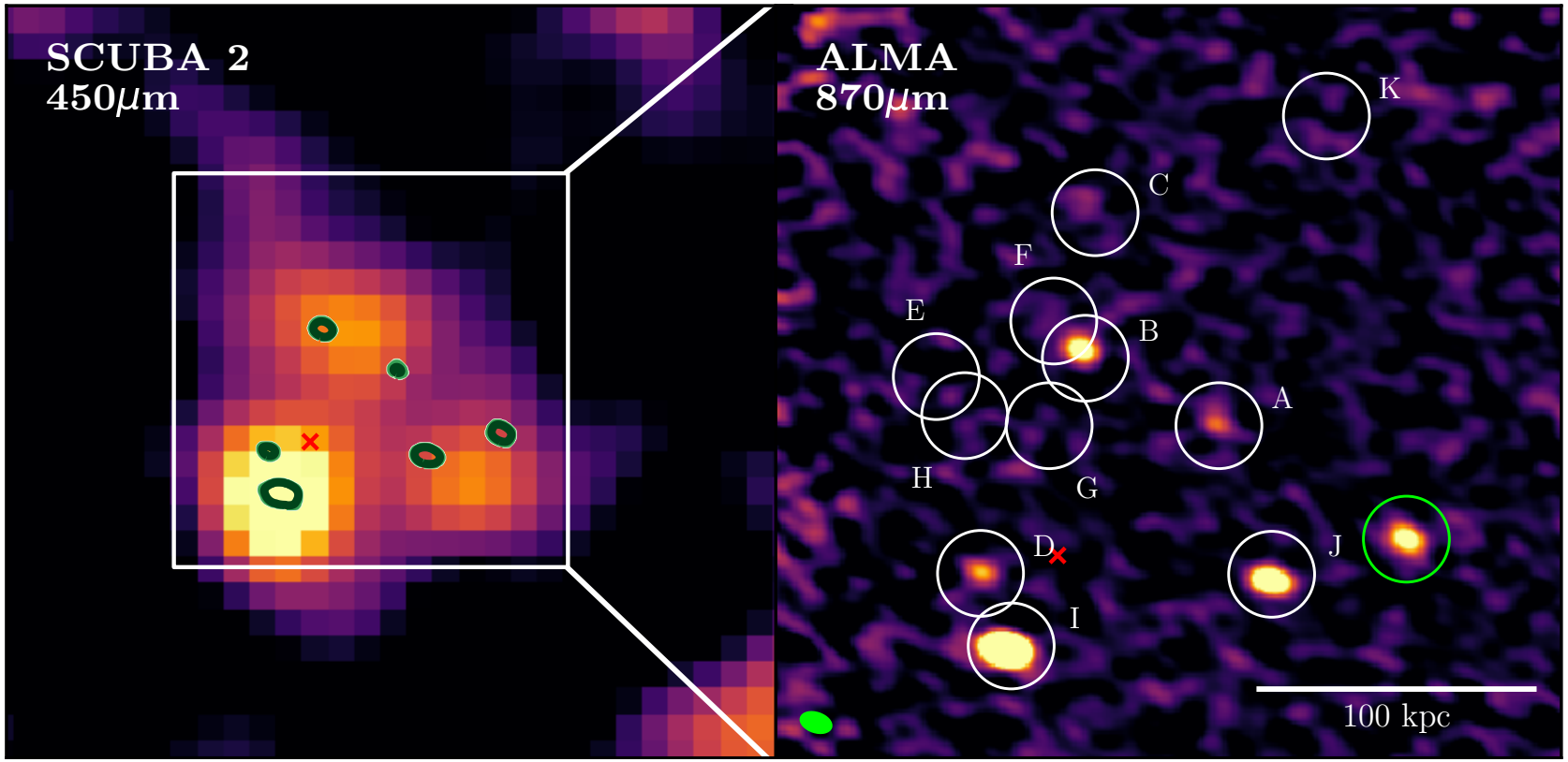

Figure 3.3. The ALMA 870 μm continuum map of the core of the cluster. The ALMA data resolve the SCUBA-2 450 μm map into 6 individual sources rather than 3. The size of the PSF can be seen in the bottom left corner. The letter represents the sources in Table 3.3, and are based on the designations from C18. A low-redshift object is known to contaminate the cluster, and is illustrated by the green circle. The red cross represents the centre of the X-ray emission from Gobat et al. 2011.

3.3 SOURCE IDENTIFICATION

To identify any potential sub-mm sources I searched for any sources in the SCUBA-2 850 μm map that have a signal-to-noise ratio (S/N) greater than 4. This uncertainty level was determined by inserting fake sources into a jackknife map, made by inverting half of the observations and co-adding. This produces a map with the same noise properties as the final map. Fake sources were then randomly inserted into the map (10^5 sources inserted in batches of ten, with fluxes picked from a uniform distribution) and SEXTRACTOR (Bertin & Arnouts 1996) was then used to extract these sources.

It was found that with an S/N of 3.5 I was over 80% complete at $\sim$5 mJy. However the number of fake sources (i.e. sources caused entirely by noise) was very high, with there being 8 sources detected. At an S/N of 4 there was only 1 fake source, which is expected in a map of this size with Gaussian fluctuations. Therefore an S/N cut of 4 was selected.

In the SCUBA-2 850 μm map I detected 32 sources that have a S/N greater than 4, with the positions of all these sources given in Table 3.2, and their locations illustrated in Figure 3.1. When I looked at the 450 μm map I found that there were 18 sources with an S/N greater than 4. When cross-matching these sources with the 850 μm ones I found only 11 sources matched. This low matching rate was also found by the S2CLS. Casey et al. (2013) found that in the COSMOS field there was only a $\sim$30% matching rate when comparing 450 and 850 sources at the same S/N cut. This implies that the 450 μm population is intrinsically different than that of the 850 μm and indicates that different redshift or luminosity populations are being probed.

From the number counts of the S2CLS, in a field of the same size, at this sensitivity I would expect to see 10$\pm$3 sources at 850 μm (Geach et al. 2017). This means that this cluster field is more than three times over-dense.

One issue that should be discussed is that of confusion noise. This noise is fluctuations of the background sky brightness below which sources cannot be detected individually. This could be an issue for the S/N maps as these only account for the instrumental noise and not this confusion noise. Whilst not including this into my noise estimates could cause an artificial increase in the S/N, it has been shown that confusion noise only begins to effect maps less then $\sim$2 mJy at 850 μm (e.g. Eales et al. 1999; Coppin et al. 2006 Chen et al.). Since all my sources are greater then 2 mJy, the confusion noise should not be a significant issue, yet there is still a chance that my S/N could be slightly lower then reported in Table 3.2.

Table 3.2. Catalogue of sources from the SCUBA-2 850 μm map that have an S/N greater than 4.

ID	RA	DEC.	r_c (Mpc)	S/N_{850}	S/N_{450}
850_1	222.30882	8.93770	0.0	10.6	7.7
850_2	222.30423	8.97015	0.958	9.8	4.0
850_3	222.22436	8.89832	2.864	8.8	6.0
850_4	222.23642	8.92864	2.229	8.1	3.5
850_5	222.35272	8.92960	1.392	8.0	6.6
850_6	222.28385	8.95749	0.938	7.8	3.4
850_7	222.28147	8.89870	1.489	7.4	10.8
850_8	222.30102	9.01891	2.456	6.6	3.5
850_9	222.32561	8.87515	2.033	6.5	3.1
850_10	222.33980	8.87835	2.100	5.7	5.6
850_11	222.26360	8.90100	1.803	5.3	<2
850_12	222.39497	8.95028	2.679	5.0	<2
850_13	222.24476	8.95221	1.990	4.9	2.5
850_14	222.37475	8.96610	2.198	4.9	<2
850_15	222.38069	8.96798	2.389	4.8	6.8
850_16	222.28853	9.01256	2.331	4.8	4.4
850_17	222.21441	8.95775	2.937	4.8	2.6
850_18	222.35692	8.86788	2.646	4.8	3.6
850_19	222.31144	8.88167	1.766	4.7	3.0
850_20	222.37582	8.99054	2.602	4.5	2.9
850_21	222.35558	8.98888	2.104	4.4	5.0
850_22	222.27984	8.98906	1.762	4.3	<2
850_23	222.34994	8.93833	1.276	4.3	2.8
850_24	222.37243	8.87388	2.806	4.3	2.9
850_25	222.32408	8.94833	0.558	4.3	5.1
850_26	222.33233	8.94313	0.746	4.2	2.2
850_27	222.29483	8.88833	1.613	4.2	3.3
850_28	222.29146	8.94833	0.589	4.1	2.8
850_29	222.36570	8.98721	2.295	4.1	<2
850_30	222.32970	8.99055	1.707	4.1	<2
850_31	222.29371	8.96277	0.851	4.0	6.0
850_32	222.31845	8.90166	1.191	4.0	2.6

3.3.1 SOURCE CONFUSION

Due to the large beam size of my SCUBA-2 data, assigning optical and NIR counterparts is difficult as several galaxies could be residing in one beam. An example of this can be seen with the SCUBA-2 images in Figure 3.1. In the 850 μm map (beam size $\sim$15 arcsec) the central region is seen as one source, but the 450 μm (beam size $\sim$8 arcsec) shows this one source resolved into 3 separate sources. The severity of this issue is fully realised when I compare the SCUBA-2 data to the ALMA 870 μm data, with a resolution of $\sim$1 arcsec. Figure 3.3 shows that the 3 sources in the 450 μm data actually is 6 individual sources, and this is only seen due to the high resolution of ALMA. It should be noted that C18 actually identify 11 galaxies within the central 200 kpc based on the positions of CO(4-3) detections.

Due to the large beam sizes of both SCUBA-2 and *Herschel* there is a high probability that several sources may be blended into one individual source. This makes associating the FIR/sub-mm sources to optical and NIR sources complicated, as it is not known which optical and NIR sources are associated with the FIR/sub-mm ones.

3.3.2 DE-BLENDING SUB-MM IMAGES

To de-blend my images and get accurate flux measurements I used the Bayesian inference tool XID+[§] (Hurley et al. 2017). XID+ uses the positional data from a tracer of dusty star formation and explores the full posterior function to extract fluxes from confused maps. To assure the most accurate results from XID+, high-resolution positional data are required from a wavelength that traces dust-obscured star formation. For the central region I use the ALMA map and the 11 sources detected at 870 μm by C18. I also included the lower right source (circled green in Figure 3.3) even though this is a known low-redshift object. This is because I need it for the de-blending process, but it is excluded from the rest of the analysis.

For the rest of the region, I had to use a different tracer. Good examples are either 24 μm (e.g. Marsden et al. 2009; Pascale et al. 2009; Elbaz et al. 2010; Béthermin et al. 2012) or radio (e.g. Ivison et al. 2010; Magnelli et al. 2010; Basu et al. 2015; Rujopakarn et al. 2016; Delhaize et al. 2017). Even though a MIPS 24 μm map was available, the beam size is still large ($\sim$6 arcsec) and galaxies will still be blended. Instead I used the 10 cm (3 GHz) JVLA map as the tracer, as it has resolution comparable to that of the ALMA map.

[§]https://github.com/H-E-L-P/XID_plus

I identified 319 significant sources in the radio map (within the same area of the SCUBA-2 maps), and combine these with the 12 ALMA sources. These sources were then passed through XID+ to obtain fluxes for both the PACS and SPIRE maps. A specially modified version of XID+ was used to work with the SCUBA-2 maps, so I also have de-blended fluxes for both 450 μm and 850 μm.

3.3.3 Association With Optical/NIR Maps

I then went about associating each of the SCUBA-2 sources with at least one radio source (and therefore can associate with optical and NIR sources). To determine the most likely radio source I use the standard Poissonian probability of positional match similar to the method outlined in Downes et al. (1986). This value P gives us the probability of a source *not* being associated with the SCUBA-2 source and is given by

$$P = 1 - \exp\left(-\pi\, n\, \theta^2\right), \tag{3.1}$$

where n is the number density of sources in the radio map, and θ is the separation between the SCUBA-2 source and the radio source. I found all radio sources within 15 arcsec of the SCUBA-2 source, and calculated the P value for all of them. For galaxies that had similar P values I picked the source that was reddest in the IRAC bands, as it has been shown that sub-mm galaxies tend to be redder at these wavelengths (e.g. Ashby et al. 2006; Yun et al. 2008; Hainline et al. 2009). I did not worry about the central source (source 850_1) as I use the ALMA sources from C18, which have been shown to have association with optical and NIR sources.

Using the prescriptions laid out in Ivison et al. (2002), Chapin et al. (2009), and Chen et al. (2016), I considered a reliable match to have a $P \leq 0.05$ and a tentative match to have $0.05 \leq P \leq 0.1$. Anything with a $P > 0.1$ is considered an untrustworthy match and removed. I found that all but 2 sources had either reliable or tentative matches, with 850_12 and 850_19 having sources too far to be considered significant. Even though 850_18 and 850_28 had low P values, in the optical and NIR images they were obscured by nearby stars and hence removed from the sample. Finally 850_30 was removed because there was no radio source within 15 arcsec. Applying these cuts I ended up with 37 sources that I can calculate redshifts for, and determine if they are likely to be within the cluster or not.

3.4 REDSHIFT DETERMINATION

To assign cluster membership I estimated redshifts for my remaining 37 galaxies, and those that had a redshift consistent with the cluster were considered members. However due to a lack of spectral data beyond the core region, I have to rely on photometric methods to determine the redshift for my sources. I performed aperture photometry on the optical and NIR maps (based on the radio positions), and accounted for difference in resolutions by applying aperture corrections. The maps were also calibrated using stars of known brightness. This resulted in a 13 band catalogue spanning from U band ($\sim 0.3\,\mu$m) to $8\,\mu$m. However due to differing map sizes, only 6 bands (B, z, I, 3.6, 4.5 and $5.8\,\mu$m) had the same coverage as the SCUBA-2 maps, meaning my catalogue is incomplete (especially at NIR wavelengths, Figure 3.2).

3.4.1 PHOTOMETRIC REDSHIFTS USING OPTICAL AND NIR DATA

To calculate the photometric redshifts I first used the template fitting code EAZY[¶] using the standard set of templates (Brammer et al. 2008, 2011, Whitaker et al. 2011). An example of the fit from EAZY in Figure 3.4, while Figure 3.5 shows the distribution of redshifts calculated with EAZY.

The main issue when using EAZY is my incomplete catalogue. While EAZY gives accurate results in areas with complete data, such as in the cluster centre (with $\sigma\, z$ being on average ~ 0.2), in regions where there are no NIR data and just the Subaru and *Spitzer* data, $\sigma\, z$ on average is ~ 1 removing any precision needed in identifying cluster members. Using the optical and NIR data on its own is therefore not the most ideal situation, so I also looked at methods that included FIR/sub-mm data.

3.4.2 PHOTOMETRIC REDSHIFTS INCLUDING SUB-MM DATA

Using FIR/sub-mm data to estimate photometric redshifts has been studied several times (e.g. Pearson et al. 2013; Ivison et al. 2016; Bakx et al. 2018) and is ideal for situations where there is little or no optical and NIR counterparts to the sub-mm sources. However, these results can have significant uncertainties (± 0.5 in some cases), and on their own would not have the accuracy to place them within the cluster. This is especially true with XID+, as areas where several sources exist (such as the centre) the errors on the fluxes are significant (up to 50% in some cases).

[¶]https://github.com/gbrammer/eazy-photoz/

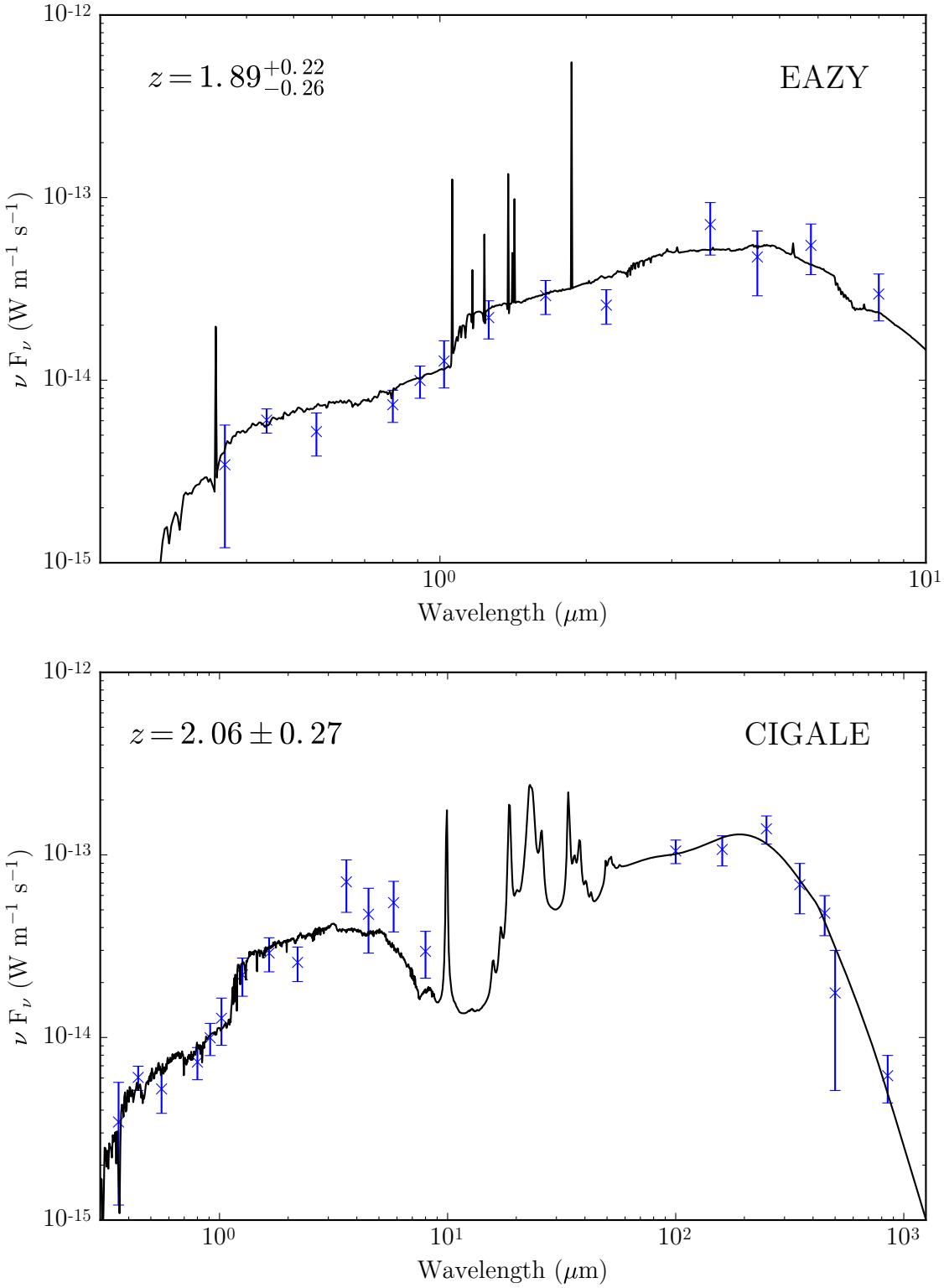

Figure 3.4. Both the EAZY SED (top) and CIGALE SED (bottom) for source 850_25

To calculate photometric redshifts using both optical, NIR, FIR and sub-mm data I use The Code Investigating GALaxy Emission (CIGALE[‖], Boquien et al. 2019). CIGALE is a dust energy balancing code, which balances any energy lost via dust attenuation to that of the emission caused by the dust. This approach is more advantageous as even with a small/incomplete optical data set, reasonably accurate results can be estimated as long as the FIR/sub-mm data are complete. The main advantage of CIGALE over similar codes is the ability to leave redshift as a free parameter, and compute photometric redshifts from the full wavelength range.

Another advantage of CIGALE is the flexibility in models that can be selected. With CIGALE the user can determine the models and parameters used (e.g. what dust emission model is used, what star formation history, etc) which allows for greater variability. I decided to use the same parameters used in the Herschel Extragalactic Legacy Project (HELP, Vaccari 2016). These parameters were selected as they cover a wide range of models and suitable for most galaxy types, and include a delayed star formation history (with additional burst), single stellar population models from Bruzual & Charlot (2003), dust attenuation from Charlot & Fall (2000), and a Draine & Li (2007) dust emission model. For more information see Małek et al. (2018).

CIGALE was run for my 37 galaxies using the HELP settings, except for redshift which was kept as a free parameter. With the added data I found that the uncertainties were smaller, especially for those galaxies that had significant uncertainties with EAZY. Again an example of a fit generated from CIGALE can be seen in Figure 3.4 and distribution of redshifts can be seen in Figure 3.5. Comparisons between all three redshifts measures can be seen in Figure 3.6. All the SEDs for all potential members from both EAZY and CIGALE can be found in Figure A.1.

3.4.3 Cluster Membership

To determine the cluster membership I compared the photometric values to the values of those sources with spectral redshifts (Figure 3.6). The only sources that had spectral redshifts are nine of the central ALMA sources discussed in C18. To determine a range of redshifts that could indicate membership, I compared the scatter between the photometric and spectroscopic redshifts. I found that for both CIGALE and EAZY the scatter was ~ 0.2. Therefore it was decided that all galaxies within 2σ of this scatter was considered a possible cluster member (i.e. any galaxy with a redshift between 1.6 and 2.4 is considered to be potentially in the cluster).

[‖] https://cigale.lam.fr/

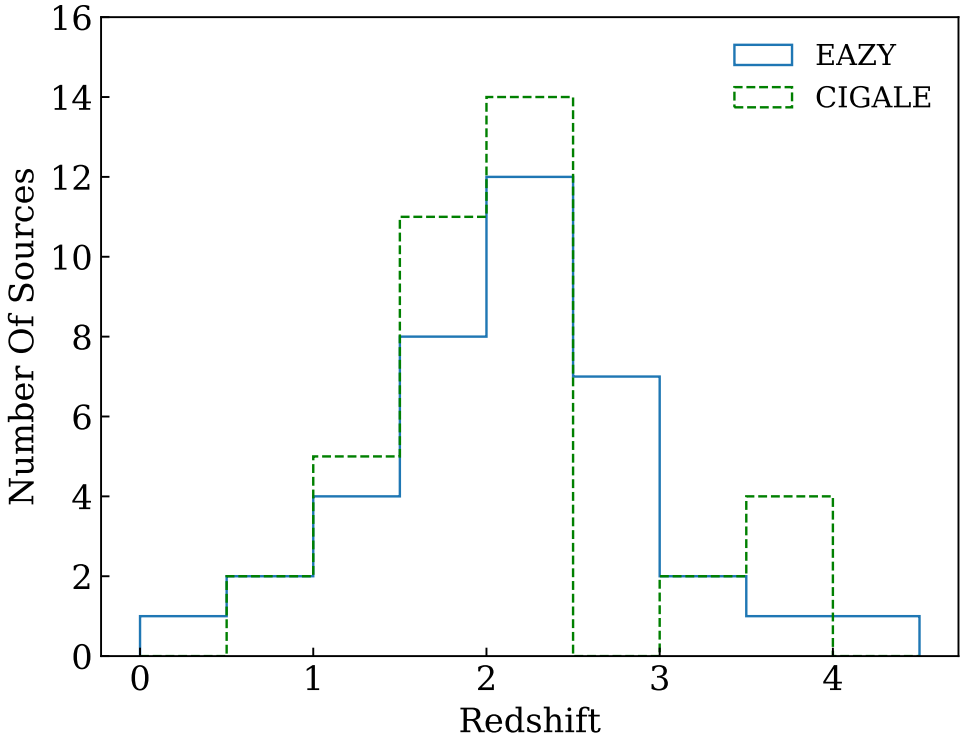

Figure 3.5. The photometric redshift distributions for both EAZY and CIGALE.

I use a combination of both the EAZY and CIGALE redshifts to help determine cluster memberships. Based on these redshifts I decided on 3 categories of cluster membership, with the first having the highest probability of being in the cluster. These galaxies either have a spectroscopic redshift or meet the redshift cut in both the EAZY *and* CIGALE redshifts. The second category are galaxies that have a much less chance of actually being a cluster member. These are galaxies that have a redshift matching the cut in either EAZY *or* CIGALE. The final category is galaxies which are very likely to *not* be in the cluster, and do not have a redshift in EAZY or CIGALE. These galaxies are excluded from the rest of the analysis.

Applying this criteria I found that 16 galaxies have a high probability of being in the cluster, with nine of these having spectra and seven having redshifts confirmed by both EAZY *and* CIGALE. Eight galaxies have a tentative membership, with two only being confirmed by EAZY, and six only being confirmed by CIGALE. Overall I am left with 24 galaxies that could be cluster members with their fluxes being presented in Table 3.3, and the locations of them can be seen in Figure 3.7. A table of all non-cluster members can be found in Table A.1.

Note that the number of galaxies that I exclude (14 galaxies) matches up well with the number of galaxies that I would expect to find in the field (Section

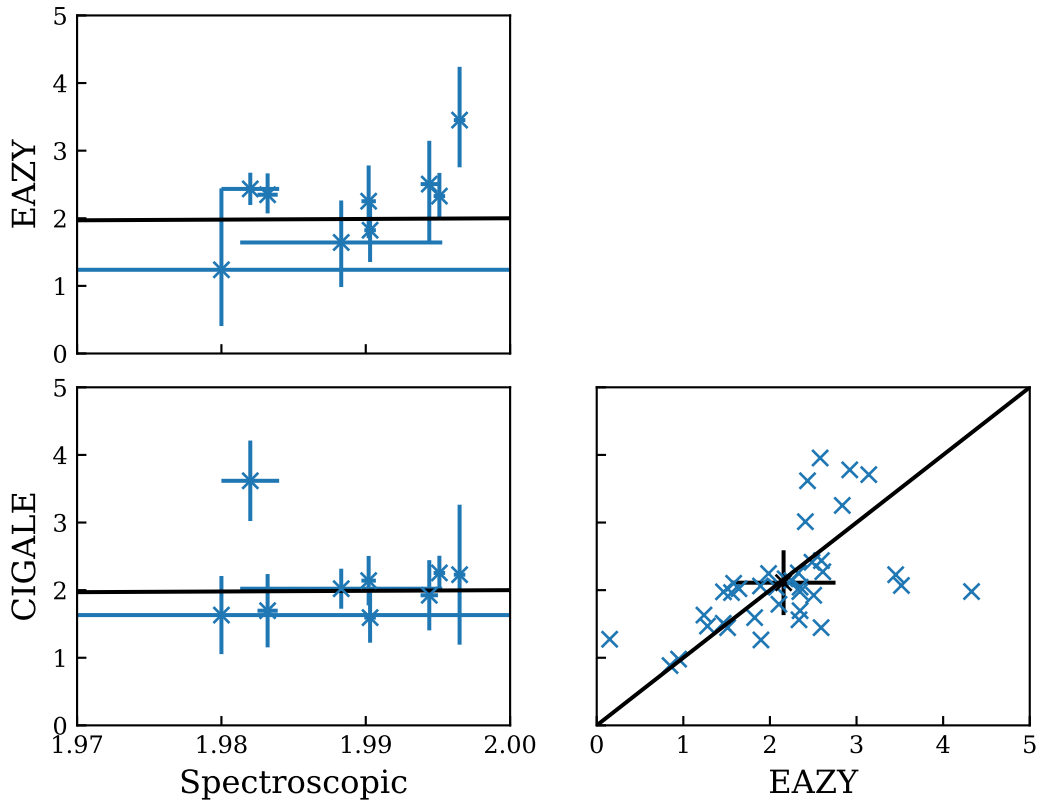

Figure 3.6. Comparing all three redshift determination methods. The black point shows the median value for both CIGALE, EAZY and errors.

3.3, 10±3). This gives a greater confidence that the remaining galaxies are actually associated with the cluster.

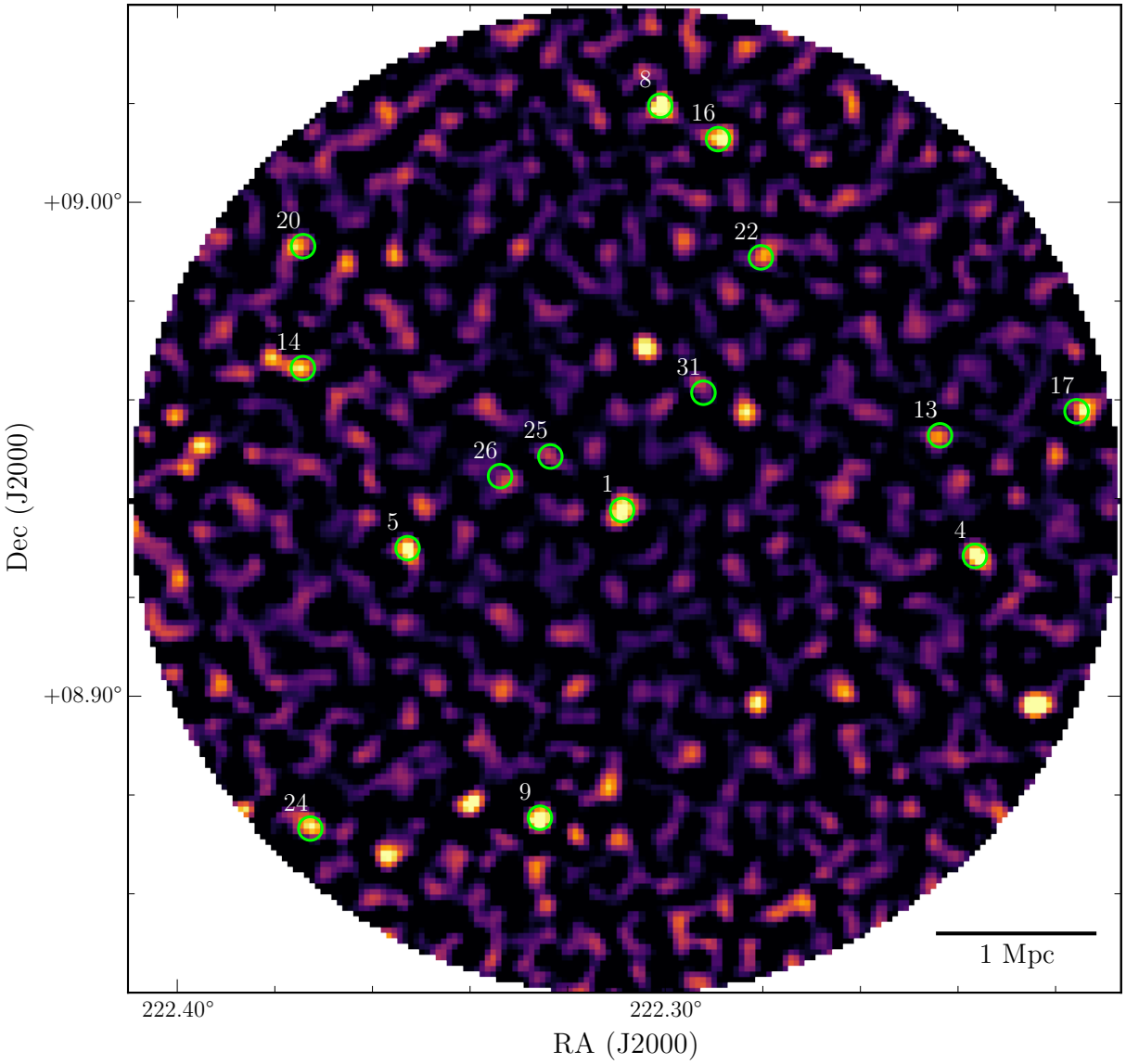

Figure 3.7. Location of the final galaxies identified as possibly being within the cluster. It should be noted 850_1 actually consists of 10 members.

Table 3.3. FIR/sub-mm fluxes of my cluster galaxies.

ID	RA	DEC.	r_c (Mpc)	f_{100} (mJy)	f_{160} (mJy)	f_{250} (mJy)	f_{350} (mJy)	f_{450} (mJy)	f_{500} (mJy)	f_{850} (mJy)	Source
850_1_A	222.307	8.9395	0.04	0.26 ± 0.26	0.74 ± 0.73	10.26 ± 5.26	6.36 ± 5.99	1.12 ± 1.19	3.63 ± 3.76	0.81 ± 0.6	Spec
850_1_B	222.309	8.9403	0.04	0.31 ± 0.32	0.77 ± 0.83	1.66 ± 1.76	2.32 ± 2.51	1.06 ± 1.17	1.88 ± 2.15	0.47 ± 0.45	Spec
850_1_C	222.309	8.942	0.09	1.35 ± 0.59	2.41 ± 1.46	2 ± 1.84	1.22 ± 1.38	2.19 ± 1.72	1.24 ± 1.4	0.2 ± 0.22	Spec
850_1_D	222.31	8.9378	0.06	0.43 ± 0.39	0.7 ± 0.83	6.57 ± 5.26	6.74 ± 5.88	0.98 ± 1.09	4.03 ± 4.29	0.31 ± 0.37	Spec
850_1_E	222.31	8.9401	0.07	0.44 ± 0.37	0.72 ± 0.77	1.53 ± 1.71	2.01 ± 2.12	0.58 ± 0.64	1.61 ± 1.95	0.26 ± 0.29	Spec
850_1_F	222.309	8.9407	0.05	0.69 ± 0.53	1.49 ± 1.32	1.4 ± 1.64	1.85 ± 2.08	1.53 ± 1.47	1.61 ± 1.92	0.37 ± 0.36	Spec
850_1_G	222.309	8.9395	0.03	0.24 ± 0.26	0.42 ± 0.47	1.61 ± 1.76	3.48 ± 3.77	0.58 ± 0.69	2.51 ± 2.88	0.38 ± 0.39	Spec
850_1_H	222.31	8.9396	0.06	0.41 ± 0.37	0.68 ± 0.68	1.56 ± 1.71	1.86 ± 2.21	0.53 ± 0.58	1.75 ± 1.95	0.25 ± 0.26	Spec
850_1_K	222.306	8.9431	0.14	0.48 ± 0.36	2.51 ± 1.08	2.3 ± 1.91	1.16 ± 1.28	0.99 ± 0.94	1.06 ± 1.16	0.09 ± 0.1	Spec
850_13	222.244	8.9528	2.03	0.38 ± 0.33	1.85 ± 1.8	17.58 ± 4.18	12.48 ± 6.43	2.44 ± 1.87	6.24 ± 4.31	1.33 ± 0.96	Both
850_14	222.374	8.9664	2.19	3.79 ± 0.55	11.74 ± 1.26	21.31 ± 2.27	19.66 ± 2.99	2.04 ± 1.76	12.61 ± 4.17	4.31 ± 0.86	Both
850_17	222.216	8.9577	2.9	3.33 ± 0.55	4.57 ± 1.08	8.44 ± 2.4	3.36 ± 2.7	6.65 ± 3.21	1.42 ± 1.6	3.55 ± 0.92	Both
850_20	222.374	8.9911	2.57	5.73 ± 0.6	19.03 ± 1.43	36.86 ± 2.86	32.48 ± 3.75	5.45 ± 2.68	21.22 ± 4.56	2.57 ± 0.88	Both
850_22	222.28	8.9889	1.75	1.93 ± 0.74	2.39 ± 1.42	4.94 ± 3.34	5.89 ± 4.27	2.12 ± 1.8	4.23 ± 3.47	3.09 ± 1.29	Both
850_25	222.324	8.9485	0.55	3.5 ± 0.52	5.71 ± 1.07	11.58 ± 2.03	8.01 ± 2.46	7.19 ± 1.78	2.93 ± 2.07	1.75 ± 0.51	Both
850_31	222.292	8.9615	0.84	3.25 ± 0.52	8.44 ± 1.12	22.21 ± 2.28	18.13 ± 2.72	9.07 ± 1.92	11.05 ± 3.46	1.38 ± 0.5	Both
850_16	222.289	9.0128	2.33	10.75 ± 0.95	22.18 ± 2.92	10.83 ± 11.3	17.04 ± 12.56	3.24 ± 2.88	8.7 ± 6.94	1.58 ± 1.45	Ez
850_26	222.334	8.9446	0.8	2.28 ± 0.57	4.73 ± 1.31	1.6 ± 1.61	3.3 ± 3.36	1.54 ± 1.35	2.46 ± 2.47	0.93 ± 0.64	Ez
850_4	222.237	8.9284	2.23	0.39 ± 0.35	1.73 ± 1.03	6.55 ± 2.52	10.6 ± 3.89	7.88 ± 2.88	9.45 ± 4.46	5.48 ± 0.89	Cg
850_5	222.353	8.93	1.39	0.22 ± 0.23	3.17 ± 0.95	9.62 ± 2.12	14.42 ± 2.5	11.36 ± 2.35	15.63 ± 2.5	6.26 ± 0.8	Cg
850_8	222.301	9.0196	2.48	2.05 ± 0.54	2.8 ± 1.09	9.2 ± 2.13	12.06 ± 2.87	9.18 ± 2.98	10.01 ± 4.26	7.03 ± 1.05	Cg
850_9	222.326	8.8754	2.03	1.86 ± 0.53	14.04 ± 1.25	26.55 ± 2.34	34.25 ± 3.04	6.75 ± 2.85	23.96 ± 2.69	6.4 ± 0.99	Cg
850_24	222.373	8.8732	2.83	1.58 ± 0.56	7.94 ± 1.23	24.82 ± 2.36	31.12 ± 2.9	8.17 ± 3.5	25.21 ± 2.75	3.73 ± 1	Cg
850_1_J	222.306	8.9378	0.07	3.48 ± 0.56	10.98 ± 1.27	17.98 ± 4.51	19.58 ± 5.81	6.58 ± 1.91	12.57 ± 6.06	2.18 ± 0.64	Cg

3.4.4 Bright Cluster Core Sources

In C18 no spectral redshifts were detected for sources 850_1_I and 850_1_J (A5 and A4 in C18). When I calculated photometric redshifts for them I found that 850_1_I was not placed in the cluster for either method, both indicating it had a redshift of ~ 2.8. When I look at the other source, 850_1_J I see that indeed EAZY placed it well outside of the cluster (z$\sim$4.3) whereas CIGALE placed it within the cluster (Figure 3.8).

Combined 850_1_I and 850_1_J contribute 70% of the 870 μm flux for the cluster core, meaning that the chance of these galaxies being interlopers is extremely small. Based on 870 μm source counts from Karim et al. (2013) the chance of not being associated with the cluster is less than 4×10^{-5} (C18). Lensing is an unlikely cause to the high fluxes simply because the mass of the cluster halo is not enough to boost the fluxes to the observed levels. A full discussion on this is presented in both C18 and S18, who exclude both sources from there analysis. For the rest of the analysis I include 850_1_J as a potential member based on its CIGALE redshift. When appropriate I also consider the situation that this galaxy is not in the cluster. It should be noted that the errors on 850_1_I are substantial for both EAZY and CIGALE, with both having $\Delta z > 1$. While there is a chance it could be in the cluster the large error means it cannot be said for sure, and therefore the source is excluded from the rest of the analysis.

3.5 Star Forming Properties Of CLJ1449

With the list of cluster members I used CIGALE to fit SEDs for the analysis. Again the same settings as before were used, this time however the redshift was fixed at 2 for all galaxies. I used CIGALE rather than conventional methods of fitting a modified blackbody, because as mentioned the uncertainties on the FIR/sub-mm data are large, and better constraints were obtained using CIGALE. I find SFRs between 20-1600 $M_\odot$ yr^{-1} with a median value of 168 $M_\odot$ yr^{-1}. The results from CIGALE can be found in Table 3.4, and all optical and NIR data can be found in Tables A.2 and A.3.

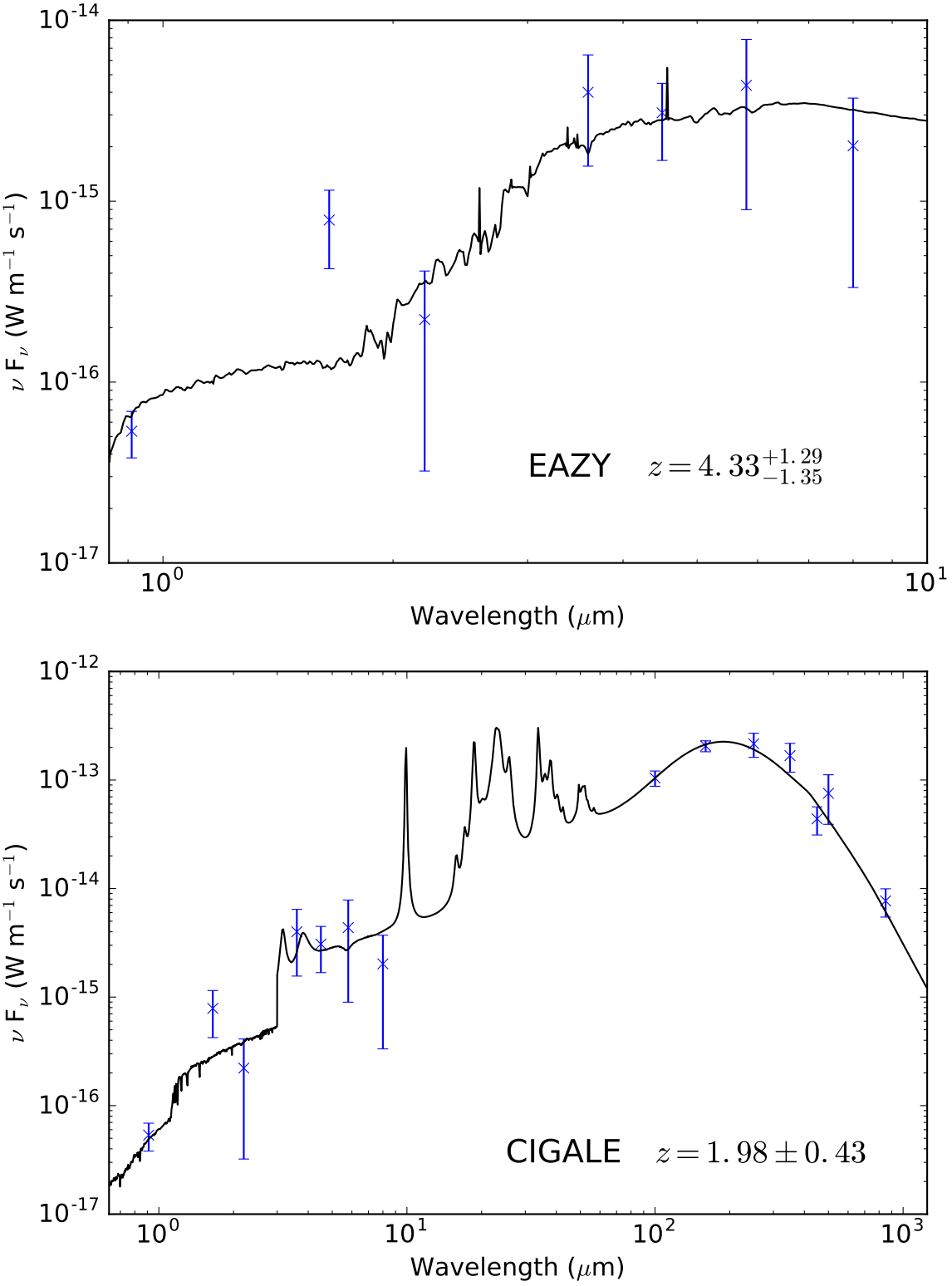

Figure 3.8. Comparing the SEDs from both EAZY and CIGALE for source 850_1_J. Notice that by including the sub-mm data the source is placed within the cluster

Table 3.4. FIR/sub-mm properties of my cluster galaxies.

ID	z_{Spec}	z_{EZ}	z_{CG}	L_{IR} ($10^{12}\,L_\odot$)	SFR ($M_\odot yr^{-1}$)	M_* ($10^{11}\,M_\odot$)	P
850_1_A	1.9951 ± 0.0004	$2.33^{+0.34}_{-0.31}$	2.25 ± 0.25	0.21 ± 0.15	32 ± 17	0.16 ± 0.08	-
850_1_B	1.9902 ± 0.0005	$2.25^{+0.53}_{-0.55}$	2.14 ± 0.37	0.18 ± 0.22	22 ± 28	0.17 ± 0.21	-
850_1_C	1.9944 ± 0.0006	$2.51^{+0.64}_{-0.87}$	1.92 ± 0.52	0.62 ± 0.38	74 ± 59	0.36 ± 0.17	-
850_1_D	1.9832 ± 0.0007	$2.35^{+0.32}_{-0.28}$	1.70 ± 0.54	0.38 ± 0.10	36 ± 13	0.43 ± 0.13	-
850_1_E	1.9965 ± 0.0004	$3.45^{+0.79}_{-0.70}$	2.23 ± 1.03	0.52 ± 0.48	66 ± 69	0.26 ± 0.37	-
850_1_F	1.9883 ± 0.0070	$1.64^{+0.62}_{-0.66}$	2.02 ± 0.30	0.37 ± 0.30	45 ± 49	0.41 ± 0.22	-
850_1_G	1.9903 ±0.0004	$1.82^{+0.39}_{-0.47}$	1.59 ± 0.37	0.41 ± 0.37	59 ± 67	0.30 ± 0.29	-
850_1_H	1.982 ± 0.002	$2.43^{+0.24}_{-0.24}$	3.62 ± 0.60	0.56 ± 0.67	73 ± 100	0.26 ± 0.44	-
850_1_K	1.98 ± 0.02	$1.24^{+1.20}_{-0.83}$	1.63 ± 0.58	0.30 ± 0.11	37 ± 16	0.30 ± 0.12	-
850_13	-	$1.98^{+0.44}_{-0.47}$	2.25 ± 0.24	0.94 ± 0.23	116 ± 22	2.08 ± 0.53	0.04
850_14	-	$2.10^{+0.42}_{-0.47}$	1.79 ± 0.24	3.03 ± 0.36	331 ± 88	4.09 ± 0.99	0.01
850_17	-	$2.34^{+0.87}_{-0.93}$	1.98 ± 0.40	3.65 ± 1.16	447 ± 156	3.86 ± 1.18	0.04
850_20	-	$2.07^{+0.52}_{-0.51}$	2.04 ± 0.21	4.98 ± 0.38	439 ± 98	6.84 ± 1.48	0.08
850_22	-	$2.35^{+0.43}_{-0.46}$	2.04 ± 0.32	3.30 ± 1.85	403 ± 214	2.28 ± 1.12	0.01
850_25	-	$1.89^{+0.22}_{-0.26}$	2.06 ± 0.27	2.46 ± 0.44	254 ± 71	2.99 ± 0.83	0.01
850_31	-	$2.18^{+0.77}_{-0.68}$	2.17 ± 0.32	2.73 ± 0.41	377 ± 117	1.33 ± 0.56	0.08
850_16	-	$2.34^{+0.58}_{-0.57}$	1.56 ± 0.21	11.64 ± 2.71	1618 ± 738	7.25 ± 6.19	0.01
850_26	-	$1.90^{+1.14}_{-0.86}$	1.26 ± 0.36	2.35 ± 0.98	313 ± 160	0.74 ± 0.52	0.09
850_4	-	$1.56^{+0.92}_{-0.97}$	1.96 ± 0.34	0.93 ± 0.18	105 ± 30	0.58 ± 0.39	0.002
850_5	-	$1.46^{+0.87}_{-0.78}$	1.98 ± 0.70	1.26 ± 0.14	142 ± 40	0.61 ± 0.32	0.004
850_8	-	$1.58^{+0.49}_{-0.41}$	2.10 ± 0.97	1.71 ± 0.28	195 ± 63	0.74 ± 0.49	0.01
850_9	-	$3.52^{+0.35}_{-0.36}$	2.07 ± 0.39	3.55 ± 0.27	357 ± 86	2.51 ± 1.22	0.002
850_24	-	$2.61^{+0.60}_{-0.56}$	2.27 ± 0.39	2.99 ± 0.34	360 ± 101	1.67 ± 0.64	0.01
850_1_J	-	$4.33^{+1.29}_{-1.35}$	1.98 ± 0.43	2.98 ± 0.28	381 ± 138	1.31 ± 1.33	-

3.5.1 RADIAL VARIATIONS IN THE STAR FORMATION RATE DENSITY

To understand the radial variation in the SFR of the cluster, I calculated the distance from the centre for each galaxy and binned them in 0.5 Mpc bins ranging from 0 to 3 Mpc. I summed up the SFRs in each radial bin, and normalise it by the volume of the bin. The resulting plot can be seen in Figure 3.9.

I confirm that the central 0.5 Mpc region is highly star forming with a total SFR of $800 \pm 200\,M_\odot\ yr^{-1}$. When converted into an SFRD I find a projected volume density of $(1.2 \pm 0.3) \times 10^4\,M_\odot yr^{-1} Mpc^{-3}$, which is almost five orders of magnitude greater than the expected value for field galaxies ($\sim 0.1\,M_\odot\ yr^{-1} Mpc^{-3}$, Madau & Dickinson 2014). With increasing radius a decrease in the SFRD of almost 2 orders of magnitude is seen, until it stabilizes at 1 Mpc, where it remains constant with the exception of a spike between 2 and 2.5 Mpc. A similar spike was seen in Santos et al. (2014) in a redshift 1.6 cluster, and was caused by an increase in the number of high-mass galaxies at this radius. This is again seen in CLJ1449 with the most massive galaxy in the sample (850_16, $M_* \sim 7.5 \times 10^{11}\,M_\odot$) being found in this radius bin.

For completeness I also considered the scenario where 850_1_J is *not* associated with the cluster (the black star in the 0-0.5 Mpc bin in Figure 3.9). I find that the SFR for the central 0.5 Mpc region decreases to $440 \pm 160\,M_\odot\ yr^{-1}$ a factor of ~ 2 lower than before. Again when converted to an SFRD this gives $(6.7 \pm 2.4) \times 10^3\,M_\odot yr^{-1} Mpc^{-3}$, which while lower than before is still much larger than the expected result from Madau & Dickinson (2014) for field galaxies.

In Figure 3.9 I also plot the number density of sources as a function of radius. Again an identical trend to what is observed with the SFR-density relation is seen. This would indicate that the observed reversal in the SF-density relation is caused by a dense population of SF galaxies, rather than a small population of extreme starbursts.

It is stressed that the high number counts in the central 1 Mpc region is down to the high-resolution ALMA data, whereas those counts at radii greater than 1 Mpc are based on radio sources. If the number counts were based entirely on the radio data then the number density in the central region reduces by half. While this is still significant, it could indicate that not all the galaxies in the cluster are being observed.

The biggest issue with the galaxies beyond 1 Mpc is the redshift and their uncertainties. When doing the CIGALE fitting I fix the redshift to that of the cluster, so if there is an interloper this could cause an increase in the SFR. To test for this I normalise the SFR with the cosmological volume in the range $1.6 < z < 2.4$ for radii greater than 1 Mpc (as opposed to the cluster volume). When accounting for

just the cosmological volume (Figure 3.9) the SF-density does indeed fall to expected field values at radii greater than 1 Mpc. This indicates that there is a high chance of significant contamination in the sample, which causes an artificial increase in the SF.

Note that the two volumes I have normalised by are the two extreme cases. Using the cluster volume assumes all sources above 1 Mpc are in the cluster, and the cosmological volume assumes that none are. While is is acknowledged that either one of these extremes could be occurring (no matter how unlikely), the fact that even at a radius greater than 1 Mpc it is still a very over-dense region ($\sim 2\times$ over-dense) the chances are the cluster exists in the middle of these scenarios. This means that there is still elevation in the SF-density relation above the expected value, but it will not be as extreme as seen in Figure 3.9.

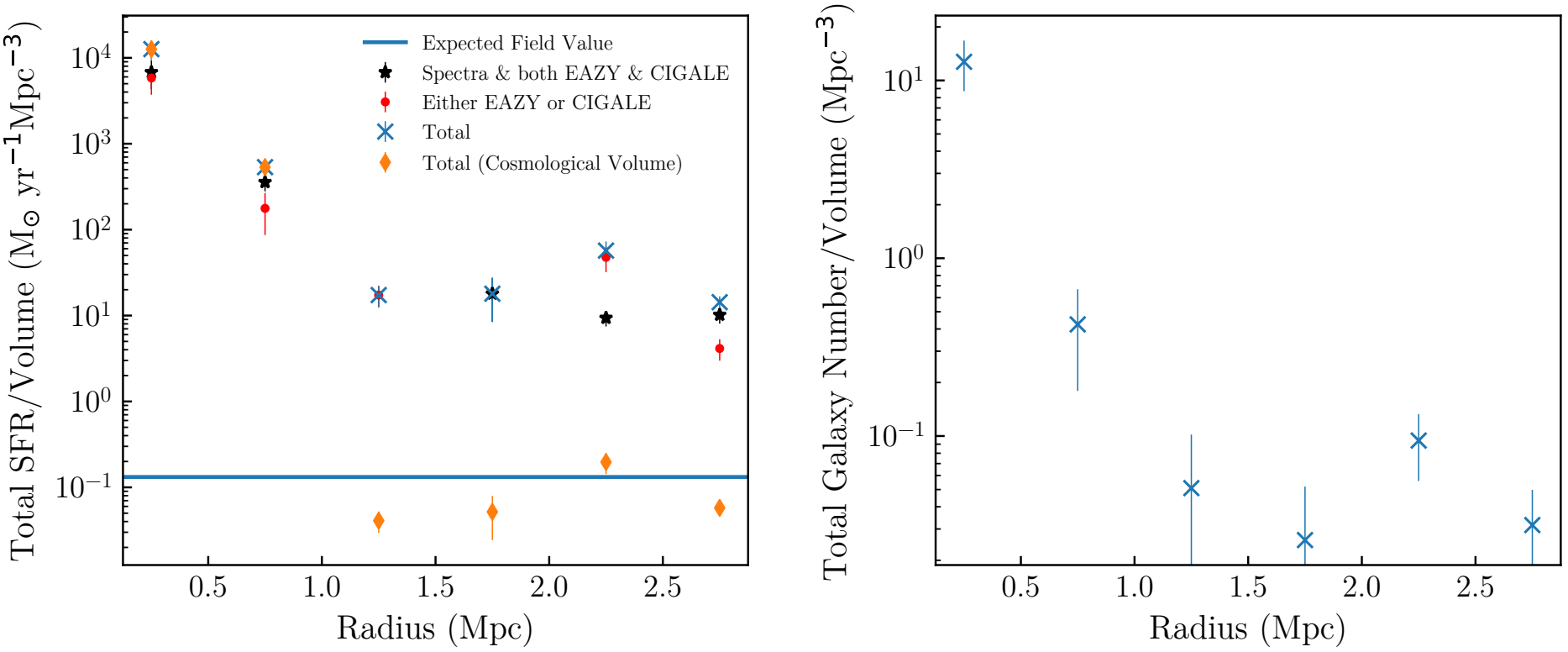

Figure 3.9. Left: The SF-density relation found in CLJ1449. I have divided the cluster into 0.5 Mpc bins, normalised by the volume of the bin. Each bin has been separated by the redshift criteria mentioned in Section 3.4. The blue line is the expected field value based on Madau & Dickinson (2014). I also plot the SF-density relation by assuming the observed cosmological volume in the range $1.6 < z < 2.4$. Right: The number density of galaxies versus the cluster radius. For sources less than 1 Mpc the counts are from ALMA, while at larger radii I use radio counts

3.5.2 Star formation rate versus stellar mass

I then investigated the relation between the stellar masses (M_*) of the cluster galaxies and their SFRs. Using stellar masses from CIGALE I compare them to the SFRs, with the resulting relation shown in Figure 3.10. I compare these galaxies to the expected galaxy Main Sequence (MS) relation for redshift 2 galaxies from Sargent et al. (2014). Even though all these galaxies are highly star forming, and are extremely luminous (with all of them being LIRGs or ULIRGs), the majority of galaxies within the cluster do not deviate from the expected main sequence. This behaviour was observed by C18 when observing the central galaxies. However they noted that these galaxies had star-burst like behaviour, based on the gas excitation.

Figure 3.10 would seem to suggest that the environment does not have a significant effect on the SF properties of these galaxies. Darvish et al. (2016) found that in the COSMOS field, galaxies at low redshift ($z < 1$) seemed to be heavily influenced by the environment they reside in, and in dense environments the SFR decreased significantly. However at $z > 1$ the SFR did not significantly change with environment, suggesting that at high redshift the SFR-M_* relation is independent of environment. This behaviour was also seen by Koyama et al. (2013) who again suggest the SFR-M_* relation is not dependent on the galaxy environment at high redshift.

The low level of starbursts can be linked to the density of sources seen in Figure 3.9. If there was a low number density of sources in the cluster core, you would expect to see far more galaxies exhibiting star burst behaviour to account for the large SF-density. The fact that there is a high number density of sources in the cluster core and limited starbursts reinforce the claim that the SFR-density relation is caused by a high density of SF galaxies sources rather than a small population of star bursting galaxies.

A small sample of the galaxies do appear to lie above the MS, being $\sim$2-3 $\times$ above the expected relation. This enhanced SF activity could indeed be down to merging events, as both Hung et al. (2013) and Cibinel et al. (2019) found that galaxies undergoing a merging event lie above the galaxy MS. This would also validate claims made by C18 that most of the activity in this cluster is driven by mergers. It should be noted that these galaxies that are above the main sequence are those galaxies that had their redshifts estimated by either EAZY *or* CIGALE. As mentioned earlier this increase in SF could be an artifact of fixing the redshift when running CIGALE.

Mergers could also explain why there is elevated SF (compared to the field) well beyond the viral radius of the cluster. Within the cluster core itself, galaxies

are moving too fast for a merger to actually occur. However in the in-fall region the speed of galaxies is much lower allowing mergers to occur, and then be accreted onto the core (Bekki 1998, Moss 2006). While measuring velocity dispersion is still very difficult at high redshift, Delahaye et al. 2017 showed evidence that the fraction of mergers in a redshift 1.6 cluster core is no higher than field values, indicating that the mergers are still happening in the outskirt rather than in the core itself. So in the outskirts of the clusters, mergers can occur more frequently and cause an increase in star formation. While signs of merger activity cannot be detected with the current ground-based optical data, it is hoped with new high resolution data this can be investigated further.

While it has been discussed that the environment and SF are independent at high redshift, it should be noted that in the left-hand panel of Figure 3.10 the galaxies with the smallest cluster radii have the lowest stellar masses. This could suggest that the cluster environment is beginning to have an impact on the cluster galaxies, and quenching is starting to occur within these galaxies. Similar conclusions were drawn by both C18 observing this cluster, and Santos et al. 2014 observing a redshift 1.6 cluster.

In Figure 3.10 I convert the SFR to a specific SFR (sSFR, SFR/M_*) and observe a large scatter from the proposed relation outlined in Sargent et al. (2014). Because the sSFR measures how the current SFR compares to the SFR of the galaxy averaged over its life, the fact that these galaxies have heightened sSFRs indicates that they are undergoing bursts of star formation.

A decrease in sSFR with increasing stellar mass has been reported at all redshifts (e.g. Ilbert et al. 2015; Lehnert et al. 2015) and is believed to show that the most massive galaxies have already formed all their stellar mass much earlier than their lighter counterparts. While these data suggest that there is a trend, it is not statistically significant enough to be considered, with a Spearman's rank ρ of only -0.3. This could indicate that the most massive galaxies are still in the process of forming within the cluster.

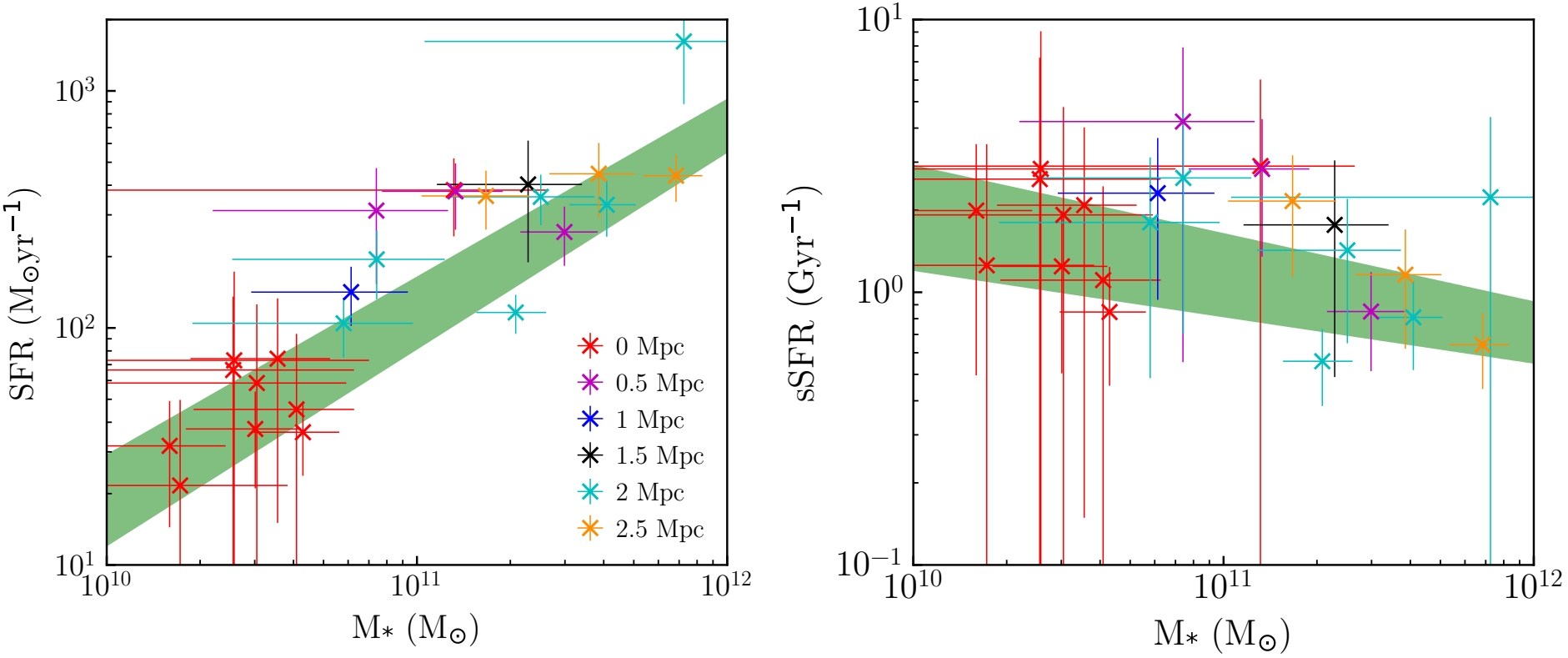

Figure 3.10. Left: The SFR-M_* relation with the shaded region showing the expected position for main-sequence galaxies at redshift 2 given by Sargent et al. (2014). I have divided the points up into there location within the cluster and colour coded them accordingly. Right: The sSFR-M_* relation with the expected value for redshift 2 main-sequence galaxies.

3.5.3 MASS NORMALISED STAR FORMATION RATE

As discussed there is strong indication for an increase in the SF activity in clusters with increasing redshift. It has been shown that CLJ1449 is still very actively star forming but is this in line with what would be expected at this redshift? To allow for direct comparisons to other studies I follow the same methodology outlined in Popesso et al. (2012). I first integrate out to a radius of 1 Mpc (as in studies such as Santos et al. 2014 and Ma et al. 2015), giving a total integrated SFR (ΣSFR) of $1800 \pm 300\,M_{\odot} yr^{-1}$. I then normalise ΣSFR by the cluster mass ($(0.5 \pm 0.1) \times 10^{14}\,M_{\odot}$) resulting in a normalised, $\Sigma SFR/M_{cl}$ of $3300 \pm 850\,M_{\odot}\ yr^{-1}/10^{14}\ M_{\odot}$.

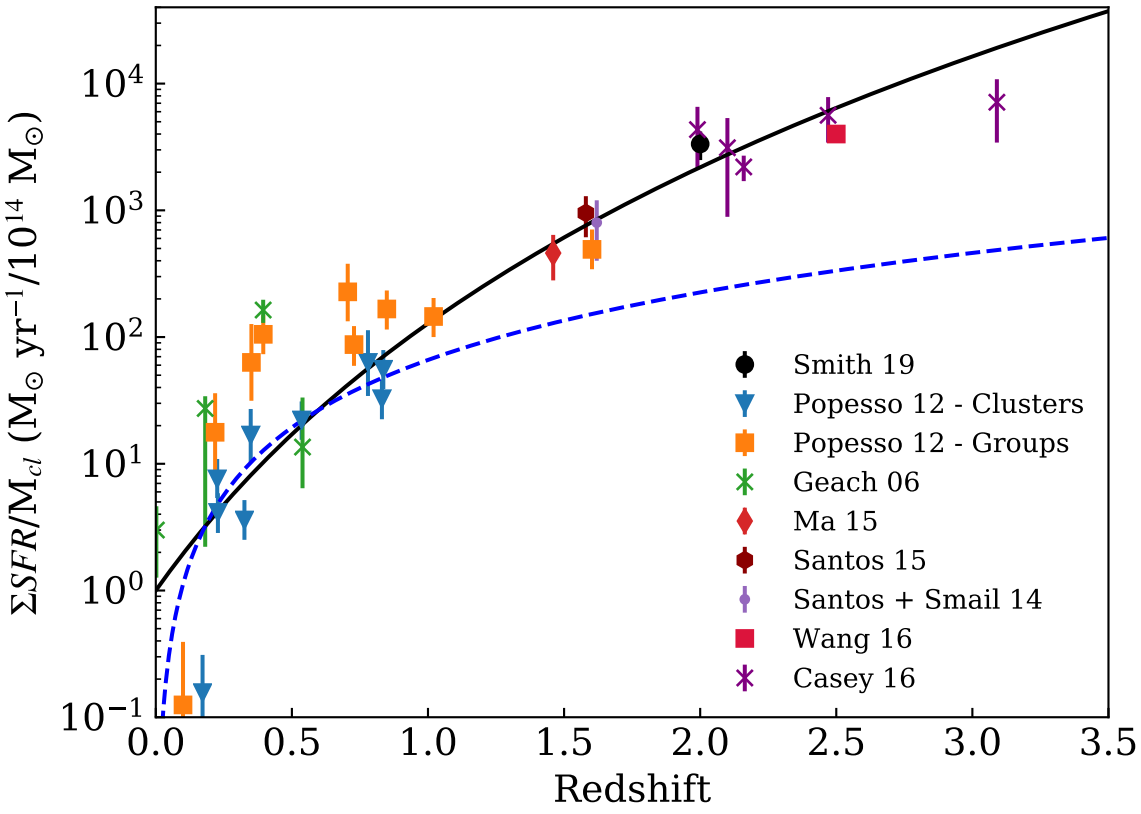

Figure 3.11. Comparison of the mass normalised ΣSFR for several clusters at different redshifts. The solid black line is the proposed relation offered by Cowie et al. (2004) and Geach et al. (2006) that follows the relation $(1 + z)^7$, and the blue dashed line follows the relation in Popesso et al. (2012) for clusters. It should be noted that the sample from Casey (2016) are proto-clusters and not fully virialized clusters.

In Figure 3.11 I compare my result to clusters at several different redshifts. It can be seen that my cluster lies above the expected empirical relation predicted by Popesso, however this cluster is at a much higher redshift than their sample. When

comparing the empirical $(1+z)^7$ line in Cowie et al. (2004) and Geach et al. (2006), to CLJ1449 you can see that there is only a $1.3\,\sigma$ offset, meaning that CLJ1449 could follow trends seen at both low and high redshift. When comparing to other high-redshift (proto-)clusters from both Wang et al. (2016) (CLJ1001) and Casey (2016), there is significant scatter. Other studies of proto-clusters such as those by Shimakawa et al. (2014) and Lacaille et al. (2018) have also showed significant scatter at $z > 2$. This scatter was observed by Geach et al. (2006) at low redshift and suggests that the cluster environments have differing, but strong influences on the star formation histories of the residing galaxies. This is very significant for the sample from Casey (2016) which are proto-clusters, and are still in the process of forming.

It should also be noted that both CLJ1449 and CLJ1001 are significantly less massive then other clusters used in previous studies, both at low and high-redshift. The fact that these clusters do not directly fit to the $(1 + z)^7$ relation, and there is some scatter that could indicate cluster mass could have some influence on the galaxies within them. This was also suggested by both Koyama et al. (2011) and Cochrane et al. (2018) who observed similar scatter in $z > 1$ clusters. However for the time being high redshift samples are still too small to determine if all clusters have enhanced SF activity, or do they behave like low-redshift galaxies and I have a biased sample.

3.6 Conclusions

I have presented new SCUBA-2 images of CLJ1449, a mature cluster at redshift two. I combine these data with pre-existing data including *Herschel*, ALMA and VLA to study the SF properties of this cluster, and build upon the work already presented in C18 and S18.

- I use SCUBA-2 and *Herschel* data to explore $\sim$0.03 deg^2 that contain the cluster CLJ1449. I identify 32 sources in the 850 μm maps that have a S/N greater than 4.

- To help estimate fluxes for confused members I use high-resolution ALMA and JVLA maps to identify positions of potential FIR/sub-mm galaxies. I then use the Bayesian inference tool XID+ to estimate fluxes for all these sources in the confused *Herschel* and SCUBA-2 maps.

- I match these sources up to the SCUBA-2 sources resulting in 37 potential cluster members. To confirm cluster membership I calculate redshifts using

both EAZY and CIGALE. I find 24 galaxies I am confident could be within the cluster.

- I use CIGALE estimates for both SFRs and stellar masses for all 24 galaxies. I find that the central 0.5 Mpc region is very highly star forming, forming $800 \pm 200\,\mathrm{M_\odot yr^{-1}}$, which corresponds to an SFRD of $(1.2 \pm 0.3) \times 10^4\,\mathrm{M_\odot yr^{-1} Mpc^{-3}}$. This is orders of magnitude greater than field values.

- When looking at the SFR-M_* relation I see galaxies lie on the expected main-sequence relation, however there is some evidence of star-bursting activity which could possibly be caused by merger events. When looking at the sSFR-M_* there is a large scatter in this relation which could indicate that the gas is undergoing complex processes.

- When comparing the mass normalised integrated SFR it is seen that CLJ1449 seems to follow previously identified scaling relations (with minimal scatter), but there is still a large scatter when considering other high-redshift systems. However due to the low number of high-redshift systems it is unknown if this is reflective of what is seen in low-redshift systems.

Chapter 4
Star Formation In JKCS041

"If you want to make an apple pie from scratch, you must first create the universe."

Carl Sagan

This chapter presents a study into the SFR-density relation in the redshift 1.8 cluster JKCS041. The work in this chapter has been submitted to MNRAS in a paper entitled "*Star formation in JKCS041: A high redshift cluster caught in the middle of transitioning?*". The JVLA map used in this study was reduced by Andreas Papageorgiou.

4.1 JKCS041

JKCS041 (RA=36.6833, DEC.=-4.6933) is one of the highest redshift mature clusters known. The cluster was first identified as an extended X-ray source in Chandra imaging, and was confirmed to be a cluster based on the abundance of red galaxies (Andreon et al. 2009). At the time JKCS041 was incorrectly assigned the redshifts of 1.9, or 2.2 (Andreon & Huertas-Company 2011), with eventual spectroscopic followup confirming the true redshift of the cluster to be 1.8 (Andreon et al. 2014; Newman et al. 2014). From the strength of the X-ray luminosity, and the X-ray luminosity-mass correlation, the mass of the cluster was found to be $(2.24 \pm 0.78) \times 10^{14}\,M_{\odot}$. This makes it one of the most massive clusters at this redshift, and a potential progenitor to a cluster similar to the Coma cluster.

Previous studies of JKCS041 have all shown that the cluster is dominated by 'red and dead' galaxies, and that a red sequence is already in place (Andreon et al.

2014; Newman et al. 2014; Prichard et al. 2017). Studies of the star formation in JKCS041 have also shown that the SFR-density relation is similar to that of present day clusters, however this result was determined with a miss-assigned cluster redshift of 2.2 (Raichoor & Andreon 2012).

4.2 DATA AND REDUCTIONS

Previous studies of the cluster all relied on optical data, which is known to be heavily influenced by dust. These studies were also focused on the very center of the cluster, so to get a more complete estimate of the star formation within the cluster, large scale FIR and sub-mm imaging is needed. I therefore use new SCUBA-2 data with archival *Herschel* data to get a detailed look at the star forming properties of JKCS041.

4.2.1 SCUBA-2

The SCUBA 2 observations were carried out over 3 nights between September - November 2015 as part of project M15BI038 (PI: W. Gear). A total integration time of 8 hours was performed using 3 arcmin daisy scans, with all the observations being carried out in good grade one weather ($\tau_{225} \leq 0.05$). I reduced the data using the same procedure outlined in Chapter 2.

The noise in these maps is 11.6 and 1.8 mJy beam^{-1} with 2 and 4 arcsec pixels, at 450 and 850 μm, respectively. When the matched filter is applied the noise drops to 4.47 and 0.7 mJy beam^{-1} respectively*. These values are averaged over the whole map, and will be less in deeper regions of the map i.e. the very centre. The matched filtered maps can be seen in Figure 4.1.

4.2.2 *Herschel*

The SPIRE maps were taken as part of the *Herschel* Multi-tiered Extragalactic Survey (HerMES, Oliver et al. 2012) observations of the XMM Large-Scale Structure (XMM-LSS) field. I made cut outs of the region containing JKCS041 using the Virtual Observatory at SusseX† (VOX). The maps reach a noise of 4.7, 5.9 and 6.6 mJy at 250, 350 and 500 μm respectively. Whilst there are PACS maps of the XMM-LSS field (and the region covering JKCS041), they are not deep enough for use in this analysis.

*The deepest regions of the map reach a noise of 4 and 0.5 mJy beam^{-1} respectively

†https://herschel-vos.phys.sussex.ac.uk/

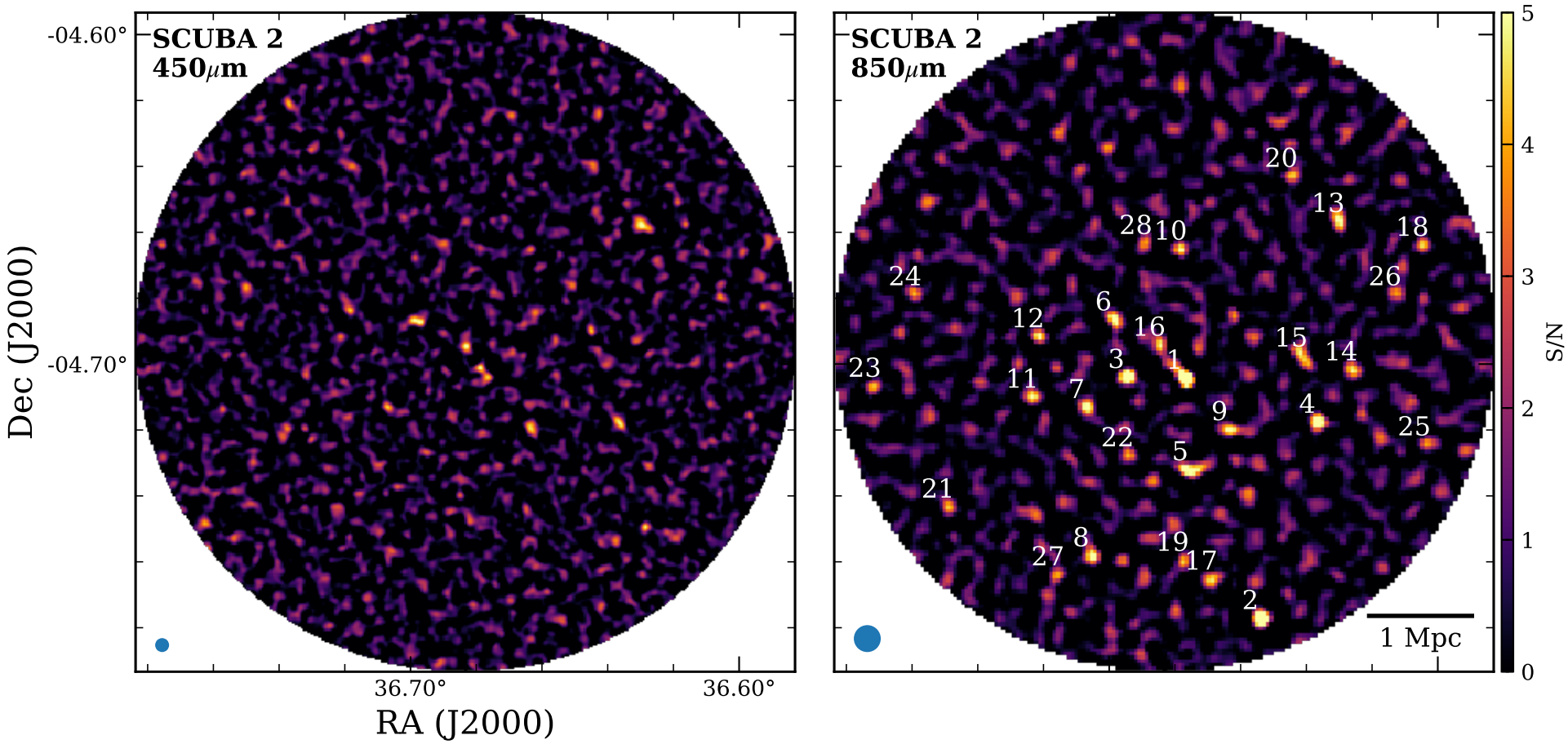

Figure 4.1. Signal to noise maps for the SCUBA-2 maps of JKCS041 with a radius of 3 Mpc. The positions of all 28 SCUBA-2 sources with an S/N greater than 4 are labeled on the 850 μm image, with the numbering the same as that in Table 4.2. The PSF size can be found in the lower left corner.

4.2.3 JVLA

I use JVLA S band (2-4 GHz) data, taken as part of project 15A-223 in 2015 (PI: M. Pannella). The raw data was downloaded from the NRAO's JVLA archive[‡] and reduced using the NRAO's Astronomical Image Processing System (AIPS). The standard JVLA data calibration procedure was followed, and for full details see either the AIPS cookbook[§], or Chapter 3. The map reaches a noise of 1.4 μJy, and has a synthesised beam of 0.8×0.6 arcsec.

4.2.4 Ancillary Data

With JKCS041 being located in the XMM-LSS field, the region is part of the *Herschel* Extragalactic Legacy Project (HELP, Vaccari 2016, Oliver et al. in prep.). The purpose of HELP is to bring together the multi-wavelength data available for all the *Herschel* survey fields, and produce homogeneously calibrated multi-wavelength catalogues (Shirley et al. 2019).

For the XMM-LSS field, HELP uses optical data from the CFHT Legacy Survey (CFHTLS, Gwyn 2012), the Pan-STARRS1 Medium-Deep Survey (Tonry et al. 2012), the Dark Energy Survey (DES, Diehl et al. 2014) and the Hyper Suprime-Cam (HSC) Deep Survey (Aihara et al. 2018).

The NIR and MIR data comes from the VISTA Deep Extragalactic Observations survey (VIDEO, Jarvis et al. 2013), the UKIRT Infrared Deep Sky Survey-Ultra Deep Survey (UKIDSS-UDS, Lawrence et al. 2007, Almaini et al. 2007), the CFHT WIRCam Deep Survey (WIRDS, Bielby et al. 2012), the *Spitzer* Extragalactic Representative Volume Survey (SERVS, Mauduit et al. 2012) and the *Spitzer* Wide-area IR Extragalactic Survey (SWIRE, Lonsdale et al. 2003). A summary of all the data used in this analysis can be found in Table 4.1, and an in depth discussion of the catalogues from which the data comes from (including the magnitude depths for each survey) can be found in Shirley et al. (2019)[¶].

[‡]https://science.nrao.edu/facilities/vla/archive/

[§]http://www.aips.nrao.edu/cook.html

[¶]The full data set can be downloaded from http://hedam.lam.fr/HELP/dataproducts/dmu32/dmu32_XMM-LSS/data/

Table 4.1. Summary of the data-sets used in our analysis.

Telescope	Instrument	Survey	Observed Band
CFHT	MegaCam	CFHTLS	u, g, r, i, z
Subaru	HSC	HSC Deep Survey	g, r, i, z, y
Blanco	DECam	DES	g, r, i, z, y
Pan-STARRS	GPC1	Pan-STAARS MDS	g, r, i, z, y
VISTA	VIRCAM	VIDEO	z, y, J, H, Ks
UKIRT	WFCAM	UKIDSS-UDS	y, J, H, K
CFHT	WIRCam	WIRDS	J, H, Ks
Spitzer	IRAC	SWIRE, SERVS	3.6, 4.5, 5.8, 8 μm
Spitzer	MIPS	SWIRE	24 μm
Herschel	SPIRE	HerMES	250, 350, 500 μm
JCMT	SCUBA-2	-	450, 850 μm
JVLA	-	-	10 cm

4.3 Assigning Cluster Membership

4.3.1 Source Identification

To detect any potential galaxies within the maps, I needed to determine an appropriate S/N threshold to use. This threshold was determined by analysing the completeness for different S/N cuts, and comparing the number of injected to recovered sources in a jackknife map made from the 850 μm map. In this analysis A jackknife map is produced by randomly inverting half of the observations before co-adding, this subtracts real sources leaving behind a map of just the noise. I inject 10^5 sources randomly into the jackknife map (in batches of 10), with fluxes picked from a uniform distribution, and SEXTRACTOR (Bertin & Arnouts 1996) was used to extract sources.

I found that a S/N of 4 gives me 80% completeness at $\sim$5 mJy, yet the number of spurious sources (i.e. sources caused entirely by noise with no association to a astronomical source), was minimal with only one spurious detection. Therefore, it was decided to use this S/N cut for detecting our sources.

Within the SCUBA-2 850 μm map there were 28 sources that have a S/N greater than 4, indicating they could be potential cluster members. The information on these sources can be seen in Table 4.2 and locations shown in Figure 4.1. Comparing number counts to field galaxies in the SCUBA-2 Cosmology Legacy Survey (S2CLS, Geach et al. 2017), in a region the same size as ours (~ 0.03 deg^2), 10 ± 3 sources would be expected at 850μm (with the error assuming Poisson statistics). Since I am getting $\sim$3 times this amount, I confirm that this is a very over-dense region.

Table 4.2. Catalogue of sources from the SCUBA-2 850 μm map that have an S/N greater than 4.

Name	RA	DEC.	r_c (Mpc)	S/N_{850}	S/N_{450}
850_1	36.677	-4.704	0.39	10.6	4.5
850_2	36.654	-4.777	2.74	10.2	3.1
850_3	36.694	-4.703	0.48	8.0	2.3
850_4	36.636	-4.717	1.62	7.7	5.0
850_5	36.675	-4.731	1.22	6.7	2.76
850_6	36.698	-4.686	0.52	6.0	5.4
850_7	36.706	-4.713	0.95	5.9	4.5
850_8	36.705	-4.758	2.11	5.9	3.3
850_9	36.663	-4.719	1.02	5.6	4.7
850_10	36.678	-4.665	0.88	5.4	2.8
850_11	36.723	-4.709	1.34	5.4	2.6
850_12	36.721	-4.691	1.18	5.3	3.6
850_13	36.630	-4.656	1.99	5.3	5.4
850_14	36.626	-4.701	1.77	5.1	< 2
850_15	36.641	-4.697	1.29	5.0	3.0
850_16	36.684	-4.694	0.05	5.0	5.3
850_17	36.669	-4.765	2.26	4.9	< 2
850_18	36.604	-4.663	2.59	4.7	2.3
850_19	36.677	-4.759	2.05	4.6	< 2
850_20	36.644	-4.642	1.96	4.4	3.7
850_21	36.749	-4.743	2.55	4.3	3.1
850_22	36.694	-4.727	1.11	4.3	3.3
850_23	36.771	-4.706	2.75	4.2	2.4
850_24	36.759	-4.678	2.38	4.2	2.3
850_25	36.604	-4.724	2.63	4.2	2.2
850_26	36.613	-4.678	2.21	4.1	2.5
850_27	36.715	-4.763	2.40	4.1	< 2
850_28	36.688	-4.663	0.94	4.0	3.6

I took the positions of the 850 μm sources and looked at the same locations in the 450 μm map. I found that only 7 of the 850 μm sources have a significant 450 μm detection (i.e. a detection greater then 4 σ). I do note that there were an additional 8 450 μm sources with significant detections, but no 850 μm source associated with them. These sources are most likely to be low redshift sources.

4.3.2 Source Confusion

An issue with FIR and sub-mm astronomy is source confusion. Single dish measurements (such as those from *Herschel* and SCUBA-2), tend to have very large beams (on order of 10 arcsec), whilst measurements from optical and NIR data tend to

have much smaller beams (on the order of sub-arcsec). This causes the situation where several galaxies that are resolved in optical and NIR images, are blended together into one source in the FIR and sub-mm images. An example of this can be seen in Figure 4.2, comparing 850_11 at 850 μm with SCUBA-2 (beam size $\sim$15 arcsec) to the JVLA 10 cm data (Beam size $\sim$1 arcsec). It can be seen that the one source at 850 μm actually resolves into 3 distinct sources with the higher resolution telescope.

Since this is a very crowded field, there is a very high probability that several of the FIR and sub-mm sources are a combination of multiple sources blended together. This causes issues when associating short and long wavelength catalogues together, as I do not know which sources are associated with each other.

4.3.3 XID+ and de-blending images

To help deal with source confusion, I use the probabilistic de-blending tool XID+ [‖] (Hurley et al. 2017). XID+ takes positions of expected sub-mm galaxies (using a high resolution tracer of dusty star formation) as a prior, and uses Bayesian inference to estimate fluxes for all these sources. It does this by creating an artificial map with similar noise to the real map, and with sources at the same positions of the prior catalogue. The fluxes for these sources are then adjusted until the difference between the artificial and real map is minimized. XID+ also produces a complete posterior probability distribution, allowing for more information to be known about the fluxes of the sources (e.g. variance and co-variances). For a full description of the process, and the full mathematical prescription I refer to Hurley et al. (2017).

Flux boosting is when a blind source extraction is carried out, the flux of a source is overestimated when in the presence of noise. As there are far more fainter objects then brighter ones, a source above some flux limit is more likely to have had its flux increased by noise (both instrumental and confusion noise) then decreased (this is known as Eddington Bias, Eddington 1913). Since I impose no flux limit when doing the fitting for XID+, I do not need to worry about this issue since I allow the flux estimate to be anything.

[‖] https://github.com/H-E-L-P/XID_plus

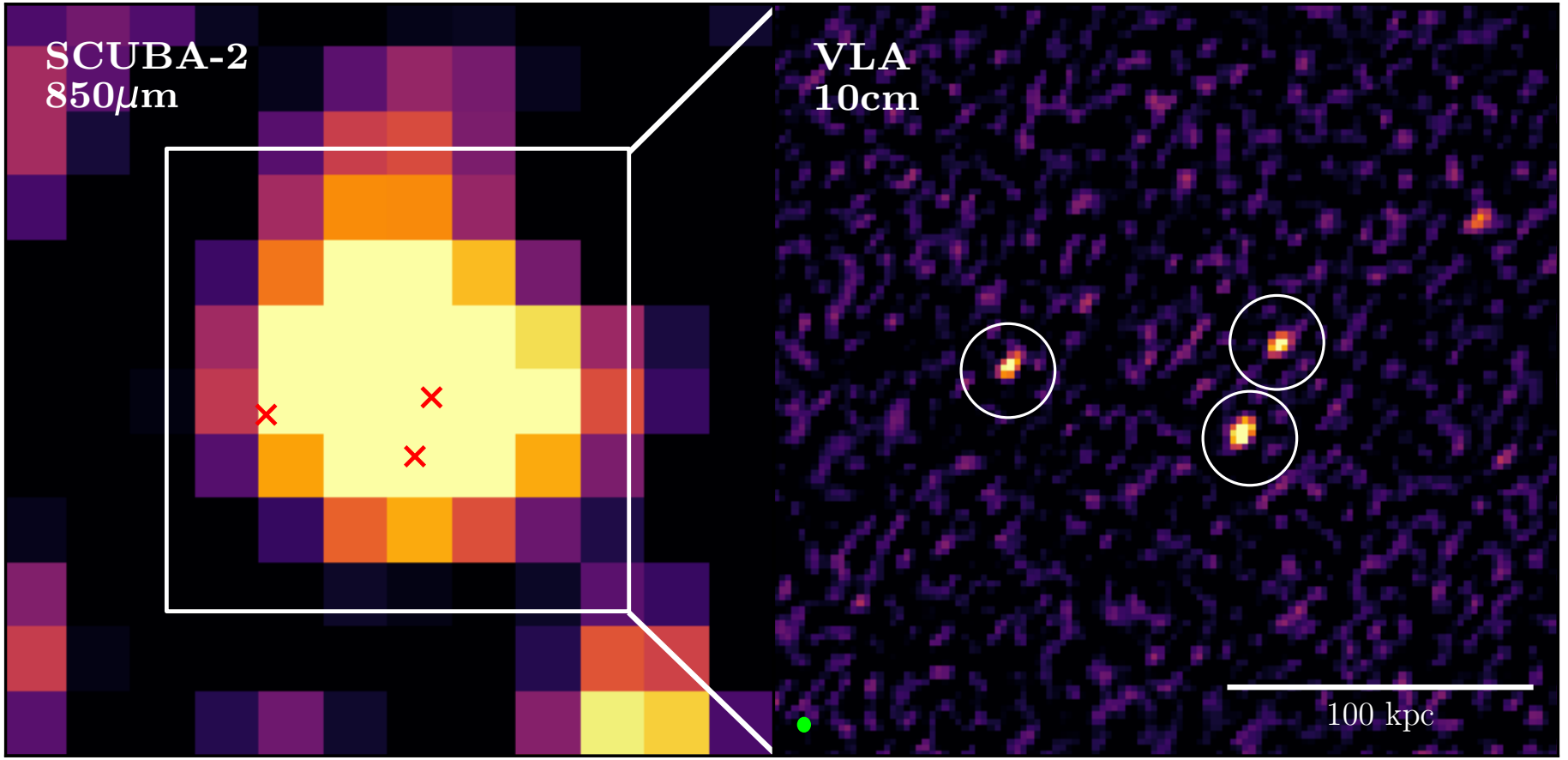

Figure 4.2. Left: the SCUBA-2 850 μm image showing source 850_11. Right: the JVLA data of the same region. I see that in the SCUBA-2 image there is only one source detected, whereas the JVLA shows that there is potentially 3 sources, and the large beam of SCUBA-2 has merged them together. The FWHM of the JVLA beam can be seen in the lower left hand corner.

For the positional prior, a high resolution tracer of dusty star formation is needed, with best results coming from 24 μm (e.g. Elbaz et al. 2010; Béthermin et al. 2012) or radio wavelengths (utilising the FIR-radio correlation, e.g. Ivison et al. 2010; Jarvis et al. 2010; Magnelli et al. 2015). To that end I elected to use the JVLA 10 cm map since the resolution is significantly better then that of the MIPS 24 μm ($\sim$0.7 arcsec for JVLA compared to 6 arcsec for MIPS). The JVLA resolution is also comparable to optical and NIR maps making cross matching easier.

Within the JVLA map I identified 228 radio sources that are in the same area of the SCUBA-2 maps, which make the basis of our prior catalogue. There was no radio source in the vicinity of sub-mm source 850_7, however there was a very bright 24 μm source in the vicinity, so I used that as the prior for that source, and add it to our prior catalogue. I also included seven, 24 μm sources that fall in the same region as the SCUBA-2 maps, yet had no obvious radio counterpart. This brings the total number of sources in our prior catalogue to 236, which are used when running XID+. It should be noted that all but 4 of the original 28 SCUBA-2 sources (Table 4.2) have at least one radio or 24 μm within 15 arcsec of it.

Whilst I am aware that HELP ran XID+ for the MIPS and *Herschel* maps, I re-ran it myself using the priors based on radio/24 μm positions. This is because for the MIPS maps, HELP use IRAC and optical/NIR positions as the prior, which are not ideal tracers for dusty star formation. For SPIRE maps, HELP uses a combination of deep MIPS maps (which have poor resolution when compared to the radio images), or use the MIPS positions that have already been through XID+ (which are based on the IRAC positions).

I ran the standard XID+ code on both the SPIRE and MIPS maps, and used a specially modified version of the code** to work with the SCUBA-2 maps. Looking at the residuals from XID+ I find that for all wavelengths, the maps constructed from XID+ are consistent with the actual maps. This procedure gives us estimates for the fluxes between wavelengths of 24-850 μm.

I compared the original catalogue of the SCUBA-2 sources (Table 4.2) with the results of XID+. I match the radio and SCUBA-2 sources, and consider any radio/24 μm sources that lie within 15 arcsec (i.e. one beam width) of a SCUBA-2 source as being potentially responsible for the sub-mm emission. Of the 28 SCUBA-2 sources, 14 had one radio/24 μm match, and 10 had multiple radio/24 μm sources match. The sub-mm fluxes estimated by XID+ are given in Table B.1.

For those 4 SCUBA-2 sources mentioned that had no radio or 24 μm within close vicinity, it is believed that these could be very high redshift sources. This is

**https://github.com/H-E-L-P/XID_plus/tree/SCUBA2-TNG

supported by the ratio of radio to 850 μm flux which has been shown to decrease with redshift (e.g. Carilli & Yun 1999; Dunne et al. 2000). There is also evidence by looking at the SPIRE fluxes. There is no SPIRE detection for these four sources, showing they must be at a redshift where the peak of FIR emission is near 850 μm, which only happens at redshifts greater than four (e.g. Riechers et al. 2017; Greenslade et al. 2019).

4.3.4 REDSHIFTS

As I want complete short wavelength data *and* accurate redshifts, I only take the radio sources that have a match with a source in the HELP catalogue. I cross matched both the radio catalogue and the HELP catalogue, and found of the 236 radio sources, only 26 did not have a HELP match, and were removed from the sample. Whilst I think these sources are not part of the cluster, since they are uniformly distributed in space, and they have no optical/NIR counterparts (meaning they could just be false detections in the radio map), there is still a small chance excluding them could cause an under-estimation in our results.

To determine if a source is a cluster member or not, I use the redshift of the source to determine membership. Since only a small sample of these galaxies have spectroscopic redshifts (~ 50) I rely on photometric redshifts. HELP estimates photometric redshifts using a Bayesian combination approach. Using the Easy and Accurate z_{phot} from Yale (EAZY, Brammer et al. 2008) code as a framework, HELP combine the standard set of templates with templates from XMM-COSMOS (Salvato et al. 2009) and the atlas of galaxy SEDs (Brown et al. 2014). For a full description of the methodology and accuracy of the photometric redshift estimations see Duncan et al. (2018).

I compare the photometric redshifts to the spectroscopic redshifts and measure the scatter (Figure 4.3). I find a scatter of $\sigma \sim 0.075$, and consider a source to be a cluster member if it lies within $\pm 2\sigma$. Therefore if a source has a measured redshift between 1.65 and 1.95 it is considered to be a potential cluster member.

Before I applied the redshift cut I looked at the galaxies that had spectroscopic redshifts. Looking at the spectroscopic redshifts from both HELP, and the catalogue of spectroscopic redshifts from Newman et al. (2014) I found 2 galaxies that lie within the cluster. For those galaxies that do not have spectroscopic redshifts, I apply the redshift cut to the photometric redshifts from HELP. I found 40 galaxies that lie within the redshift range, and are considered potential cluster members. When combined with the spectroscopic selected sources, I have a final list of 42 potential cluster

members.

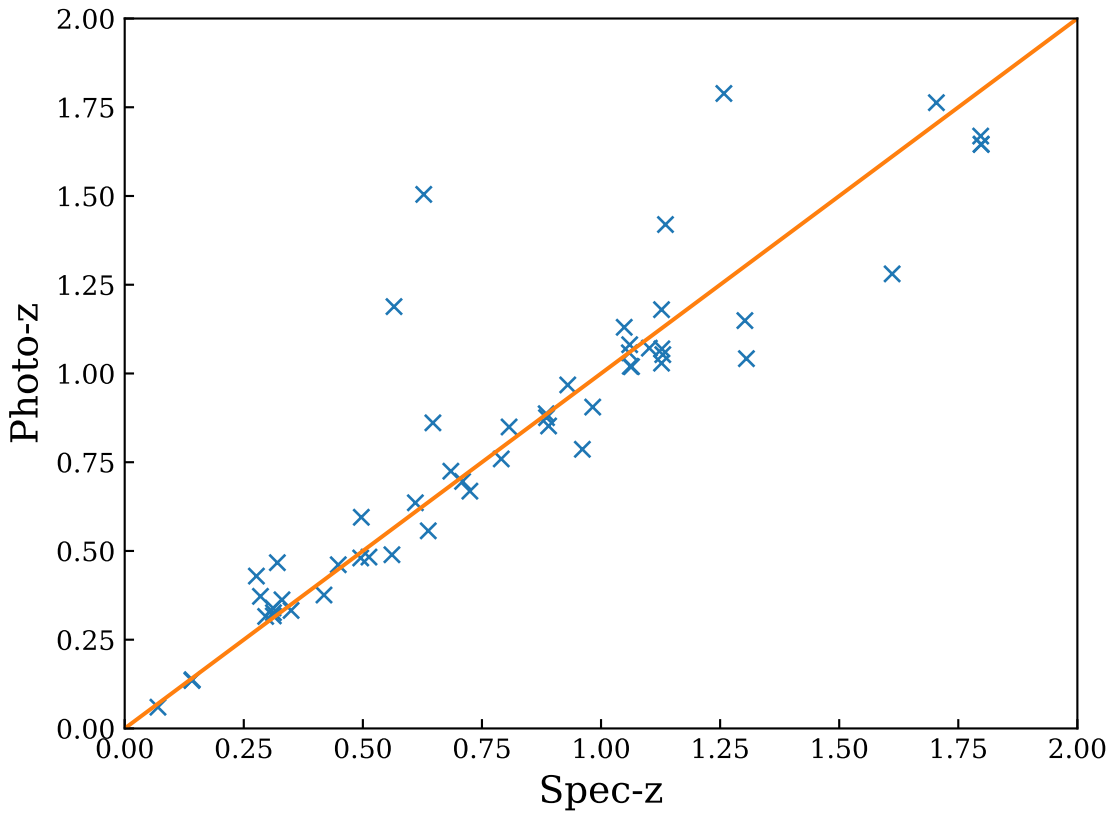

Figure 4.3. Comparison of the spectroscopic redshift, to those of the photometric redshifts from HELP. The solid line shows the one to one relation.

4.4 Star Formation properties of JKCS041

4.4.1 Association with SCUBA-2 sources

When associating the cluster members with the SCUBA-2 sources, I found that 14 of the 42 potential cluster sources were within the vicinity of a SCUBA-2 source (with 5 of the sources being in the vicinity of just 2 SCUBA-2 sources). Figure 4.4 shows all the potential cluster sources. Whilst these 42 sources do have redshifts consistent with being in the cluster, I do acknowledge the fact that there is a chance that some of these may not actually be cluster members. For the rest of the analysis (unless stated) I make the assumption that all 42 sources are members of the cluster.

All 42 sources were then ran through the Code Investigating GALaxy Emission (CIGALE[††], Boquien et al. 2019), an SED fitting code that uses dust-energy balancing

[††]https://cigale.lam.fr/

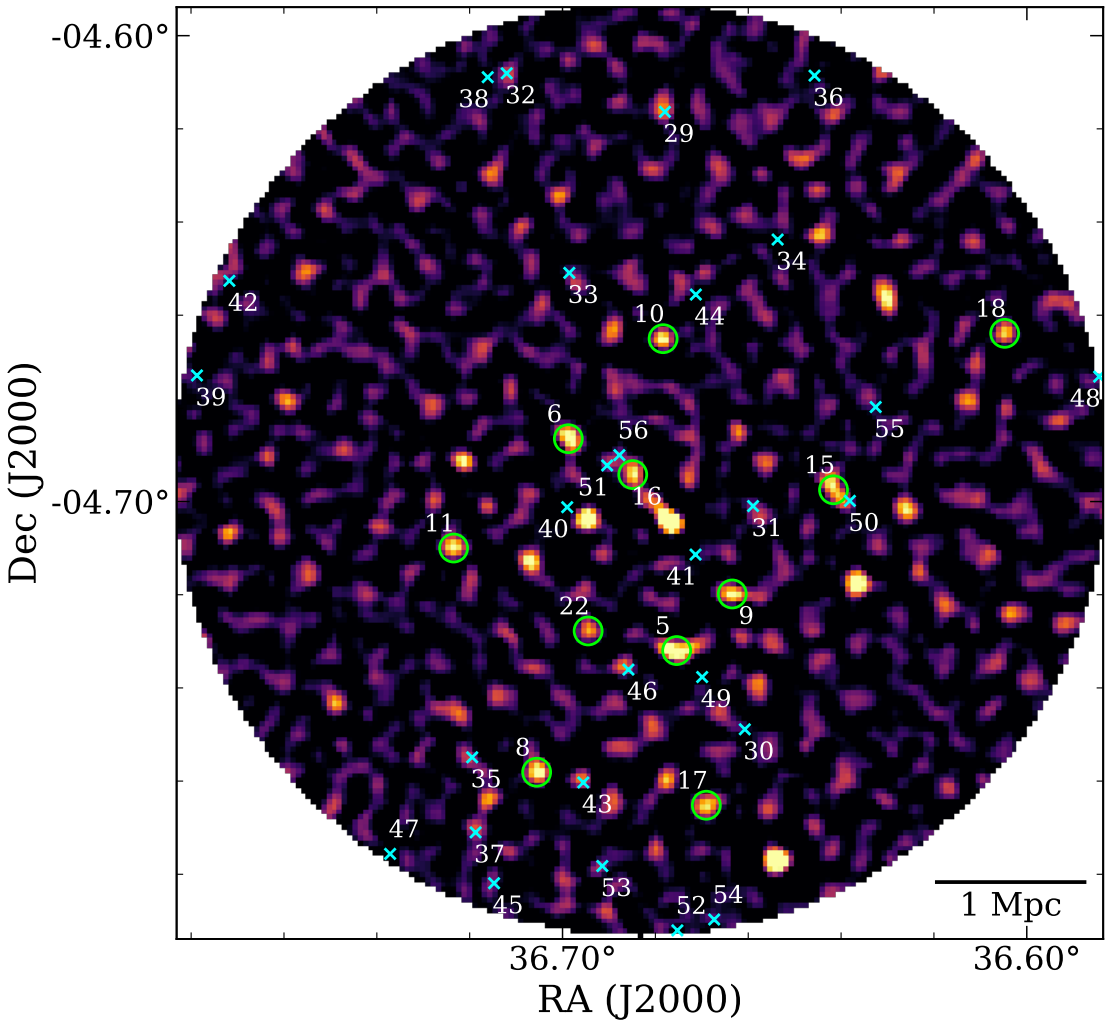

Figure 4.4. Signal to noise map of the SCUBA-2 850 μm data showing the location of the 42 sources potentially within the cluster. A green circled sources show a source that has a radio counterpart, a match in the HELP database, and is associated with a SCUBA-2 source. The blue crossed sources represents a source that only has a radio counterpart, and a detection in the HELP database. It should be noted that sources 11 and 17 actually have several sources associated with the SCUBA-2 source. The numbering matches up with that found in Table 4.3.

to fit both the optical and FIR parts of the SED. The models used to generate the templates are the same as HELP. These involve a delayed star formation history (with additional burst), Bruzual & Charlot (2003) single stellar population models, a Charlot & Fall (2000) dust attenuation law, and the Draine & Li (2007) dust emission model. These models were selected as they cover a wide range of galaxy types, and full details can be found in Małek et al. (2018). When fitting I fix the redshift for all sources to that of the cluster.

I find SFRs that vary between 12 and $500\,\mathrm{M_\odot\,yr^{-1}}$ with a median value of $119\,\mathrm{M_\odot\,yr^{-1}}$. All results from CIGALE can be seen in Table 4.3.

4.4.2 SFR vs cluster radius

To investigate any radial variation in the SFR I first calculate the projected distance of each source to the center of the cluster. It should be noted that I do not know the position of the galaxies along the line of sight. These were then binned in 0.5 Mpc bins ranging from 0 to 3 Mpc. The SFR was summed in each bin and then normalised by the volume of that radial shell (assuming the cluster is spherical). The results of this can be seen in Figure 4.5.

In the central 0.5 Mpc region there are high levels of star formation, with a total SFR of $770 \pm 100\ \mathrm{M_\odot\,yr^{-1}}$. When converted to a SFRD this has a projected volume density of $(1.3 \pm 0.1) \times 10^4\,\mathrm{M_\odot\,yr^{-1}Mpc^{-3}}$. This value is over 5 orders of magnitude greater then expected field galaxy values ($\sim 0.1\,\mathrm{M_\odot\,yr^{-1}Mpc^{-3}}$, Madau & Dickinson 2014), and is comparable to clusters found at similar redshifts (e.g. Clements et al. 2014; Dannerbauer et al. 2014 Kato et al. 2016; Smith et al. 2019b). There is a gradual decline in the SFRD all the way out to 3 Mpc, but even at these large radii the SFRD is $\sim$2 orders of magnitude greater then field galaxy values.

The issue in using a spherical volume for the cluster radius is that I make the assumption that all our galaxies are definitely in the cluster. This will not be the case, as since I used such a large redshift range, there is a high chance I will have a few interloping galaxies. Since the redshift is fixed when running CIGALE, the interlopers will have a wrongly assigned redshift which could cause a deviation from the "true" SFR of the cluster.

To account for this, instead of normalising by the spherical cluster volume, I normalise by the observable cosmological volume in the region between $1.65 < z < 1.95$. This changes the SFRD in the central 0.5 Mpc region from 5 orders of magnitude above expected field galaxy values, to $\sim$1.5 dex above the expected field value (Figure 3.9). I also find that at radii above 1 Mpc I reach the expected field galaxy values. This

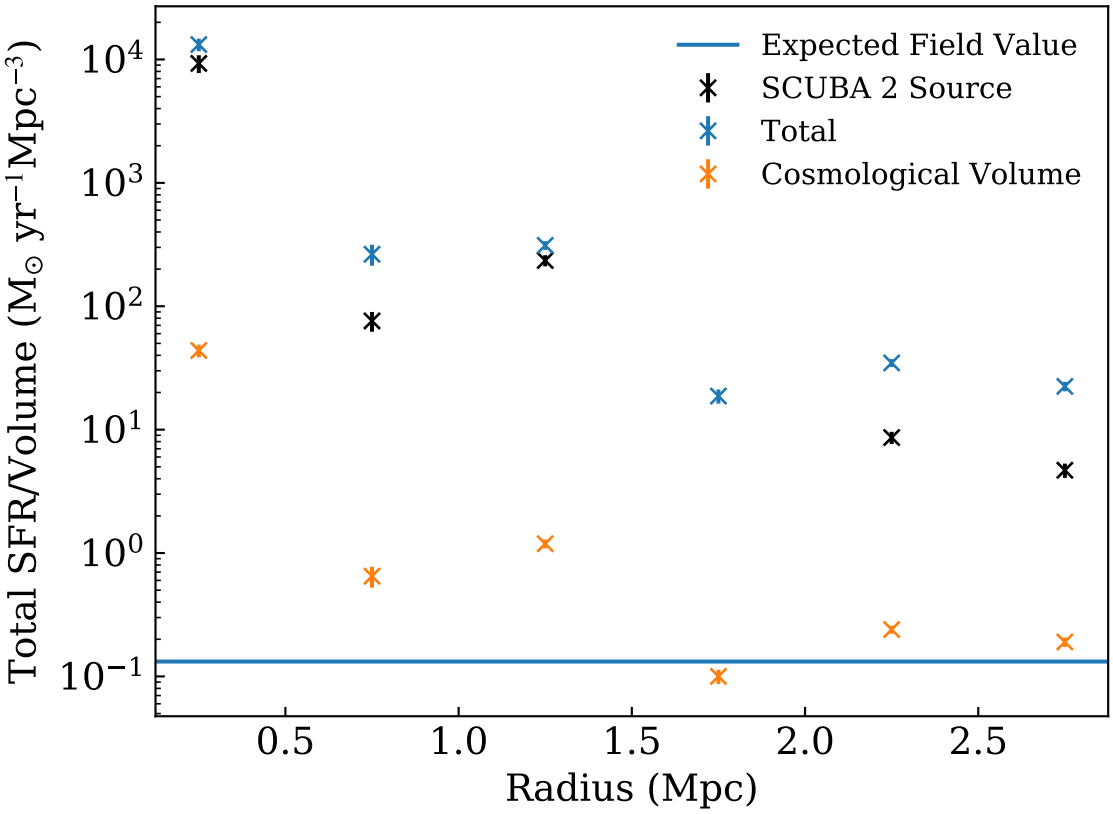

Figure 4.5. The SF-density relation for JKCS041. The cluster has been divided into 0.5 Mpc bins, and normalised by the volume of each of these bins. I also show the relationship if I only consider sources associated with a 4σ SCUBA-2 source. The blue line shows the expected relation for field galaxies from Madau & Dickinson (2014). The orange points represent the SF-density relation where instead of assuming a spherical volume for the cluster, it is the observable cosmological volume in the range $1.65 < z < 1.95$.

means that I could have a large fraction of interlopers, and if that is so the SFRD is actually much lower, especially when compared to other clusters at the same redshift.

To check whether the SFR-density profile I found in Figure 4.5 is not dominated by our redshift selection, I perform an additional Monte Carlo test. Since I expect 10 sources not to be within the cluster (Geach et al. 2017), I take a random 18 sources from my SCUBA-2 sources and make the assumption they are in the cluster. With these sources I create a new SFR-density profile, and repeat this process 1000 times. As for Figure 4.5, I calculate the SFR-density assuming both a spherical cluster volume, and the observable cosmological volume. The results of the Monte Carlo test are shown in Figure 4.6, where the data-points and error-bars show the average, and standard deviation of the profiles, respectively.

Table 4.3. Properties of our cluster sources based on the radio positions. The first 14 sources are those associated with a SCUBA-2 source.

Name	RA	DEC.	z	r_c Mpc	$L_{\rm IR}$ ($10^{12}\,{\rm L}_\odot$)	$\sigma_{L_{\rm IR}}$ ($10^{12}\,{\rm L}_\odot$)	SFR ($\rm M_\odot yr^{-1}$)	$\sigma_{\rm SFR}$ ($\rm M_\odot yr^{-1}$)	M_* ($10^{11}\,{\rm M}_\odot$)	σ_{M_*} ($10^{11}\,{\rm M}_\odot$)
850_5_B	36.672	-4.732	1.95	1.26	1.83	0.31	224	44	0.35	0.12
850_6_A	36.697	-4.689	1.86	0.44	1.24	0.15	96	19	1.72	0.23
850_8	36.705	-4.758	1.86	2.11	0.94	0.1	79	10	1.62	0.17
850_9_A	36.663	-4.721	1.88	1.06	2.27	0.41	267	54	0.77	0.14
850_10	36.678	-4.666	1.84	0.87	1.39	0.14	129	24	1.54	0.15
850_11_A	36.723	-4.71	1.86	1.34	1.26	0.96	147	122	0.68	0.13
850_11_B	36.724	-4.711	1.84	1.36	1.03	0.18	89	23	1.35	0.1
850_11_C	36.726	-4.71	1.77	1.42	1.31	0.26	158	40	0.33	0.1
850_15	36.642	-4.697	1.95	1.28	3.66	0.2	502	32	0.59	0.13
850_16_A	36.684	-4.695	1.66	0.06	3.6	0.71	431	98	1.81	0.15
850_16_B	36.686	-4.692	1.65	0.1	0.81	0.05	82	6	1.73	0.1
850_17_A	36.669	-4.766	1.84	2.28	1.71	0.14	139	23	2.53	0.16
850_18	36.604	-4.664	1.88	2.61	1.79	0.14	185	24	1.49	0.11
850_22	36.694	-4.728	1.76	1.12	1.57	0.25	120	38	2.19	0.35
29	36.678	-4.616	1.94	2.39	3.14	0.35	262	52	3.5	0.3
30	36.661	-4.749	1.93	1.86	0.61	0.12	73	18	0.29	0.07
31	36.659	-4.701	1.91	0.79	0.37	0.14	46	19	0.18	0.05
32	36.712	-4.608	1.89	2.78	1.17	0.17	155	44	0.32	0.1
33	36.699	-4.651	1.88	1.39	0.78	0.04	61	5	1.28	0.07
34	36.654	-4.644	1.88	1.79	0.47	0.14	38	14	0.65	0.14

The RA and DEC. are the positions of the sources in the radio map. The redshifts comes from the HELP database, and all parameters are the results from our CIGALE fitting.

Table 4.3. *(Continued)*

Name	RA	DEC.	z	r_c Mpc	$L_{\rm IR}$ ($10^{12}\,{\rm L}_\odot$)	$\sigma_{L_{\rm IR}}$ ($10^{12}\,{\rm L}_\odot$)	SFR ($\rm M_\odot yr^{-1}$)	$\sigma_{\rm SFR}$ ($\rm M_\odot yr^{-1}$)	M_* ($10^{11}\,{\rm M}_\odot$)	σ_{M_*} ($10^{11}\,{\rm M}_\odot$)
35	36.719	-4.755	1.88	2.21	1.85	0.14	229	23	0.52	0.13
36	36.646	-4.609	1.87	2.87	0.33	0.04	25	3	0.54	0.06
37	36.719	-4.771	1.84	2.64	0.67	0.18	116	47	0.09	0.03
38	36.716	-4.609	1.83	2.8	1.15	0.1	118	17	0.97	0.11
39	36.779	-4.673	1.81	3.02	0.18	0.05	14	4	0.29	0.08
40	36.699	-4.701	1.79	0.54	0.34	0.06	31	5	0.68	0.1
41	36.671	-4.711	1.78	0.67	1.45	0.32	244	81	0.29	0.21
42	36.772	-4.653	1.76	3.01	2.42	0.57	276	80	1.3	1.39
43	36.696	-4.76	1.75	2.11	2.24	0.14	169	20	3.39	0.19
44	36.671	-4.656	1.74	1.23	0.95	0.12	96	18	0.81	0.08
45	36.715	-4.782	1.71	2.91	1.65	0.2	180	33	1.09	0.19
46	36.686	-4.736	1.71	1.32	1.73	0.27	141	38	2.09	0.33
47	36.737	-4.776	1.71	3.04	0.07	0.05	12	7	0.03	0.01
48	36.584	-4.673	1.7	3.12	0.56	0.15	47	10	1.0	0.23
49	36.67	-4.738	1.7	1.43	0.83	0.04	70	4	1.53	0.08
50	36.638	-4.7	1.7	1.41	1.54	0.1	123	17	2.11	0.14
51	36.69	-4.692	1.67	0.22	2.32	0.12	175	11	3.71	0.19
52	36.675	-4.792	1.67	3.06	0.31	0.08	28	8	0.52	0.09
53	36.691	-4.778	1.66	2.64	1.25	0.06	103	10	2.16	0.11
54	36.667	-4.79	1.65	3.02	1.02	0.1	93	12	1.52	0.14
55	36.633	-4.68	1.65	1.63	0.91	0.22	156	27	1.23	0.14
56	36.688	-4.69	1.65	0.17	1.06	0.21	82	15	1.83	0.34

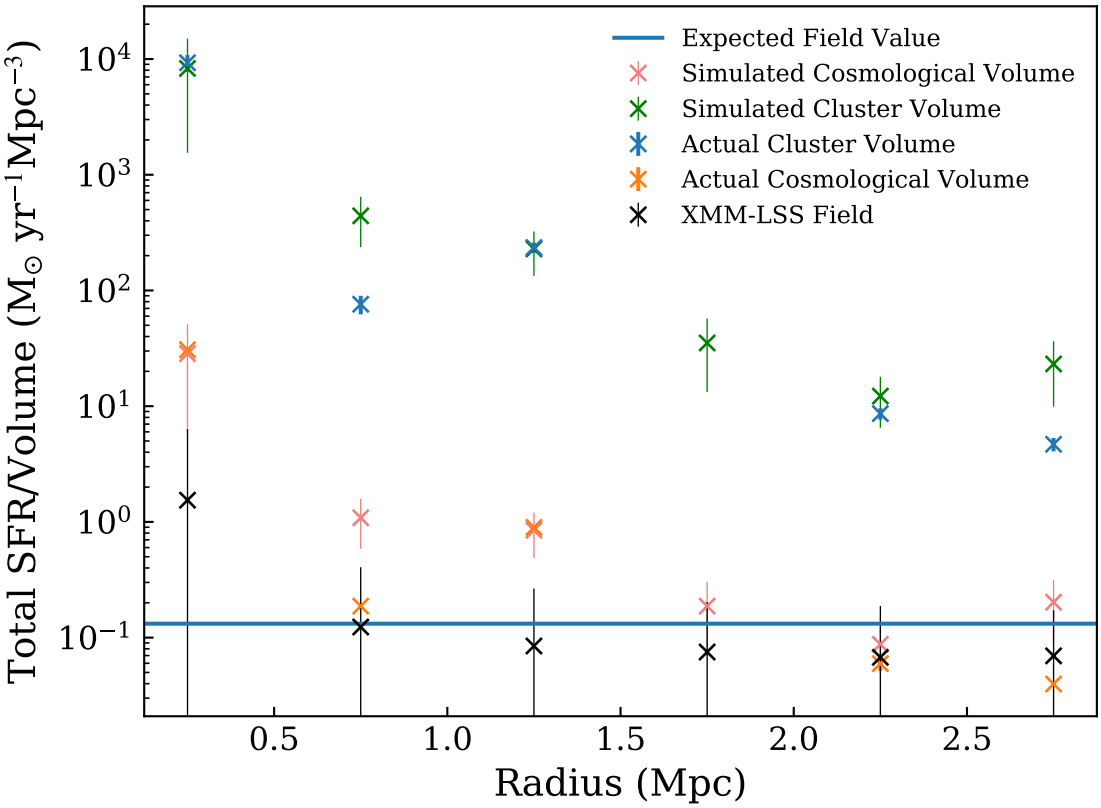

Figure 4.6. Comparison of the SFR-density radial profiles for both the Monte Carlo test, and the actual cluster data. Again I use both a spherical cluster volume, and the observable cosmological volume. I also compare the radial profiles when using random positions in the XMM-LSS field.

It can be seen that the relation from randomly sampling the SCUBA-2 sources is similar to that of my actual cluster selection, and the radially declining profile is significant. This is further confirmed by applying the same process to random positions in the XMM-LSS field, where I see the SFR-density fall below the field average (due to not sampling lower luminosity objects, Figure 4.6). As the Monte Carlo profiles often show the same radial profile, and since I randomly pick our SCUBA-2 sources from our initial sample, it could show that some of the sources excluded could actually be cluster members.

4.4.3 The SFR-stellar mass relation

I then investigated the relation between stellar masses (M_*) and SFR for the 42 cluster galaxies. I use stellar masses from CIGALE and compare them to the SFRs, with the resulting relationship being seen in Figure 4.7. This was then compared to the expected galaxy star forming main sequence (MS) for redshift 1.8 galaxies from

Sargent et al. (2014).

Since the region below the MS is home to quiescent galaxies (i.e. galaxies no longer forming stars), on first glance it would appear that JKCS041 has a large population of these quiescent galaxies (or at least galaxies transitioning into this region), which is seen in low redshift clusters. This would indicate that JKCS041 is very similar to that of a low redshift ($z < 1$) cluster, dominated by quiescent galaxies (e.g. Brodwin et al. 2013; Lin et al. 2014; Jian et al. 2017, 2018; Wagner et al. 2017; Wu et al. 2018). However there is also a significant fraction ($\sim$1/3) of galaxies lying above the MS, which is a region dominated by star-burst galaxies and is not seen in low redshift clusters (e.g. Koyama et al. 2013; Santos et al. 2015; Alberts et al. 2016; Darvish et al. 2016; Wang et al. 2018; Gómez-Guijarro et al. 2019; Smith et al. 2019b).

For those galaxies that lie below the MS, I see that there is no radial trend, with galaxies from all different radii being present in this region. This would go against expectations, since most of the environmental processes that effect galaxies get stronger the closer to the cluster core, therefore you would expect those sources in the center to be most quenched (e.g. Boselli & Gavazzi 2006; Moran et al. 2007). Work by Chung et al. (2011) has shown (for local clusters at least) the cluster effects can be seen to at least 3 times that of the virial radius. The virial radius of JKCS041 is $\sim$800 kpc (Andreon et al. 2014) and since JKCS041 is similar to a low redshift cluster (in mass terms at least), it is not surprising the the effects of quenching are being observed so far away from the cluster core.

However this trend could also be explained by considering the orbits of galaxies within a cluster. Galaxies within clusters tend to have radial orbits (e.g. Frenk et al. 1996; White et al. 2010), which means a galaxy could make multiple passes through the center of the cluster, and thus the environmental effects could be taking effect causing quenching.

For those galaxies that lie above the main sequence, their high star formation rates could be driven by merger activity. Several studies have shown the galaxies above the MS tend to be undergoing some sort of merging behaviour (e.g. Hung et al. 2013; Silva et al. 2018; Cibinel et al. 2019). For now the data is not good enough to confirm this. Other explanations for the enhanced SF could be these are younger galaxies still forming the bulk of their stellar mass (e.g. Mancuso et al. 2016), or internal instabilities within the galaxy causing enhanced star formation (e.g. Zolotov et al. 2015; Tacchella et al. 2016).

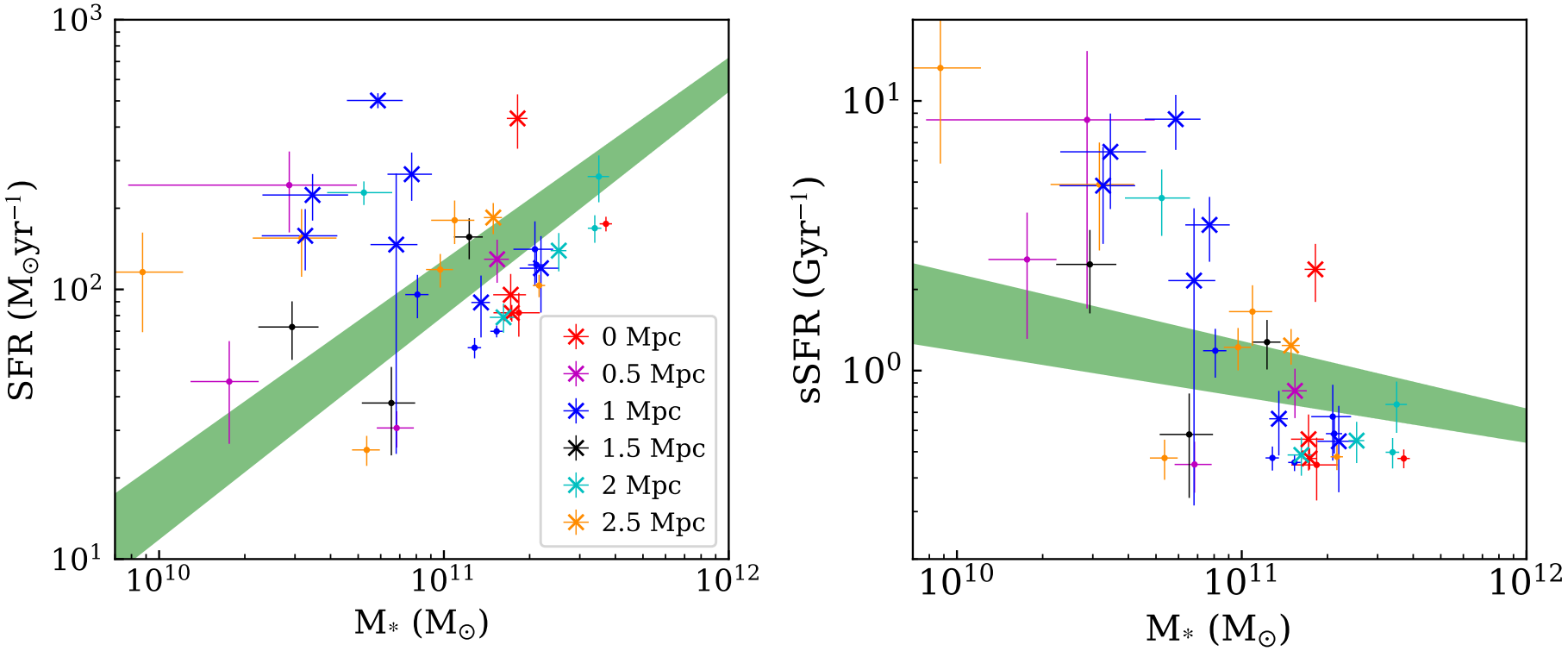

Figure 4.7. Left: The SFR-M_* relation for JKCS041. The shaded region showing the expected MS for redshift 1.8 galaxies from Sargent et al. (2014). The points have been divided up and colour coded based on their position within the cluster. The different markers show association with SCUBA-2 sources, with the crosses representing sources associated with a SCUBA-2 source, and the points showing those that are not. Right: The sSFR-M_* relation, with the expected relation for redshift 1.8 galaxies.

In Figure 4.7 I also compute the specific SFR (sSFR = SFR/M_*), and compare it to the expected relation from Sargent et al. (2014) for MS galaxies. Similar to the SFR-M_* relation there is a distinct split in the positioning of the galaxies. I also see a strong negative correlation (Spearman's rank ρ = -0.6) in this relation with this negative trend being seen at all redshifts (e.g. Ilbert et al. 2015; Lehnert et al. 2015). Since the sSFR compares the instantaneous SFR to that of the SFR averaged over its whole lifetime, a negative trend suggests that the more massive galaxies form all their stars much more rapidly and much earlier then their lighter counterparts.

For those galaxies that are lying below the main sequence, they could be forming less stars then any other point in their life. This could suggest that they have already formed all their stars (especially since they are so massive) much more rapidly. It could also show that the hostile cluster environment is effecting these galaxies and influencing the gas within them and causing a suppression in star formation.

It should be noted that the SFR-MS is an empirical relationship, and not an evolutionary track. It was determined by taking an average of thousands of galaxies, and it was found that the majority of galaxies fit this tight relationship. Whilst it is possible that the cause of these galaxies lying below the MS is due to environmental effects, it is not certain and motivates the need for additional data.

4.4.4 INTEGRATED SFR

JKCS041 is an interesting cluster, as it shows evidence for increased star formation activity in the core, but also shows evidence that the galaxies within are undergoing quenching. To see how JKCS041 compares to other clusters I compute the mass normalised SFR. I follow the prescription laid out in Popesso et al. (2012), which first involves summing the SFR out to a radius of 1 Mpc. Using this radius allows me to compare to other high redshift clusters. I find a total integrated SFR (ΣSFR) of $1300 \pm 130\,M_\odot\,yr^{-1}$. I then normalise ΣSFR by the cluster mass ($(2.24 \pm 0.78) \times 10^{14}\,M_\odot$) resulting in a $\Sigma SFR/M_{cl}$ of $590 \pm 210\,M_\odot\,yr^{-1}/10^{14} M_\odot$.

Figure 4.8 shows the $\Sigma SFR/M_{cl}$ of JKCS041 compared to other clusters, at both low and high redshift. I also compare the $\Sigma SFR/M_{cl}$ to trends predicted by Popesso et al. (2012) and the $(1+z)^7$ trend predicted by Geach et al. (2006). It is seen that JKCS041 does not follow the trend predicted by Popesso, however this trend was calibrated on low redshift clusters. I also find that (unlike other high redshift clusters) JKCS041 does not follow the $(1+z)^7$ from Geach, with there being a $3.5\,\sigma$ offset. With this relation JKCS041 would fit if it were a at a redshift of 1.4. This is noteworthy since several studies seem to indicate that redshift 1.4 is a key moment in

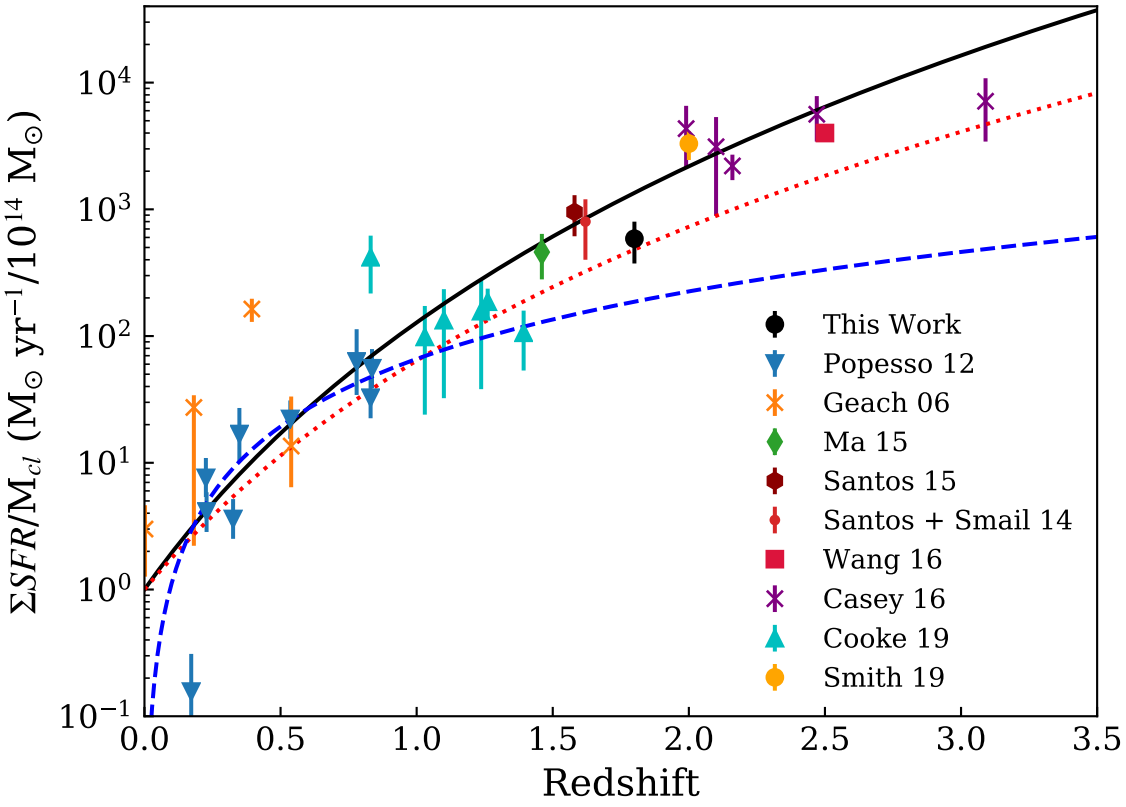

Figure 4.8. Comparing ΣSFR/M_{cl} for several clusters with redshifts $0 < z < 3$. The solid black line shows the $(1+z)^7$ from Geach et al. (2006). The blue dashed line shows the relation from Popesso et al. (2012), and the red dotted line shows the $(1+z)^6$ relation, which indicates a less rapid evolution in the SFR.

cluster evolution and represents a transition time for galaxies going from star forming to being quenched (e.g. Brodwin et al. 2013; Santos et al. 2013; Alberts et al. 2014, 2016; Stach et al. 2017; Hayashi et al. 2018). This could indicate that JKCS041 is currently undergoing this transitioning phase and it's galaxies are going from star forming to quiescent.

Replacing the power law with a index of 6, JKCS041 falls nicely on this relation (with there only being $0.5\,\sigma$ offset). This would indicate that the evolution of star formation in JKCS041 is not as rapid as that in other high redshift clusters, yet is still more rapid then field galaxies, which have a power law index of 3-4, (e.g. Ilbert et al. 2015).

No matter the power law index selected, there is still noticeable scatter (especially at high redshift). Geach et al. (2006) observed this in low redshift clusters, and suggested that cluster environment is having an effect on the star formation histories of the galaxies residing within them. One such influence could be the mass of the

cluster, which has been suggested by both Koyama et al. (2011) and Cochrane et al. (2018) who observed significant scatter in other samples of clusters. Since there is some scatter with JKCS041 compared to other clusters at similar redshifts *and* it is significantly more massive then clusters seen at similar redshifts, this could be some of the first direct evidence that the mass of a cluster is having a direct impact on the galaxies that reside in it. However for the time being there is not enough high redshift clusters to determine if this is actually happening or I just have a biased sample.

4.5 CONCLUSIONS

I presented new SCUBA-2 images of JKCS041, a mature cluster at redshift 1.8. I combined these images with pre-existing *Herschel* maps, and combined this with optical and NIR data from HELP. I then went and studied the SF properties of this cluster.

- I use SCUBA-2 and *Herschel* maps to explore $\sim$0.03 deg^2 that contain JKCS041. I identify 28 sources in the 850 μm maps that have a S/N greater than 4.

- To deal with source confusion I use high resolution JVLA maps, and the Bayesian inference tool XID+ to de-blend my images and get accurate fluxes for wavelengths between 24-850 μm. These fluxes were combined with data from HELP to get complete wavelength coverage for all our potential cluster galaxies. I use the redshifts from HELP and previous spectral measurements, to help identify potential cluster members. Making a redshift cut I identify 42 galaxies that are likely to be within the cluster.

- I use CIGALE to estimate both SFRs and stellar masses for all 42 galaxies. In the central 0.5 Mpc region I find high levels of star formation with a total SFR of 770 ± 100 M$_\odot$ yr^{-1}, which is a SFRD of $(1.3 \pm 0.1) \times 10^4$ M$_\odot$ yr^{-1}Mpc^{-3}. This is several orders of magnitude greater than values expected for field galaxies. When calculating a SFRD, accounting for potential contamination for interloper galaxies, I find that the SFRD in the central 0.5 Mpc region is only $\sim$2 orders of magnitude greater then expected field galaxy values.

- When I look at the SFR-M$_*$ relation I see that $\sim$2/3 of the galaxies lie below the expected main sequence. This could indicate that the harsh environment of the cluster is already in the process of quenching these galaxies. For the other $\sim$1/3 of the galaxies, these lie above the main sequence. This means that

these galaxies could be undergoing star-burst behaviour which could be fueled by mergers.

- When comparing JKCS041 to other clusters I see that it deviates from previously identified scaling relations. This could indicate that the cluster mass is having a direct effect on the galaxies within it, more so then clusters at similar redshifts.

Even though there is evidence for a reversal in the SFR-density relation in JKCS041, there is also evidence that the galaxies within the cluster are being quenched and having star formation suppressed. Given that this is not seen in other clusters at similar redshifts, and the only difference is that JKCS041 is significantly more massive, this could be some of the first direct evidence that cluster mass plays an important part in influencing the evolution of galaxies within it. However at the picture is not clear, and more studies and larger samples need to be collected before anything definite can be said.

Chapter 5
Formation Of A Cluster At Redshift 3.6

"Do. Or do not. There is no try."

Yoda - *Star Wars*

In this chapter I present the discovery of a redshift 3.6 proto-cluster using data from ALMA. The reduction of the ALMA data in Section 5.2.1 was done with the assistance of George Bendo and the UK ALMA regional center.

5.1 Introduction

Proto-clusters are the progenitors to the massive clusters seen today (for an overview see Overzier 2016). Found in the high redshift universe (z >2), proto-clusters make ideal laboratories to trace the formation of the most massive dark matter halos and allow for the testing of different cosmological models. They are also key in understanding the star formation history of the universe, since simulations have suggested that over-dense regions in the early universe are the home to the majority of star formation (e.g. Chiang et al. 2013, 2017).

Due to the deep potential well caused by the dark matter halo, gas that accretes onto a mature cluster heats up and emits X-rays (Figure 1.12). Due to the fact that a proto-cluster has not yet virilaised, it has not got this deep potential and hence the gas cannot get hot enough to emit X-rays. This means the standard methods of cluster detection (X-rays/Sunyaev-Zeldovich effect) cannot be used, neither can searching for over-densities of red galaxies.

To identify proto-clusters, over-densities of highly star forming galaxies need to be identified, such as Lyman-α emitters, Lyman break galaxies or H-α emitters (e.g. Onoue et al. 2018; Shimakawa et al. 2018; Higuchi et al. 2019; Suzuki et al. 2019). Quasi-stellar objects (QSOs) can also act as tracers for proto-clusters. It has been shown that QSOs exist in the most massive halos (e.g. Efstathiou & Rees 1988; Turner 1991) meaning they are the perfect tracer for over-densities in the early universe. This means that any galaxy associated with these objects are also likely to be in said over-density (e.g. Kurk et al. 2004; Tanaka et al. 2011; Husband et al. 2013).

Other methods to discover proto-clusters rely on FIR/sub-mm searches. Thanks to the negative K-correction (Chapter 1) the discovery of these high redshift systems is more efficient thanks to the little loss of flux. SMGs can also trace proto-clusters, since it is believed that SMGs are the progenitors to the massive ellipticals seen in the local universe. Therefore clusters of SMGs in the high redshift universe are the best candidates for proto-clusters.

An effective way of searching for proto-clusters at FIR/sub-mm wavelengths was suggested by Negrello et al. (2005). They suggested the use of 2 different FIR/sub-mm instruments, one low resolution and one at a much higher resolution. If there was a cluster of SMGs, the low resolution instrument would blend them together and they would appear as one very bright clump. When these clumps are observed with the high resolution instrument, the clump should begin to be resolved, and individual galaxies (and hopefully a proto-cluster) identified. This means low resolution, all sky surveys can help us identify the locations of potential proto-clusters, which can be followed up and studied in detail.

This method has shown great success with both the *Planck* satellite's High Frequency Instrument (HFI, Lamarre et al. 2010) and the SPIRE instrument on *Herschel*. Thanks to the large surveys conducted with *Herschel* such as HerMES, and the *Herschel* Astrophysical Terahertz Large Area Survey (H-ATLAS, Eales et al. 2010) large portions of the sky have been observed at FIR/sub-mm wavelengths. Several proto-clusters have already been identified following up the *Planck* clumps with *Herschel* (e.g. Herranz et al. 2013; Clements et al. 2014, 2016; Greenslade et al. 2018; Martinache et al. 2018; Cheng et al. 2019).

Whilst this method is very effective at detecting proto-clusters, characterising them is still rather difficult due to the poor resolution of *Hershel*. Follow up observations need to be performed using higher resolution instruments such as ALMA. Follow up of several proto-clusters have revealed large populations of dusty star forming galaxies, with most of the large structures breaking up into multiple components,

and sources with SFRs well over $1000\,M_{\odot}\,yr^{-1}$ (e.g. Hodge et al. 2013; Lewis et al. 2018; Oteo et al. 2018; Gómez-Guijarro et al. 2019; Lee et al. 2019).

Other searches for proto-clusters can involve searching directly for over-densities in the *Herschel* images themselves. Eales et al. (in prep) recently conducted a search within the $\sim 600\,deg^2$ of the H-ATLAS fields. Over-densities were searched for in the three dimensional space of RA, DEC and redshift (using redshifts derived from *Herschel* photometry, Pearson et al. 2013). For each source, the number of sources within 1.5 Mpc, and ± 1 of redshift was calculated. This number was then compared to those that would be expected by chance, and if it was significantly larger it is considered a potential proto-cluster.

15 potential proto-clusters were detected within the H-ATLAS fields. Of those 15 PLCKERC857 G017.8668.67 (hereafter PLCKERC857, RA= 348.790, DEC=-30.591) is considered the best candidate due to the tight clustering of five *Herschel* sources (Figure 5.1, Table 5.1). It is also a good candidate since it lines up with a known *Planck* source (Greenslade et al. 2018). Based on the redshifts of the sources, the estimated redshift of this cluster lies somewhere between 3.4-4.1.

Table 5.1. Positions and fluxes for the sources within PLCKERC857. The positions and fluxes come from Maddox et al. 2018, and the redshifts are derived from the methodology in Pearson et al. 2013.

Pointing	RA (J2000)	DEC (J2000)	z	f_{250} (mJy)	f_{350} (mJy)	f_{500} (mJy)
1	348.870	-30.600	3.5±0.5	29	35	38
2	348.827	-30.592	3.6±0.5	31	35	40
3	348.822	-30.612	4.1±0.5	24	37	40
4	348.793	-30.617	3.8±0.5	37	48	53
5	348.788	-30.626	-	-	-	-
6	348.764	-30.646	3.4±0.5	33	36	41

Pointings 4 and 5 belong to the same *Herschel* source. Due to the extended nature two pointings were taken to assure the whole source was covered.

5.2 Observations

5.2.1 ALMA

To investigate this potential proto-cluster further, band 3 observations were taken as part of ALMA cycle 6 (ObsId: 2017.1.00033.s, PI: S. Eales). Since one of the main aims is to estimate the redshift of the cluster, the spectral scan mode was used.

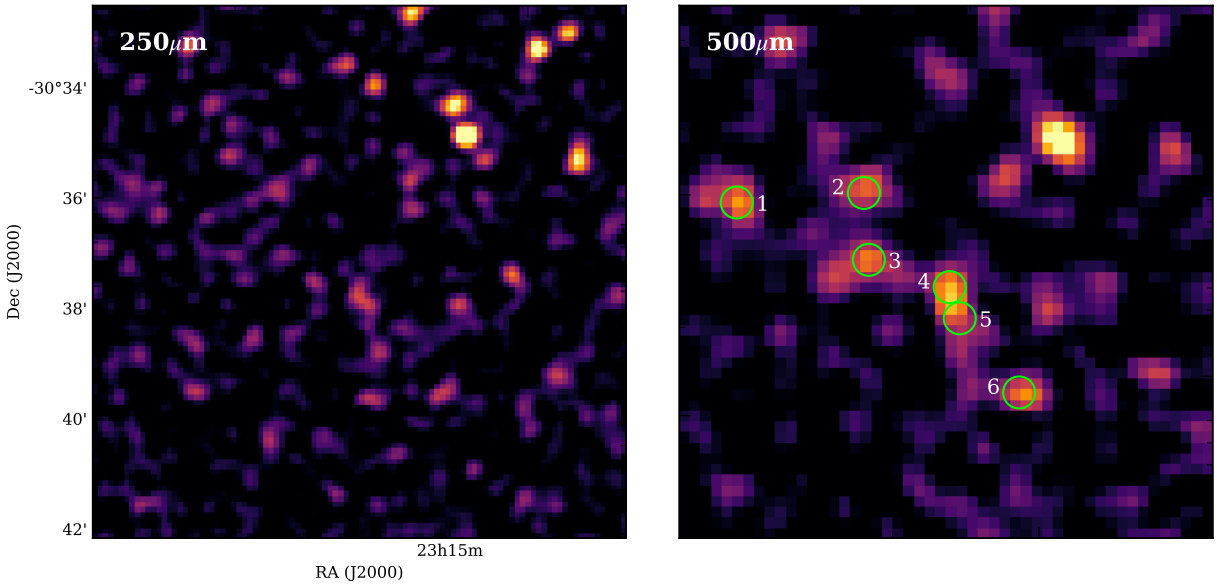

Figure 5.1. *Herschel* 250 and 500 μm images of the proto-cluster PLCKERC857. The images are set to the same range of flux densities. This shows that the proto-cluster has to be at high redshift, since if it was at low redshift the sources would be more luminous at 250 μm. The green circles show the positions of each ALMA observation, with the numbers showing the pointings from Table 5.1. The bright source in the upper right hand corner is a known low redshift galaxy.

This means the entire band-with was scanned (∼85-115 Ghz, ∼2.5-3.5 mm) allowing the best chance to detect one or more lines. Given that the expected redshift of the cluster is ∼4, then based on Figure 5.2, I would expect to see both the CO(4-3) and CO(5-4) lines. There is also a possibility of detecting the CI(1-0) line.

Each *Herschel* source was observed with one pointing, since each source is smaller than the ALMA band 3 primary beam (∼ 60 arcsec). The exception to this is source four, since it looks extended and was covered with two pointings (Table 5.1). The observations were taken between March and December 2018, with a total integration time of 8 hours (including calibration time).

The ALMA correlator was set up into five tunings, each consisting of four spectral windows (SPWs). Each SPW had a bandwidth of 1.875 GHz and a resolution of 31.25 MHz (23.491 kms^{-1}). I reduced the data using the Common Astronomy Software Applications(CASA, McMullin et al. 2007). The data reduction procedure is broken up into two parts, calibration and imaging.

The first step of calibration involves taking the raw data from the telescope, and flagging the data for any erroneous data points or bad data. These can include contamination from sky lines, antennae dropping out, or any antennae exhibiting odd behaviour. Using either a solar system object or quasar the flux scale is determined.

Next band-pass and gain calibrators are applied. Band-pass calibration determines the variations of phase and amplitude with respect to the frequency, whilst gain calibration determines variation of phase and amplitude with respect to time. These variations can be due to change in weather conditions or elevation of the source during observing. The calibrator to correct for these variations needs to be a high signal-to-noise point source, therefore is often chosen to be the same as the flux calibrator, such as a bright quasar. Finally phase calibrations are applied, which are key since they are used to determine the time delay between all the dishes. A point like object, near the target is observed frequently, since atmospheric changes can cause deviations in the phase.

After the calibration is done the data is in the form of visibilities, which consists of phase and amplitude data. The data is converted into a usable image via the process of cleaning (Högbom 1974). The first step is to grid the visabilities onto the $u-v$ plane (the equivalent of the $x-y$ plane but in Fourier space). This $u-v$ plane is then Fourier transformed to get a dirty map, which is the true map convolved with a dirty beam (a poor PSF based on the sampling of the $u-v$ plane).

The true brightness of the map is determined by selecting the brightest areas of the map, and create a model map based on the positions of those bright sources. The dirty beam is then subtracted from these positions in the original map, producing a residual map, and revealing any fainter emission. More bright emission is detected in this residual map, and the process is repeated until a stopping criteria is met (normally a noise threshold). The model map is convolved with a synthesised beam (which is Gaussian in shape) and added to the residual map, producing the final map.

I reduced the data for each pointing, and created a data cube for each SPW. For my observations the radio quasar J2357-5311 was observed as a band-pass and flux calibrator, and radio quasar J2258-2758 as an amplitude and phase calibrator. The resulting synthesised beam was $\sim 1.5 \times 1.3$ arcsec at 3 mm, with a typical rms noise of 0.4 mJy beam^{-1} per 31.25 MHz channel.

I combined all the SPWs to measure the continuum at 3 mm. The rms noise for all six pointings was $\sim 9\,\mu$Jy beam^{-1}. Of the six pointings five had a continuum source within them (with three pointings having more then one continuum source). The flux measurements for all the continuum sources can be found in Table 5.2 and the sources can be seen in Figure 5.3.

When reducing the SPWs for the line data, an additional step that can be carried out is continuum subtraction. This models the continuum and subtracts it from the spectra. Since the continuum level is negligible at the rms noise of the line channels, continuum subtraction is not required. This is with exception to pointing

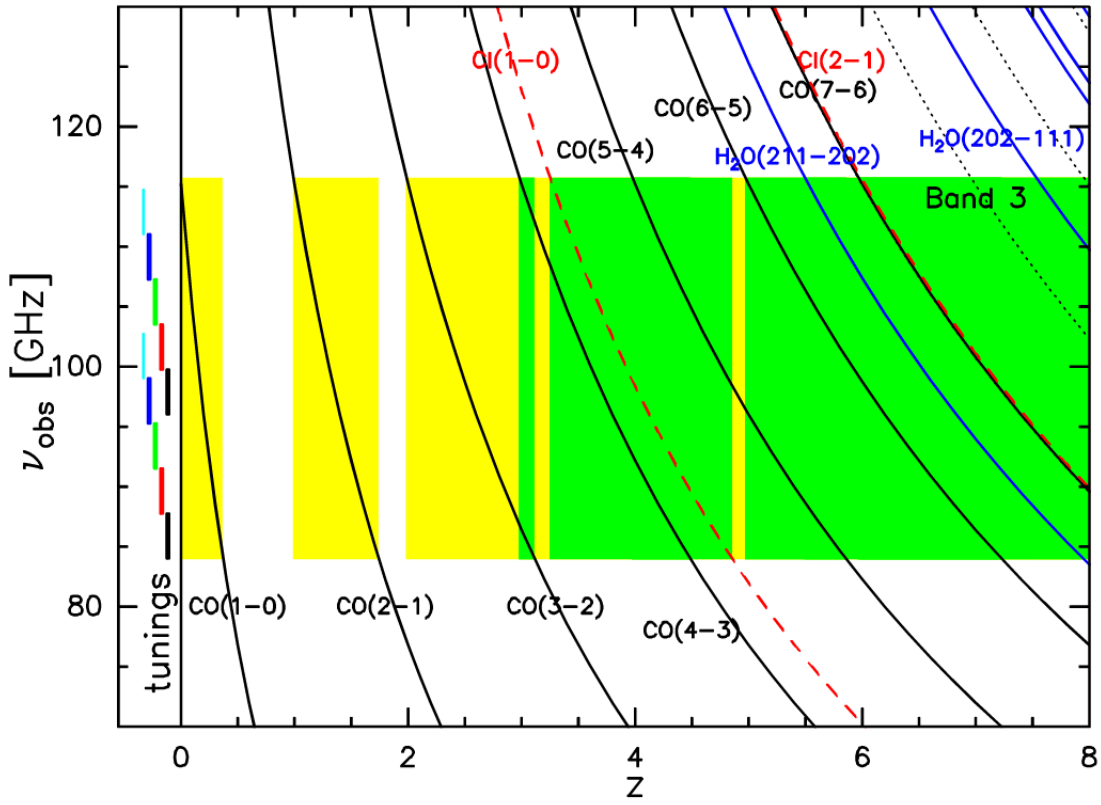

Figure 5.2. Expected frequencies of certain spectral lines in the region covered by the ALMA band 3 window. The shaded region shows the bandwidth of ALMA band 3. Yellow regions shows redshifts where only one line will be detected, and the green shows where two lines will be detected. Image credit Weiß et al. 2013.

four. Due to the brightness of one of the continuum sources, continuum subtraction was deemed necessary, so there is no contamination to the lines.

5.2.2 SPITZER

Complementary IR data of PLCKERC857 was obtained with the IRAC camera on *Spitzer*. As this data was taken as part of the *Spitzer* warm mission only data at 3.6 and 4.5 μm is available (PI: R. Cooray, ObdId 14088). The field was observed for two hours, and the resulting images of the IRAC data can be seen in Figure 5.4. Unfortunately the IRAC data does not cover all the same pointings, with only 5 of the 6 ALMA pointings being covered. The rms noise in the 3.5μm map is 0.4 μJy and 0.6 μJy at 4.6 μm.

Table 5.2. Positions and fluxes for all the continuum sources detected within PLCKERC857

ID	RA (J2000)	DEC (J2000)	$S_{3\,mm}$ (μJy beam^{-1})
CS_1_A	348.877	-30.601	57±12
CS_1_B	348.865	-30.603	39±16
CS_2	348.823	-30.591	50±19
CS_3	348.824	-30.613	49±15
CS_4_A	348.793	-30.611	3000±19
CS_4_B	348.793	-30.616	57±14
CS_6_A	348.768	-30.646	69±13
CS_6_B	348.758	-30.643	29±12

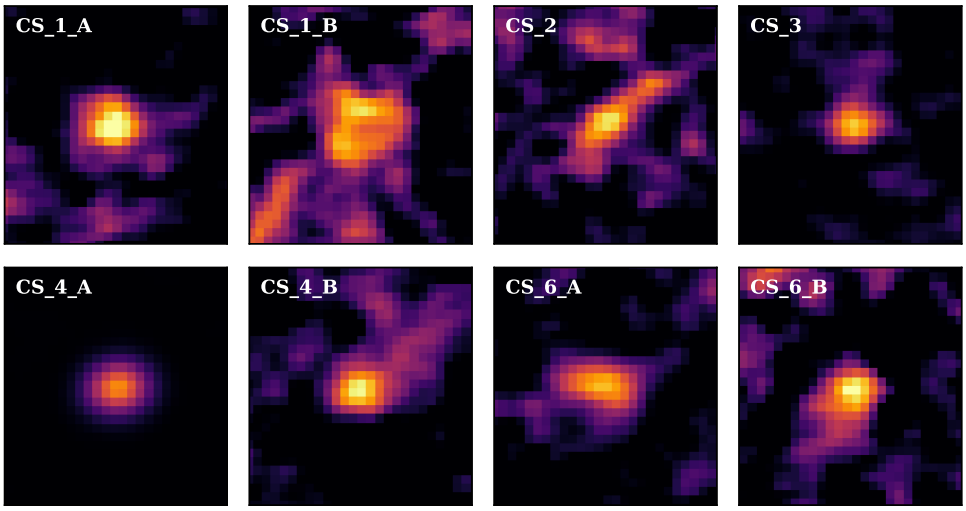

Figure 5.3. The eight continuum sources detected in PLCKERC857.

5.3 Searching For Sources

The reduced SPWs are searched in order to try and detect any potential spectral lines. To determine the significance of a line I assign it a S/N value, and consider anything above a certain S/N threshold to be a likely line candidate. To give the best chances of a detection, I conduct a pixel by pixel search in each SPW.

At high redshift, the expected profile shape for a line will be a Gaussian, and can have a FWHM on the order of a few hundred kms^{-1} (Carilli & Walter 2013). With this information I can use a matched filtering method to help detect any lines within the spectra. As discussed in Section 2.3.2 matched filtering is a technique designed to search for signals with a known shape. For the SCUBA-2 data I convolved the image with a 2-D Gaussian, and this helped reveal sources the same size of the beam. The exact same process is used here, but instead of a 2-D Gaussian, a 1-D Gaussian is used, with a certain FWHM. This will suppress the noise in the spectra and concentrate

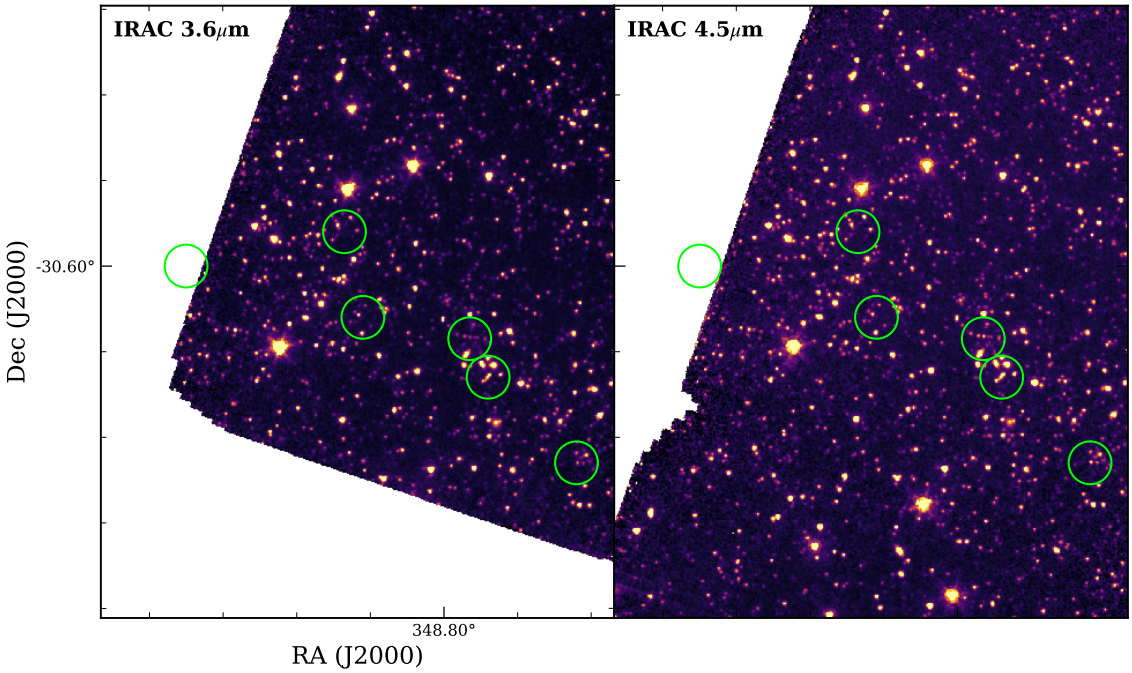

Figure 5.4. The *Spitzer* data of PLCKERC857. The green circles represent the six ALMA pointings taken.

the full S/N of the source in the peak. An example of the matched filtering in action can be seen in Figure 5.5

Once the spectra has been matched filtered, sigma clipping can be used to estimate the noise. This is then used to estimate the S/N for any point along the spectra. I consider any significant detection to be anything above $4\,\sigma$, in line with other blind search studies (e.g. Walter et al. 2016; Pavesi et al. 2018b).

I search every pixel, convolving it first with a $200\,\mathrm{kms}^{-1}$ Gaussian, then again with a $500\,\mathrm{kms}^{-1}$ Gaussian and search for any $4\,\sigma$ peaks. As an added precaution I ignore any pixels that are at the edge of the image (within 30 pixels of the edge of the image). This is because this area is at the very edge of the primary beam, and hence less sensitive. This means that there is a greater chance of random noise being selected as a source.

I found 57 line candidates that had a peak greater than $4\,\sigma$. Of this 57 candidates, six were at the same position of the continuum sources. The only continuum sources without a detection were CS_4_A and CS_4_B. As a check I looked at the positions of CS_4_A and CS_4_B, but with a $3\,\sigma$ detection threshold, but still no line was detected.

To check the fidelity of my detections, I estimate the number of fake sources that could be detected. Based on the number of pixels, and the $4\,\sigma$ threshold, I expect

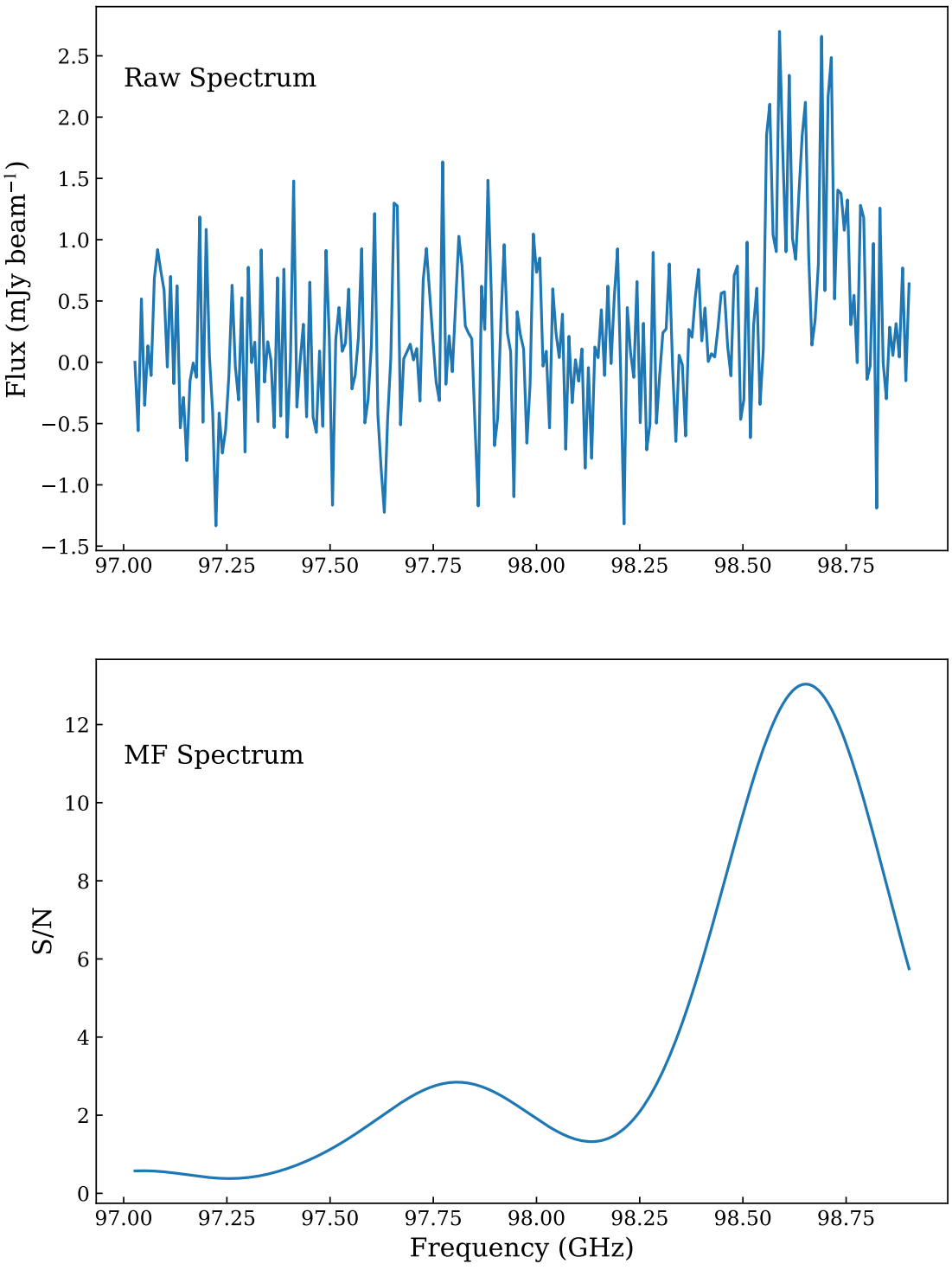

Figure 5.5. An example of a spectra before and after matched filtering. In the raw spectrum ($\sim 25\,\mathrm{kms}^{-1}$ channels) there is a possible detection at $\sim 98.6\,\mathrm{GHz}$, however there is till too much noise. After being matched filtered with a $500\,\mathrm{kms}^{-1}$ Gaussian the noise is suppressed and the S/N is maximised in the peak.

there to be no more then 10 sources caused entirely by noise. This value is consistent with several other blind search studies, who also suggest a 20% chance of each source being a spurious detection (e.g. Decarli et al. 2016; Walter et al. 2016; Franco et al. 2018)

For all 57 lines I fit a Gaussian to estimate the properties for each line. Whilst in practice, the kinematics of the galaxy make the CO line a more complex shape, due to the limited spectral resolution a Gaussian fit is suitable to estimate the parameters for each line. The properties of all the lines can be found in Table 5.3 and the spectra themselves can be found in Figure C.1.

As a test to help see if these detected lines are real and not due random noise, I look at the *Spitzer* data. If there is a strong *Spitzer* source associated with one of the ALMA sources, this increases the chances that the source is real, since the chances of having both a spurious ALMA and *Spitzer* source is low.

I used SEXTRACTOR and found 5712 and 5238 sources in the 3.6 and 4.5 μm maps respectively. To see if these sources are associated I match any *Spitzer* and ALMA source that lie within 1.3 arcsec of each other (approximately the size of the IRAC beam). I find 14 and 16 matches at 3.6 and 4.5 μm respectively. To see if these matches are significant, I use the method outlines in Section 3.3.3 and use Equation 3.1 to calculate the probability that the ALMA and *Spitzer* sources are not associated.

Using the same criteria in Section 3.3.3, at 3.6 μm I find that only two sources have P values too large (P >0.1) to be considered associated, and at 4.5 μm three are too large. The P values for all sources can be found in Table 5.3. Those sources that have significant matches in both bands are considered to be real sources, and not caused by noise. Whilst there are some sources that only appear significant in one band, these sources have the stronger detection in the 4.5 μm band, which could mean they are still real, they are just at higher redshifts (or have more dust). For the sources that have no *Spitzer* detection, whilst I do acknowledge that they could be spurious detections, I still use them in my analysis but understand my results could be slightly biased by including them.

Table 5.3. The properties of all line candidates after being fitted with a Gaussian. Sources with CS prefix are continuum sources, whilst those with BS are from the blind search.

ID	RA (J2000)	DEC (J2000)	SN	Freq (GHz)	Peak Flux ($\mathrm{mJy\,beam^{-1}}$)	FWHM ($\mathrm{kms^{-1}}$)	I_{CO} ($\mathrm{Jy\,kms^{-1}}$)	$f_{3.6}$ (μJy)	$P_{3.6}$	$f_{4.5}$ (μJy)	$P_{4.5}$
CS_1_A	348.877	-30.601	6.9	94.172 ± 0.045	0.38 ± 0.13	850 ± 336	0.34 ± 0.05	-	-	-	-
CS_1_B	348.865	-30.603	4.1	106.909 ± 0.021	0.7 ± 0.19	447 ± 141	0.33 ± 0.03	21.9 ± 2.5	0.01	-	0.14
CS_2	348.823	-30.592	12.9	98.659 ± 0.014	0.81 ± 0.1	699 ± 101	0.6 ± 0.01	30.4 ± 3.1	0.04	52.1 ± 5.2	0.01
CS_3	348.824	-30.613	5.9	99.357 ± 0.03	0.2 ± 0.07	504 ± 215	0.11 ± 0.02	14.3 ± 1.5	0.02	32.6 ± 3.3	0.01
CS_6_A	348.768	-30.646	5.2	99.363 ± 0.029	0.24 ± 0.11	411 ± 207	0.11 ± 0.02	11.1 ± 1.2	0.02	29.3 ± 3.0	0.01
CS_6_B	348.758	-30.643	5.5	99.011 ± 0.011	0.5 ± 0.13	254 ± 79	0.14 ± 0.01	14.4 ± 1.5	0.01	32.2 ± 3.2	0.01
BS_1	348.88	-30.6054	5.2	100.127 ± 0.015	0.5 ± 0.17	268 ± 105	0.14 ± 0.02	-	-	-	-
BS_2	348.834	-30.595	12.1	98.972 ± 0.013	0.69 ± 0.15	374 ± 90	0.28 ± 0.01	36.1 ± 3.6	0.04	53.9 ± 5.4	0.01
BS_3	348.829	-30.587	7.7	98.982 ± 0.021	0.43 ± 0.15	377 ± 149	0.17 ± 0.02	-	-	-	-
BS_4	348.820	-30.594	6.1	99.777 ± 0.0070	0.85 ± 0.21	177 ± 50	0.16 ± 0.01	-	-	-	-
BS_5	348.828	-30.598	8.6	101.514 ± 0.032	0.39 ± 0.12	644 ± 223	0.27 ± 0.03	-	-	-	-
BS_6	348.825	-30.595	6.5	111.856 ± 0.0070	1.21 ± 0.29	151 ± 42	0.2 ± 0.01	-	-	-	-
BS_7	348.829	-30.611	7.3	101.136 ± 0.013	0.69 ± 0.16	341 ± 90	0.25 ± 0.02	-	-	-	-
BS_8	348.792	-30.619	7.8	99.767 ± 0.011	0.66 ± 0.16	279 ± 80	0.2 ± 0.01	-	-	-	-
BS_9	348.791	-30.614	7.7	99.749 ± 0.011	0.65 ± 0.19	231 ± 77	0.16 ± 0.02	-	-	-	-
BS_10	348.764	-30.655	8.0	89.265 ± 0.0090	1.39 ± 0.35	249 ± 73	0.37 ± 0.03	-	-	-	-
BS_11	348.878	-30.605	7.1	93.937 ± 0.02	0.85 ± 0.29	374 ± 148	0.34 ± 0.05	-	-	-	-
BS_12	348.792	-30.622	7.8	94.308 ± 0.011	1.46 ± 0.36	283 ± 80	0.44 ± 0.03	-	-	-	-
BS_13	348.790	-30.630	4.4	107.062 ± 0.015	1.03 ± 0.34	251 ± 96	0.27 ± 0.04	-	-	-	-
BS_14	348.771	-30.651	9.2	104.172 ± 0.016	1.15 ± 0.33	318 ± 106	0.39 ± 0.04	-	-	-	-
BS_15	348.823	-30.586	5.3	85.363 ± 0.021	0.63 ± 0.22	436 ± 173	0.29 ± 0.04	23.3 ± 2.3	0.13	40.4 ± 4.1	0.12
BS_16	348.793	-30.618	10.1	85.658 ± 0.01	1.08 ± 0.26	298 ± 81	0.34 ± 0.02	-	-	-	-
BS_17	348.786	-30.612	9.5	85.798 ± 0.015	0.97 ± 0.24	427 ± 124	0.44 ± 0.03	-	-	-	-
BS_18	348.797	-30.616	6.2	87.069 ± 0.021	0.69 ± 0.16	629 ± 165	0.46 ± 0.03	-	-	37.1 ± 3.7	0.13
BS_19	348.791	-30.612	6.9	87.662 ± 0.021	0.7 ± 0.22	464 ± 168	0.35 ± 0.04	-	-	-	-
BS_20	348.790	-30.612	6.3	87.914 ± 0.0080	1.12 ± 0.23	273 ± 65	0.33 ± 0.02	-	-	-	-
BS_21	348.866	-30.594	5.8	99.387 ± 0.012	0.64 ± 0.2	239 ± 87	0.16 ± 0.02	-	-	-	-
BS_22	348.823	-30.618	4.9	99.282 ± 0.015	0.59 ± 0.18	307 ± 105	0.19 ± 0.02	18.0 ± 1.8	0.09	34.2 ± 3.4	0.08
BS_23	348.787	-30.616	4.8	99.096 ± 0.023	0.5 ± 0.13	534 ± 162	0.29 ± 0.02	-	-	-	-
BS_24	348.790	-30.627	8.7	98.969 ± 0.021	0.47 ± 0.12	495 ± 148	0.25 ± 0.02	-	-	-	-
BS_25	348.788	-30.632	4.1	98.951 ± 0.031	0.37 ± 0.16	449 ± 221	0.18 ± 0.04	12.4 ± 1.3	0.09	26.6 ± 2.7	0.07
BS_26	348.777	-30.627	4.7	111.702 ± 0.012	0.81 ± 0.28	190 ± 77	0.16 ± 0.02	60.0 ± 6.0	0.02	61.8 ± 6.2	0.03
BS_27	348.879	-30.601	4.4	102.201 ± 0.018	0.68 ± 0.22	328 ± 123	0.24 ± 0.03	-	-	-	-

Table 5.3. *(Continued)*

ID	RA	DEC	SN	Freq (GHz)	Peak Flux ($\mathrm{mJy\,beam^{-1}}$)	FWHM ($\mathrm{kms^{-1}}$)	I_{CO} ($\mathrm{Jy\,kms^{-1}}$)	$f_{3.6}$ (μJy)	$P_{3.6}$	$f_{4.5}$ (μJy)	$P_{4.5}$
BS_28	348.789	-30.611	4.5	101.399 ± 0.029	0.48 ± 0.16	515 ± 200	0.27 ± 0.03	-	-	-	-
BS_29	348.780	-30.622	7.5	103.271 ± 0.012	1.04 ± 0.22	331 ± 79	0.37 ± 0.02	-	-	-	-
BS_30	348.829	-30.597	4.0	94.482 ± 0.034	0.76 ± 0.3	556 ± 253	0.45 ± 0.08	-	-	-	-
BS_31	348.830	-30.585	4.0	106.955 ± 0.031	0.69 ± 0.26	487 ± 208	0.36 ± 0.06	-	-	-	-
BS_32	348.799	-30.614	4.0	92.563 ± 0.036	0.7 ± 0.24	711 ± 276	0.53 ± 0.07	-	0.14	35.7 ± 3.6	0.09
BS_33	348.787	-30.612	5.3	92.634 ± 0.025	1.04 ± 0.25	696 ± 191	0.77 ± 0.05	-	-	-	-
BS_34	348.796	-30.612	4.9	105.833 ± 0.032	0.79 ± 0.21	684 ± 213	0.57 ± 0.05	-	-	-	-
BS_35	348.792	-30.626	4.0	93.875 ± 0.03	0.81 ± 0.24	661 ± 225	0.57 ± 0.06	9.9 ± 1.0	0.04	15.6 ± 2.6	0.09
BS_36	348.764	-30.647	4.8	104.918 ± 0.013	1.24 ± 0.41	222 ± 84	0.29 ± 0.04	-	-		
BS_37	348.867	-30.594	5.0	97.495 ± 0.017	0.66 ± 0.22	308 ± 120	0.22 ± 0.03	-	-	-	-
BS_38	348.820	-30.593	4.8	109.789 ± 0.017	0.86 ± 0.26	317 ± 110	0.29 ± 0.03	-	-	-	-
BS_39	348.819	-30.608	4.0	97.388 ± 0.0050	1.26 ± 0.37	104 ± 34	0.14 ± 0.01	-	-	-	-
BS_40	348.792	-30.615	4.6	97.836 ± 0.019	0.6 ± 0.19	376 ± 136	0.24 ± 0.03	-	-	-	-
BS_41	348.786	-30.625	4.8	108.885 ± 0.029	0.67 ± 0.22	489 ± 187	0.35 ± 0.04	-	-	-	-
BS_42	348.779	-30.631	8.2	96.232 ± 0.014	0.79 ± 0.2	348 ± 102	0.29 ± 0.02	-	-	-	-
BS_43	348.787	-30.626	4.2	107.623 ± 0.036	0.49 ± 0.14	705 ± 235	0.37 ± 0.04	-	-	-	-
BS_44	348.764	-30.649	4.6	98.104 ± 0.025	0.44 ± 0.14	485 ± 178	0.23 ± 0.03	-	-	-	-
BS_45	348.799	-30.617	5.2	97.663 ± 0.026	0.57 ± 0.18	501 ± 184	0.3 ± 0.04	-	-	-	-
BS_46	348.765	-30.651	8.6	102.012 ± 0.014	0.6 ± 0.17	286 ± 94	0.18 ± 0.02	-	-	-	-
BS_47	348.796	-30.613	9.6	92.95 ± 0.014	1.25 ± 0.32	374 ± 108	0.5 ± 0.04	-	-	-	-
BS_48	348.795	-30.612	5.8	105.047 ± 0.027	0.93 ± 0.24	627 ± 184	0.62 ± 0.05	-	-	-	-
BS_49	348.797	-30.612	6.4	106.429 ± 0.021	1.03 ± 0.3	410 ± 138	0.45 ± 0.04	12.7 ± 1.3	0.06	18.7 ± 2.9	0.01
BS_50	348.792	-30.611	8.8	109.752 ± 0.032	0.6 ± 0.19	573 ± 204	0.37 ± 0.04	156 ± 15	0.07	217 ± 21	0.09
BS_51	348.791	-30.612	6.2	109.171 ± 0.012	0.98 ± 0.3	217 ± 77	0.23 ± 0.03	-	-	-	-

The SN is the S/N from the matched filter spectrum, and the frequency corresponds to where the peak flux is. I_{CO} is the integrated line flux. $f_{3.6}$ and $f_{4.5}$ are the fluxes at 3.6 and 4.5 μm respectively. $P_{3.6}$ and $P_{4.5}$ are the probability of the ALMA source and IRAC source not being associated.

5.4 Assigning Redshift

The next step is to identify the redshift of this potential proto-cluster. To do this CO transitional lines need to be identified, and from this a redshift can be estimated. The most secure way of determining both the redshift of the system (and the transition line) is to look for any other potential lines within the same spectrum. Since any strong detection would have already been detected, any other lines must be less then $4\,\sigma$.

To search for additional, weaker lines in each of the line candidates spectrum, I assume the line detected is a certain CO transition e.g. CO(1-0). I estimate what the redshift would be and calculate where all the other spectral lines would be at that redshift. If the line falls within the band-width, I look at the spectral position and see if there is detection (using the matched filter technique described previously). I lower the detection threshold to $2\,\sigma$ to give me the best chance of detecting a line.

Doing this I found that 4/6 continuum sources had a secondary line, and 11/51 of the blind search sources had an additional line. The transition of both lines, and resulting redshifts can be found in Table 5.4.

For the remaining 42 sources I have to estimate what spectral line is being detected. To check if the object is low redshift ($z < 2$), and therefore any of the low transition lines (CO(1-0) and CO(2-1), CO(3-2)), I look the to ancillary data available. This proto-cluster is part of the South Galactic Pole (SGP) and therefore has several shallow optical and NIR studies, such as the VISTA Kilo-Degree Infrared Galaxy Survey (VIKING, Edge et al. 2013), and Pan-STARRS (for a full list of overlapping surveys see Smith et al. 2017). Looking in the HELP database, I found no matches between the low redshift data, and the line candidates. This means there is a high chance these sources are high redshift, and therefore highly unlikely to be any of the low transitions.

The higher CO transitions (CO(5-4), CO(6-5), CO(7-6)) can also be eliminated as potentially being the detected line. Figure 5.2 shows that at redshifts greater than $\sim$4, if the line was CO(5-4) then I would detect either the CO(4-3) or the CO(6-5) (with there being only a very small redshift range where this CO(5-4) the only line). Also the CO(5-4), CO(4-3) and CO(6-5) all have very similar brightness (e.g. Papadopoulos et al. 2012; Daddi et al. 2015), so if you detected one you would detect one of the others. If the detection was either the CO(6-5) or CO(7-6) line then again you would detect other CO transitions, CI and H_2O lines. Since I only detect one line for each spectra I can eliminate these lines.

I can also eliminate the CI lines as being responsible for the line. If the line

was CI(1-0), then the CO(4-3) line would be detected, and it would be a significantly stronger detection then the CI(1-0) line. This is because the CI(1-0) line only tends to be ∼25% the brightness of the CO(4-3) line (e.g. Walter et al. 2011; Valentino et al. 2018). The line is also highly unlikely to be the CI(2-1) line since again, you would expect to see the CO(7-6) line, and again it would be significantly brighter then the CI(2-1) line.

For the 42 lines with one detection, I make the assumption that it is CO(4-3) based on the arguments above. Whilst you would expect to see the CI(1-0), since the brightness of it is less then the CO(4-3) line, it is not surprising if there is no CI(1-0) detection. The redshifts derived from this assumption can be seen in Table 5.4.

Table 5.4. The assumed line transitions and redshifts for all the line candidates.

ID	Line 1	Line 2	Redshift	ID	Line 1	Line 2	Redshift
CS_1_A	CO(4-3)	CI(1-0)	3.886	BS_26	CO(4-3)	-	4.159
CS_1_B	CO(4-3)	CI(1-0)	3.312	BS_27	CO(4-3)	-	3.511
CS_2	CO(4-3)	CI(1-0)	3.673	BS_28	CO(4-3)	-	3.545
CS_3	CO(4-3)	-	3.637	BS_29	CO(4-3)	-	3.465
CS_6_A	CO(4-3)	CI(1-0)	3.635	BS_30	CO(4-3)	-	3.879
CS_6_B	CO(4-3)	-	3.655	BS_31	CO(4-3)	-	3.311
BS_1	CO(4-3)	CI(1-0)	3.605	BS_32	CO(4-3)	-	3.98
BS_2	CO(4-3)	-	3.66	BS_33	CO(4-3)	-	3.977
BS_3	CO(4-3)	-	3.66	BS_34	CO(4-3)	-	3.365
BS_4	CO(5-4)	CI(1-0)	4.776	BS_35	CO(4-3)	-	3.912
BS_5	CO(4-3)	-	3.541	BS_36	CO(4-3)	-	3.393
BS_6	CO(4-3)	-	4.151	BS_37	CO(4-3)	-	3.724
BS_7	CO(4-3)	-	3.559	BS_38	CO(5-4)	CO(4-3)	4.247
BS_8	CO(4-3)	-	3.62	BS_39	CO(4-3)	-	3.733
BS_9	CO(4-3)	-	3.622	BS_40	CO(4-3)	-	3.712
BS_10	CO(4-3)	-	4.163	BS_41	CO(4-3)	-	4.292
BS_11	CO(4-3)	CI(1-0)	3.908	BS_42	CO(4-3)	CI(1-0)	3.792
BS_12	CO(4-3)	CI(1-0)	3.889	BS_43	CO(4-3)	-	4.353
BS_13	CO(4-3)	-	4.382	BS_44	CO(4-3)	-	3.7
BS_14	CO(4-3)	-	3.425	BS_45	CO(4-3)	-	3.72
BS_15	CO(3-2)	CO(4-3)	3.05	BS_46	CO(4-3)	-	3.519
BS_16	CO(4-3)	-	4.384	BS_47	CO(4-3)	-	3.959
BS_17	CO(4-3)	-	4.374	BS_48	CO(4-3)	-	3.388
BS_18	CO(4-3)	CI(1-0)	4.294	BS_49	CO(4-3)	CI(1-0)	3.331
BS_19	CO(4-3)	-	4.259	BS_50	CO(4-3)	-	4.259
BS_20	CO(4-3)	-	4.244	BS_51	CO(4-3)	-	4.278
BS_21	CO(4-3)	-	3.638				
BS_22	CO(4-3)	-	3.644				
BS_23	CO(4-3)	CI(1-0)	3.655				
BS_24	CO(4-3)	-	3.661				
BS_25	CO(4-3)	CI(1-0)	3.66				

5.4.1 Redshift of the Proto-Cluster

Now that I have assigned a redshift to each source, I can now determine the redshift of the proto-cluster. Figure 5.6 shows the redshift distribution of all the sources, and there is a clear peak at $z \sim 3.6$. However, due to the non-Gaussianity of the distribution, simply taking the median will not give the correct redshift of the proto-cluster. To estimate the redshift I remove any galaxy that has an absolute velocity difference greater then 2000 kms^{-1}, with respect to the proto-cluster being at redshift 3.6 (Figure 5.7). This removes those galaxies that definitely have no physical or causal relation to the proto-cluster. With those remaining galaxies I take the mean of the redshift and find a redshift of 3.64, which I take as the redshift of the proto-cluster. This redshift makes PLCKERC857 one of the highest redshift proto-clusters discovered, with there being only a handful of systems at higher redshifts (e.g. Daddi et al. 2009; Capak et al. 2011; Walter et al. 2012; Lewis et al. 2018; Miller et al. 2018; Oteo et al. 2018).

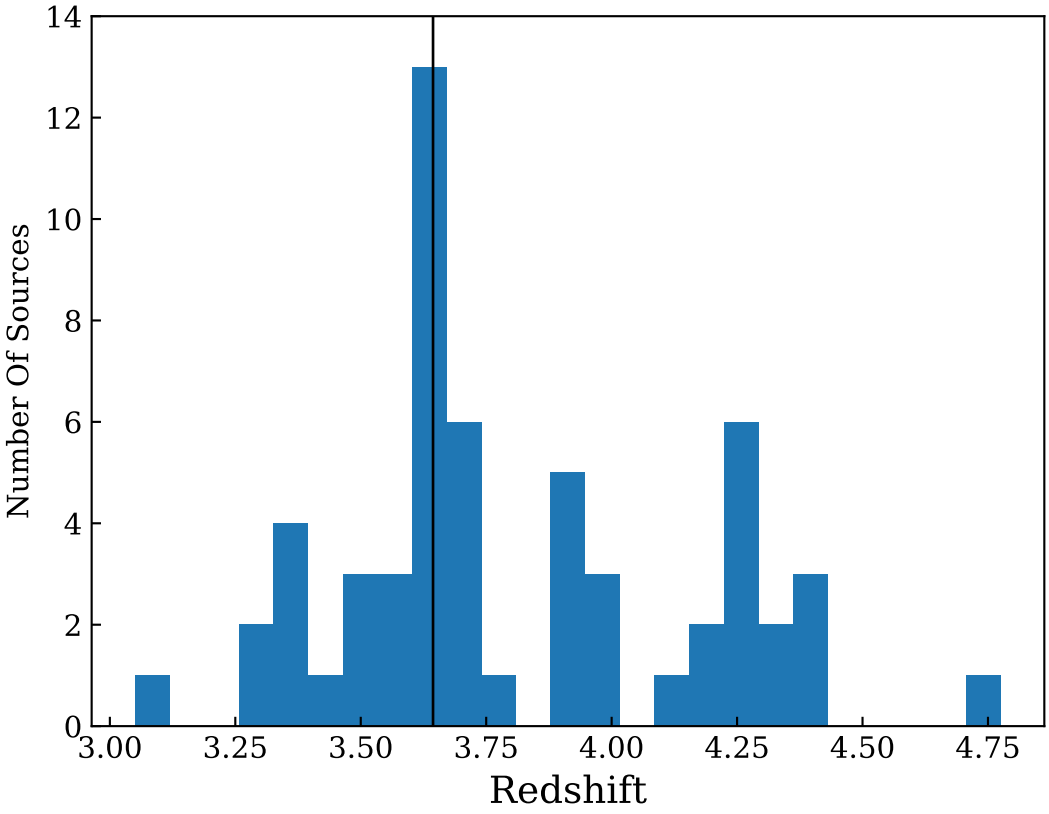

Figure 5.6. The redshift distribution for the sources in PLCKERC857.

With this redshift, I can determine which sources are cluster members, by calculating the velcoity dipsersion for each source. Galaxy clusters tend to have

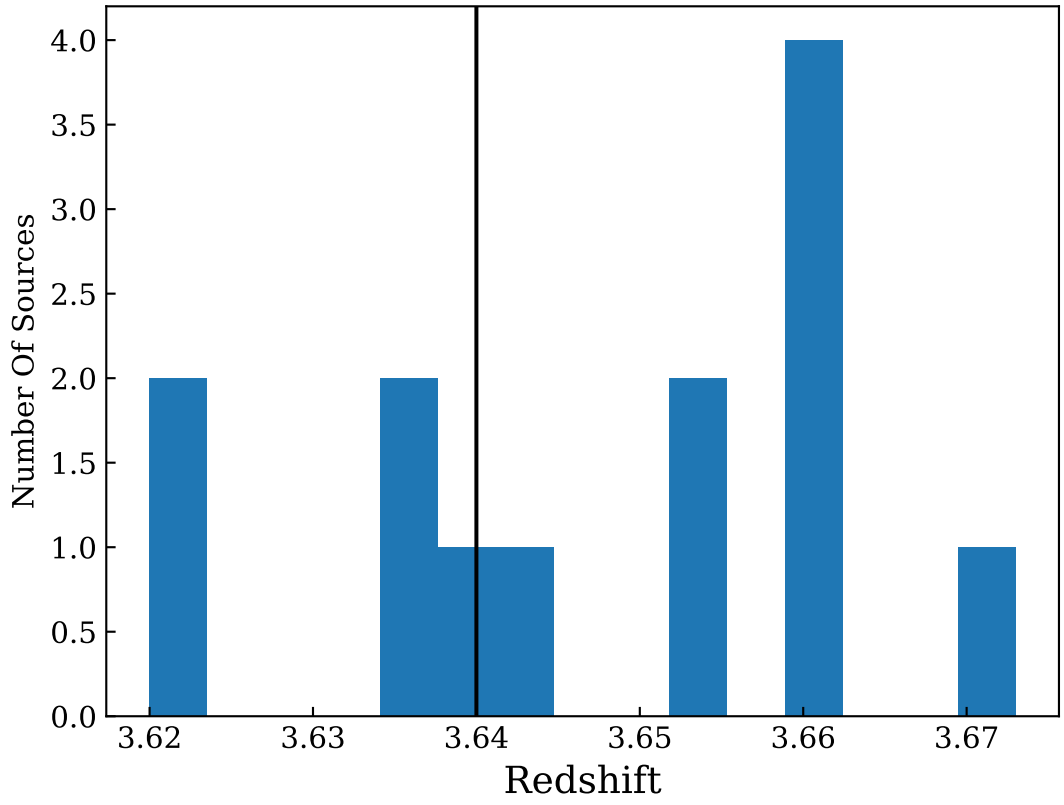

Figure 5.7. A close up of those galaxies with a velocity within 2000 kms^{-1} with respect to the cluster redshift. The three galaxies in the outermost bins are not part of the cluster as they have a velocity dispersion greater then 1000 kms^{-1}.

velocity dispersions on the order of 1000 kms^{-1} (e.g. Girardi et al. 1993; Struble & Rood 1999), so any source that has a velocity within 1000 kms^{-1} is considered a member (based on the redshift of the proto-cluster having a redshift of 3.64).

Applying this cut I find 10 sources that could be within the cluster. These sources can be seen in Figure 5.8 and table 5.5. Whilst I do acknowledge that 1000 kms^{-1} is a very liberal value to use (especially since this cluster is not virialised), studies of high redshift (proto-)clusters have shown values between 500-800 kms^{-1} (e.g. Gobat et al. 2011; Wang et al. 2016; Miller et al. 2018; Oteo et al. 2018).

5.5 PROPERTIES OF PROTO-CLUSTER GALAXIES

5.5.1 CLUSTER MASS

With the velocity distributions calculated in the previous section, the mass of the proto-cluster can be estimated. Using the biweight method (Beers et al. 1990), the velocity dispersion of the proto-cluster is found to be $\sim$570 kms^{-1}. The relation

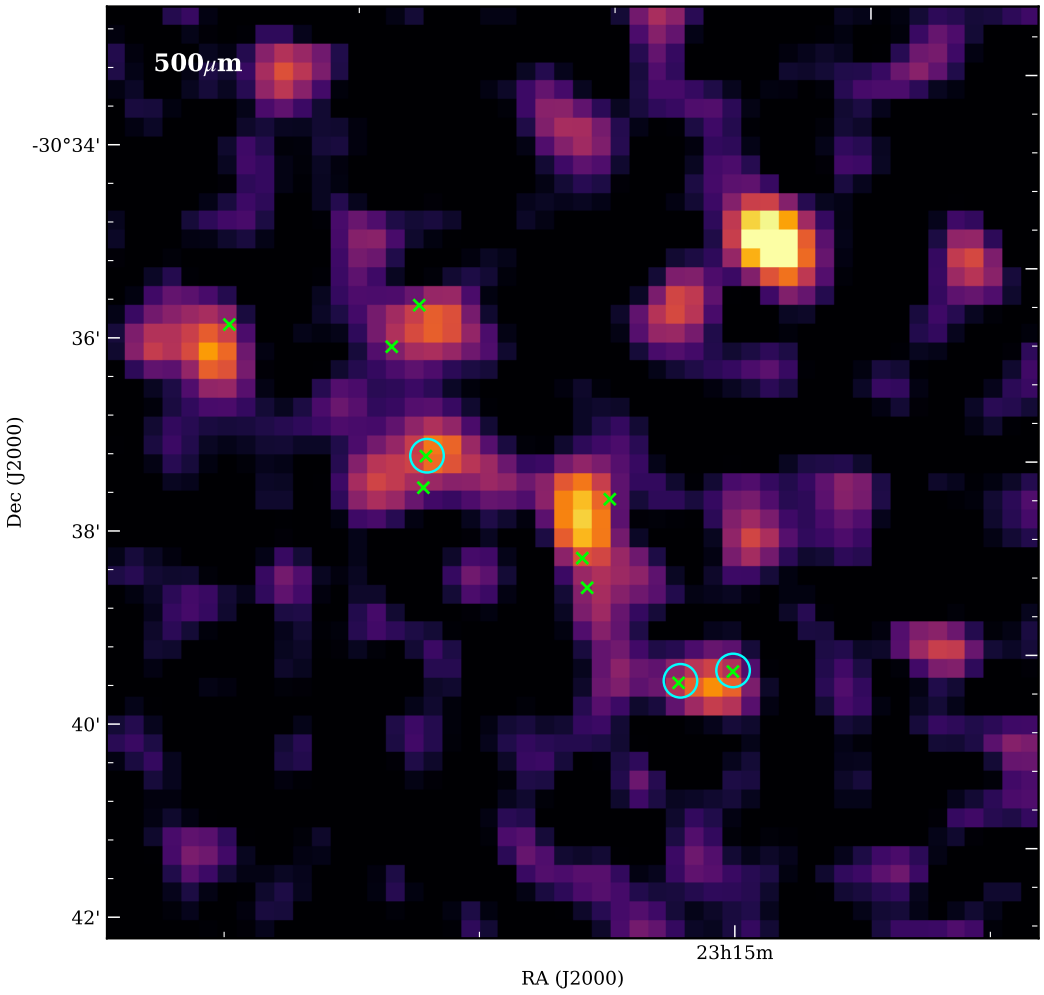

Figure 5.8. Positions of the sources confirmed to be within the proto-cluster. The three sources circled represent continuum sources.

between velocity dispersion and cluster mass from Evrard et al. (2008) is,

$$\sigma_{\rm DM}(M,z) = \sigma_{\rm DM,15}\left(\frac{h(z)M_{total}}{10^{15}M_{\odot}}\right)^{\alpha} \tag{5.1}$$

where $h(z)$ is the dimensionless Hubble constant, $\sigma_{\rm DM,15}$ the normalisation at $10^{15}M_{\odot}$ and α the logarithmic slope. Using this equation, and the the canonical values of $\sigma_{\rm DM,15}$ =1083 kms^{-1} and α =0.336, I derive a total mass of M_{total} $\sim$2.5 $\times$ 10^{13} M$_{\odot}$.

I do note that this value is highly uncertain. This method assumes that the cluster is fully virialised, which will not be the case. Whilst the system might be mostly virialised, this value acts as an upper limit. Another issue is that I have a very biased sample of galaxies. I am only using those that have a spectroscopic detection, and there could be many more galaxies within the proto-cluster that have

simply not been detected, and this could significantly change this result.

Whilst the uncertainties are large, this cluster is very similar in mass to high redshift clusters such as CLJ1449, and CLJ1001 (which are fully vrialised, Gobat et al. 2011, 2013; Wang et al. 2016), and other proto-clusters at similar redshifts, such as the Dusty Red Core (DRC) from Oteo et al. (2018) and SPT2349-56 from Miller et al. (2018).

Using the evolutionary tracks from Chiang et al. (2013), this proto-cluster will most likely become a massive cluster at $z = 0$, with a mass in excess of $10^{15}\,M_{\odot}$. This would mean PLCKERC857 could be a progenitor to a Coma like cluster.

5.5.2 Gas Masses

The first steps into calculating the gas masses is to calculate the CO luminosity. This is done by using the following equation from Solomon et al. (1992),

$$L' = 3.25 \times 10^7 \times S_{line}\Delta v \frac{D_L^2}{(1+z)^3 \nu_{obs}^2} \tag{5.2}$$

where $S_{line}\Delta v$ is the integrated line flux (I_{CO} in Table 5.3), D_L is the luminosity distance, and ν_{obs} is the observed frequency. This will give the CO luminosity for the CO(4-3) line.

To find the total gas mass the CO(4-3) luminosity needs to be converted to the CO(1-0) luminosity, which is done using a line ratio. Whilst Carilli & Walter (2013) find that r_{4-1} can vary between 0.17 for the Milky Way, to 0.87 for quasars, typical star forming galaxies tend to be find a fairly consistent average of r_{4-1} ∼0.31-0.46 (Ivison et al. 2011; Bothwell et al. 2013; Decarli et al. 2016). I use the r_{4-1}=0.31 ± 0.06 from Decarli et al. (2016), as it is appropriate for galaxies on the star forming main sequence (which I assume my galaxies are on). The properties of the lines, and redshifts being probed are very similar to mine, so using this line ratio seems appropriate. The CO(1-0) luminosity can be seen in Table 5.5.

To convert to a gas mass I use the following equation,

$$M_{gas} = \alpha_{CO} L'_{CO(1-0)} \tag{5.3}$$

where α_{CO} is the conversion factor. Several assumptions have to be made when using α_{CO}, such as assuming the CO is optically thick, and also assume a metallicity and mode of star formation. For a full review see Bolatto et al. (2013). Following both Daddi et al. (2010) and Magdis et al. (2017), I assume a α_{CO} of $3.5\,M_{\odot}(\mathrm{Kkms^{-1}pc^2})^{-1}$,

which is appropriate for normal star forming galaxies at solar metallicity. The resulting gas masses can be found in Table 5.5.

5.5.3 Stellar Mass

The simplest way of estimating the stellar mass of a galaxy is to use stellar population models (e.g. Bruzual & Charlot 2003), and connect the stellar mass to an observable such as luminosity in one or more passbands (e.g. SED fitting). The issue with this method is you need a lot of photometric or spectral data covering a large wavelength range, which is not always possible. As mentioned PLCKERC857 is within the SGP, which has very limited and very shallow coverage from other multi-wavelength surveys. This means SED fitting is impossible for the proto-cluster galaxies, meaning a different approach is needed to estimate the stellar mass.

New approaches to estimate stellar masses rely on NIR/MIR wavelengths such as those provided by *Spitzer*. At wavelengths between 3-5 μm, the emission is dominated by the photosphere of old stars, giving us a direct probe of the stellar mass. The effect of dust emission are also minimised at these wavelengths. This means for the proto-cluster galaxies, I can use the *Spitzer* fluxes to estimate the stellar mass.

I can estimate the stellar masses from IRAC using the relations from Zhu et al. (2010),

$$\log_{10} M_* = (-0.79 \pm 0.03) + (1.19 \pm 0.01) \times \log_{10} \nu L_\nu[3.6\,\mu m] \tag{5.4}$$

$$\log_{10} M_* = (-0.25 \pm 0.03) + (1.15 \pm 0.01) \times \log_{10} \nu L_\nu[4.5\,\mu m] \tag{5.5}$$

where L_ν is given by

$$L_\nu = 4\pi D_L^2\, S_{\nu\,Obs}\, K[z]\, (1+z)^{-1} \tag{5.6}$$

where D_L is the luminosity distance, $S_{\nu\,Obs}$ the observed flux density and $K[z]$ is the K-correction. To calculate the K-correction, I take a template of a well studied star forming galaxy and take the ratio of the intrinsic luminosity through a filter transmission profile, for the template in the rest frame, and shifted to the redshift of the proto-cluster (for a full description see Bourne et al. 2011). I use a template of ARP220 from Pope et al. (2006), which is a good analogue for high redshift galaxies due to its high SFR, and hot dust. I calculate a mass for each the 3.6 and 4.5 μm fluxes, and take an average of the two. The results can be seen in Table 5.5.

A further test as to whether or not these masses are correct is to look at the dynamical mass, that can be derived from the CO data. This would give me an indication if our methods are giving accurate answers, or is there an issue with an

Table 5.5. Physical properties for the proto-cluster galaxies.

ID	$L'_{CO(1-0)}$ (10^{10}Kkms^{-1}pc^2)	M$_{gas}$ (10^{10}M$_\odot$)	M$_*$ (10^{10}M$_\odot$)
CS_3	1.12 ± 0.31	3.95 ± 1.09	9.83 ± 1.75
CS_6_A	1.23 ± 0.37	4.32 ± 1.29	8.35 ± 1.54
CS_6_B	1.59 ± 0.33	5.57 ± 1.15	9.66 ± 1.95
BS_2	3.18 ± 0.62	11.14 ± 2.19	20.93 ± 3.16
BS_3	1.9 ± 0.43	6.65 ± 1.52	-
BS_21	1.81 ± 0.44	6.35 ± 1.56	-
BS_22	2.12 ± 0.47	7.44 ± 1.65	10.75 ± 2.19
BS_23	3.3 ± 0.69	11.55 ± 2.42	-
BS_24	2.86 ± 0.59	10.01 ± 2.08	-
BS_25	1.96 ± 0.49	6.87 ± 1.72	8.58 ± 1.77

assumption I have used. Whilst this is beyond the scope of this thesis, it would act as a good motivator for future follow up observations.

5.5.4 DUST PROPERTIES

To help understand the dust properties within the proto-cluster, I use the three sources that have continuum emission. I combine the 3 mm flux measurements with the *Herschel* fluxes to estimate the dust properties. Even though source six has two distinct continuum detections in the ALMA data, for the purpose of estimating the dust properties, I combine the 2 fluxes together and treat it as one object. I fit both the *Herschel* and ALMA fluxes (in the rest-frame) with a Modified Blackbody (MBB) of the form,

$$S = \frac{M_d}{D_L^2}\kappa_0 \left(\frac{\nu}{\nu_0}\right)^\beta B(T)(1+z) \tag{5.7}$$

where M$_D$ is the dust mass, $B(T)$ is the Planck function, D_L the luminosity distance, β is the dust emissivity spectral index, and κ_0 is the dust mass co-efficient at a reference frequency (ν_0). When fitting I assume a value of κ_0=0.051 m^{2}kg^{-1} (at a reference wavelength of 500 μm, Clark et al. 2016) and β=2,which has been shown to be acceptable for U/LIRGs (e.g. Dunne & Eales 2001; Chapin et al. 2011).

To estimate the FIR luminosity, I integrate the SED between 3-1100 μm, and then use the prescription in Kennicutt & Evans (2012) to estimate SFRs. The resulting SEDs can be seen in Figure 5.9, and all the properties can be found in Table 5.6. It should be noted that the fit is poor, with the MBB significantly underestimating the flux at 500 μm (more so with source 3, with there being a $\sim 3\sigma$ deviation). This could be down to the fact I assume all the *Herschel* emission is caused by the ALMA

Table 5.6. Dust properties as a result of the MBB fit, for the two continuum sources.

ID	L_{IR} ($10^{13}L_\odot$)	M_d ($10^9 M_\odot$)	T_d (K)	SFR ($M_\odot yr^{-1}$)	M_{gas}^{CO} ($10^{10}M_\odot$)	M_{gas}^{RJ} ($10^{10}M_\odot$)
CS_3	1.94 ± 0.23	0.75 ± 0.14	48 ± 2	1600 ± 350	3.95 ± 1.09	8.16 ± 1.35
CS_6	1.37 ± 0.22	1.58 ± 0.16	43 ± 2	2000 ± 300	9.90 ± 1.74	16.24 ± 1.46

continuum sources. There could be several continuum sources at 3 mm, yet they simply fall below the detection threshold. This means that the *Herschel* source could be made of multiple sources, and explain the discrepancy between the measured fluxes and the MBB.

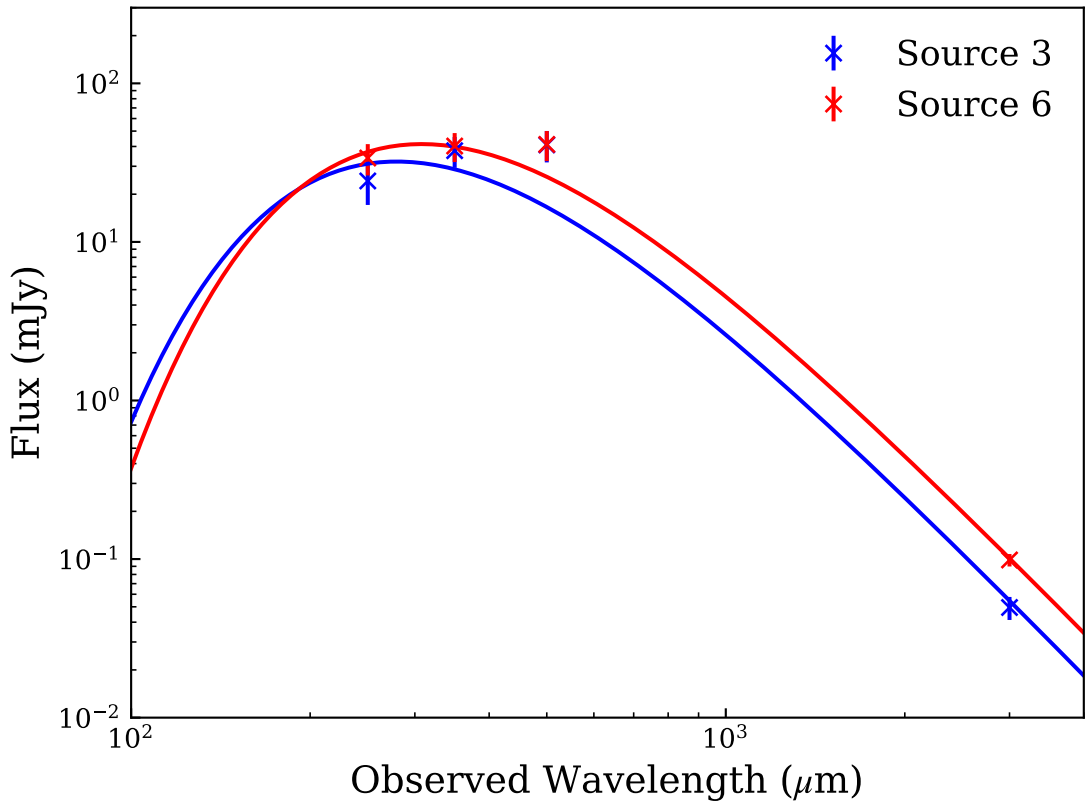

Figure 5.9. The MBBs for the two continuum sources. Note that the 500μm point is the same for both sources (see Table 5.1)

5.6 Discussion

5.6.1 Gas fractions

Since molecular gas is the fuel for star formation, the amount of gas in a galaxy can give us an idea how the galaxy is evolving. A good way of seeing if the amount

of gas is significant or not is to look at the gas fraction ($f_{gas} = M_{gas}/(M_{gas} + M_*)$) and essentially see how much fuel is left for star formation.

In figure 5.10, I plot the gas fraction as a function of stellar mass (with the exception of the four galaxies that do not have IRAC fluxes). It can be seen that all the galaxies have moderate gas fractions, with a median of ∼35%.

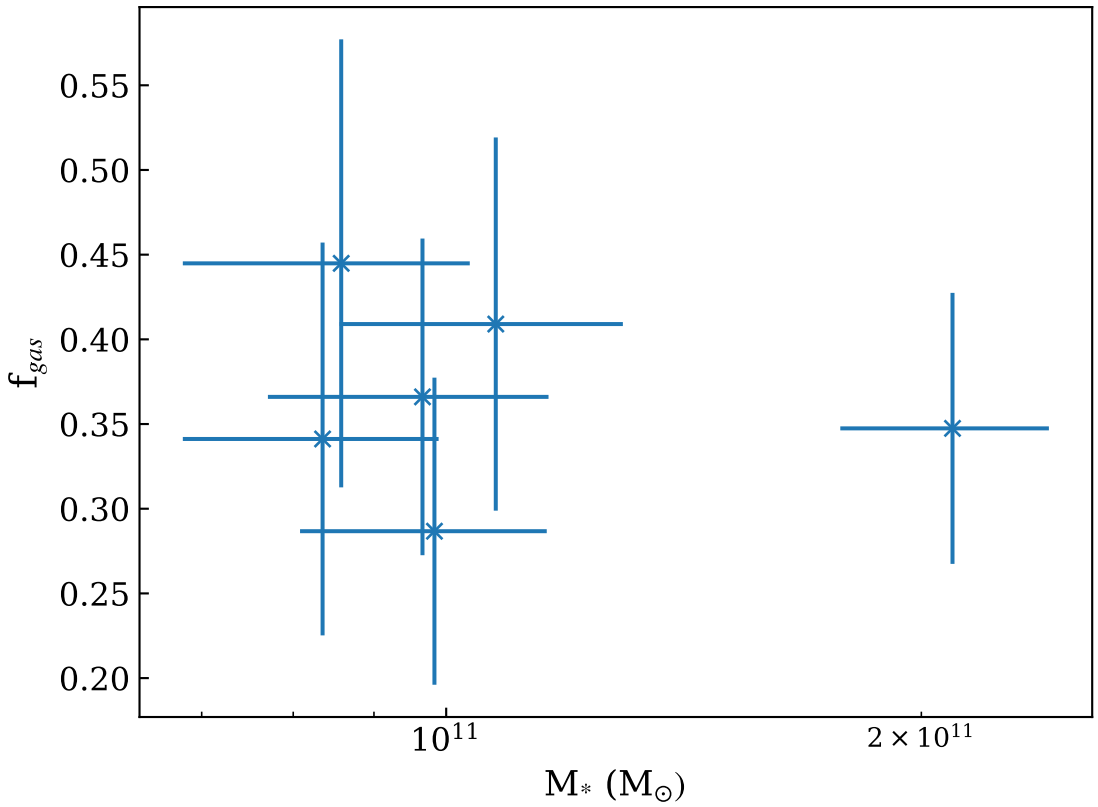

Figure 5.10. Gas fraction as a function of stellar mass for all the proto-cluster galaxies.

Based on scaling relations at stellar masses similar to those of my sample, the expected gas fraction is ∼50-60% (e.g. Genzel et al. 2015; Scoville et al. 2017; Tacconi et al. 2018). This means my galaxies have less gas then expected at these redshifts. When compared to field galaxies I also find significantly less gas, with field galaxies agreeing with the scaling relations (e.g. Millard et al. 2020).

Low gas fractions have also been observed in several other high redshift galaxies (e.g. Spilker et al. 2016, 2018; Miettinen et al. 2017a). The explanation for these low gas fractions, is that the galaxies are undergoing (or have just finished undergoing) an extreme period of star formation (e.g. Steidel et al. 2005).

Studies have also shown that if these galaxies are still undergoing their starburst phase, they will not be able to maintain their gas reservoirs, and will have depletion times scales >0.5 Gyr (e.g. Aravena et al. 2019; Liu et al. 2019; Cassata et al. 2020). This means that these galaxies will eventually run out of gas, and will simply passively evolve (e.g. Casey 2016). This could also go to explain how there is already a red sequence in place by redshift two (e.g. Newman et al. 2014; Strazzullo et al. 2016).

When comparing PLCKERC857 to other high redshift (proto-)clusters I find something quiet striking. Comparing to $z < 3$ (proto-)clusters I find that PLCKERC857 has significantly lower gas fractions then these low redshift counterparts. On average the gas fractions match scaling relations, and tends to be anywhere between 40-60% (e.g. Dannerbauer et al. 2017; Hayashi et al. 2018; Wang et al. 2018; Tadaki et al. 2019). A study by Noble et al. (2017) showed that in a redshift 1.6 cluster, the gas fractions were significantly higher then scaling relations. Even in some higher redshift proto-clusters, the gas fractions still follow, or exceed what is expected from scaling relations (e.g. Riechers et al. 2010; Tan et al. 2014; Pavesi et al. 2018b).

Zavala et al. (2019) found similar gas fractions to this study, in two proto-clusters at redshift ~ 2.3. Since their values lie below scaling relations, and field values they suggested that quenching could be occurring, and the environment is starting to have an effect. A similar situation could be occurring within PLCKERC857 as well. This means these type of systems are ideal to study quenching mechanisms, especially the effects of environmental quenching.

There are a few possible environmental processes that can be causing the quenching of these galaxies, and some process is causing the consumption or removal of the gas. The first could be starvation. Any cold supplies of gas to these galaxies are being shut off, so the galaxies are not being replenished. Without a fresh supply of gas, the currently supply gets used up and a galaxy becomes quenched.

Another explanation could be AGN feedback (e.g. Kauffmann et al. 2004; Fabian 2012). If there is a AGN within the galaxy then AGN outflows could cause the low density gas to be driven out (e.g. Gabor & Bournaud 2014). This would explain the low gas fractions.

An interesting comparison to make is to the DRC from Oteo et al. (2018). In the DRC, all the galaxies (which are far closer together then my sample) are extremely star forming. It was suggested that there could be an environmental effect that triggered the extreme star formation in all the galaxies, but the exact nature of what this effect could be is still unknown. Since PLCKERC857 could be exhibiting the same behaviour, it could be a similar environmental effect at work here. To

confirm this more detailed follow-up observations are needed.

If the environment is having a significant effect at this early stage, since the proto-cluster has not yet viriliased, it could show that galaxy pre-processing (e.g.Fujita 2004; Mihos 2004; Cortese et al. 2006) is an important mechanism related to environmental quenching. However due to the limited data, environmental effects cannot be observed.

It should be noted that there are several issues with the stellar mass estimator used here. The first is that the relation used to estimate stellar mass has been calibrated for low redshift objects. This could mean that applying these relations to high redshift objects could cause an over-estimation of the stellar mass. There is also the fact that I may have a biased sample. Since the relation relies on the brightness of sources, the fact that I am only detecting the brightest sources means I will only detect the most massive sources. This motivates the need for deeper imaging to try and detect the lighter members of this proto-cluster.

5.6.2 CONTINUUM SOURCES

A good indication to understand what star formation mode the galaxies are currently experiencing, is to compare certain properties (such as M_*, M_{gas}, and SFR), and observe what star formation phases these galaxies are undergoing.

In Figure 5.11, I plot the SFR-M_* for the two continuum sources, and several literature values. It can be immediately seen that these galaxies are above the main sequence, and are very similar to SMGs. This backs up previous claims that these galaxies are currently undergoing a period of extreme star formation, which has built up their stellar mass.

In Figure 5.12 I plot the SFR against the gas mass for both the continuum sources, and several literature values. When I compare their positions to that of other galaxies, I see that again these galaxies are undergoing a burst of star formation, and closely resemble SMGs.

The timescales for this star-bursting phase can be constrained via the gas depletion time scale $\tau_{\rm dep}$ (M_{gas}/SFR). The depletion time scales are 24 and 47 Myr for source 3 and 6 respectively. These values are significantly shorter then normal star forming galaxies, which have time scales of ∼0.5-1 Gyr (e.g. Tacconi et al. 2010). These values are consistent with those found in SMGs (e.g. Chapman et al. 2008; Miettinen et al. 2017b), which can have timescales anywhere from ∼10-500 Myr. This could mean that these galaxies will soon come to the end of their extreme star formation, and simply be passively evolving.

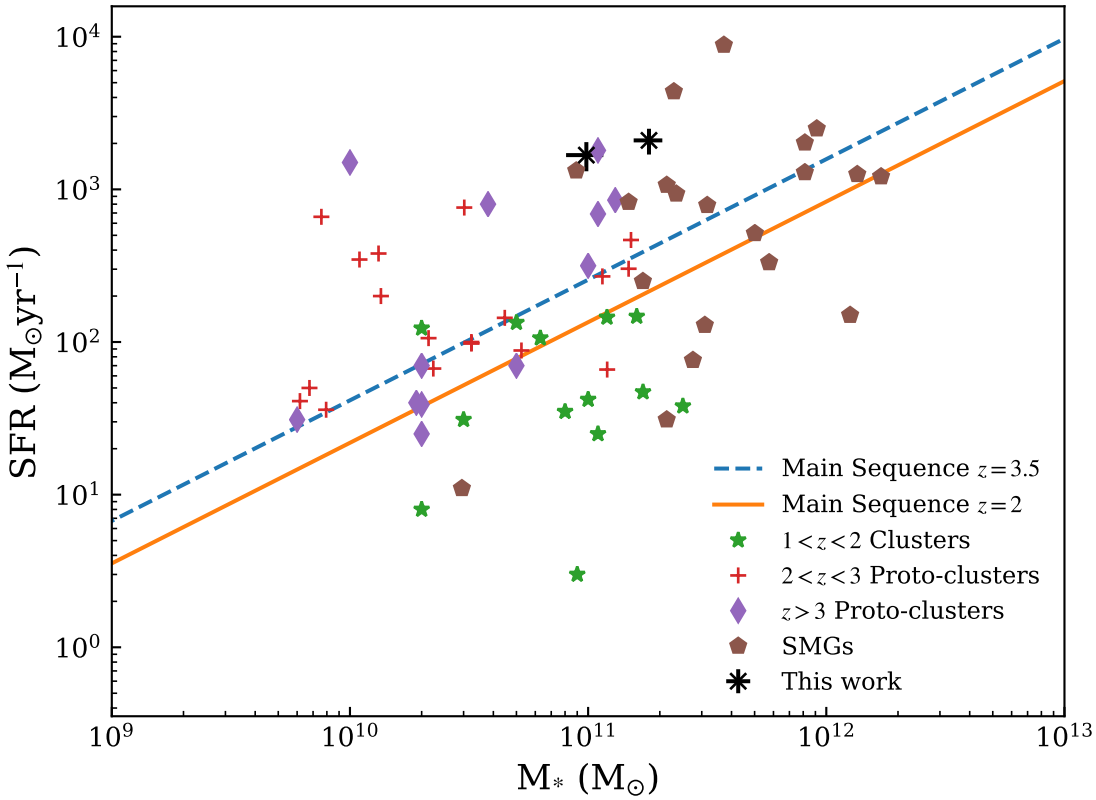

Figure 5.11. The stellar mass-SFR relation for the continuum sources. The positions of the main sequences are estimated from Sargent et al. (2014). The $1 < z < 2$ cluster values come from; Rudnick et al. (2017); Stach et al. (2017) and Hayashi et al. (2018). The $2 < z < 3$ proto-cluster values come from Gómez-Guijarro et al. (2019) and Tadaki et al. (2019). The $z > 3$ values come from; Tan et al. (2014); Lemaux et al. (2018) and Pavesi et al. (2018a). The SMG measurements are from Michałowski et al. (2010).

It should be noted that the SFRs could be overestimated. I made the assumption that the ALMA continuum measurements are responsible for all the *Herschel* emission, which may not be the case. It could be that the *Herschel* sources have several sources associated with them and they are not being detected in my observations. It could be that these galaxies are actually less star forming, and could actually have longer depletion time scales.

An issue with this analysis is the assumption for α_{CO}. I used a value of $3.5\,M_\odot(\mathrm{Kkms^{-1}pc^2})^{-1}$, which is suitable for normal star forming galaxies. However, I have shown that there is a chance some of these galaxies are more star bursting, and are more analogous to SMGs. For SMGs a different value of α_{CO} is needed, with a typical value being 0.8 (e.g. Solomon et al. 1997; Tacconi et al. 2008; Harris et al. 2010).

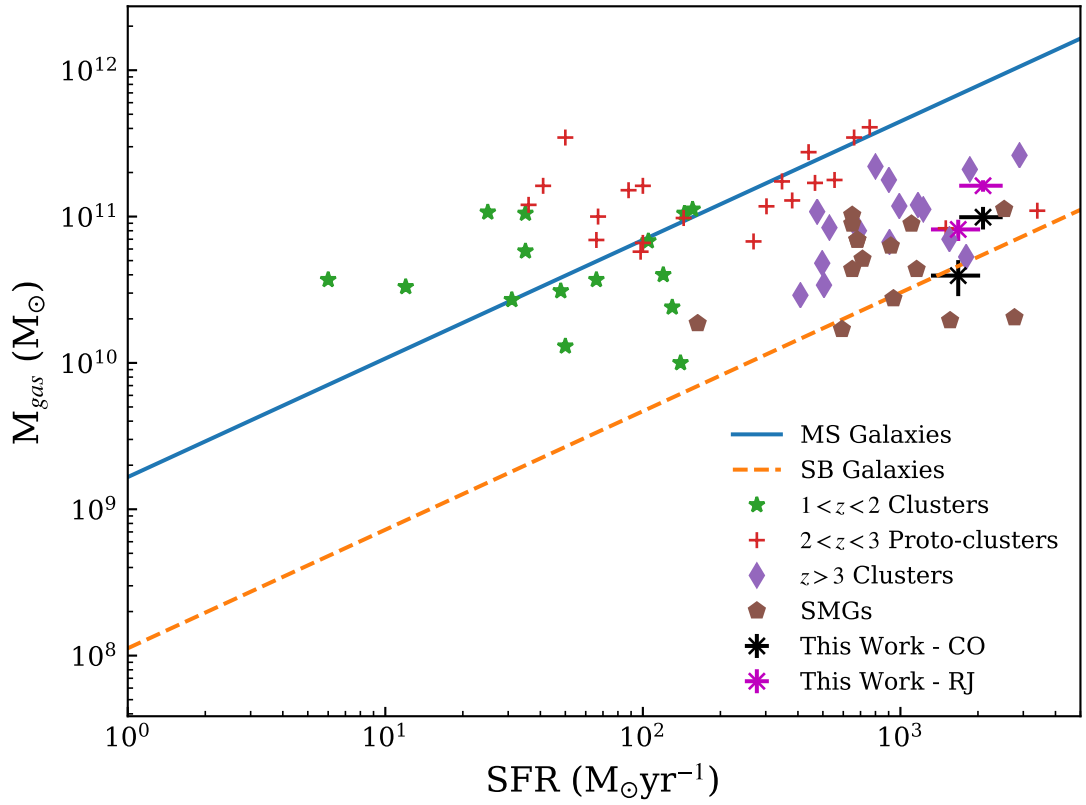

Figure 5.12. Comparing the molecular gas mass for the two continuum sources. The MS and star-burst relations come from Sargent et al. (2014). The $1 < z < 2$ cluster values come from; Rudnick et al. (2017); Stach et al. (2017) and Hayashi et al. (2018). The $2 < z < 3$ proto-cluster values come from Gómez-Guijarro et al. (2019) and Tadaki et al. (2019). The $z > 3$ data comes from Daddi et al. (2009), Riechers et al. (2010), Walter et al. (2012), Miller et al. (2018) and Pavesi et al. (2018a). The SMG data is from Bothwell et al. (2013).

As a test I use the dust continuum to estimate a gas mass. It has been shown by Eales et al. (2012) and Scoville et al. (2014, 2016) that the dust emission can be estimated by FIR wavelengths alone. As detailed by Scoville et al. (2016, 2017), there is a direct relation between the CO(1-0) luminosity and the 850 μm luminosity. By making use of standard CO(1-0) conversion factors Scoville et al. 2016 showed that the RJ emission from dust can be used to calculate gas masses using,

$$M_{\rm gas} = 1.78\, S_{\nu \rm obs}\, (1+z)^{-4.8} \left(\frac{\nu_{850}}{\nu_{obs}}\right)^{3.8} D_L^2 \left(\frac{6.7 \times 10^{19}}{\alpha_{850}}\right) \frac{\Gamma_0}{\Gamma_{RJ}} \qquad (5.8)$$

where $S_{\nu \rm obs}$ is the flux density of the source at the observation frequency (ν_{obs}), D_L^2, the luminosity distance and α_{850} is the conversion factor from 850 μm luminosity to gas mass. The factor of Γ_0/Γ_{RJ} accounts for the deviation of the Planck function in

the rest frame from the RJ form,

$$\Gamma_{RJ}(\nu_{obs}, T_d, z) = \frac{h\,\nu_{obs}\,(1+z)/kT_d}{\exp(h\nu_{obs}(1+z)/kT_d) - 1} \tag{5.9}$$

where T_d is the mass weighted dust temperature. Using the same values in Scoville et al. (2016) I assume T_d=25K, $\Gamma_0 = 0.7$ and α_{850}=$6.7 \times 10^{19}\,\mathrm{ergs^{-1}Hz^{-1}M_{\odot}^{-1}}$. For more details on the calibration details I refer you to Scoville et al. 2016. For $S_{\nu\mathrm{obs}}$ I use the 3 mm fluxes. Whilst the dust temperature assumed is less then those results from the MBB fitting, it has been shown warm dust radiates better then cold dust (e.g. Eales et al. 1989; Scoville et al. 2017).

The results from this gas mass estimation can be found in Table 5.6, with there being a factor of two difference between the mass estimates. To account for this α_{CO} would have to be increased significantly, which would not be representative of the potential star-burst nature of these galaxies.

One issue is that for the method from Scoville et al. (2016) to work, you have to make the assumption you are on the RJ tail. In the rest-frame the 3 mm emission will be $\sim$600 μm which is only just on the RJ tail. This could be a cause for the discrepancy. Also there is a chance that these galaxies could be hosting AGN. If that was the case then it would contribute to the FIR SED, and cause an increase in the dust based gas mass estimate.

Whilst I do not know the cause for the difference in gas masses, the nature of these galaxies do not change. Figure 5.12 still shows that the galaxies will be in the star burst region of the M_{gas}-SFR plane, and still have gas fractions comparable to scaling relations. Whilst there is a slight increase in τ_{dep}, it is still less then 80 Myr.

5.7 Conclusions

In this chapter I have presented ALMA data to confirm that an over-density of *Herschel* 500 μm risers is indeed a proto-cluster.

- I searched the ALMA SPWs using a matched filter technique, and identified 57 potential line candidates. I also found eight continuum sources within the data, six of which had a line candidate associated with them.

- Of these 57 lines, 14 had an additional line associated with them, which allowed me to assign a redshift immediately. For the remaining lines, I used the lack of a secondary line to estimate the CO transition being detected, and hence estimate a redshift.

- Looking at the redshift distribution, a clear over-density of sources was detected at a redshift of 3.64. This make PLCKERC857 one of the highest redshift proto-clusters detected.

- Using velocity dispersions I found that 10 sources belong to the proto-cluster. From these velocity dispersions I estimated the mass to be $\sim 2.5 \times 10^{13}\,M_{\odot}$. This means that PLCKERC857 could be the progenitor to a Coma like cluster.

- Based on gas and stellar mass estimates, I find low gas fractions in the proto-cluster galaxies. This could mean that these galaxies are undergoing (or have undergone) a large burst of star formation, and have already used up their gas reservoirs.

- When comparing the gas fractions to field values, I again see that the proto-cluster galaxies have less gas then those field galaxies. This could show the possibility of environmental effects already at play, and causing quenching within the galaxies.

- Looking at the continuum sources within the proto-cluster, again their is strong evidence that they are under-going a period of extreme star formation. However based on the gas masses within this extreme star formation can only be maintained for $\sim 50\,\mathrm{Myr}$.

PLCKERC857 makes an ideal proto-cluster for further study. The gas fractions within PLCKERC857 are less then both field values, and other proto-clusters. This could mean PLCKERC857 has been caught at a period of extreme star formation, or it could be a good example of galaxy pre-processing, and show the importance of environmental effects on galaxy evolution. Either way further observations are needed for PLCKERC857 to help get a better understanding of the processes occurring within.

Chapter 6
Conclusion

"The past is written. But we are left to write the future."

Admiral Jean-Luc Picard - *Star Trek: Picard*

6.1 Thesis Overview

In this thesis I have used FIR and sub-mm imaging to investigate the properties of galaxies within high redshift galaxy clusters. I optimised the SCUBA-2 data reduction pipeline, and combined this data with archival *Herschel* data. With this I was able to investigate the star forming properties for the galaxies that reside in the high redshift clusters CLJ1449 and JKCS041. I also used ALMA data of a overdense region of red *Herschel* sources. Doing a blind search of the data, I found a proto-cluster at a redshift of 3.6.

6.2 Key Results

In Chapter 3, I used new SCUBA-2 data with archival data to investigate the star forming properties within CLJ1449, a cluster at redshift two.

- I find that in CLJ1449 there is a large population of star forming galaxies. There is a reversal in the SFR-density relation within this cluster. Within the central 0.5 kpc region, there is five orders of magnitude difference in the star formation density when compared to the field. Even in the 3 Mpc region, there is still a difference of two orders of magnitude between the cluster and the field.

- When looking at the M_*-SFR relation I see that most of the galaxies within CLJ1449 either lie on the main sequence, or are exhibiting star-burst behaviour. Those galaxies that lie closest to the cluster core have the lowest stellar masses, which could show that cluster environment is already causing quenching within these galaxies.

- When looking at the mass normalised SFR, I find that CLJ1449 seems to follow relations observed in other high redshift clusters. Whilst there is some scatter at high redshift, this could be down to cluster mass, or some other factor that is as yet unknown.

In Chapter 4, I investigated the star forming properties in the redshift 1.8 cluster JKCS041.

- In the very center of the cluster, I found a population of star forming galaxies, and again there is a reversal in the SFR-density relation. However, when accounting for the redshift selection, the difference in the center between the cluster and field galaxies is only two orders of magnitude.

- When looking at the M_*-SFR relation, there is less galaxies on the main sequence, with more galaxies residing below the main sequence where passive galaxies are found. This could indicate that the harsh environment of the cluster is already in the process of quenching these galaxies.

- When looking at the mass normalised SFR, I found that JKCS041 deviates from expected scaling relations. Since JKCS041 is significantly more massive then clusters at similar redshifts, it could be some of the first evidence that cluster mass could be a factor when influencing the galaxies within them.

In Chapter 5, I used ALMA data to search for, and identify the redshift 3.6 cluster PLCKERC857.

- Using a matched filter technique I identified 57 line detections. Assigning redshifts, I found an over-density of sources at redshift 3.64, making this one of the highest redshift proto-clusters discovered. From this 10 of the sources are believed to be within the cluster

- Estimates of the mass of the proto-cluster puts the mass $\sim 2.5 \times 10^{13}\,M_\odot$, making PLCKERC857 the progenitor to a coma like cluster.

- Calculating gas and stellar masses, I estimate the gas fraction for the proto-cluster galaxies to be ∼35%, lower then scaling relations. This could show that these galaxies are undergoing an extreme period of star formation.
- Since the gas fraction values are lower then those seen in field galaxies, it could show that the galaxies are undergoing quenching, and the environment is already having an impact on these galaxies.
- With the three sources that have continuum emission, I find that these galaxies are undergoing extreme star formation, having SFRs in excess of $1000\,M_{\odot}yr^{-1}$. However, this star formation cannot be maintained, and the gas will be used up in less then 50 Myr unless the gas is replenished.

6.3 Future work

6.3.1 Gas In CLJ1449 and JKCS041: How far is the environments influence?

In Chapters 3 and 4 I showed that both CLJ1449 and JKCS041 have populations of highly star forming galaxies. However, there is evidence that the environment could be taking an effect and causing quenching in these galaxies. The best way to understand the environmental effects is to extend the study by Coogan et al. (2018) and study the gas properties for all the sources in the 3 Mpc region probed in both CLJ1449 and JKCS041.

Using ALMA, I will be able to obtain both CO spectra and continuum images for all the galaxies in both JKCS041 and CLJ1449. The continuum maps would prove very useful in helping us see if these large singular sources break up into more components. This data will allow us to observe any populations of galaxies that could have been missed by the radio data. This information can be fed back into XID+ and more accurate flux measurements an be determined. It will also allow for better cross matching with optical and NIR data, which will help with the SED fitting.

With the CO spectra I would be able to accurately assign a redshift to each source. This would let me know whether or not each source belongs to the cluster, which is a source of great error in my analysis. With an accurate source list I should be able to get a more accurate SFR-density relation for these clusters (especially JKCS041). These more accurate results will give a better indication of both the star formation and stellar masses for the cluster galaxies, and hence allow us to see if quenching is actually occurring.

The best way to understand environmental effects is to directly observe the gas within the cluster galaxies. Certain properties such as gas mass, and depletion time scales allow us to directly observe how much fuel is available to form stars, and how long for. Any radial trends, or deviation from what is seen in field galaxies could allow us to see directly that the environment is having an effect on the galaxies within. Coogan et al. (2018) already showed that in CLJ1449, the environment is having an effect on the galaxies within, but how far does this influence extend to, and do certain factors such as cluster mass effect this.

With high resolution ALMA data, the kinematics of the cluster galaxies could start to be probed. A study by Pavesi et al. (2018a) showed that the star formation in a galaxy in a proto-cluster at redshift 5.7 is driven by a merger. With similar observations for CLJ1449 and JKCS041, the kinematics could be probed and I can answer the question as to what is driving the extreme star formation in these galaxies.

A study of the gas properties within JKCS041 would be of great interest, since this has never been studied before. Seeing how the gas is behaving is key especially since JKCS041 shows some of the first evidence that cluster mass is having some impact on the galaxies within them. JKCS041 was also shown to have a small population of galaxies undergoing extreme star formation. So the question that needs to be answered is what is driving this extreme star formation? Is it similar to CLJ1449 and mergers are driving this extreme star formation, or is it some other process. Also what processes are occurring that is causing this quenching in the galaxies?. These questions need to be answered if we want to know the role the environment is having on these galaxies.

6.3.2 PLCKERC857: A TEST FOR NATURE VS NURTURE?

PLCKERC857 has been shown to be a rather interesting proto-cluster. Its mass suggests that it may evolve into a Coma like cluster, and the gas fractions suggest we have a proto-cluster of galaxies under-going extreme star formation. At the same time it could show that the environment is having an effect on these cluster galaxies, since they have less gas then those galaxies found in the field.

To fully understand what is happening, additional ALMA, and deep multi-wavelength observations are needed. Deeper ALMA data could help reveal the low mass population within this cluster (if it exists at all). At the moment my sample is very biased with the most massive galaxies, but with deeper observations the low mass population may be discovered. From this we can get a better estimation of the population as a whole, and truly understand the star formation properties within.

Additional CO lines would allow for the better estimation of the redshift of the proto-cluster galaxies. Due to the lack of any additional lines I make the assumption that the lines are CO(4-3), which might not be the case. With additional line detections, I can confirm the redshifts for all the sources, and confirm that they are indeed cluster galaxies. It could turn out that these galaxies are actually not within the cluster, which while still noteworthy, would not help us understand the processes occurring within proto-clusters.

Additional CO lines would also give better constraints on the gas masses. I assumed a line ratio between CO(4-3) and CO(1-0), based on other similar studies. Doing this I could be under-estimating (or over-estimating) my gas masses. With the additional lines I would be able to use a CO Spectral Line Distribution (CO SLED, Papadopoulos et al. 2012; Daddi et al. 2015) and get an accurate CO(1-0) luminosity, and hence accurate gas masses.

Additional multi-wavelength data would be imperative for any further study. Firstly, to confirm my lines are real I use the *Spitzer* data. If there is both a line detection, and *Spitzer* source, there is a very high chance that the source is real. However, the *Spitzer* data does not cover the whole region, and some sources do not have a *Spitzer* detection. In my analysis I assumed that they are real, but there is a high chance they may not be. Additional data at different wave-lengths will give me confirmation that the lines and sources are real.

The multi-wavelength data will also allow me to do accurate SED fitting. If I can get good continuum measurements of the dust (especially near the peak of the FIR SED) from ALMA and deep optical and NIR measurements (from VLT for example) I will be able to do SED fitting for all these sources. This will give me accurate stellar masses and SFRs, which at the moment are plagued with uncertainties. This will allow me to accurately look at the gas fractions. The SFRs will tell me whether or not all the sources are undergoing extreme star formation, are normal star forming galaxies, or are already passively evolving. This will help me understand if the environmental processes are already in place at these high redshift, or is there something in the galaxy formation that is causing extreme star formation.

6.3.3 The future of (proto-)clusters

The biggest set back so far for studies into high redshift galaxy clusters is the lack of known systems. Currently, above redshift one there is $\sim$50 mature clusters detected (with only another $\sim$50 proto-clusters). In comparison there are well over 4000 systems discovered in the low redshift universe ($z < 0.1$), meaning to draw any

meaningful conclusions, and truly understand the role the environment plays more systems need to be discovered. We also need detailed follow ups for those systems that have already been discovered.

Above redshift 1.5 there has been a handful of systems detected (e.g. Fassbender et al. 2011 Brodwin et al. 2012; Zeimann et al. 2012; Cooke et al. 2016), yet there have been very little follow up on these systems. This means that the star forming properties are still largely unknown, and studying them could help us see the role the environment is playing within these systems. FIR and sub-mm follow ups are most important, since as mentioned in Chapter 1 these wavelengths are most important to study high redshift star formation.

Strazzullo et al. (2019) conducted a study on some of the most massive galaxies discovered between $1.4 < z < 1.7$, and found evidence of quenching in these galaxies. This study is very limited since they only used a handful of photometric bands. It is important to get multi-wavelength data for systems like this, as just like JKCS041 it could show that cluster mass is having an influence on the galaxies within it.

Whilst follow up of known systems is key, discovering more systems is just as important. The most foolproof way of confirming the presence of a cluster is to detect X-ray emission. This works very well for low redshift clusters, but becomes increasingly more difficult at higher redshifts, and very long integration times are needed to make a confident detection via X-rays. Instead methods that rely on the optical properties of clusters is needed.

At all redshifts, all clusters already have a red sequence of early type galaxies (or at least very red galaxies) in place (e.g. Andreon et al. 2014; Cerulo et al. 2016; Strazzullo et al. 2016). Gladders & Yee (2000) developed an algorithm that exploits this fact, and searches for over-densities of red galaxies in optical and NIR images. This means that large optical and NIR maps can be used to search for clusters incredibly easily, and requires a fraction of the time needed when compared to X-ray observations. This method has been used to great effect and has already been used to discover several high redshift clusters (e.g. Mei et al. 2015; Bonaventura et al. 2017; Casasola et al. 2018). Future missions such as Euclid and WFIRST will produce deep NIR maps of the entire sky, from which large numbers of high redshift clusters should be detected.

The Sunyaev-Zel'dovich (SZ) could be an effective method for detecting high redshift clusters. Surveys using the South pole Telescope, and the Atacama cosmology telescope have detected $\sim$750 clusters using the SZ effect (Hasselfield et al. 2013; Bleem et al. 2015). Whilst most of these detections are low redshifts clusters, there have been a handful of clusters detected at redshifts greater then one. The limiting

factor when it comes to SZ studies is the sensitivity of current facilities. For example the south pole telescope is only sensitive to the most massive clusters ($> 5 \times 10^{14}\,M_{\odot}$), and since it is expected that these massive clusters are rare above redshift 1.5 (e.g. Chen et al. 2013), a lot of potential systems simply will not be detected. With the future of new CMB missions, such as the Simons Observatory (Ade et al. 2019) or LiteBIRD (Hazumi et al. 2012), and upgrades to already existing facilities, it is hoped that this mass limit can be lowered. For example the Simons observatory is hoping to detect ∼200-300 clusters at a redshift greater then 1.5, with a minimum mass of $10^{14}\,M_{\odot}$ (Ade et al. 2019). It is is hoped that with other similar facilities hundreds more of these systems can be detected.

A recent study bu Gobat et al. (2019) has used ALMA observations to observe a significant SZ signal in CLJ1449 (Figure 6.1). This observation is one of the lowest mass single SZ detections so far, and shows the potential in the detection high redshift clusters. However, the issue with this method is that prior knowledge of the FIR sources within the cluster is needed. This is because FIR sources can obscure the SZ signal, and their contribution needs to be subtracted. Whilst this method may not be ideal for the direct detection of clusters, when used in conjecture with other detection methods such as red sequence method, it could help confirm potential cluster candidates.

Whilst searching for mature clusters is important, the search for additional proto-clusters is also imperative. It has been shown that looking for the clustering of SMGs in *Herschel* images is a very effective way to directly detect proto-clusters. Whilst the initial search was in the H-ATLAS fields, there are still several *Herschel* fields that can be explored. For example as part of HerMES, several deep fields were observed making them ideal fields to search for proto-clusters. Follow up observations can then be conducted with instruments such as SCUBA-2 or LABOCA on APEX, and help confirm that there is an over-density. Cheng et al. (2019) did SCUBA-2 follow-up on several Planck clumps, and found strong over-densities of SMGs, confirming them to be proto-clusters. Once the proto-cluster has been confirmed, high resolution follow ups can be done and the properties of the galaxies studied.

Whilst the method described in Negrello et al. (2005) is very effective, there are still a few shortfalls that are related to it. The method relies on a combination of low and high resolution instruments, so whilst *Planck* looked at the entire sky, *Herschel* only looked at certain fields. This means that the only regions that can be studied are those that overlap. Future CMB space based missions should be expected to have resolutions greater than that of *Planck*. Not only does this mean that similar catalogues of clumpy sources can be created, but these missions will have a resolution

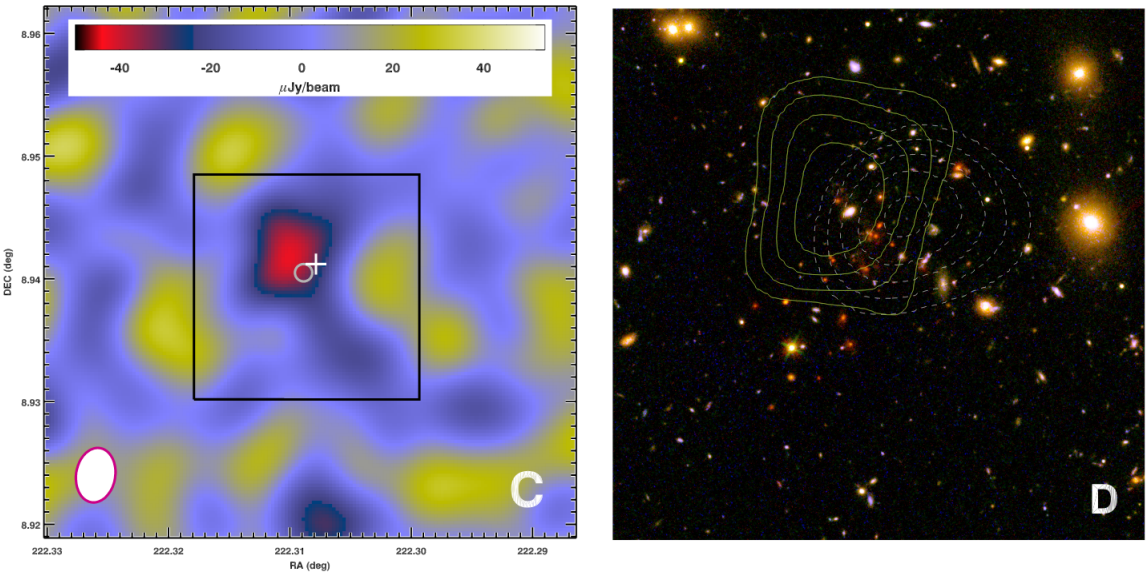

Figure 6.1. Left: ALMA 92 GHz map showing the SZ decrement. The galaxies in the field of view have been modelled and subtracted from this image,in order to uncover the SZ decrement. The cross and the circle represent the center of X-ray emission. Right: HST image of the cluster, overlaid with white dashed Chandra X-ray contours, and solid yellow contours of the SZ decrement. Image credit: Gobat et al. (2019).

capable of starting to resolve the clumps. Also these instruments will be far more sensitive then *Planck*, meaning that more systems can be detected and those clumps that could not be classified by *Planck* can be observed and identified (Greenslade et al. 2018). The next generation of CMB missions will be able to directly detect proto-clusters, without the need to having to match up with FIR instruments.

6.4 Concluding remarks

Studying high redshift galaxy clusters gives us a way of answering the nature vs nurture debate that has plagued studies of galaxy evolution. While the number of studied systems are still too low to draw any meaningful conclusions, in the coming years with the advent of new facilities (and upgrades to current ones), it is hoped that hundreds of these systems should be detected. With these large numbers it will give us the ability once and for all to see if the environment a galaxy lives in shapes its evolution.

Appendix A
Additional material for CLJ1449

A.1 Redshifts For All Non-Cluster Members

Table A.1. Redshifts for the non-cluster members.

ID	RA	DEC	z_{EZ}	z_{CG}
850_1_I	222.309	8.936	$2.48^{+0.72}_{-1.18}$	2.41±1.21
850_2	222.304	8.970	$2.92^{+0.49}_{-0.54}$	3.77±0.74
850_3	222.225	8.897	$2.59^{+0.81}_{-1.06}$	1.44±0.56
850_6	222.284	8.957	$2.57^{+0.33}_{0.34}$	3.95±0.50
850_7	222.281	8.899	$1.27^{+0.29}_{-0.30}$	1.46±0.35
850_10	222.340	8.878	$2.40^{+0.75}_{-0.76}$	3.01±0.64
850_11	222.263	8.901	$3.14^{+0.62}_{-0.61}$	3.70±0.56
850_15	222.380	8.968	$0.94^{+0.46}_{-0.46}$	0.97±0.30
850_21	222.355	8.990	$2.83^{+0.67}_{-0.64}$	3.25±0.58
850_23	222.348	8.937	$0.14^{+0.07}_{-0.09}$	1.27±1.31
850_27	222.295	8.889	$2.59^{+0.43}_{-0.63}$	2.43±0.35
850_29	222.363	8.988	$1.51^{+0.55}_{-0.47}$	1.44±0.24
850_32	222.317	8.902	$1.46^{+0.23}_{-0.22}$	1.50±0.18

A.2 SEDs FOR ALL GALAXIES FROM THE 2 DIFFERENT REDSHIFT METHODS

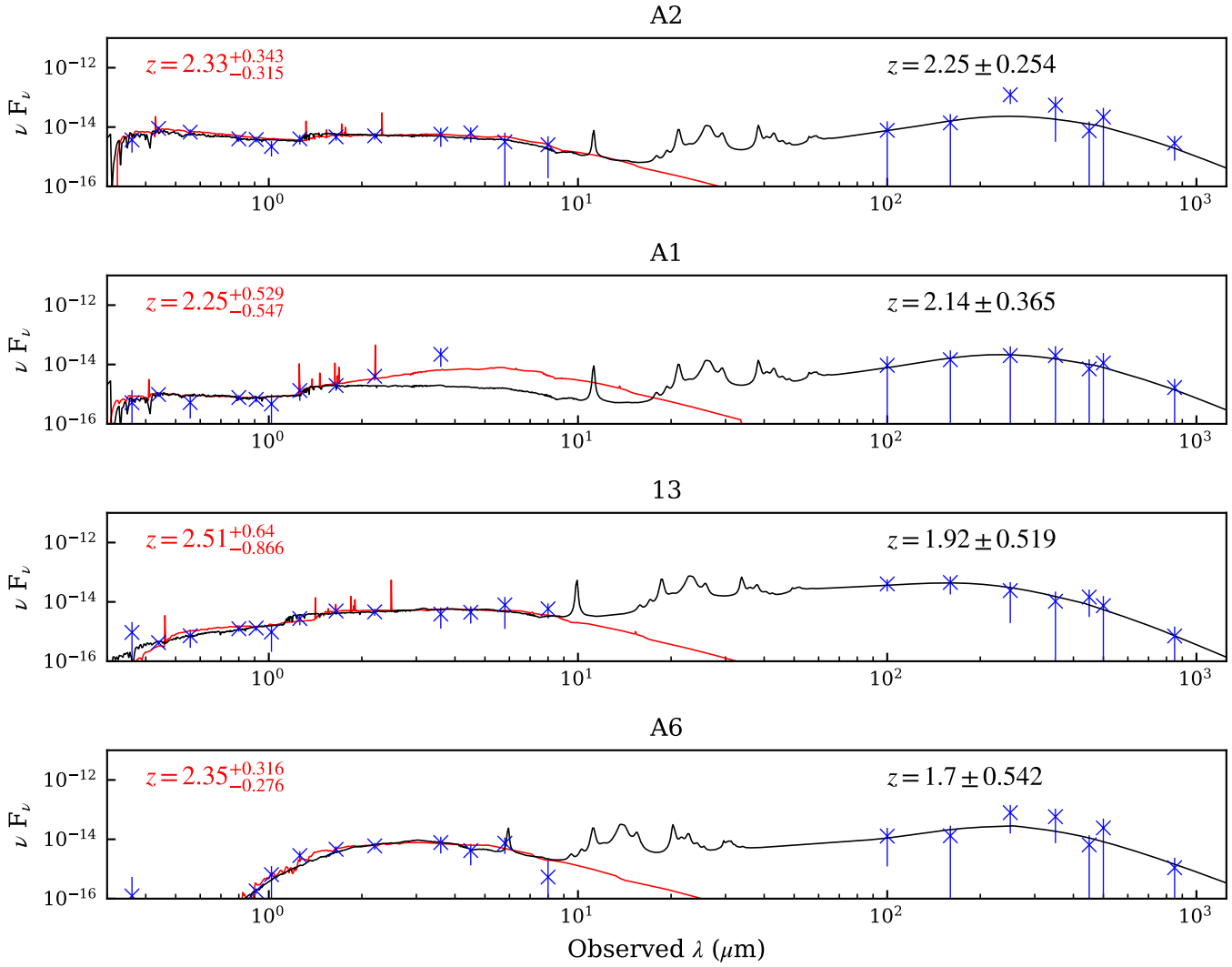

Figure A.1. SEDs from both my redshift fitting methods. The red line shows the fit from EAZY, and the black line shows the fit from CIGALE

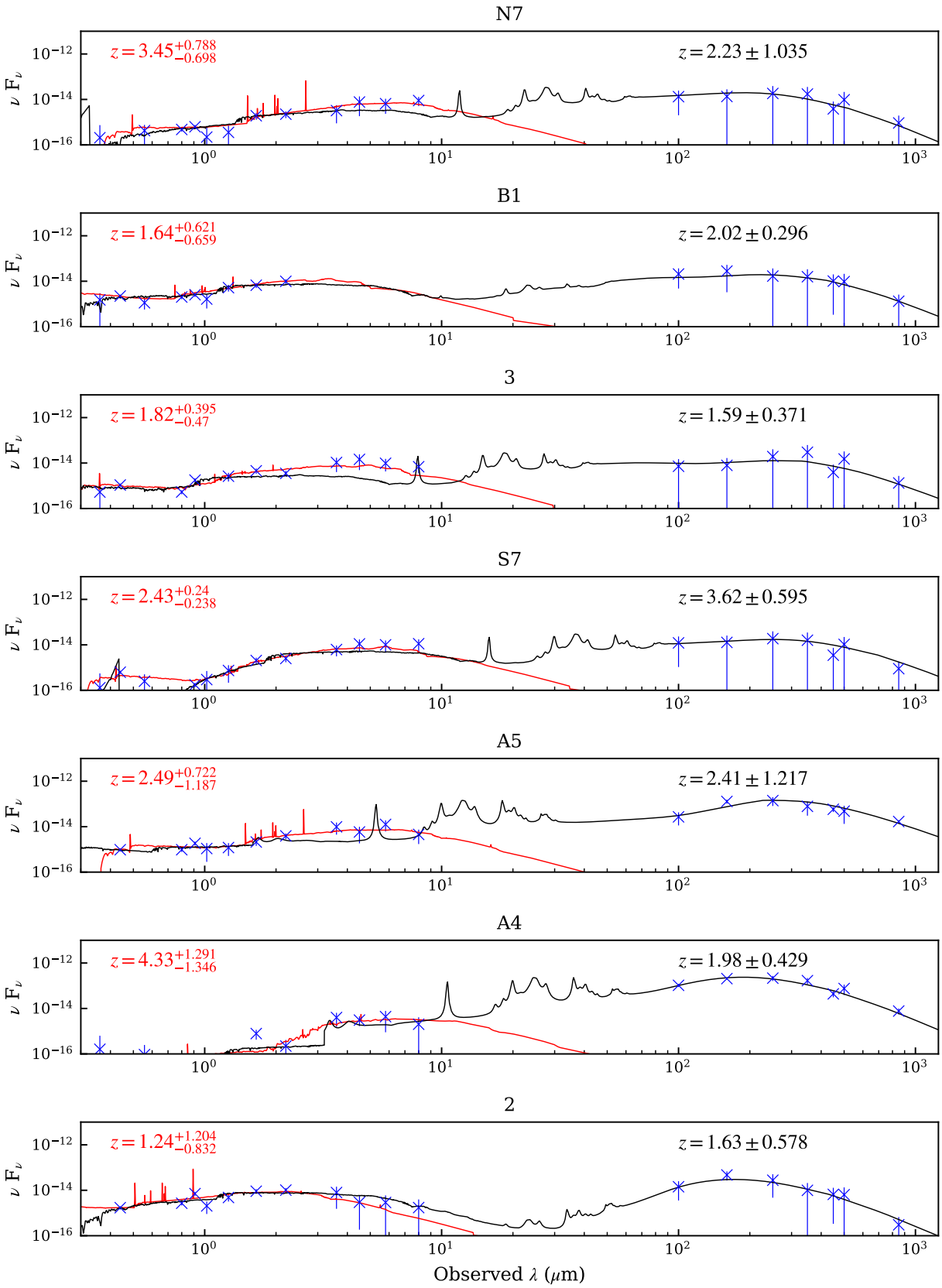

Figure A.1. *(Continued)*

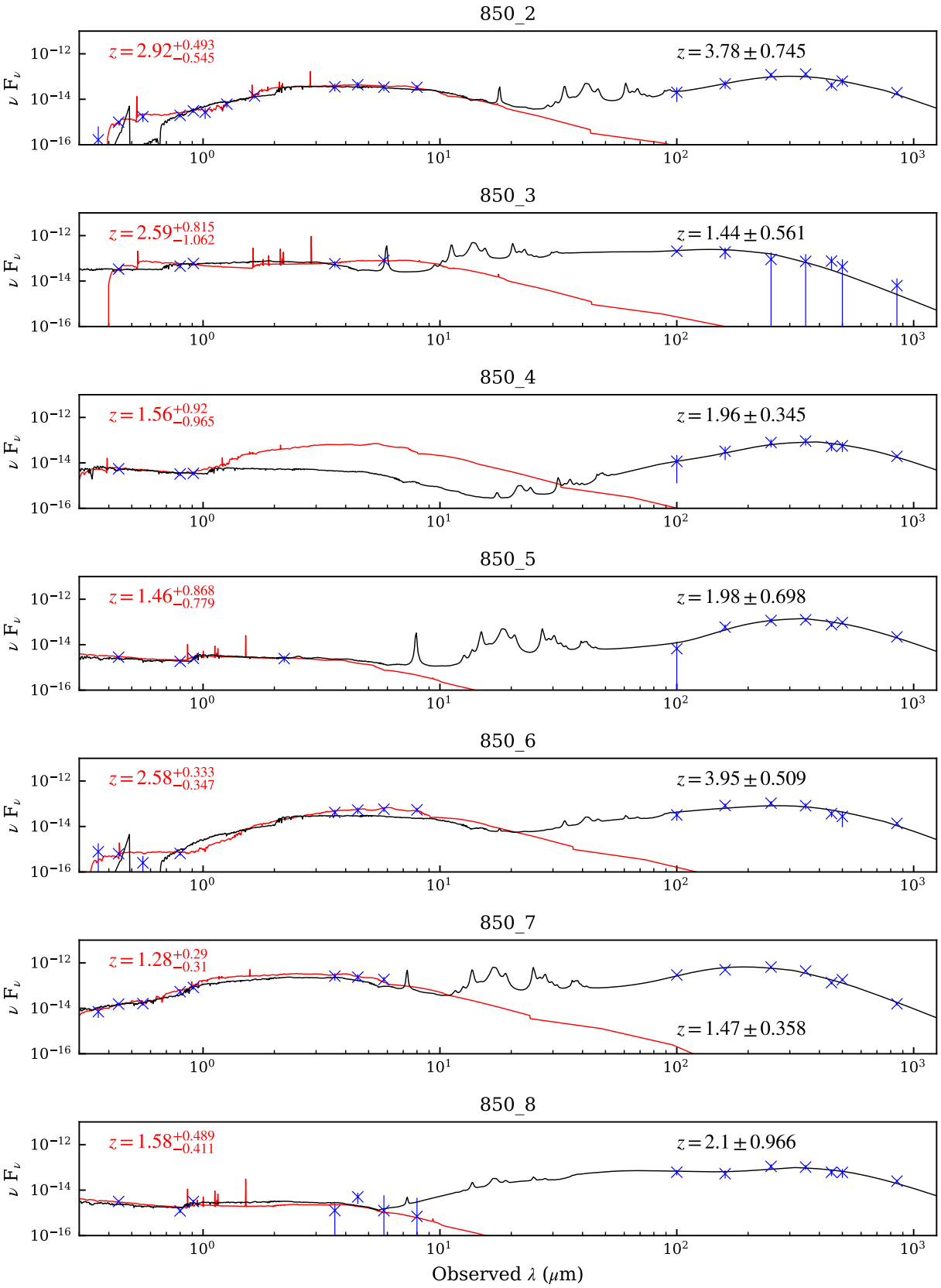

Figure A.1. *(Continued)*

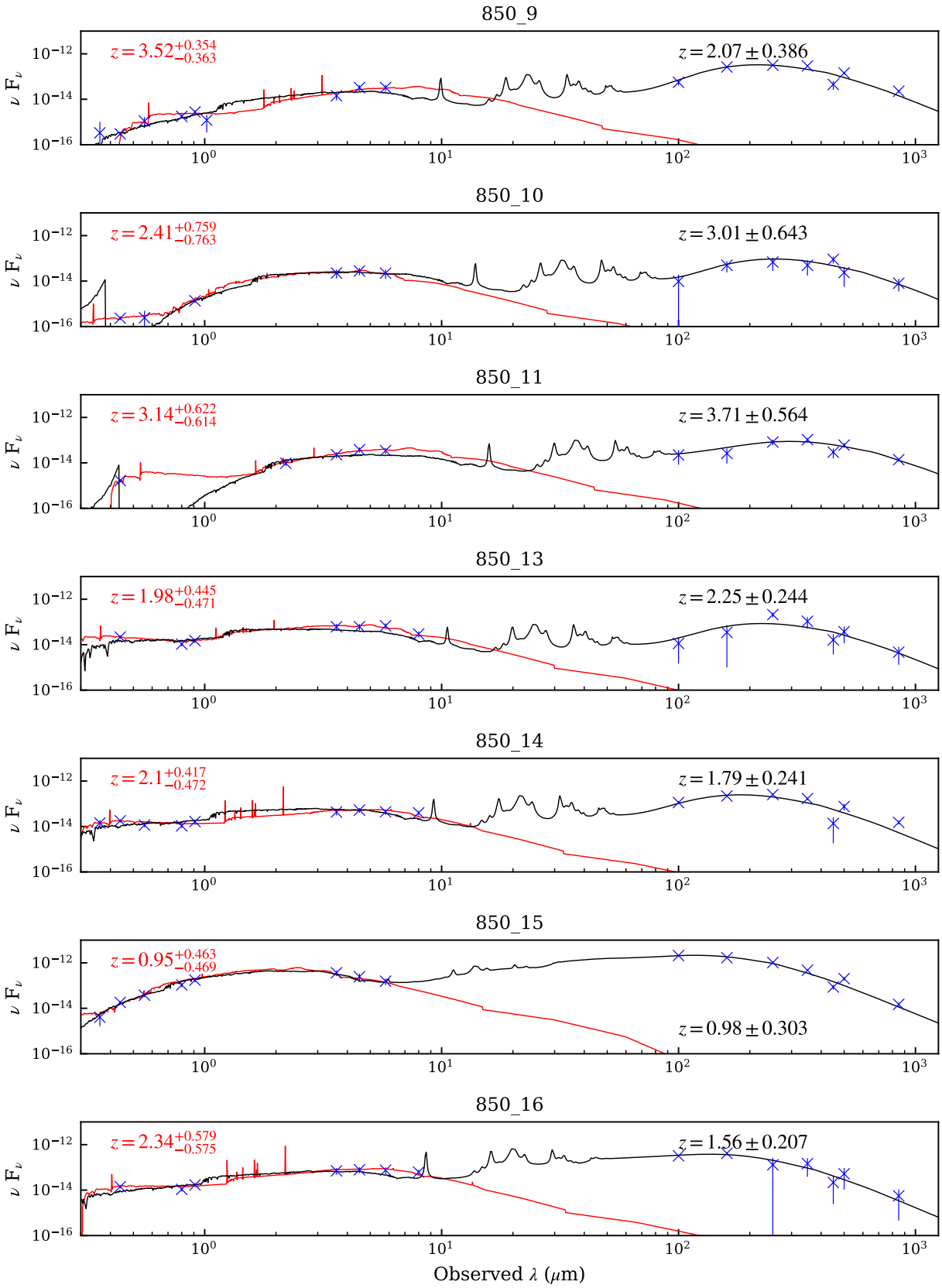

Figure A.1. *(Continued)*

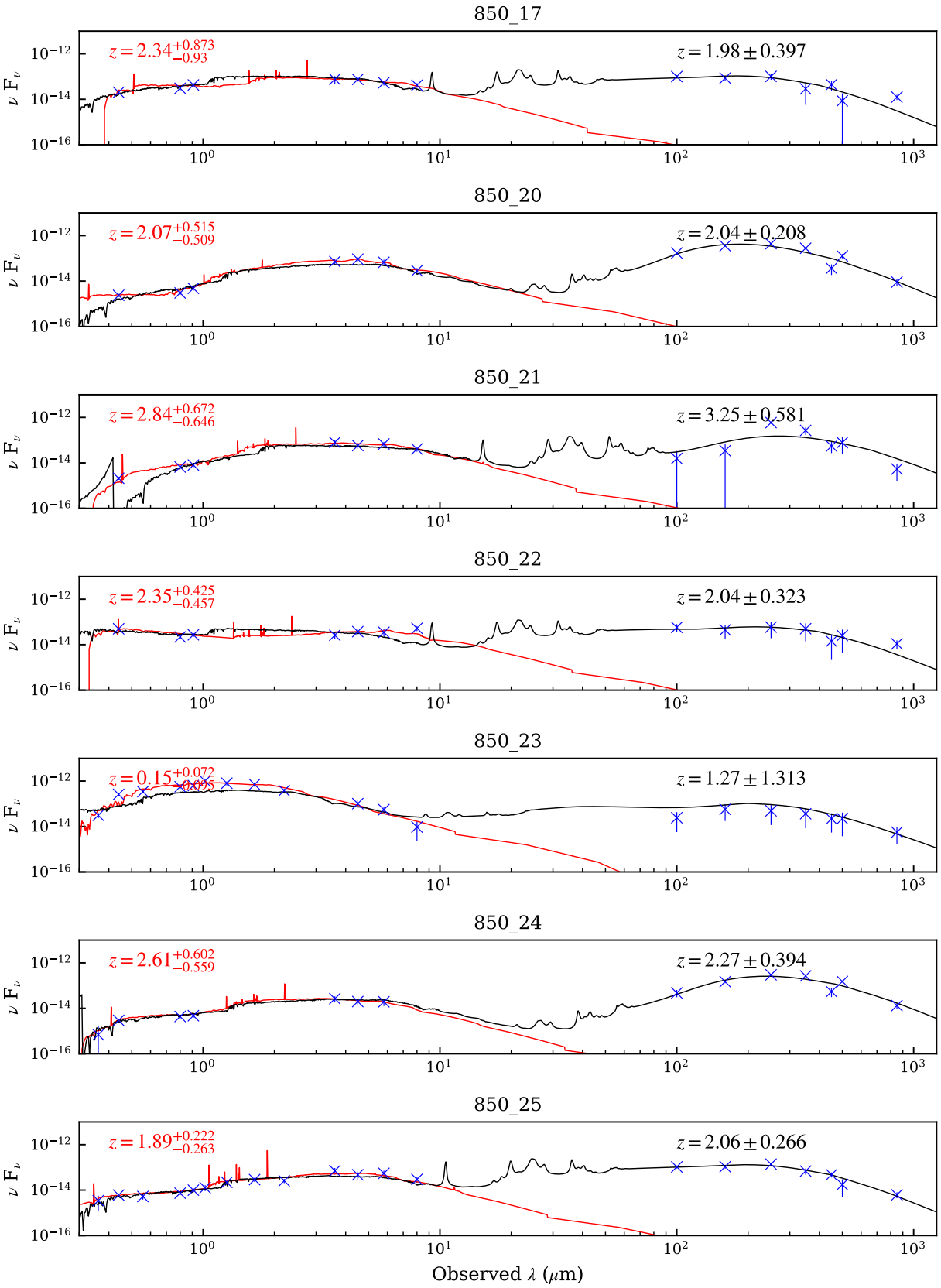

Figure A.1. *(Continued)*

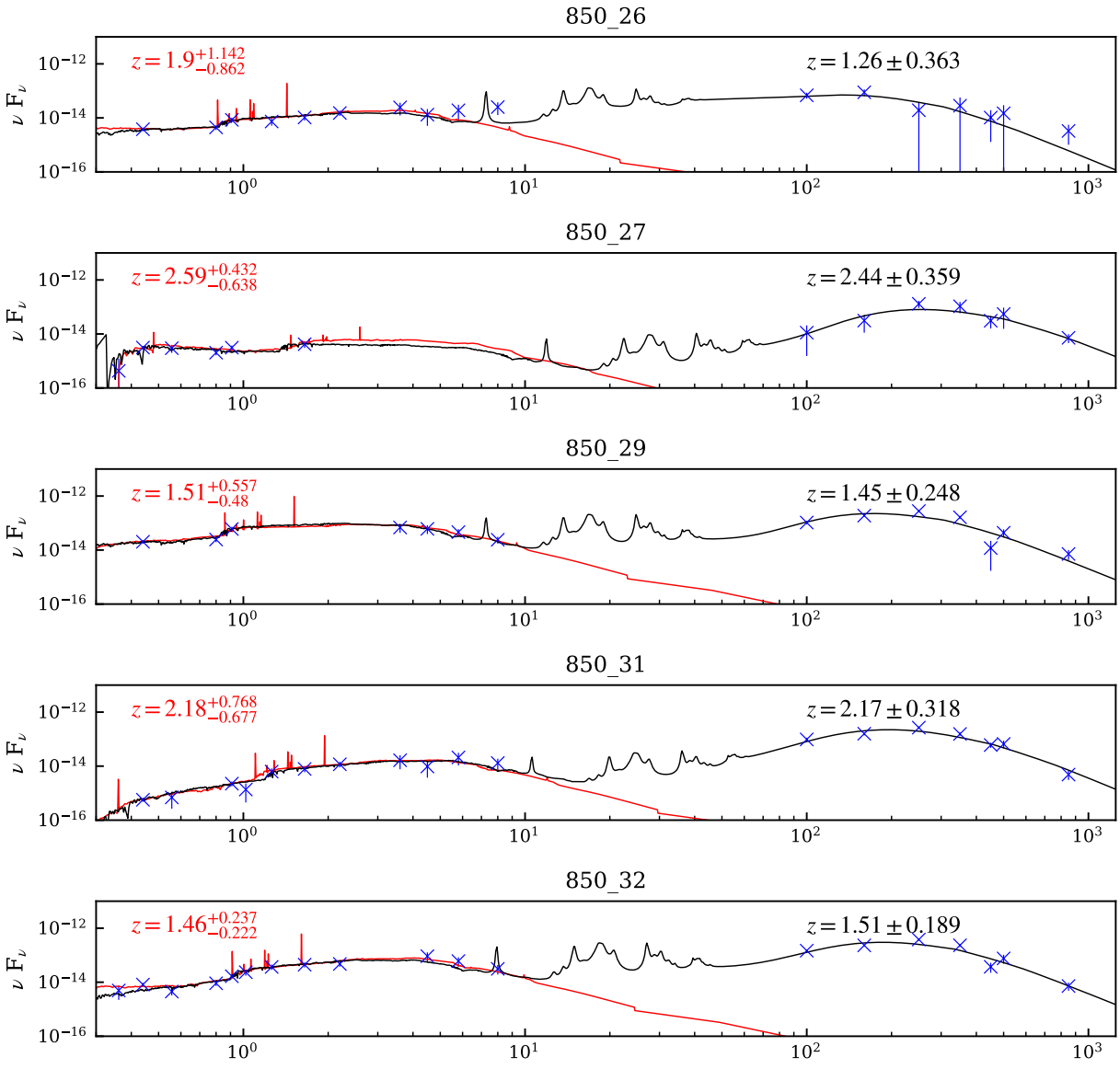

Figure A.1. *(Continued)*

A.3 Optical and NIR Data For Cluster Members

Table A.2. Optical and NIR data of my cluster galaxies. The units are in μJy.

ID	U	B	V	I	Z	Y
850_1_A	0.45 ± 0.28	1.32 ± 0.2	1.25 ± 0.31	0.07 ± 0.22	1.15 ± 0.23	0.75 ± 0.41
850_1_B	0.06 ± 0.1	0.14 ± 0.02	0.1 ± 0.07	0.21 ± 0.04	0.2 ± 0.04	0.16 ± 0.18
850_1_C	0.11 ± 0.14	0.06 ± 0.01	0.13 ± 0.08	0.33 ± 0.07	0.4 ± 0.08	0.33 ± 0.26
850_1_D	0.01 ± 0.05	-	-	-	0.06 ± 0.01	0.22 ± 0.21
850_1_E	0.02 ± 0.06	-	0.08 ± 0.06	0.13 ± 0.03	0.19 ± 0.04	0.07 ± 0.12
850_1_F	0.18 ± 0.18	0.33 ± 0.05	0.21 ± 0.1	0.54 ± 0.11	0.77 ± 0.15	0.56 ± 0.34
850_1_G	0.06 ± 0.1	0.16 ± 0.02	-	0.14 ± 0.03	0.54 ± 0.11	-
850_1_H	0.02 ± 0.05	0.09 ± 0.01	0.05 ± 0.05	-	0.05 ± 0.01	0.1 ± 0.14
850_1_K	-	0.25 ± 0.04	-	0.72 ± 0.14	2.16 ± 0.43	0.7 ± 0.39
850_13	-	3.19 ±0.48	-	2.81 ± 0.56	4.57 ± 0.91	-
850_14	1.73 ± 0.59	2.61 ± 0.4	2.16 ± 0.45	2.87 ± 0.57	4.99 ± 1.0	-
850_17	-	2.98 ± 0.45	-	8.14 ± 1.63	12.96 ± 2.59	-
850_20	-	0.35 ± 0.05	-	0.8 ± 0.16	1.45 ± 0.29	-
850_22	-	7.32 ± 1.1	-	5.84 ± 1.17	8.24 ± 1.65	-
850_25	0.41 ± 0.27	0.89 ± 0.13	0.97 ± 0.26	1.96 ± 0.39	3.02 ± 0.6	4.33 ± 1.25
850_31	-	0.08 ± 0.01	0.13 ± 0.08	-	0.68 ± 0.14	0.46 ± 0.31
850_16	-	2.08 ± 0.31	-	2.89 ± 0.58	5.13 ± 1.03	-
850_26	-	0.56 ± 0.08	-	1.18 ± 0.24	2.56 ± 0.51	-
850_4	-	0.81 ± 0.12	-	0.87 ± 0.17	1.05 ± 0.21	-
850_5	-	0.42 ± 0.06	-	0.49 ± 0.1	0.76 ± 0.15	-
850_8	-	0.46 ± 0.07	-	0.33 ± 0.07	0.95 ± 0.19	-
850_9	0.04 ± 0.08	0.04 ± 0.01	0.2 ± 0.1	0.47 ± 0.09	0.84 ± 0.17	0.41 ± 0.29
850_24	0.08 ± 0.12	0.43 ± 0.07	-	1.16 ± 0.23	1.43 ± 0.29	-
850_1_J	0.02 ± 0.06	-	0.02 ± 0.03	-	-	-

Table A.3. NIR and MIR data for my cluster galaxies. The units are in μJy.

ID	J	H	K	3.6 μm	4.8 μm	5.8 μm	8 μm
850_1_A	1.68 ± 0.6	2.57 ± 0.68	3.72 ± 0.98	6.92 ± 4.34	9.59 ± 5.05	6.16 ± 6.36	6.77 ± 6.26
850_1_B	0.16 ± 0.18	0.56 ± 0.31	1.08 ± 0.36	2.94 ± 0.82	26.35 ± 16.39	-	-
850_1_C	1.15 ± 0.47	2.72 ± 0.71	3.39 ± 0.92	4.66 ± 3.15	6.72 ± 3.92	15.28 ± 12.91	15.59 ± 8.21
850_1_D	1.19 ± 0.48	2.54 ± 0.67	4.41 ± 1.13	9.31 ± 5.33	6.25 ± 4.27	14.27 ± 8.04	1.43 ± 4.74
850_1_E	0.15 ± 0.15	1.05 ± 0.35	1.65 ± 0.54	3.88 ± 2.81	11.54 ± 8.79	12.59 ± 8.08	23.9 ± 10.32
850_1_F	2.19 ± 0.72	3.67 ± 0.9	7.27 ± 1.71	-	-	-	-
850_1_G	1.1 ± 0.46	2.51 ± 0.66	2.58 ± 0.75	12.71 ± 7.9	21.75 ± 14.4	18.86 ± 10.62	18.39 ± 8.9
850_1_H	0.31 ± 0.22	1.13 ± 0.37	1.84 ± 0.58	7.46 ± 3.71	16.56 ± 9.36	19.43 ± 10.69	29.89 ± 16.48
850_1_K	2.02 ± 0.68	5.0 ± 1.17	7.46 ± 1.75	9.55 ± 7.71	4.43 ± 4.15	5.62 ± 5.84	4.61 ± 5.89
850_13	-	-	-	73.78 ± 24.98	93.43 ± 28.31	130 ± 39	78.39 ± 23.33
850_14	-	-	-	52.14 ± 14.9	78.91 ± 18.42	85.72 ± 22.91	107 ± 24
850_17	-	-	-	91.62 ± 33.41	112 ± 27	103 ± 25	110 ± 25
850_20	-	-	-	86.18 ± 27.08	137 ± 37	129 ± 40	76.1 ± 22.79
850_22	-	-	-	31.29 ± 10.45	56.36 ± 16.74	67.86 ± 23.89	140 ± 35
850_25	9.25 ± 2.18	15.96 ± 3.38	18.89 ± 4.05	85.41 ± 27.26	70.97 ± 27.49	105 ± 32	79.02 ± 22.71
850_31	2.63 ± 0.81	4.32 ± 1.03	8.59 ± 1.98	19.77 ± 10.58	14.54 ± 8.93	40.47 ± 19.89	34.77 ± 15.6
850_16	-	-	-	84.42 ± 26.66	117 ± 35	145.42 ± 49.35	166 ± 42
850_26	3.08 ± 0.91	5.71 ± 1.32	11.13 ± 2.49	29.33 ± 14.59	19.75 ± 12.12	36.97 ± 22.32	67.18 ± 33.45
850_4	-	-	-	-	-	-	-
850_5	-	-	1.8 ± 0.58	-	-	-	-
850_8	-	-	-	1.52 ± 1.54	7.59 ± 3.91	2.43 ± 8.95	1.86 ± 10.4
850_9	-	-	-	17.08 ± 6.34	49.19 ± 14.08	63.37 ± 21.07	-
850_24	-	-	-	31.74 ± 8.33	29.72 ± 9.43	37.5 ± 13.05	-
850_1_J	-	0.43 ± 0.2	0.16 ± 0.14	4.8 ± 2.92	4.62 ± 2.1	8.44 ± 6.71	5.4 ± 5.51

Appendix B
FIR and sub-mm fluxes for JKCS041

Table B.1. FIR/sub-mm fluxes from XID+ for those galaxies associated with SCUBA-2 sources.

Name	RA	DEC.	f_{24} (mJy)	σ_{24} (mJy)	f_{250} (mJy)	σ_{250} (mJy)	f_{350} (mJy)	σ_{350} (mJy)	f_{450} (mJy)	σ_{450} (mJy)	f_{500} (mJy)	σ_{500} (mJy)	f_{850} (mJy)	σ_{850} (mJy)
850_1_A	36.673	-4.704	0.03	0.02	4.69	2.27	3.29	2.53	3.01	2.78	2.95	2.69	0.68	0.55
850_1_B	36.676	-4.705	0.06	0.03	3.58	2.39	8.59	3.71	9.17	2.13	12.19	5.16	5.5	0.49
850_1_C	36.678	-4.702	0.6	0.03	10.19	2.18	15.31	3.23	9.98	1.99	8.85	5.66	2.53	0.43
850_2	36.654	-4.778	0.19	0.02	19.55	2.01	28.39	2.09	10.87	4.12	25.48	2.04	9.35	0.87
850_3	36.694	-4.704	0.01	0.01	3.97	2.0	6.17	2.46	1.67	1.49	7.75	3.18	3.84	0.49
850_4	36.636	-4.719	1.01	0.03	29.14	1.9	34.38	2.15	17.66	3.33	33.52	2.21	5.39	0.66
850_5_A	36.673	-4.734	0.29	0.03	4.56	2.95	1.72	1.83	1.79	1.58	3.01	2.94	0.51	0.50
850_5_B	36.672	-4.732	0.15	0.03	16.49	2.93	16.18	3.03	3.7	2.42	4.65	3.52	2.99	0.59
850_5_C	36.677	-4.732	0.79	0.03	41.73	1.95	33.82	2.24	6.62	2.52	25.49	3.05	4.41	0.56
850_6_A	36.697	-4.689	0.35	0.03	12.5	4.66	15.81	6.53	1.4	1.38	5.77	4.86	1.18	0.6
850_6_B	36.698	-4.688	0.65	0.03	33.01	5.58	11.33	9.11	10.36	2.96	10.96	7.85	1.08	0.75
850_6_C	36.695	-4.687	1.29	0.03	3.62	3.55	3.8	3.95	1.33	1.31	3.8	3.51	0.4	0.36
850_6_D	36.699	-4.686	0.28	0.03	5.11	3.58	16.45	5.8	4.82	2.6	11.01	5.91	3.44	0.65
850_7	36.706	-4.714	0.27	0.03	16.42	2.09	17.89	2.01	7.82	2.51	17.06	2.12	3.6	0.56
850_8	36.706	-4.759	0.2	0.04	30.64	5.0	31.28	5.43	3.42	3.01	18.9	4.32	2.83	1.42
850_9_A	36.663	-4.721	0.22	0.03	22.71	2.69	20.45	4.06	6.49	2.77	6.06	4.95	2.55	0.63
850_9_B	36.664	-4.718	0.08	0.03	8.97	2.7	11.89	3.88	6.78	2.88	20.53	4.37	1.1	0.55

The RA and DEC. are the positions of the sources in the radio map. All flux values are the results that come from XID+. For those sources that appear to have 850 μm errors lower then the quoted noise, these sources are in the very centre of the image where the map is much deeper.

Table B.1. *(Continued)*

Name	RA	DEC.	f_{24} (mJy)	σ_{24} (mJy)	f_{250} (mJy)	σ_{250} (mJy)	f_{350} (mJy)	σ_{350} (mJy)	f_{450} (mJy)	σ_{450} (mJy)	f_{500} (mJy)	σ_{500} (mJy)	f_{850} (mJy)	σ_{850} (mJy)
850_10	36.678	-4.666	0.51	0.02	7.77	2.01	4.79	2.27	4.14	2.13	4.81	2.47	3.23	0.54
850_11_A	36.723	-4.71	0.04	0.03	18.9	6.61	12.49	9.34	3.09	2.51	5.66	5.47	2.73	1.08
850_11_B	36.724	-4.711	0.35	0.03	5.07	5.12	12.86	7.51	1.7	1.82	18.79	7.86	1.02	0.91
850_11_C	36.726	-4.71	0.02	0.01	14.82	2.76	16.22	4.4	4.07	2.54	9.55	4.95	0.71	0.57
850_11_D	36.721	-4.709	0.65	0.03	11.46	3.5	8.92	4.42	4.71	2.53	1.86	2.04	0.48	0.42
850_12_A	36.721	-4.692	0.28	0.04	6.98	6.15	18.2	9.58	3.11	2.55	13.96	6.66	0.61	0.62
850_12_B	36.721	-4.692	0.78	0.04	32.2	6.43	16.18	9.62	3.91	2.82	6.75	6.39	2.65	0.83
850_13_A	36.629	-4.658	11.08	0.04	181.77	2.65	74.09	3.53	22.44	3.35	35.16	3.15	2.33	0.85
850_13_B	36.629	-4.656	3.91	0.03	66.1	2.78	25.53	3.6	3.46	2.71	2.97	2.73	3.26	0.86
850_14	36.626	-4.699	0.35	0.02	16.64	1.98	17.21	2.03	4.71	2.63	14.01	2.03	1.69	0.59
850_15	36.642	-4.696	0.78	0.03	28.16	2.04	28.52	2.41	5.18	2.31	23.04	2.87	3.74	0.57
850_16_A	36.684	-4.695	0.54	0.03	25.65	2.51	25.31	3.92	5.34	1.92	8.86	6.28	1.48	0.48
850_16_B	36.686	-4.692	0.08	0.03	1.44	1.4	2.8	2.73	0.74	0.72	4.36	3.77	0.52	0.39
850_17_A	36.669	-4.769	0.56	0.03	1.3	1.18	1.64	1.72	1.16	1.23	1.6	1.62	0.64	0.51
850_17_B	36.669	-4.766	0.25	0.03	11.39	2.14	15.13	2.29	2.0	1.75	13.16	2.62	3.89	0.72
850_18	36.605	-4.663	0.32	0.02	14.06	2.0	13.34	2.11	3.15	2.54	15.8	2.02	3.85	0.79
850_21_A	36.748	-4.744	1.06	0.03	30.8	2.81	31.67	4.39	4.28	3.14	14.35	5.94	2.71	0.94
850_21_B	36.75	-4.742	1.17	0.02	26.49	3.0	22.53	4.78	7.75	3.94	19.44	6.29	1.64	0.9
850_22	36.694	-4.728	0.02	0.02	15.46	1.94	18.27	2.3	4.72	2.3	14.21	2.22	2.71	0.56
850_23	36.77	-4.707	1.08	0.02	30.61	2.05	22.16	1.98	8.48	3.81	10.07	2.14	1.93	0.93
850_26	36.612	-4.679	0.4	0.02	16.57	1.97	15.39	2.14	3.12	2.33	11.3	2.23	3.13	0.68
850_27	36.715	-4.764	0.21	0.02	8.15	2.0	12.51	2.28	3.91	2.84	7.26	2.39	3.66	0.76
850_28	36.688	-4.664	1.85	0.03	33.37	2.08	27.62	2.27	5.86	2.3	15.1	2.51	1.8	0.53

Appendix C
Spectra for all line detections in PLCKERC857

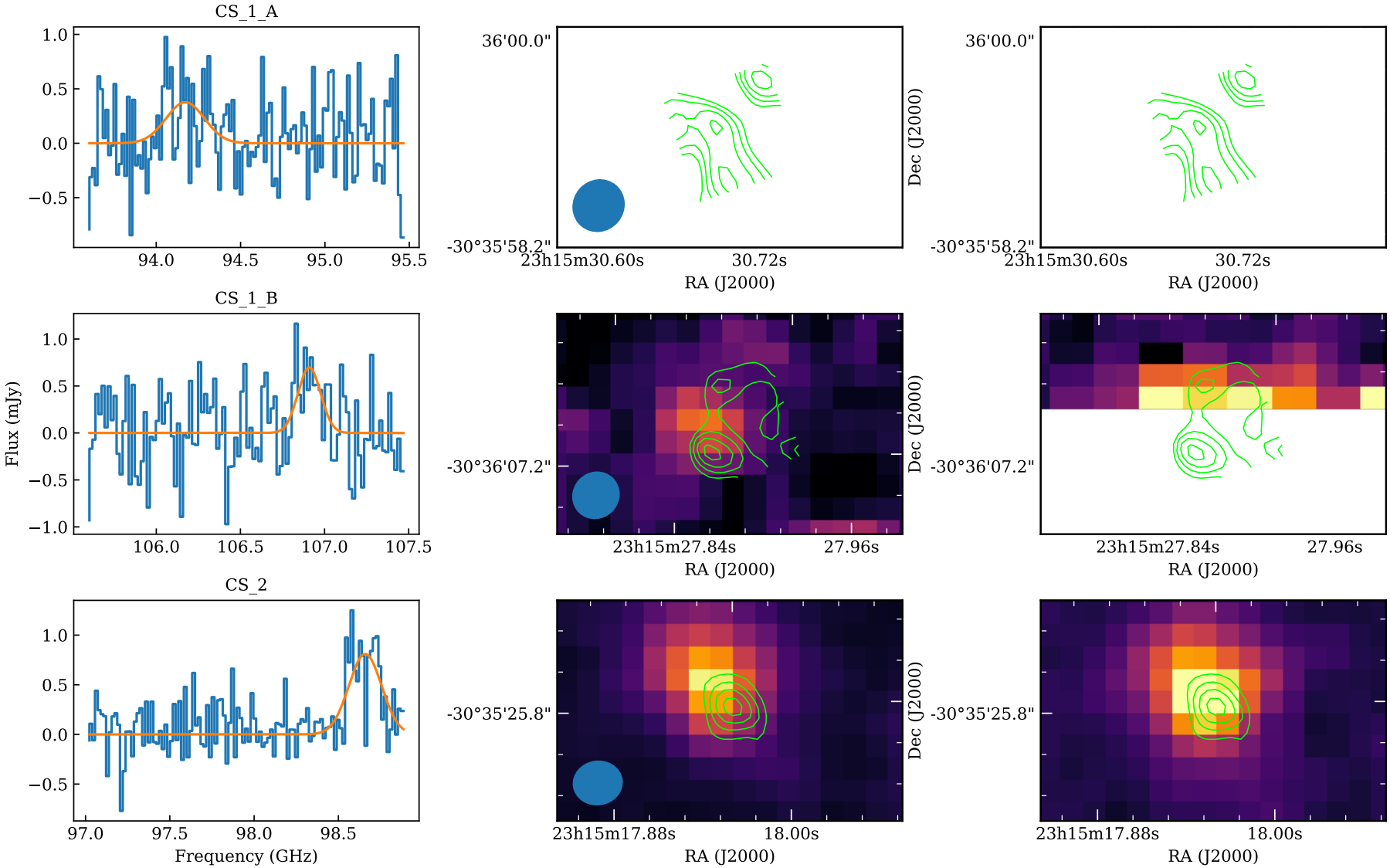

Figure C.1. Spectra detections for all 57 sources from Table 5.3. The first column shows the detection, the second shows the IRAC 3.6 μm and the final column shows the IRAC 4.5 μm.

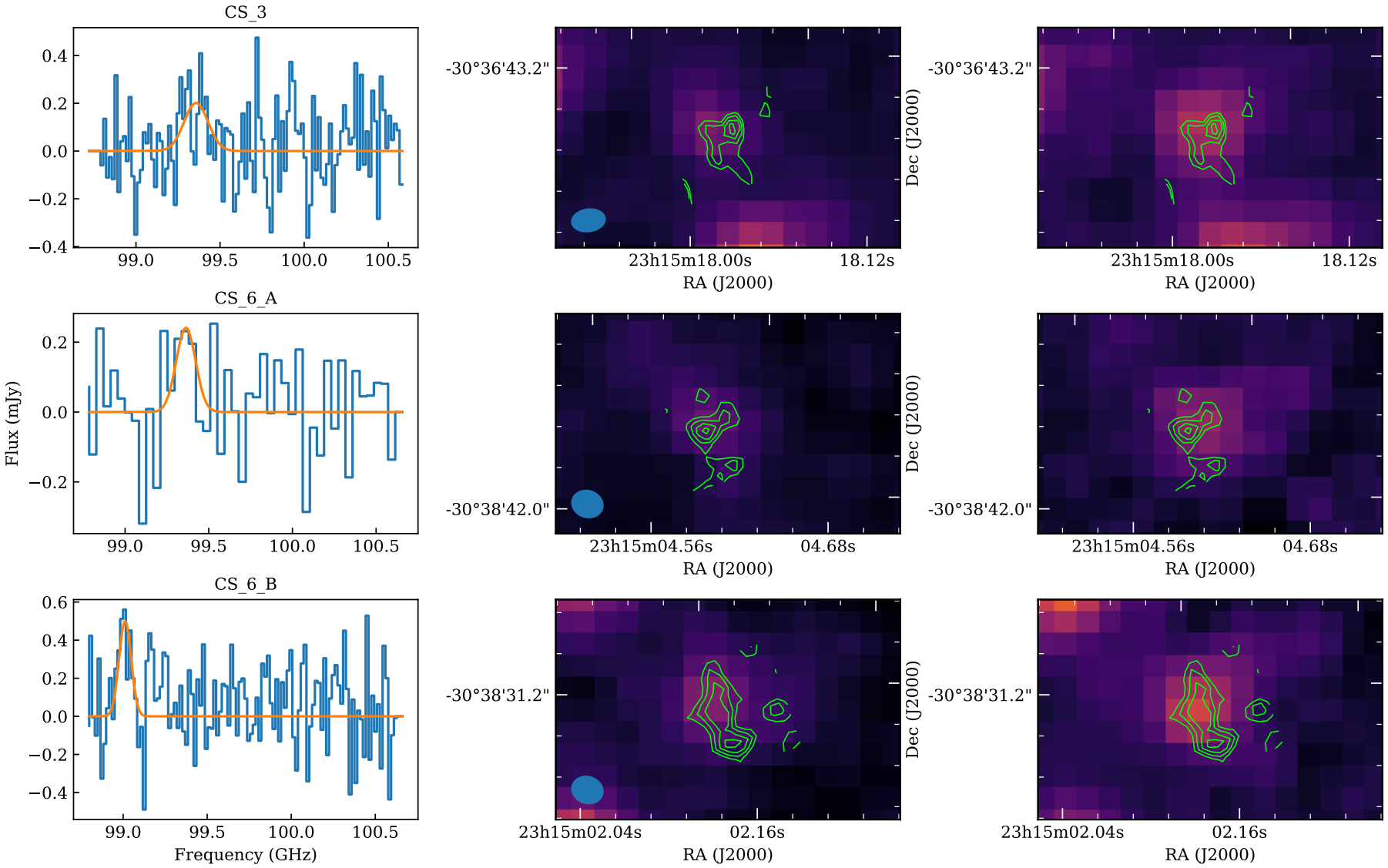

Figure C.2. *(Continued)*

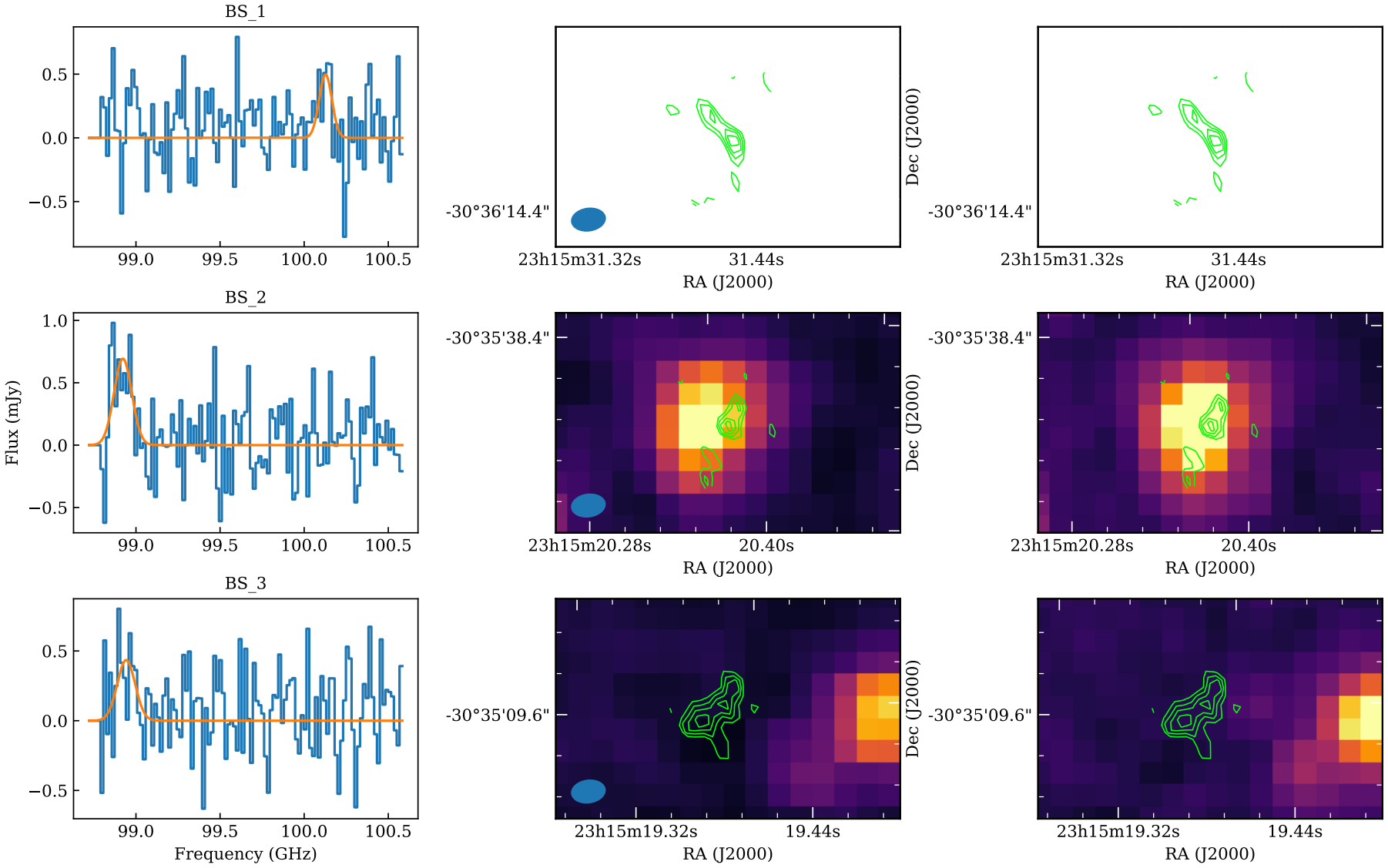

Figure C.3. *(Continued)*

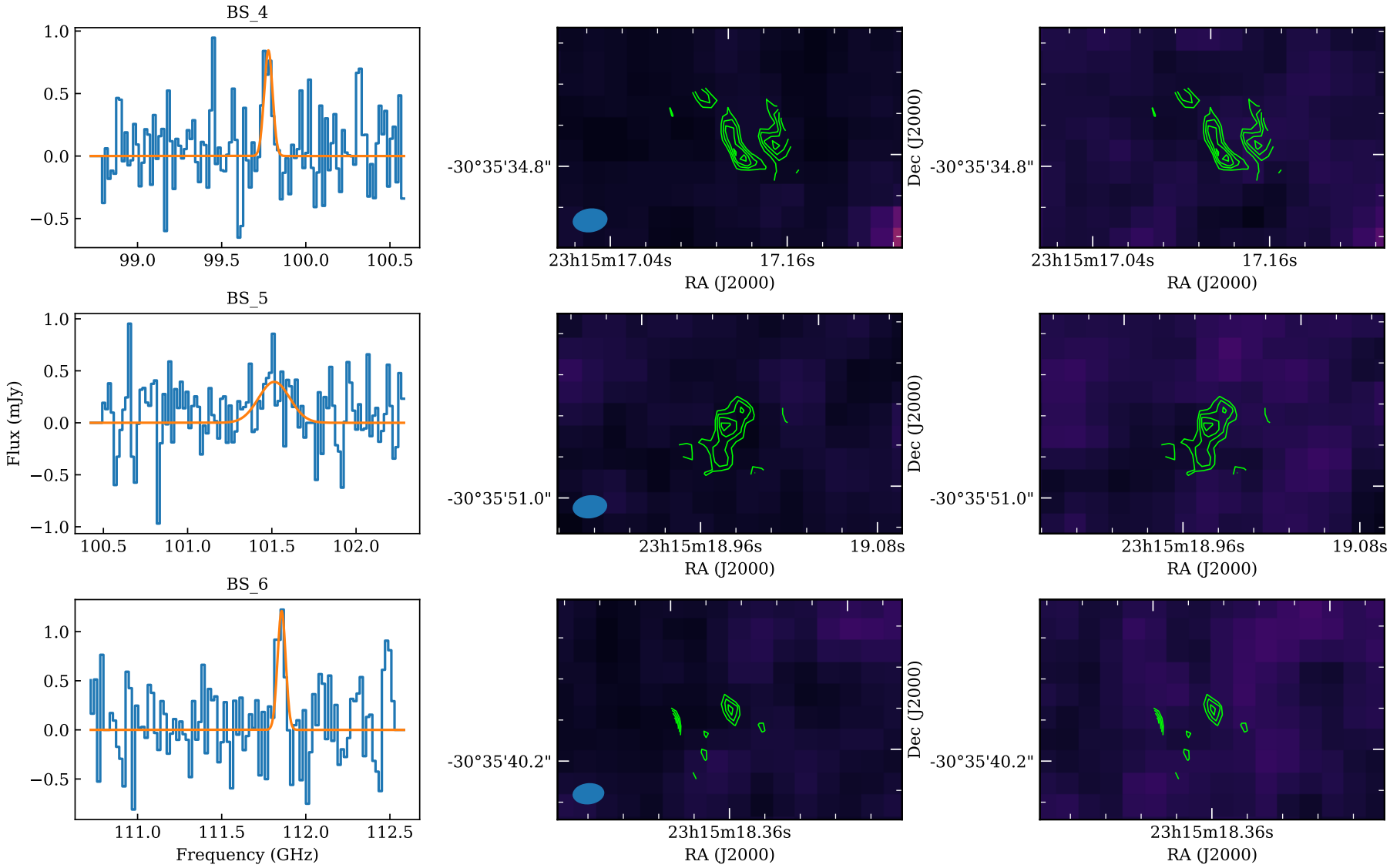

Figure C.4. *(Continued)*

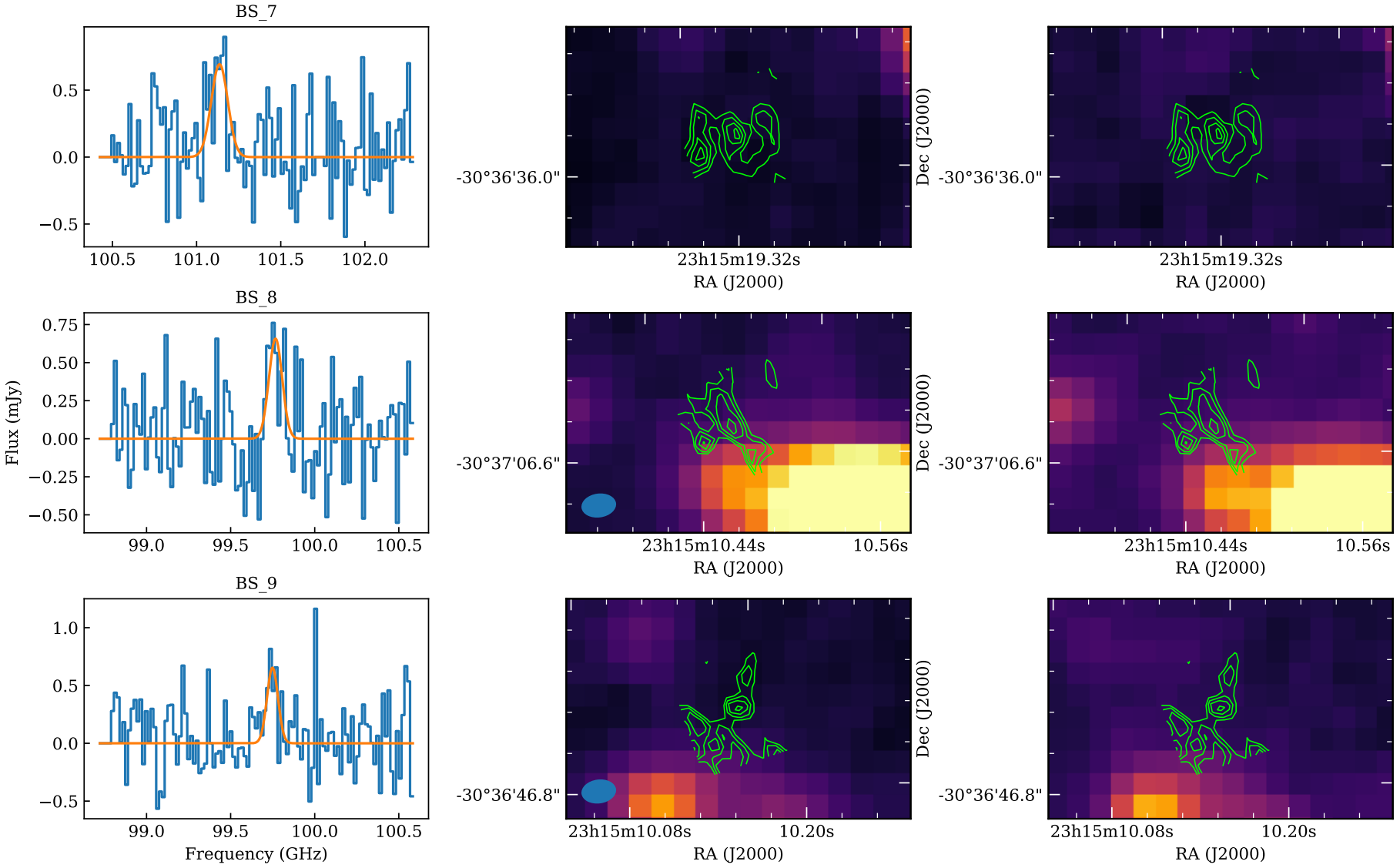

Figure C.5. *(Continued)*

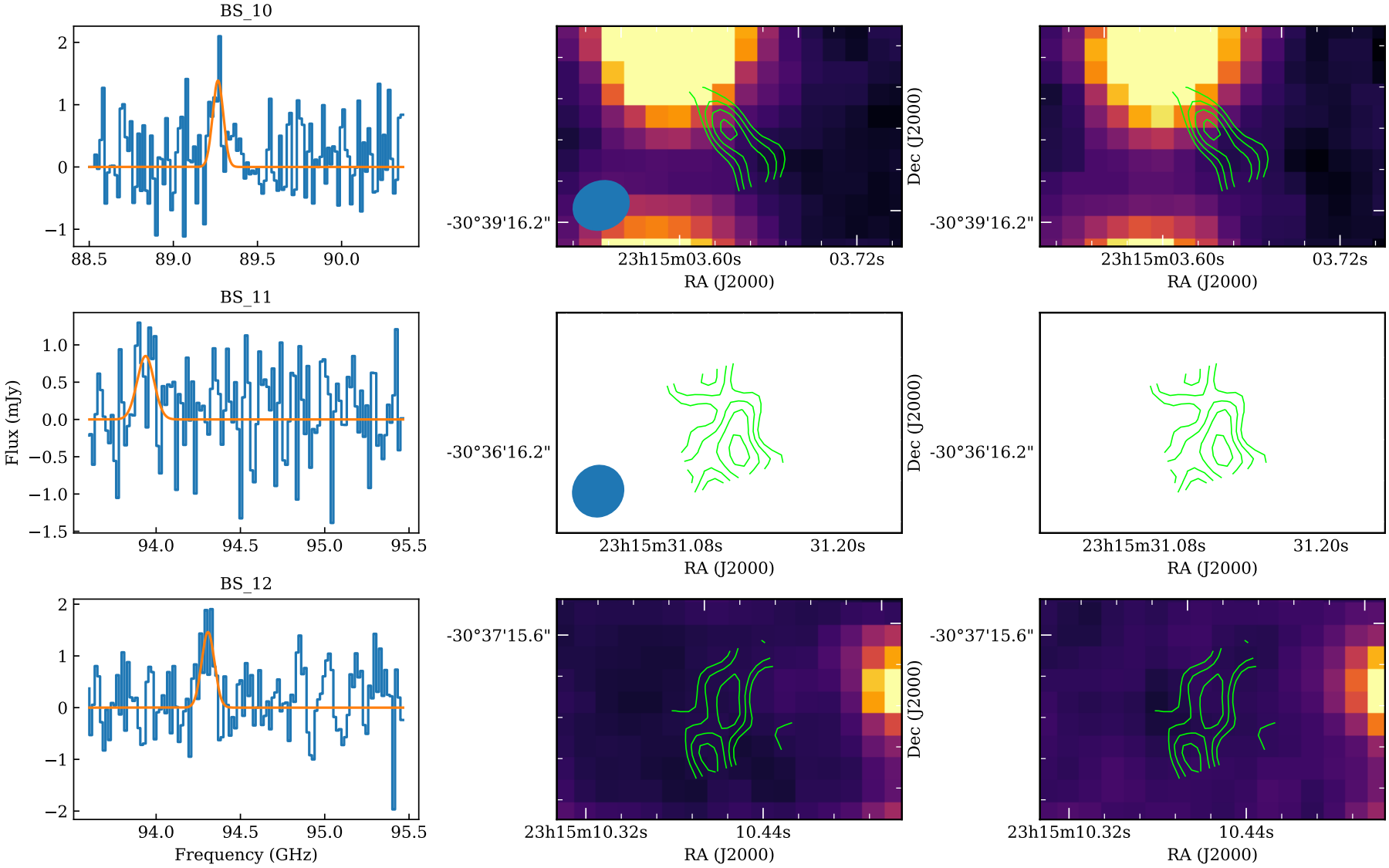

Figure C.6. *(Continued)*

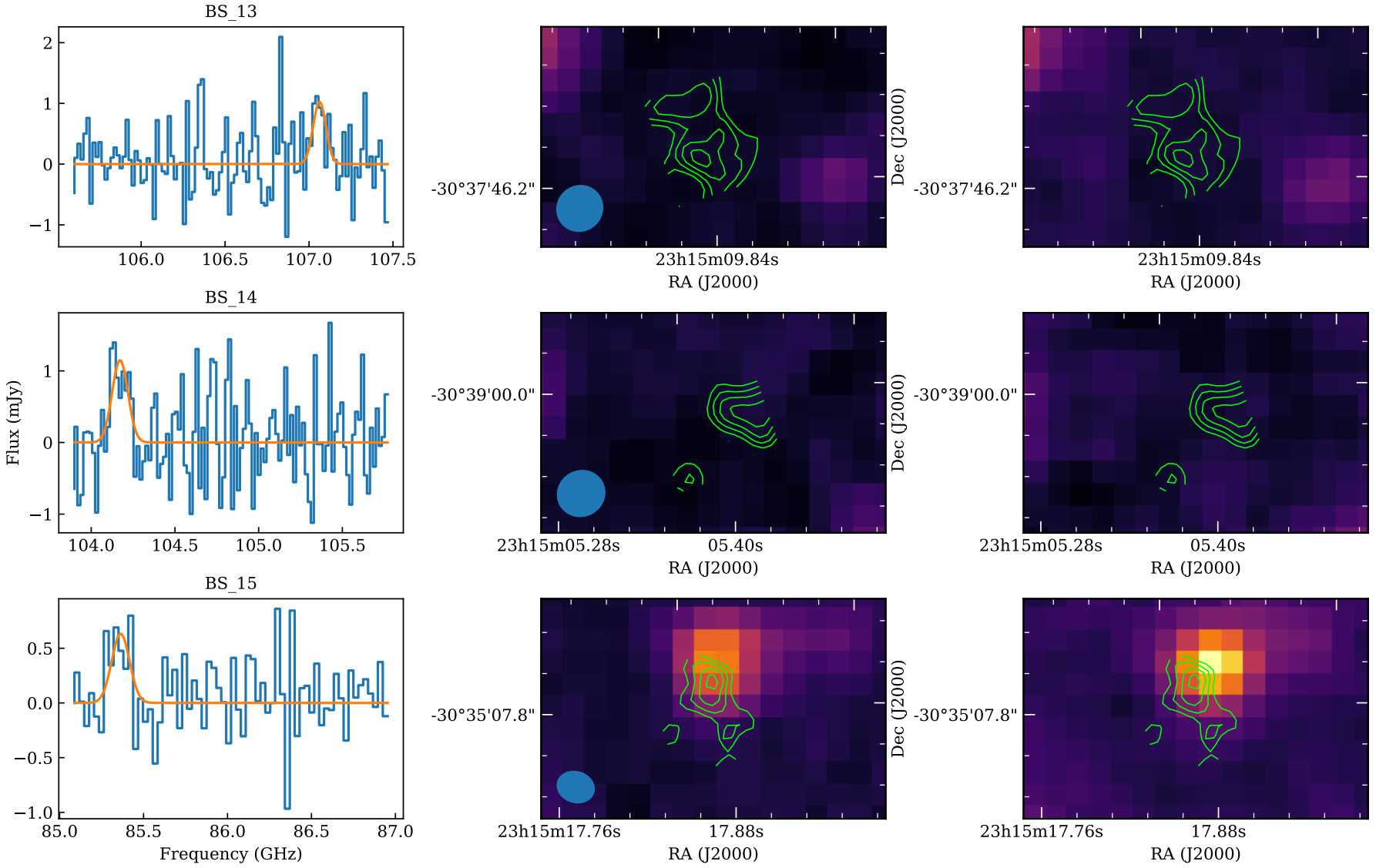

Figure C.7. *(Continued)*

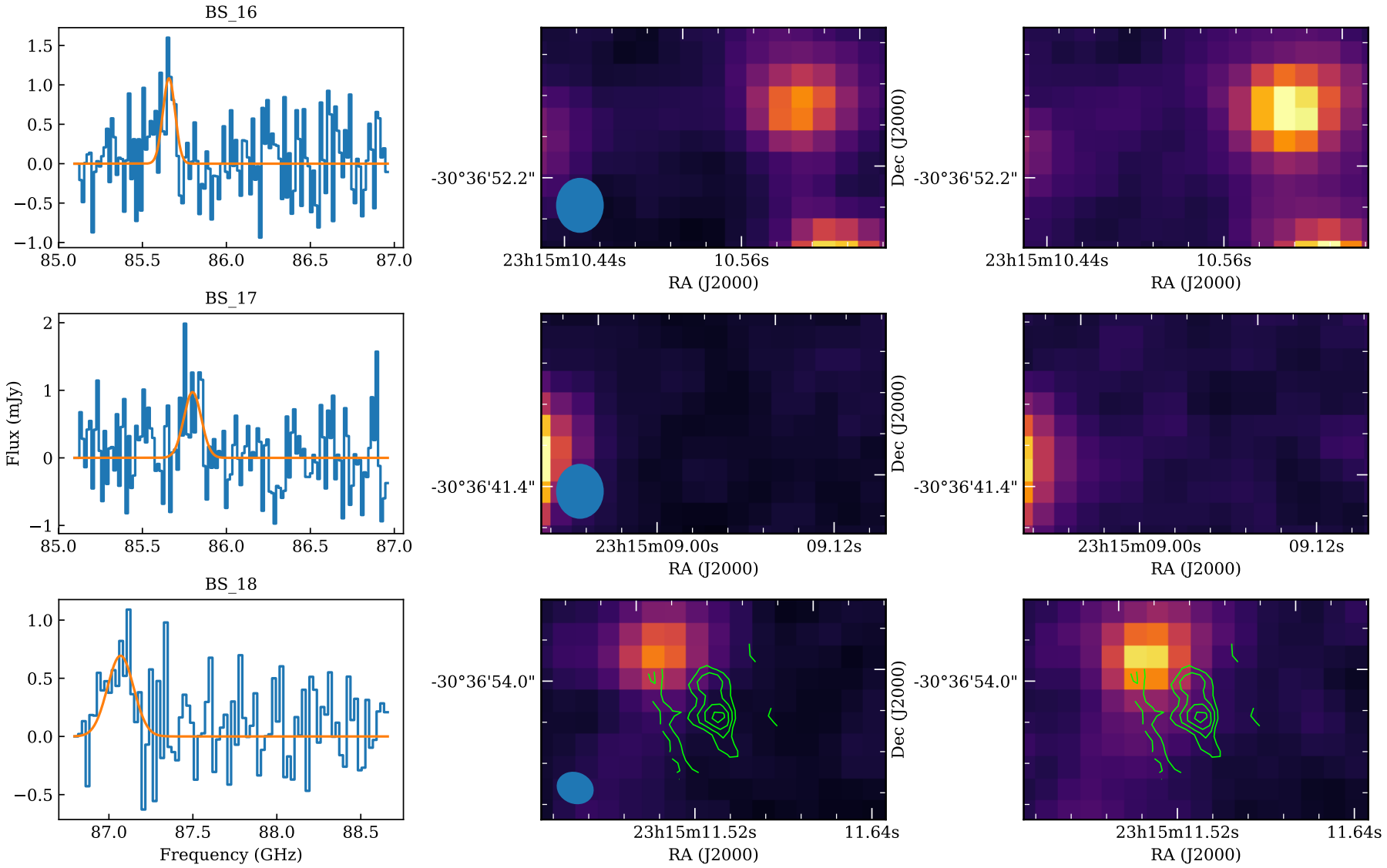

Figure C.8. *(Continued)*

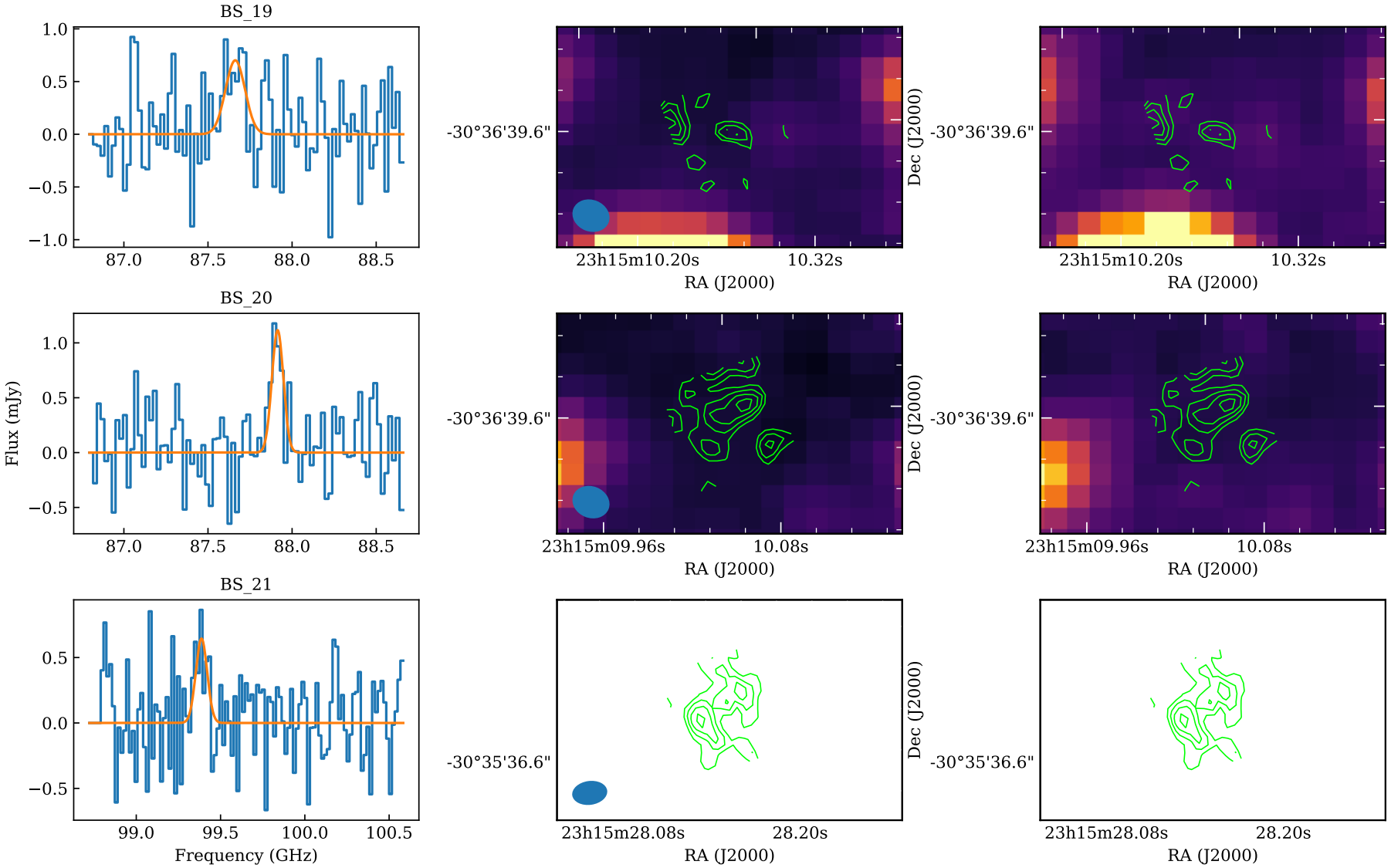

Figure C.9. *(Continued)*

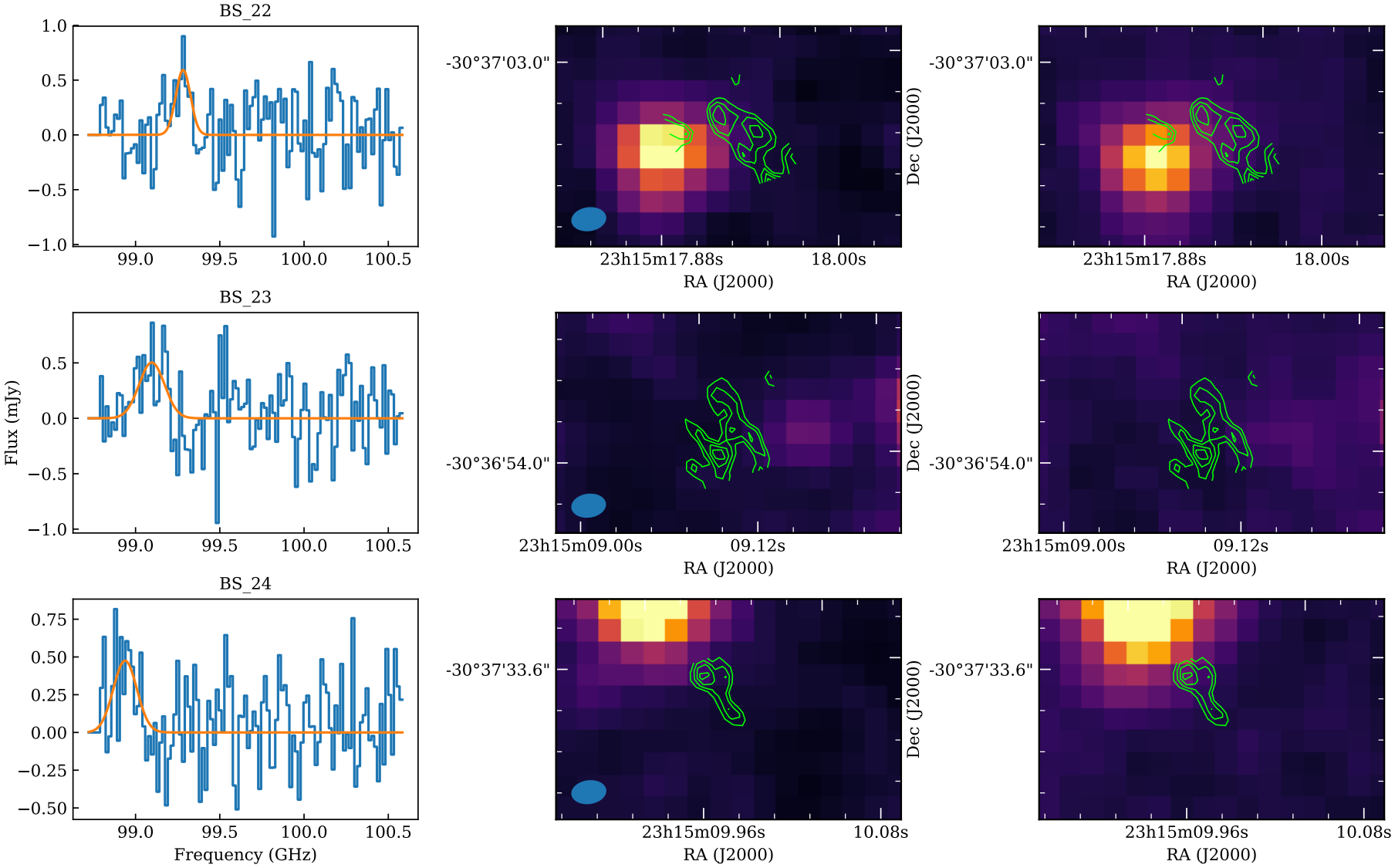

Figure C.10. *(Continued)*

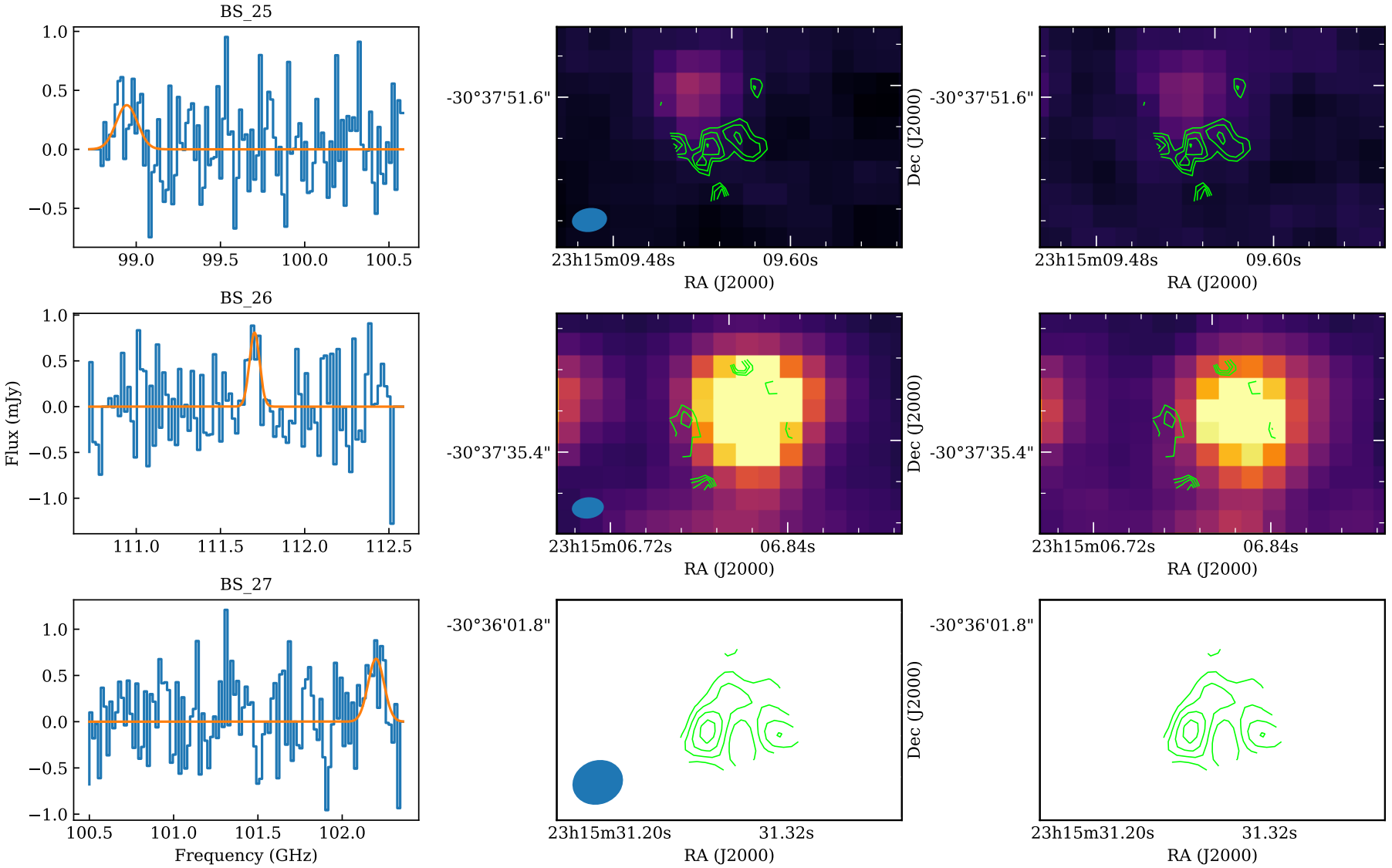

Figure C.11. *(Continued)*

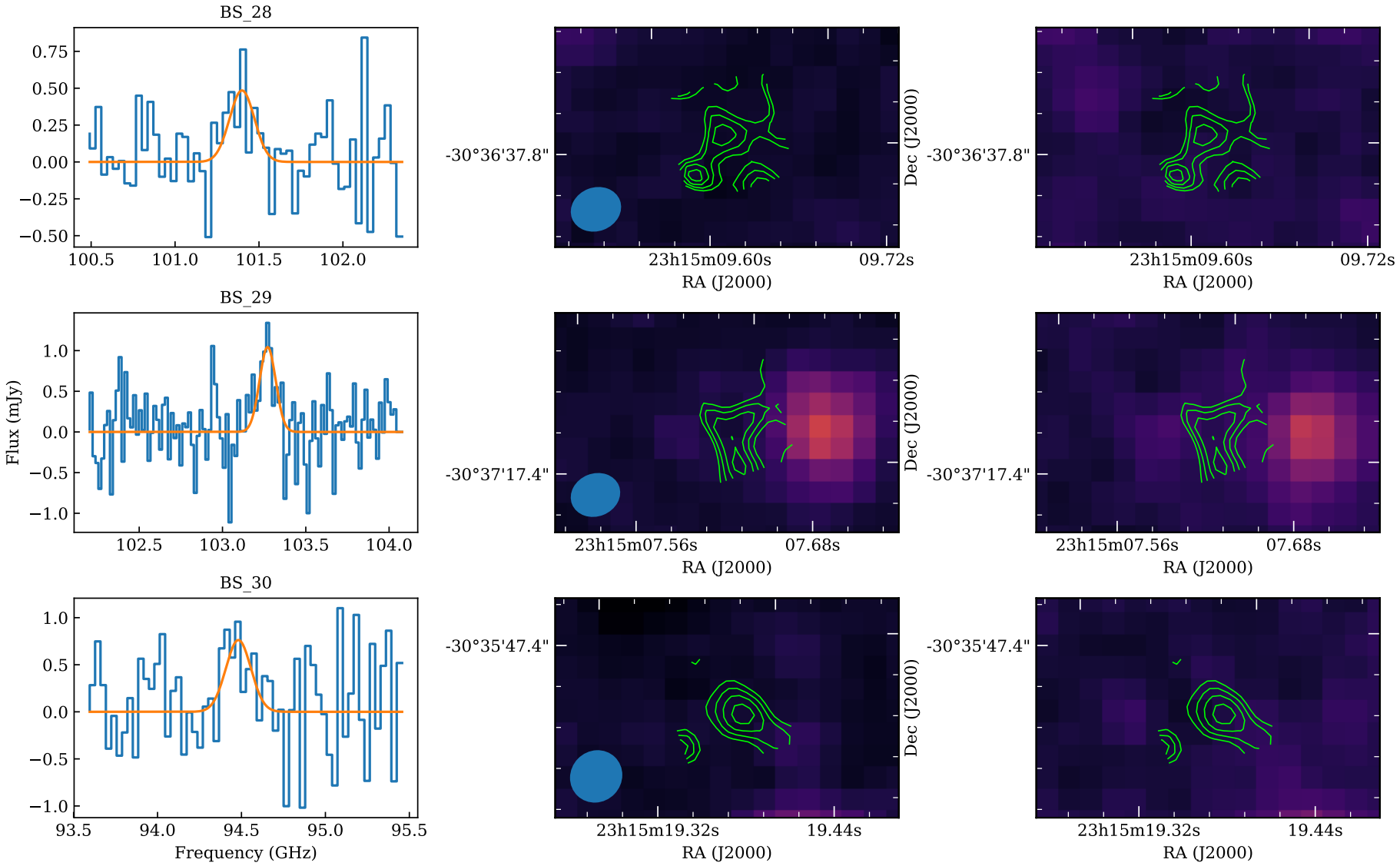

Figure C.12. *(Continued)*

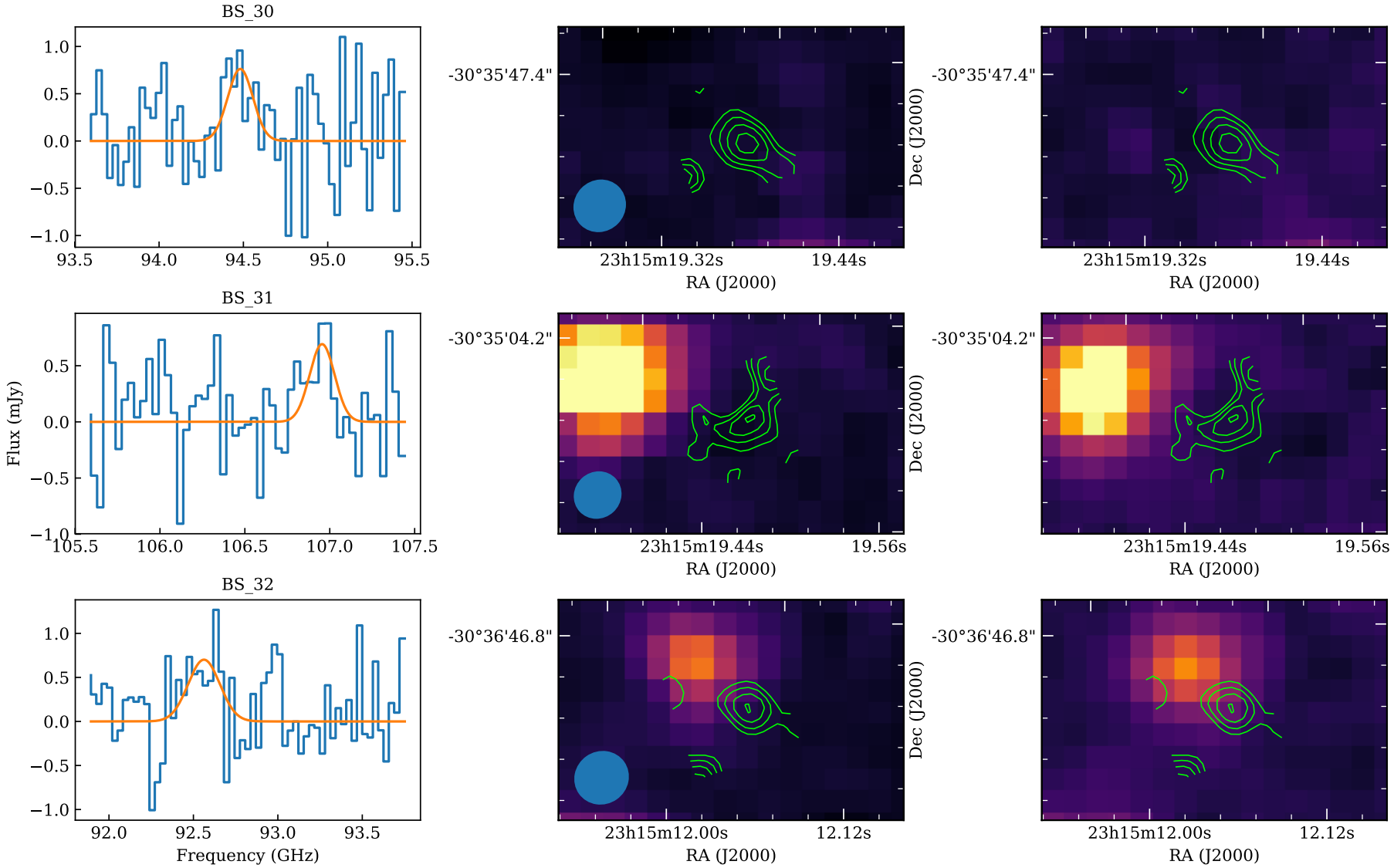

Figure C.13. *(Continued)*

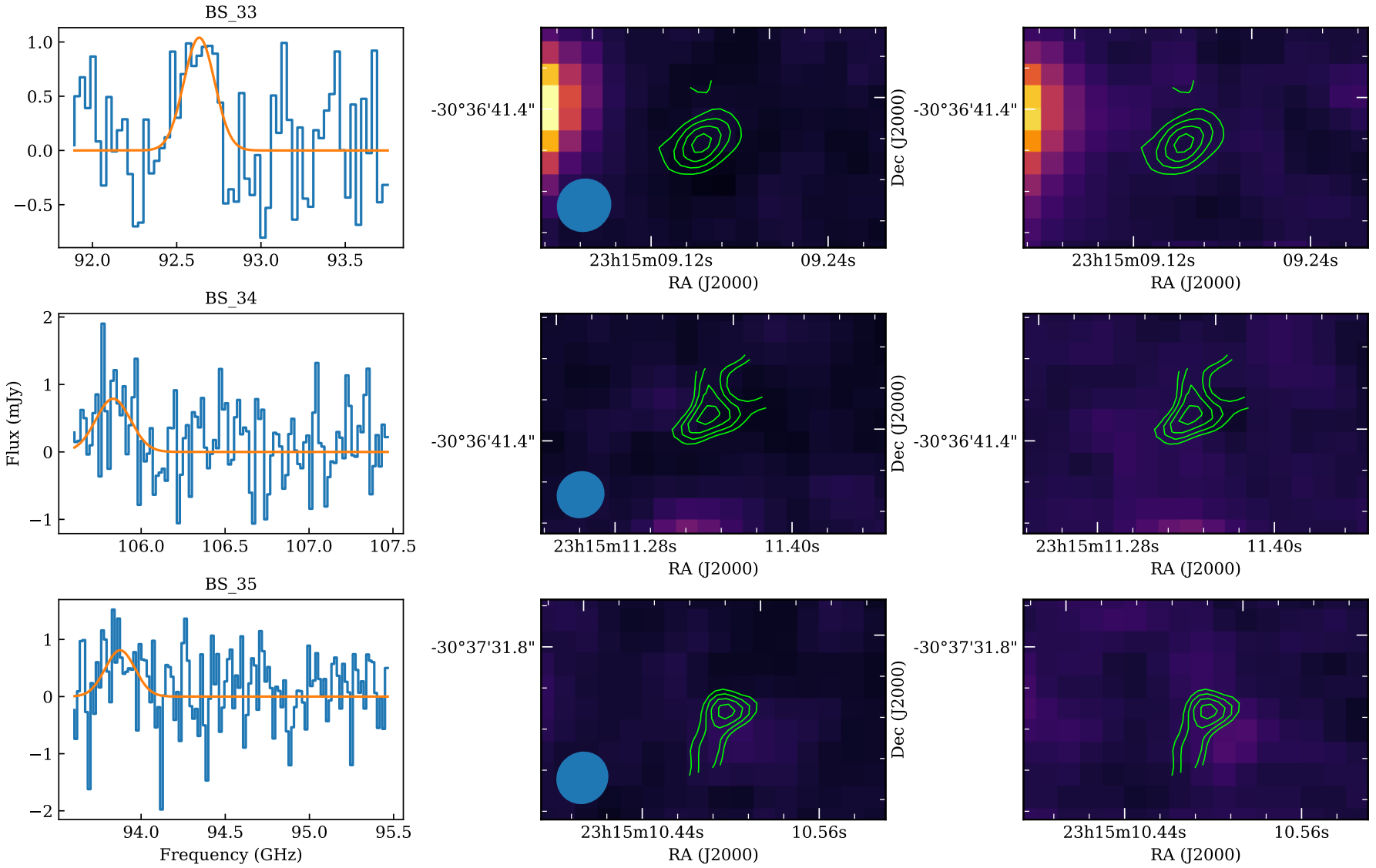

Figure C.14. *(Continued)*

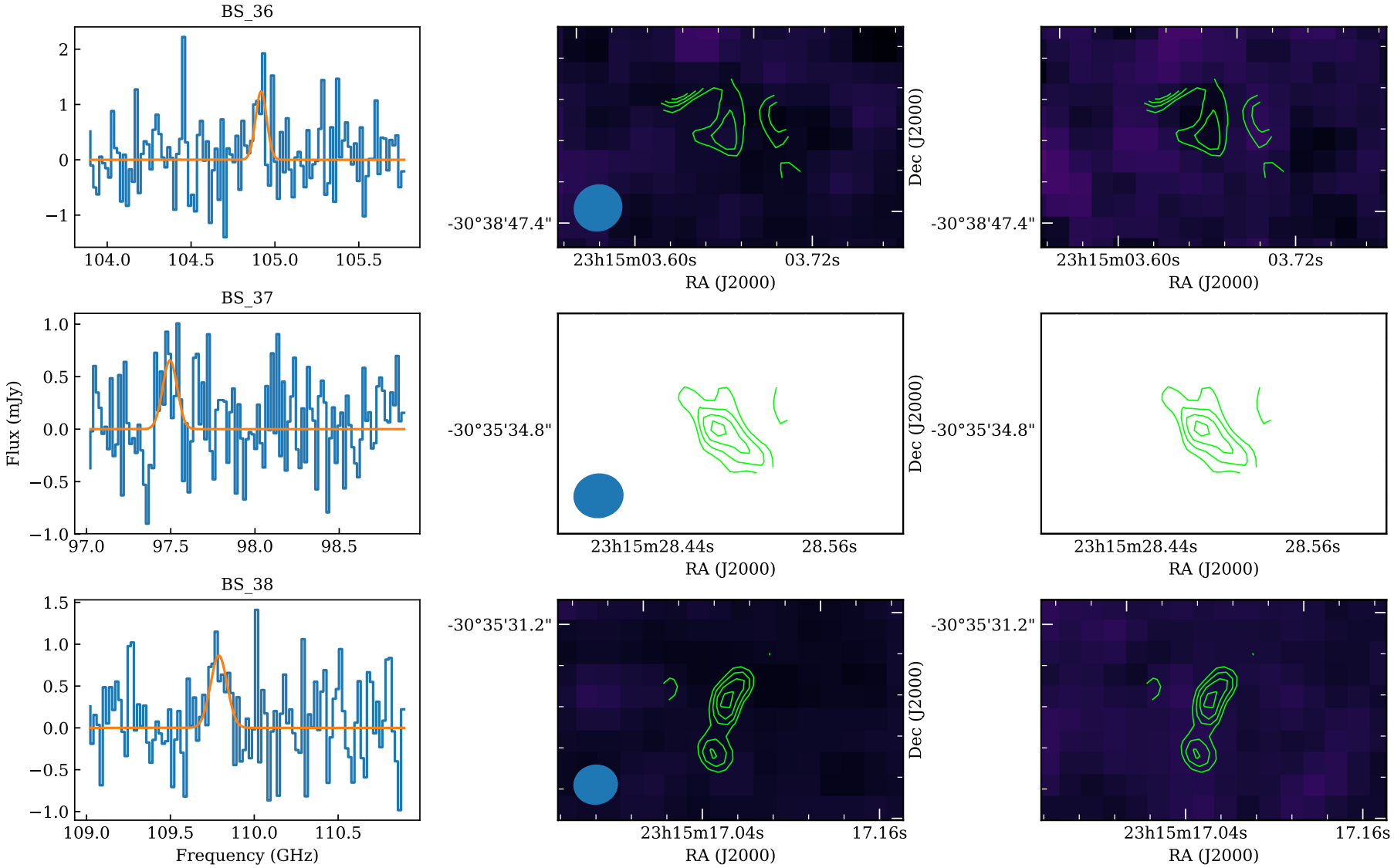

Figure C.15. *(Continued)*

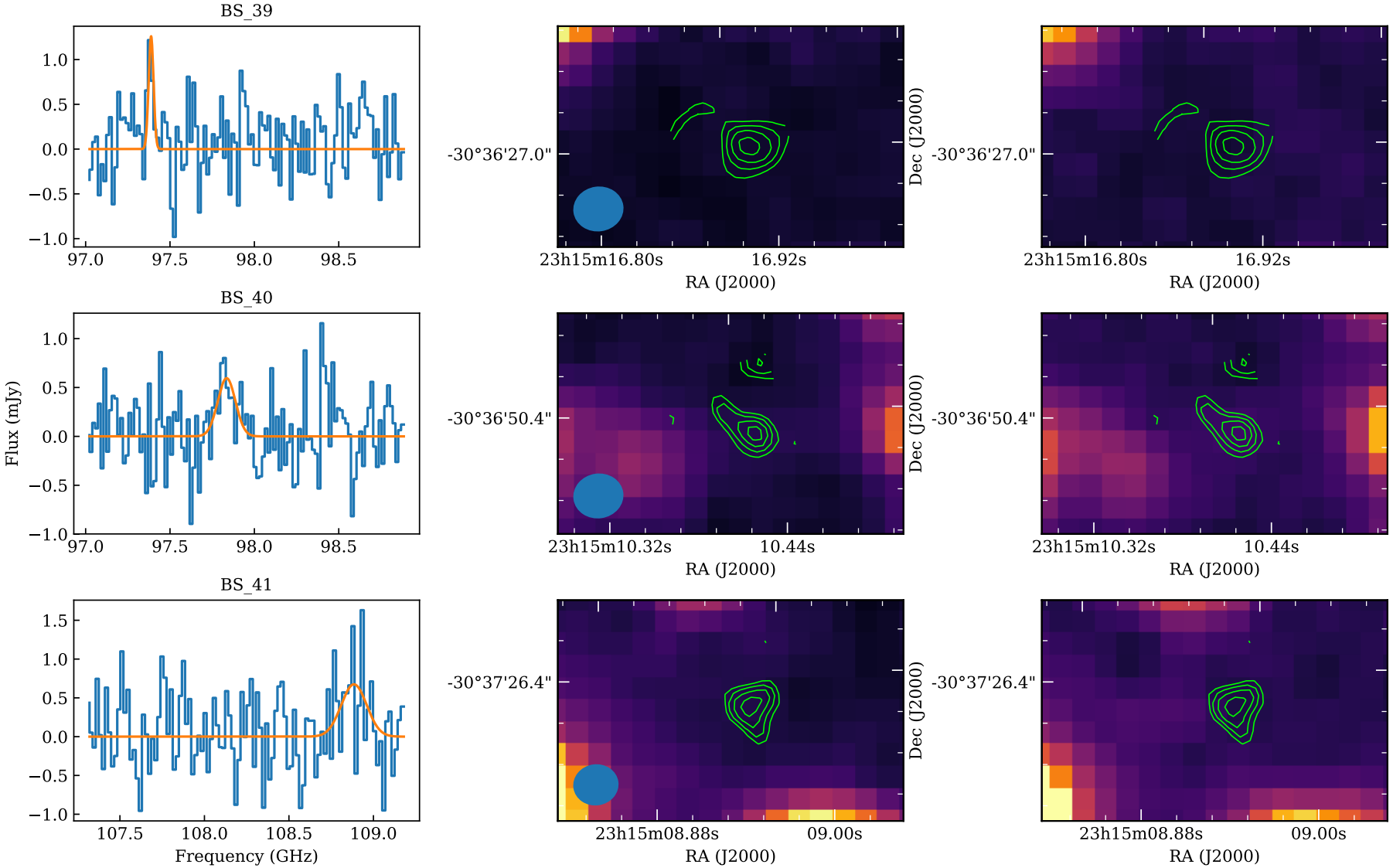

Figure C.16. *(Continued)*

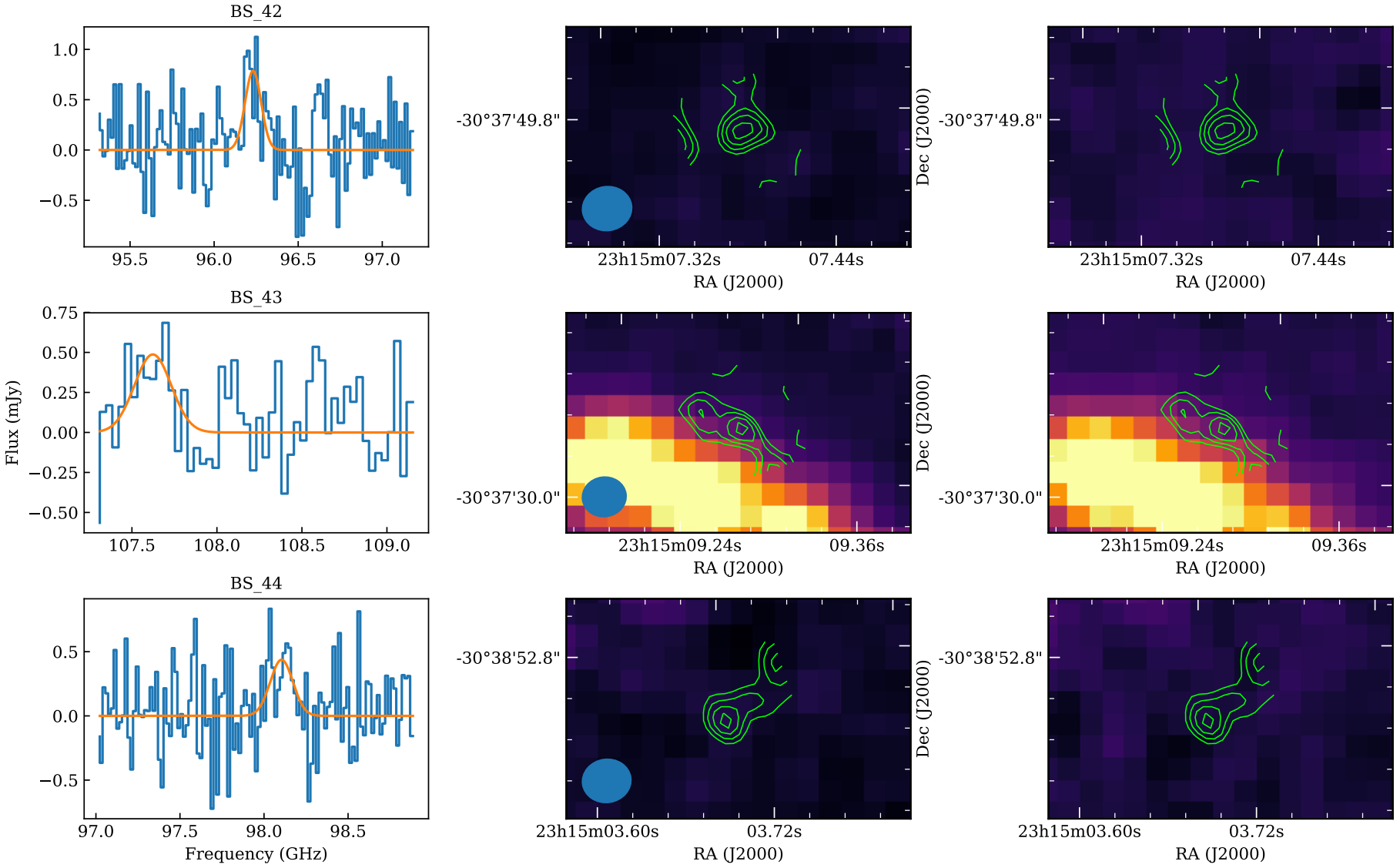

Figure C.17. *(Continued)*

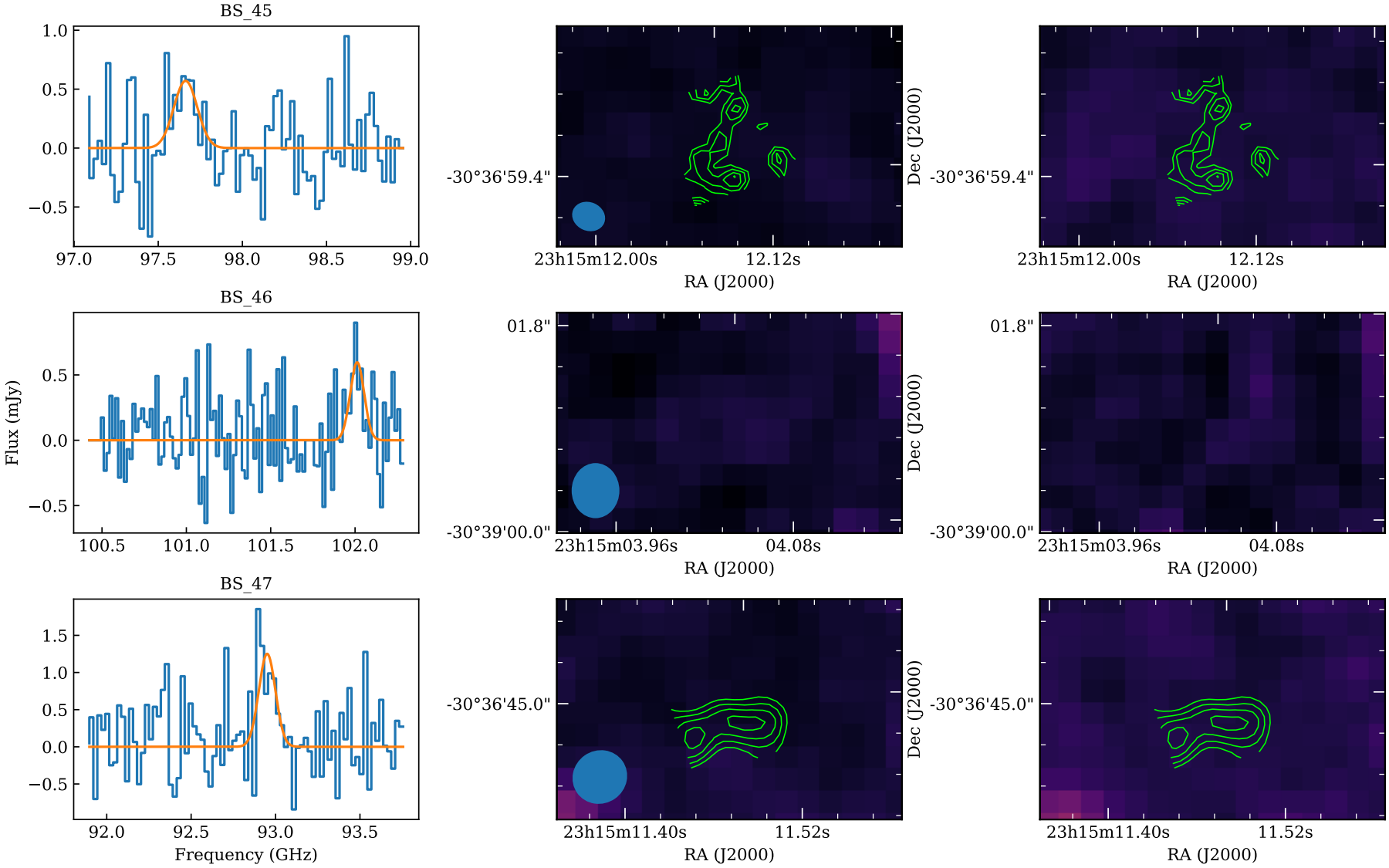

Figure C.18. *(Continued)*

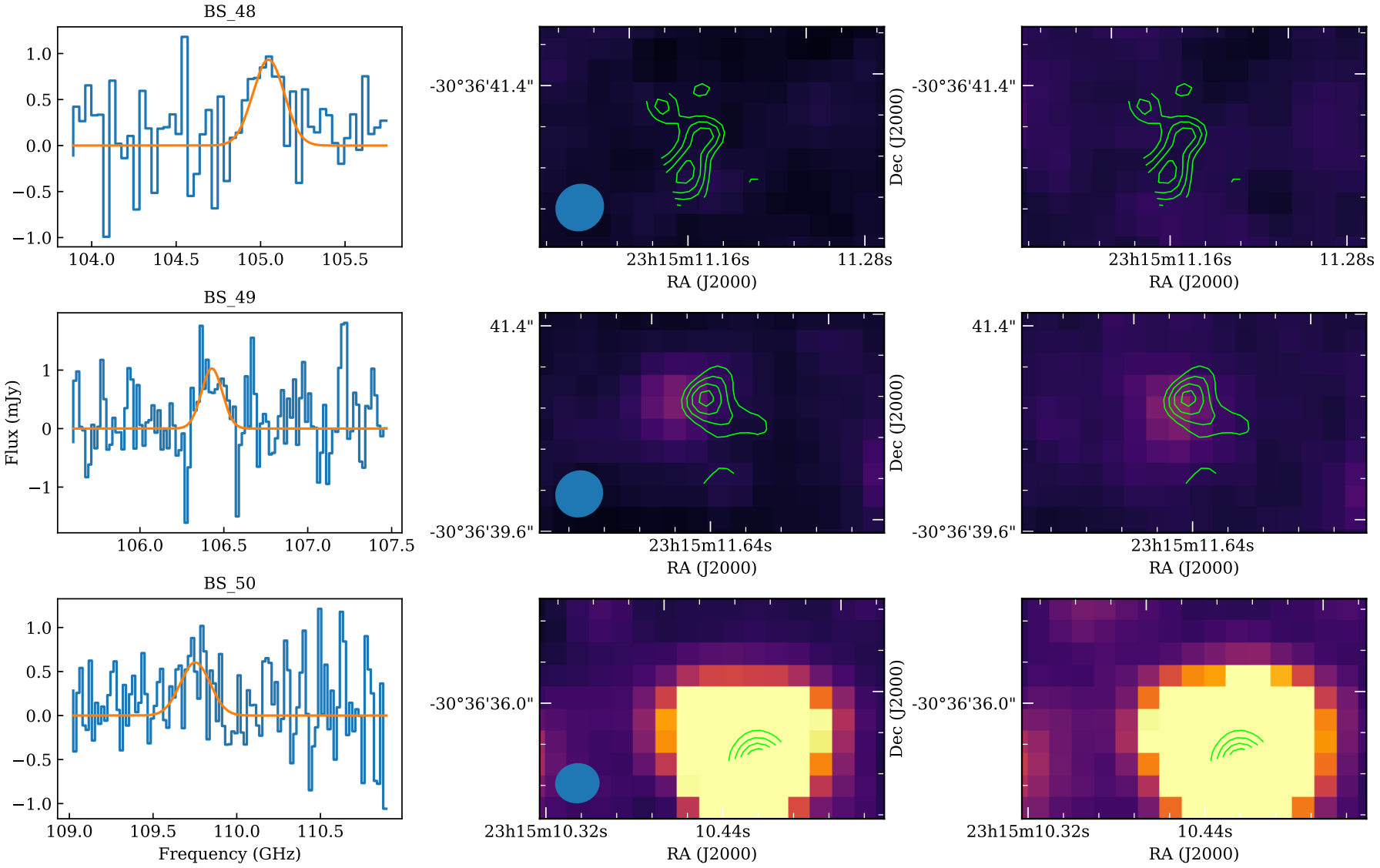

Figure C.19. *(Continued)*

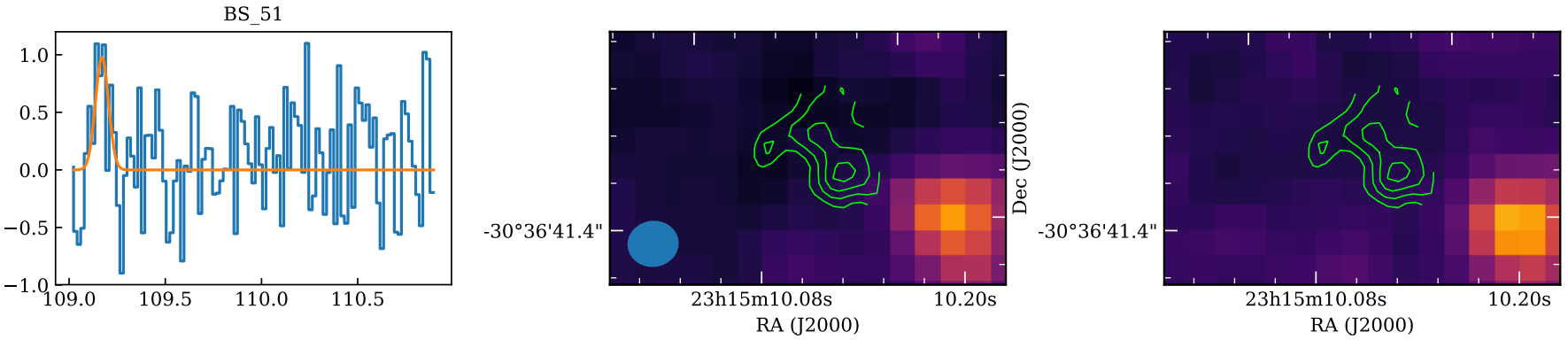

Figure C.20. *(Continued)*

Bibliography

Abell G. O., 1958, *ApJS*, 3, 211

Abell G. O., Corwin Jr. H. G., Olowin R. P., 1989, *ApJS*, 70, 1

Ade P., et al., 2019, J. Cosmology Astropart. Phys., 2019, 056

Aihara H., et al., 2018, *Pub. Astron. Soc. Japan*, 70, S8

Alberts S., et al., 2014, *MNRAS*, 437, 437

Alberts S., et al., 2016, *ApJ*, 825, 72

Almaini O., et al., 2007, in Metcalfe N., Shanks T., eds, Astronomical Society of the Pacific Conference Series Vol. 379, Cosmic Frontiers. p. 163

Andreon S., Huertas-Company M., 2011, *A&A*, 526, A11

Andreon S., Maughan B., Trinchieri G., Kurk J., 2009, *A&A*, 507, 147

Andreon S., Newman A. B., Trinchieri G., Raichoor A., Ellis R. S., Treu T., 2014, *A&A*, 565, A120

Andrews S. K., Driver S. P., Davies L. J. M., Lagos C. d. P., Robotham A. S. G., 2018, *MNRAS*, 474, 898

Appenzeller I., et al., 1998, The Messenger, 94, 1

Aravena M., et al., 2019, *ApJ*, 882, 136

Arrigoni Battaia F., et al., 2018, *A&A*, 620, A202

Ashby M., et al., 2006, in American Astronomical Society Meeting Abstracts 208. p. 145

Bakx T. J. L. C., et al., 2018, *MNRAS*, 473, 1751

Baldry I. K., Balogh M. L., Bower R. G., Glazebrook K., Nichol R. C., Bamford S. P., Budavari T., 2006, *MNRAS*, 373, 469

Barger A. J., Cowie L. L., Sanders D. B., Fulton E., Taniguchi Y., Sato Y., Kawara K., Okuda H., 1998, *Nature*, 394, 248

Barlow M. J., et al., 2010, *A&A*, 518, L138

Basu A., Wadadekar Y., Beelen A., Singh V., Archana K. N., Sirothia S., Ishwara-Chandra C. H., 2015, *ApJ*, 803, 51

Baum W. A., 1959, *PASP*, 71, 106

Beers T. C., Flynn K., Gebhardt K., 1990, *AJ*, 100, 32

Bekki K., 1998, *ApJ*, 502, L133

Bekki K., 1999, *ApJ*, 510, L15

Bekki K., Shioya Y., Couch W. J., 2001, *ApJ*, 547, L17

Bertin E., Arnouts S., 1996, A&AS, 117, 393

Béthermin M., et al., 2012, *A&A*, 542, A58

Bielby R., et al., 2012, *A&A*, 545, A23

Blain A. W., Kneib J. P., Ivison R. J., Smail I., 1999, *ApJ*, 512, L87

Bleem L. E., et al., 2015, *ApJS*, 216, 27

Bolatto A. D., Wolfire M., Leroy A. K., 2013, *ARAA*, 51, 207

Bonaventura N. R., et al., 2017, *MNRAS*, 469, 1259

Boquien M., Burgarella D., Roehlly Y., Buat V., Ciesla L., Corre D., Inoue A. K., Salas H., 2019, *A&A*, 622, A103

Boselli A., Gavazzi G., 2006, *PASP*, 118, 517

Bothwell M. S., et al., 2013, *MNRAS*, 429, 3047

Bourne N., Dunne L., Ivison R. J., Maddox S. J., Dickinson M., Frayer D. T., 2011, *MNRAS*, 410, 1155

Bower R. G., Lucey J. R., Ellis R. S., 1992, *MNRAS*, 254, 589

Brammer G. B., van Dokkum P. G., Coppi P., 2008, *ApJ*, 686, 1503

Brammer G. B., et al., 2011, *ApJ*, 739, 24

Brodwin M., et al., 2012, *ApJ*, 753, 162

Brodwin M., et al., 2013, *ApJ*, 779, 138

Brown M. J. I., et al., 2014, *ApJS*, 212, 18

Bruzual G., Charlot S., 2003, *MNRAS*, 344, 1000

Butcher H., Oemler A. J., 1978, *ApJ*, 219, 18

Calzetti D., et al., 2007, *ApJ*, 666, 870

Capak P. L., et al., 2011, *Nature*, 470, 233

Cappellari M., et al., 2011, *MNRAS*, 416, 1680

Carico D. P., Sanders D. B., Soifer B. T., Elias J. H., Matthews K., Neugebauer G., 1988, *AJ*, 95, 356

Carilli C. L., Walter F., 2013, *ARAA*, 51, 105

Carilli C. L., Yun M. S., 1999, *ApJ*, 513, L13

Casasola V., et al., 2018, preprint, (`arXiv:1806.09493`)

Casey C. M., 2016, *ApJ*, 824, 36

Casey C. M., et al., 2012, *ApJ*, 761, 140

Casey C. M., et al., 2013, *MNRAS*, 436, 1919

Casey C. M., Narayanan D., Cooray A., 2014, *Phys. Repts.*, 541, 45

Casey C. M., et al., 2018, *ApJ*, 862, 77

Cassata P., et al., 2020, arXiv e-prints, p. arXiv:2002.04040

Cavaliere A. G., Gursky H., Tucker W. H., 1971, *Nature*, 231, 437

Cerulo P., et al., 2016, *MNRAS*, 457, 2209

Chapin E. L., et al., 2009, *MNRAS*, 398, 1793

Chapin E. L., et al., 2011, *MNRAS*, 411, 505

Chapin E. L., Berry D. S., Gibb A. G., Jenness T., Scott D., Tilanus R. P. J., Economou F., Holland W. S., 2013, *MNRAS*, 430, 2545

Chapman S. C., Blain A. W., Smail I., Ivison R. J., 2005, *ApJ*, 622, 772

Chapman S. C., et al., 2008, *ApJ*, 689, 889

Charlot S., Fall S. M., 2000, *ApJ*, 539, 718

Chen C.-C., Cowie L. L., Barger A. J., Casey C. M., Lee N., Sanders D. B., Wang W.-H., Williams J. P., 2013, *ApJ*, 762, 81

Chen C.-C., et al., 2016, *ApJ*, 820, 82

Cheng T., et al., 2019, *MNRAS*, 490, 3840

Chiang Y.-K., Overzier R., Gebhardt K., 2013, *ApJ*, 779, 127

Chiang Y.-K., Overzier R. A., Gebhardt K., Henriques B., 2017, *ApJ*, 844, L23

Chung S. M., Eisenhardt P. R., Gonzalez A. H., Stanford S. A., Brodwin M., Stern D., Jarrett T., 2011, *ApJ*, 743, 34

Cibinel A., et al., 2019, *MNRAS*, 485, 5631

Clark C. J. R., Schofield S. P., Gomez H. L., Davies J. I., 2016, *MNRAS*, 459, 1646

Clements D. L., et al., 2014, *MNRAS*, 439, 1193

Clements D. L., et al., 2016, *MNRAS*, 461, 1719

Cochrane R. K., Best P. N., Sobral D., Smail I., Geach J. E., Stott J. P., Wake D. A., 2018, *MNRAS*, 475, 3730

Coia D., et al., 2005, *A&A*, 430, 59

Conselice C. J., Chapman S. C., Windhorst R. A., 2003, *ApJ*, 596, L5

Coogan R. T., et al., 2018, *MNRAS*, 479, 703

Cooke E. A., et al., 2016, *ApJ*, 816, 83

Cooke E. A., Smail I., Stach S. M., Swinbank A. M., Bower R. G., Chen C.-C., Koyama Y., Thomson A. P., 2019, *MNRAS*, 486, 3047

Coppin K., et al., 2006, *MNRAS*, 372, 1621

Cortese L., Gavazzi G., Boselli A., Franzetti P., Kennicutt R. C., O'Neil K., Sakai S., 2006, *A&A*, 453, 847

Couch W. J., Newell E. B., 1984, *ApJS*, 56, 143

Couch W. J., Ellis R. S., Godwin J., Carter D., 1983, *MNRAS*, 205, 1287

Cowie L. L., Barger A. J., Fomalont E. B., Capak P., 2004, *ApJ*, 603, L69

Crocker A. F., Bureau M., Young L. M., Combes F., 2011, *MNRAS*, 410, 1197

Daddi E., Cimatti A., Pozzetti L., Hoekstra H., Röttgering H. J. A., Renzini A., Zamorani G., Mannucci F., 2000, *A&A*, 361, 535

Daddi E., et al., 2009, *ApJ*, 694, 1517

Daddi E., et al., 2010, *ApJ*, 714, L118

Daddi E., et al., 2015, *A&A*, 577, A46

Dannerbauer H., et al., 2014, *A&A*, 570, A55

Dannerbauer H., et al., 2017, *A&A*, 608, A48

Darvish B., Mobasher B., Sobral D., Rettura A., Scoville N., Faisst A., Capak P., 2016, *ApJ*, 825, 113

Davis T. A., et al., 2011, *MNRAS*, 417, 882

De Lucia G., Springel V., White S. D. M., Croton D., Kauffmann G., 2006, *MNRAS*, 366, 499

Decarli R., et al., 2016, *ApJ*, 833, 69

Delahaye A. G., et al., 2017, *ApJ*, 843, 126

Delhaize J., et al., 2017, *A&A*, 602, A4

Dempsey J. T., et al., 2013, *MNRAS*, 430, 2534

Diehl H. T., et al., 2014, in Observatory Operations: Strategies, Processes, and Systems V. p. 91490V, doi:10.1117/12.2056982

Dole H., et al., 2006, *A&A*, 451, 417

Downes A. J. B., Peacock J. A., Savage A., Carrie D. R., 1986, *MNRAS*, 218, 31

Draine B. T., Li A., 2007, *ApJ*, 657, 810

Dressler A., 1980, *ApJ*, 236, 351

Duncan K. J., et al., 2018, *MNRAS*, 473, 2655

Dunne L., Eales S. A., 2001, *MNRAS*, 327, 697

Dunne L., Clements D. L., Eales S. A., 2000, *MNRAS*, 319, 813

Dunne L., Eales S. A., Edmunds M. G., 2003, *MNRAS*, 341, 589

Eales S. A., Wynn-Williams C. G., Duncan W. D., 1989, *ApJ*, 339, 859

Eales S., Lilly S., Gear W., Dunne L., Bond J. R., Hammer F., Le Fèvre O., Crampton D., 1999, *ApJ*, 515, 518

Eales S., et al., 2010, *PASP*, 122, 499

Eales S., et al., 2012, *ApJ*, 761, 168

Eales S., et al., 2015, *MNRAS*, 452, 3489

Eales S. A., et al., 2018, *MNRAS*, 481, 1183

Eddington A. S., 1913, *MNRAS*, 73, 359

Edge A., Sutherland W., Kuijken K., Driver S., McMahon R., Eales S., Emerson J. P., 2013, The Messenger, 154, 32

Efstathiou G., Rees M. J., 1988, *MNRAS*, 230, 5p

Elbaz D., et al., 2007, *A&A*, 468, 33

Elbaz D., et al., 2010, *A&A*, 518, L29

Elbaz D., et al., 2011, *A&A*, 533, A119

Engel H., et al., 2010, *ApJ*, 724, 233

Event Horizon Telescope Collaboration et al., 2019, *ApJ*, 875, L1

Evrard A. E., 1991, *MNRAS*, 248, 8P

Evrard A. E., et al., 2008, *ApJ*, 672, 122

Fabian A. C., 2012, *ARAA*, 50, 455

Fassbender R., et al., 2011, *A&A*, 527, L10

Fazio G. G., et al., 2004, *ApJS*, 154, 10

Franck J. R., McGaugh S. S., 2016, *ApJ*, 833, 15

Franco M., et al., 2018, *A&A*, 620, A152

Frenk C. S., Evrard A. E., White S. D. M., Summers F. J., 1996, *ApJ*, 472, 460

Fujita Y., 2004, *Pub. Astron. Soc. Japan*, 56, 29

Gabor J. M., Bournaud F., 2014, *MNRAS*, 441, 1615

Geach J. E., et al., 2006, *ApJ*, 649, 661

Geach J. E., et al., 2013, *MNRAS*, 432, 53

Geach J. E., et al., 2017, *MNRAS*, 465, 1789

Genzel R., et al., 2015, *ApJ*, 800, 20

Giodini S., Lovisari L., Pointecouteau E., Ettori S., Reiprich T. H., Hoekstra H., 2013, Space Sci. Rev., 177, 247

Girardi M., Biviano A., Giuricin G., Mardirossian F., Mezzetti M., 1993, *ApJ*, 404, 38

Gladders M. D., Yee H. K. C., 2000, *AJ*, 120, 2148

Gobat R., et al., 2011, *A&A*, 526, A133

Gobat R., et al., 2013, *ApJ*, 776, 9

Gobat R., et al., 2019, *A&A*, 629, A104

Gómez-Guijarro C., et al., 2019, *ApJ*, 872, 117

Gómez P. L., et al., 2003, *ApJ*, 584, 210

Gomez H. L., et al., 2012, *MNRAS*, 420, 3557

Gorjian V., Wright E. L., Chary R. R., 1999, ArXiv Astrophysics e-prints,

Goto T., Yamauchi C., Fujita Y., Okamura S., Sekiguchi M., Smail I., Bernardi M., Gomez P. L., 2003, *MNRAS*, 346, 601

Governato F., Baugh C. M., Frenk C. S., Cole S., Lacey C. G., Quinn T., Stadel J., 1998, *Nature*, 392, 359

Greaves J. S., et al., 1998, *ApJ*, 506, L133

Greenslade J., et al., 2018, *MNRAS*, 476, 3336

Greenslade J., et al., 2019, *MNRAS*, 490, 5317

Griffin M. J., et al., 2010, *A&A*, 518, L3

Gunn J. E., Gott III J. R., 1972, *ApJ*, 176, 1

Gursky H., Kellogg E., Murray S., Leong C., Tananbaum H., Giacconi R., 1971, *ApJ*, 167, L81

Gwyn S. D. J., 2012, *AJ*, 143, 38

Haines C. P., Merluzzi P., Mercurio A., Gargiulo A., Krusanova N., Busarello G., La Barbera F., Capaccioli M., 2006, *MNRAS*, 371, 55

Haines C. P., et al., 2013, *ApJ*, 775, 126

Hainline L. J., Blain A. W., Smail I., Frayer D. T., Chapman S. C., Ivison R. J., Alexander D. M., 2009, *ApJ*, 699, 1610

Harris A. I., Baker A. J., Zonak S. G., Sharon C. E., Genzel R., Rauch K., Watts G., Creager R., 2010, *ApJ*, 723, 1139

Hasselfield M., et al., 2013, J. Cosmology Astropart. Phys., 2013, 008

Hayashi M., Kodama T., Koyama Y., Tanaka I., Shimasaku K., Okamura S., 2010, *MNRAS*, 402, 1980

Hayashi M., et al., 2018, *ApJ*, 856, 118

Hazumi M., et al., 2012, LiteBIRD: a small satellite for the study of B-mode polarization and inflation from cosmic background radiation detection. p. 844219, doi:10.1117/12.926743

Herranz D., et al., 2013, *A&A*, 549, A31

Herschel W., 1800, Phil. Trans., 90, 284

Herschel W., 1811, Phil. Trans., 101, 269

Higuchi R., et al., 2019, *ApJ*, 879, 28

Hodge J. A., et al., 2013, *ApJ*, 768, 91

Högbom J. A., 1974, A&AS, 15, 417

Holland W. S., et al., 1998, *Nature*, 392, 788

Holland W. S., et al., 1999, *MNRAS*, 303, 659

Holland W. S., et al., 2013, *MNRAS*, 430, 2513

Hsu L.-Y., Cowie L. L., Chen C.-C., Barger A. J., Wang W.-H., 2016, *ApJ*, 829, 25

Huang J. S., et al., 2014, *ApJ*, 784, 52

Hubble E. P., 1936, Realm of the Nebulae

Hubble E., Humason M. L., 1931, *ApJ*, 74, 43

Hughes D. H., et al., 1998, *Nature*, 394, 241

Hung C.-L., et al., 2013, *ApJ*, 778, 129

Hurley P. D., et al., 2017, *MNRAS*, 464, 885

Husband K., Bremer M. N., Stanway E. R., Davies L. J. M., Lehnert M. D., Douglas L. S., 2013, *MNRAS*, 432, 2869

Ichikawa T., et al., 2006, in Society of Photo-Optical Instrumentation Engineers (SPIE) Conference Series. p. 626916, doi:10.1117/12.670078

Ilbert O., et al., 2015, *A&A*, 579, A2

Ivison R. J., et al., 2002, *MNRAS*, 337, 1

Ivison R. J., et al., 2010, *A&A*, 518, L31

Ivison R. J., Papadopoulos P. P., Smail I., Greve T. R., Thomson A. P., Xilouris E. M., Chapman S. C., 2011, *MNRAS*, 412, 1913

Ivison R. J., et al., 2016, *ApJ*, 832, 78

Jarvis M. J., et al., 2010, *MNRAS*, 409, 92

Jarvis M. J., et al., 2013, *MNRAS*, 428, 1281

Jian H.-Y., et al., 2017, *ApJ*, 845, 74

Jian H.-Y., et al., 2018, *Pub. Astron. Soc. Japan*, 70, S23

Jiang L., et al., 2018, Nature Astronomy, 2, 962

Johnstone D., Bally J., 1999, *ApJ*, 510, L49

Karim A., et al., 2013, *MNRAS*, 432, 2

Kato Y., et al., 2016, *MNRAS*, 460, 3861

Kauffmann G., 1995, *MNRAS*, 274, 153

Kauffmann G., White S. D. M., Heckman T. M., Ménard B., Brinchmann J., Charlot S., Tremonti C., Brinkmann J., 2004, *MNRAS*, 353, 713

Kennicutt R. C., Evans N. J., 2012, *ARAA*, 50, 531

Kessler M. F., et al., 1996, *A&A*, 315, L27

Knudsen K. K., Watson D., Frayer D., Christensen L., Gallazzi A., Michałowski M. J., Richard J., Zavala J., 2017, *MNRAS*, 466, 138

Kodama T., Balogh M. L., Smail I., Bower R. G., Nakata F., 2004, *MNRAS*, 354, 1103

Kong X., et al., 2006, *ApJ*, 638, 72

Kormendy J., Kennicutt Jr. R. C., 2004, *ARAA*, 42, 603

Koyama Y., et al., 2008, *MNRAS*, 391, 1758

Koyama Y., Kodama T., Shimasaku K., Hayashi M., Okamura S., Tanaka I., Tokoku C., 2010, *MNRAS*, 403, 1611

Koyama Y., Kodama T., Nakata F., Shimasaku K., Okamura S., 2011, *ApJ*, 734, 66

Koyama Y., et al., 2013, *MNRAS*, 434, 423

Kurk J. D., Pentericci L., Overzier R. A., Röttgering H. J. A., Miley G. K., 2004, *A&A*, 428, 817

Lacaille K., et al., 2018, arXiv e-prints,

Lagage P. O., Claret A., Ballet J., Boulanger F., Cesarsky C. J., Cesarsky D., Fransson C., Pollock A., 1996, *A&A*, 315, L273

Lamarre J. M., et al., 2010, *A&A*, 520, A9

Larson R. B., Tinsley B. M., Caldwell C. N., 1980, *ApJ*, 237, 692

Lawrence A., et al., 2007, *MNRAS*, 379, 1599

Le Floc'h E., et al., 2005, *ApJ*, 632, 169

Leavitt H. S., Pickering E. C., 1912, Harvard College Observatory Circular, 173, 1

Lee M. M., et al., 2019, arXiv e-prints, p. arXiv:1909.02028

Lehnert M. D., van Driel W., Le Tiran L., Di Matteo P., Haywood M., 2015, *A&A*, 577, A112

Lemaux B. C., et al., 2018, *A&A*, 615, A77

Lewis I., et al., 2002, *MNRAS*, 334, 673

Lewis A. J. R., et al., 2018, *ApJ*, 862, 96

Lilly S. J., Eales S. A., Gear W. K. P., Hammer F., Le Fèvre O., Crampton D., Bond J. R., Dunne L., 1999, *ApJ*, 518, 641

Lin L., et al., 2014, *ApJ*, 782, 33

Liu D., et al., 2019, *ApJ*, 887, 235

Lonsdale C. J., et al., 2003, *PASP*, 115, 897

Luo W., Yang X., Zhang Y., 2014, *ApJ*, 789, L16

Ma C.-J., et al., 2015, *ApJ*, 806, 257

Madau P., Dickinson M., 2014, *ARAA*, 52, 415

Maddox S. J., et al., 2018, *ApJS*, 236, 30

Magdis G. E., et al., 2017, *A&A*, 603, A93

Magnelli B., et al., 2010, *A&A*, 518, L28

Magnelli B., et al., 2015, *A&A*, 573, A45

Maiolino R., et al., 2015, *MNRAS*, 452, 54

Małek K., et al., 2018, *A&A*, 620, A50

Mancuso C., Lapi A., Shi J., Cai Z. Y., Gonzalez-Nuevo J., Béthermin M., Danese L., 2016, *ApJ*, 833, 152

Mantz A. B., Allen S. W., Morris R. G., Simionescu A., Urban O., Werner N., Zhuravleva I., 2017, *MNRAS*, 472, 2877

Marcillac D., et al., 2008, *ApJ*, 675, 1156

Marriage T. A., et al., 2011, *ApJ*, 737, 61

Marsden G., et al., 2009, *ApJ*, 707, 1729

Martinache C., et al., 2018, *A&A*, 620, A198

Mauduit J.-C., et al., 2012, *PASP*, 124, 714

McAlpine S., et al., 2019, *MNRAS*, p. 1605

McMullin J. P., Waters B., Schiebel D., Young W., Golap K., 2007, CASA Architecture and Applications. p. 127

Meekins J. F., Fritz G., Chubb T. A., Friedman H., 1971, *Nature*, 231, 107

Mei S., et al., 2015, *ApJ*, 804, 117

Messier C., 1784, Connaissance des Temps

Metcalfe L., Fadda D., Biviano A., 2005, Space Sci. Rev., 119, 425

Michałowski M., Hjorth J., Watson D., 2010, *A&A*, 514, A67

Michałowski M. J., et al., 2017, *MNRAS*, 469, 492

Miettinen O., et al., 2017a, *A&A*, 606, A17

Miettinen O., et al., 2017b, *A&A*, 606, A17

Mihos J. C., 2004, in Mulchaey J. S., Dressler A., Oemler A., eds, Clusters of Galaxies: Probes of Cosmological Structure and Galaxy Evolution. p. 277

Millard J. S., et al., 2020, *MNRAS*, 494, 293

Miller T. B., et al., 2018, *Nature*, 556, 469

Miyazaki S., et al., 2002, *Pub. Astron. Soc. Japan*, 54, 833

Moore B., Katz N., Lake G., Dressler A., Oemler A., 1996, *Nature*, 379, 613

Moorwood A., et al., 1998, The Messenger, 94, 7

Moran S. M., Ellis R. S., Treu T., Smith G. P., Rich R. M., Smail I., 2007, *ApJ*, 671, 1503

Moss C., 2006, *MNRAS*, 373, 167

Murakami H., et al., 2007, *Pub. Astron. Soc. Japan*, 59, S369

Negrello M., González-Nuevo J., Magliocchetti M., Moscardini L., De Zotti G., Toffolatti L., Danese L., 2005, *MNRAS*, 358, 869

Neugebauer G., et al., 1984, *ApJ*, 278, L1

Newman A. B., Ellis R. S., Andreon S., Treu T., Raichoor A., Trinchieri G., 2014, *ApJ*, 788, 51

Noble A. G., et al., 2012, *MNRAS*, 419, 1983

Noble A. G., et al., 2017, preprint, (`arXiv:1705.03062`)

Noeske K. G., et al., 2007, *ApJ*, 660, L43

Oliver S. J., et al., 2012, *MNRAS*, 424, 1614

Onoue M., et al., 2018, *Pub. Astron. Soc. Japan*, 70, S31

Oteo I., et al., 2018, *ApJ*, 856, 72

Ouchi M., et al., 2013, *ApJ*, 778, 102

Overzier R. A., 2016, A&A Rev., 24, 14

Papadopoulos P. P., van der Werf P. P., Xilouris E. M., Isaak K. G., Gao Y., Mühle S., 2012, *MNRAS*, 426, 2601

Pascale E., et al., 2009, *ApJ*, 707, 1740

Pavesi R., et al., 2018a, *ApJ*, 861, 43

Pavesi R., et al., 2018b, *ApJ*, 864, 49

Pearson E. A., et al., 2013, *MNRAS*, 435, 2753

Peng Y.-j., et al., 2010, *ApJ*, 721, 193

Peng Y., Maiolino R., Cochrane R., 2015, *Nature*, 521, 192

Pilbratt G. L., et al., 2010, *A&A*, 518, L1

Poglitsch A., et al., 2010, *A&A*, 518, L2

Pope A., et al., 2006, *MNRAS*, 370, 1185

Popesso P., et al., 2012, *A&A*, 537, A58

Prichard L. J., et al., 2017, *ApJ*, 850, 203

Raichoor A., Andreon S., 2012, *A&A*, 537, A88

Richstone D. O., 1976, *ApJ*, 204, 642

Riechers D. A., et al., 2010, *ApJ*, 720, L131

Riechers D. A., et al., 2013, *Nature*, 496, 329

Riechers D. A., et al., 2017, *ApJ*, 850, 1

Rosati P., Borgani S., Norman C., 2002, *ARAA*, 40, 539

Rudnick G., et al., 2017, *ApJ*, 849, 27

Rujopakarn W., et al., 2016, *ApJ*, 833, 12

Saintonge A., Tran K.-V. H., Holden B. P., 2008, *ApJ*, 685, L113

Salvato M., et al., 2009, *ApJ*, 690, 1250

Santos J. S., et al., 2013, *MNRAS*, 433, 1287

Santos J. S., et al., 2014, *MNRAS*, 438, 2565

Santos J. S., et al., 2015, *MNRAS*, 447, L65

Sargent M. T., et al., 2014, *ApJ*, 793, 19

Schwan D., et al., 2003, New A Rev., 47, 933

Scoville N., et al., 2014, *ApJ*, 783, 84

Scoville N., et al., 2016, *ApJ*, 820, 83

Scoville N., et al., 2017, *ApJ*, 837, 150

Sekiguchi K., 1987, *ApJ*, 316, 145

Serjeant S., et al., 2003, *MNRAS*, 344, 887

Shimakawa R., Kodama T., Tadaki K.-i., Tanaka I., Hayashi M., Koyama Y., 2014, *MNRAS*, 441, L1

Shimakawa R., et al., 2018, *MNRAS*, 473, 1977

Shirley R., et al., 2019, *MNRAS*, 490, 634

Silva A., et al., 2018, *ApJ*, 868, 46

Smail I., Ivison R. J., Blain A. W., 1997, *ApJ*, 490, L5

Smail I., Ivison R. J., Blain A. W., Kneib J. P., 2002, *MNRAS*, 331, 495

Smail I., et al., 2014, *ApJ*, 782, 19

Smith S., 1936, *ApJ*, 83, 23

Smith G. P., Treu T., Ellis R. S., Moran S. M., Dressler A., 2005, *ApJ*, 620, 78

Smith M. W. L., et al., 2012a, *ApJ*, 748, 123

Smith M. W. L., et al., 2012b, *ApJ*, 756, 40

Smith M. W. L., et al., 2017, *ApJS*, 233, 26

Smith M. W. L., et al., 2019a, *MNRAS*, 486, 4166

Smith C. M. A., Gear W. K., Smith M. W. L., Papageorgiou A., Eales S. A., 2019b, *MNRAS*, 486, 4304

Solomon P. M., Downes D., Radford S. J. E., 1992, *ApJ*, 398, L29

Solomon P. M., Downes D., Radford S. J. E., Barrett J. W., 1997, *ApJ*, 478, 144

Spilker J. S., Bezanson R., Marrone D. P., Weiner B. J., Whitaker K. E., Williams C. C., 2016, *ApJ*, 832, 19

Spilker J., et al., 2018, *ApJ*, 860, 103

Stach S. M., Swinbank A. M., Smail I., Hilton M., Simpson J. M., Cooke E. A., 2017, *ApJ*, 849, 154

Staniszewski Z., et al., 2009, *ApJ*, 701, 32

Steidel C. C., Adelberger K. L., Shapley A. E., Erb D. K., Reddy N. A., Pettini M., 2005, *ApJ*, 626, 44

Strazzullo V., et al., 2013, *ApJ*, 772, 118

Strazzullo V., et al., 2016, *ApJ*, 833, L20

Strazzullo V., et al., 2018, *ApJ*, 862, 64

Strazzullo V., et al., 2019, *A&A*, 622, A117

Struble M. F., Rood H. J., 1999, *ApJS*, 125, 35

Sturm E., et al., 1996, *A&A*, 315, L133

Sunyaev R. A., Zeldovich Y. B., 1972, Comments on Astrophysics and Space Physics, 4, 173

Suzuki R., et al., 2008, *Pub. Astron. Soc. Japan*, 60, 1347

Suzuki T. L., Minowa Y., Koyama Y., Kodama T., Hayashi M., Shimakawa R., Tanaka I., Tadaki K.-i., 2019, *Pub. Astron. Soc. Japan*, 71, 69

Swinbank A. M., Chapman S. C., Smail I., Lindner C., Borys C., Blain A. W., Ivison R. J., Lewis G. F., 2006, *MNRAS*, 371, 465

Tacchella S., Dekel A., Carollo C. M., Ceverino D., DeGraf C., Lapiner S., Mand elker N., Primack Joel R., 2016, *MNRAS*, 457, 2790

Tacconi L. J., et al., 2008, *ApJ*, 680, 246

Tacconi L. J., et al., 2010, *Nature*, 463, 781

Tacconi L. J., et al., 2018, *ApJ*, 853, 179

Tadaki K.-i., et al., 2019, *Pub. Astron. Soc. Japan*, 71, 40

Tan Q., et al., 2014, *A&A*, 569, A98

Tanaka I., et al., 2011, *Pub. Astron. Soc. Japan*, 63, 415

Tonry J. L., et al., 2012, *ApJ*, 745, 42

Tran K.-V. H., et al., 2010, *ApJ*, 719, L126

Turner E. L., 1991, *AJ*, 101, 5

Umehata H., et al., 2015, *ApJ*, 815, L8

Vaccari M., 2016, The Universe of Digital Sky Surveys, 42, 71

Valentino F., et al., 2018, *ApJ*, 869, 27

Vidal-Madjar A., Lecavelier des Etangs A., Désert J. M., Ballester G. E., Ferlet R., Hébrard G., Mayor M., 2003, *Nature*, 422, 143

Wagner C. R., Courteau S., Brodwin M., Stanford S. A., Snyder G. F., Stern D., 2017, *ApJ*, 834, 53

Walter F., Weiß A., Downes D., Decarli R., Henkel C., 2011, *ApJ*, 730, 18

Walter F., et al., 2012, *Nature*, 486, 233

Walter F., et al., 2016, *ApJ*, 833, 67

Wang L., et al., 2013, *MNRAS*, 431, 648

Wang T., et al., 2016, *ApJ*, 828, 56

Wang W.-H., et al., 2017, *ApJ*, 850, 37

Wang T., et al., 2018, *ApJ*, 867, L29

Wardlow J. L., et al., 2011, *MNRAS*, 415, 1479

Webb T. M. A., et al., 2013, *AJ*, 146, 84

Webb T., et al., 2015, *ApJ*, 809, 173

Weinmann S. M., van den Bosch F. C., Yang X., Mo H. J., 2006, *MNRAS*, 366, 2

Weiß A., et al., 2013, *ApJ*, 767, 88

Werner M. W., et al., 2004, *ApJS*, 154, 1

Whitaker K. E., et al., 2011, *ApJ*, 735, 86

White M., Cohn J. D., Smit R., 2010, *MNRAS*, 408, 1818

Williams C. C., et al., 2014, *ApJ*, 780, 1

Wright T., 1750, An original theory or new hypothesis of the universe., doi:10.3931/e-rara-28672.

Wright E. L., Reese E. D., 2000, *ApJ*, 545, 43

Wright E. L., et al., 2010, *AJ*, 140, 1868

Wu J. F., et al., 2018, *ApJ*, 853, 195

Yun M. S., et al., 2008, *MNRAS*, 389, 333

Zavala J. A., et al., 2019, *ApJ*, 887, 183

Zeimann G. R., et al., 2012, *ApJ*, 756, 115

Zeimann G. R., et al., 2013, *ApJ*, 779, 137

Zhu Y.-N., Wu H., Li H.-N., Cao C., 2010, Research in Astronomy and Astrophysics, 10, 329

Zolotov A., et al., 2015, *MNRAS*, 450, 2327

Zwicky F., 1937, *ApJ*, 86, 217

al-Sufi A. a.-R., 964, Book of Fixed Stars

de Graauw T., et al., 2010, *A&A*, 518, L6

du Châtelet E., 1737, Dissertation sur la nature et la propagation du feu